https://journals.vsu.ru/kcmf/about

ISSN 1606-867X
eISSN 2687-0711

Конденсированные среды и межфазные границы

РЕЦЕНЗИРУЕМЫЙ НАУЧНЫЙ ЖУРНАЛ

Condensed Matter and Interphases

Kondensirovannye Sredy i Mezhfaznye Granitsy

PEER-REVIEWED SCIENTIFIC JOURNAL

Том / Vol. 24, № / No. 1
2022

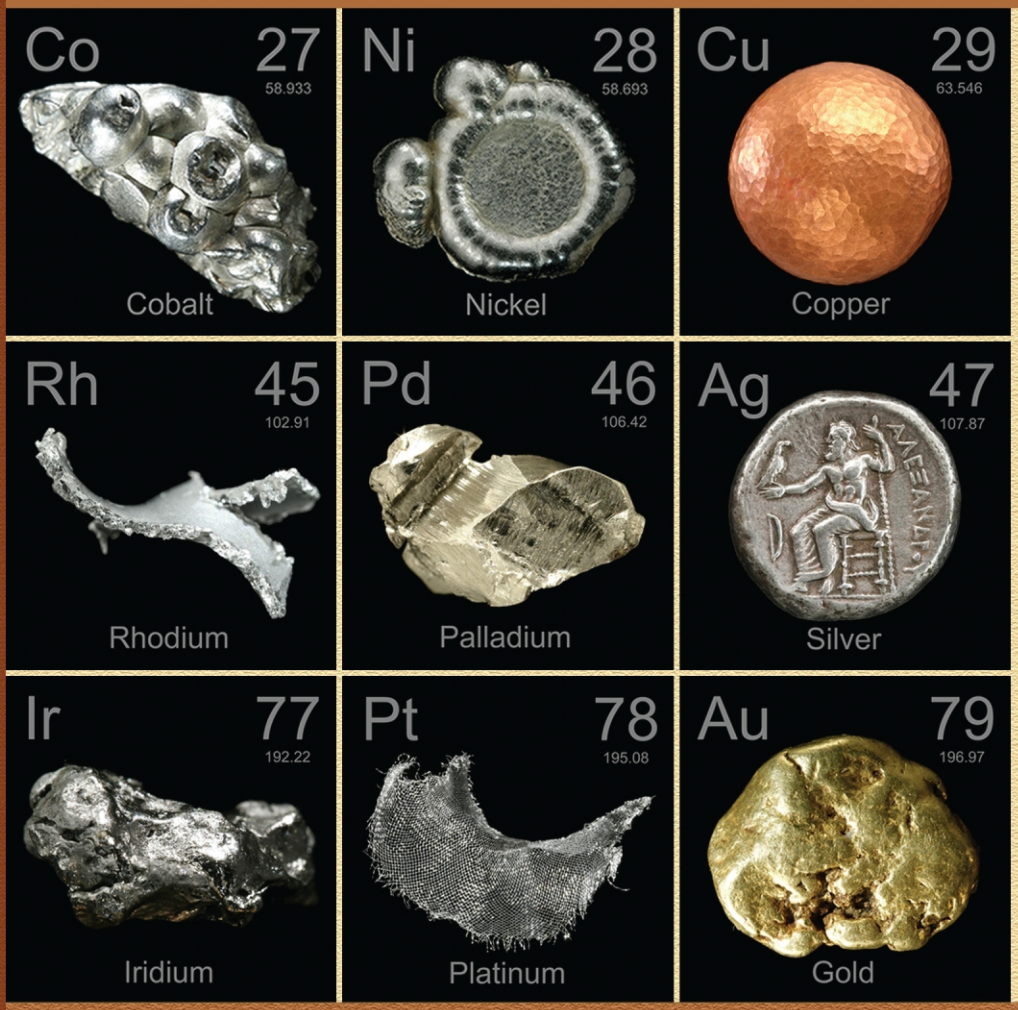

Condensed Matter and Interphases
Kondensirovannye sredy i mezhfaznye granitsy

Peer-reviewed scientific journal
Published since January 1999
Periodicity: Quarterly
Volume 24, No. 1, 2022

Full-text version is available in the Russian language on the website: https://journals.vsu.ru/kcmf

Condensed Matter and Interphases (Kondensirovannye Sredy i Mezhfaznye Granitsy) publishes articles in Russian and English dedicated to key issues of condensed matter and physicochemical processes at interfaces and in volumes.

The mission of the journal is to provide open access to the results of original research (theoretical and experimental) at the intersection of contemporary condensed matter physics and chemistry, material science and nanoindustry, solid state chemistry, inorganic chemistry, and physical chemistry, and to share scientific data in the **following sections**: atomic, electron, and cluster structure of solids, liquids, and interphase boundaries; phase equilibria and defect formation processes; structure and physical and chemical properties of interphases; laser thermochemistry and photostimulated processes on solid surfaces; physics and chemistry of surface, thin films and heterostructures; kinetics and mechanism of formation of film structures; electrophysical processes in interphase boundaries; chemistry of surface phenomena in sorbents; devices and new research methods.

The journal accepts for publication: reviews, original articles, short communications by leading Russian scientists, foreign researchers, lecturers, postgraduate and undergraduate students.

FOUNDER AND PUBLISHER:
Voronezh State University

The journal is registered by the Russian Federal Service for Supervision of Communications, Information Technology and Mass Media, Certificate of Registration ПИ № ФС77-78771 date 20.07.2020

The journal is included in the List of peer reviewed scientific journals published by the Higher Attestation Commission in which major research results from the dissertations of Candidates of Sciences (PhD) and Doctor of Science (DSc) degrees are to be published. Scientific specialties of dissertations and their respective branches of science are as follows: 1.4.1 – Inorganic Chemistry, 1.4.4 – Physical Chemistry, 1.4.6 – Electrochemistry, 1.4.15 – Solid State Chemistry (Chemical sciences); 1.3.8 – Condensed Matter Physics (Physical Sciences)

The journal is indexed and archived in: Russian Scientific Index Citations, Scopus, Chemical Abstract, EBSCO, DOAJ, CrossRef

Editorial Board and Publisher Office:
1 Universitetskaya pl., Voronezh 394018
Phone: +7 (432) 2208445
https://journals.vsu.ru/kcmf
E-mail: kcmf@main.vsu.ru

Signed for printing 30.03.2022

Price – not fixed

Subscription index in the Catalogue «Russian Post» is ПН134

CONTENTS

Agaeva R. M., Mammadov Sh. H., Azhdarova D. S., Ragimova V. M., Aliyev O. M.
Synthesis and study of the properties of synthetic analogues of the mineral naffildite with the participation of rare earth elements 3

Alakbarova T. M., Meyer H.-J., Orujlu E. N., Babanly M. B.
A refined phase diagram of the GeTe-Bi_2Te_3 system 11

Haiduk Yu. S., Korobko E. V., Kotsikau D. A., Svito I. A., Usenka A. E., Pankov V. V.
Preparation and characterisation of cobalt and cobalt-zinc ferrites for magnetorheological materials 19

Zlomanov V. P., Eshmakov R. S., Prolubshchikov I. V.
Formation of a solvate of manganese(III) acetylacetonate with chloroform 29

Kovaleva A. S., Sladkopevtsev B. V., Samsonov A. A., Alferova S. I., Kovalev D. G., Titov S. A., Pryakhin N. D., Mittova I. Ya.
The influence of the physicochemical nature of the components of the V_2O_5/GaAs, MnO_2/GaAs, V_2O_5/InP, MnO_2/InP, TiO_2/InP, and SnO_2/InP heterostructures and the oxidation conditions on the surface morphology of the synthesised films 33

Kozlov G. V., Dolbin I. V.
The interconnection of efficiency and the degree of aggregation of nanofiller in polymer nanocomposites 45

Lenshin A. S., Seredin P. V., Zolotukhin D. S., Beltyukov A. N., Mizerov A. M., Kasatkin I. A., Radam A. O., Domashevskaya E. P.
Characteristics of the formation and composition of $Al_xGa_{1-x}N$/AlN/por-Si/Si(111) heterostructures grown using a porous silicon buffer layer 51

Lyapun D. V., Kruzhilin A. A., Shevtsov D. S., Aseeva Yu. V., Shikhaliev Kh. S.
Corrosion inhibition of steel by selected homologues of the class 3-alkyl-5-amino-1H-1,2,4-triazoles in acidic media 59

Maslov V. A., Kravtsov S. B., Novikov I. A., Usachev V. A., Fedorov P. P., Tsvetkov V. B., Yarotskaya E. G.
Specifics of the formation of regular opal structures from spherical silica particles in various colloidal solutions 69

Menshchikov V. S., Belenov S. V., Nikulin A. Yu.
Effect of the morphology and composition of trimetallic PtCuAu/C catalysts on the activity and stability of the methanol oxidation reaction 76

Tretyakova V. V., Panteleeva V. V., Shein A. B.
The kinetics of cathodic hydrogen evolution on titanium disilicide in a sulphuric acid solution 88

Tutov E. A., Alekseeva E. V., Samoylov A. M., Berezina O. Ya., Boriskov P. P.
Effect of ethanol vapour sorption on the semiconductor-metal phase transition in powdered vanadium dioxide 95

Fedoseev V. B., Fedoseeva E. N.
Polycondensation in a spray of aqueous-alcoholic solution of lactic acid 101

Hoang Bao Khanh, Mittova V. O., Nguyen Anh Tien, Pham Thi Hong Duyen
Structural and magnetic properties of Ho-doped $CuFe_2O_4$ nanoparticles prepared by a simple co-precipitation method 109

Shvedova M. A., Artamonova O. V., Slavcheva G. S.
Investigation of the effect of a multicomponent additive on the structure formation and hardening of cement composites 116

Afonin N. N., Logachova V. A.
A model of interdiffusion occurring during the formation of thin metal films on single-crystal silicon under conditions of limited solubility of the components 129

Professor Mahammad B. Babanly's anniversary 136

Guide for Authors – 2022 139

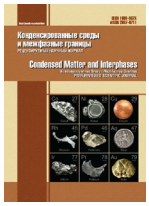

ISSN 1606-867X (Print)
ISSN 2687-0711 (Online)
Condensed Matter and Interphases
Kondensirovannye Sredy i Mezhfaznye Granitsy
https://journals.vsu.ru/kcmf/

Original articles

Research article
https://doi.org/10.17308/kcmf.2022.24/9049

Synthesis and study of the properties of synthetic analogues of the mineral naffildite with the participation of rare earth elements

R. M. Agaeva[2], Sh. H. Mammadov[1]✉, D. S. Azhdarova[1], V. M. Ragimova[1], O. M. Aliyev[1]

[1]*Nagiev Institute of Catalysis and Inorganic Chemistry of Azerbaijan National Academy of Sciences, 113 G. Javid ave., Baku, Az1143, Azerbaijan*

[2]*Azerbaijan State Pedagogical University, 68 G. Hajibekli ave., Baku, AZ1000, Azerbaijan*

Abstract

In recent years, there has been a significant increase in interest in ternary and quaternary compounds with the participation of rare earth elements (REE), as well as copper, antimony, and bismuth, which have a wider range of physical properties. Due to their valuable physical properties, they have become promising targets of research for modern materials science. Therefore, the purpose of this work is to study the properties of synthetic analogues of naffildite with the participation of rare earth elements.

The samples were synthesised from ternary sulphides (in the case of obtaining $Cu_2LaSb_3S_7$, $Cu_2CeSb_3S_7$, $Cu_2PrSb_3S_7$ and $Cu_2NdSb_3S_7$) by fusion in sealed quartz ampoules, preliminarily evacuated to a residual pressure of 10^{-3} mmHg at 950–1100 K for 8 hours. The remaining antimony and bismuth-containing analogues, due to the peritectic nature of formation, were synthesised through batches (2Cu + Ln + 3Sb(Bi) + 7S) from especially pure elements. After completion of the reaction, homogenizing annealing was carried out for a month at 600–700 K, depending on the composition. The obtained samples were investigated by differential thermal (DTA), X-ray phase (XRD) and microstructural (MSA) analyzes, as well as by measuring the microhardness and determining the density.

Compounds of the $Cu_2LnSb_3S_7$ or $Cu_2LnBi_3S_7$ (Ln – REE) type have been synthesised by direct synthesis from elements or from the ligature $CuSbS_2$($CuBiS_2$) and $LnSbS_3$($LnBiS_3$). It was found that they are isostructural and crystallize in the orthorhombic system ($Cu_2LnSb_3S_7$ – a = 14.490÷14.264, b = 21.422÷21.206, c = 3.902–3.804 Å; $Cu_2LnBi_3S_7$ – a = 14.722÷14.506, b = 21.864÷21.564, c = 4.142÷3.464 Å; Z = 4, simple group Pbnm or $Pbn2_1$) and belong to the structure type of naffildite Pb_2Cu (Pb, Bi) Bi_2S_7. $Cu_2LaSb_3S_7$, $Cu_2PrSb_3S_7$ and $Cu_2NdSb_3S_7$ melt congruently at 975, 985, and 1015 K, respectively, and other compounds are formed by a peritectic reaction.

Keywords: Compound, Crystal structure, Naffildite, Lattice parameters, Electrical conductivity, Thermal electromotive force

For citation: Agaeva R. M., Mammadov Sh. H., Azhdarova D. S., Ragimova V. M., Aliyev O. M. Synthesis and study of the properties of synthetic analogues of the mineral naffildite with the participation of rare earth elements. *Kondensirovannye sredy i mezhfaznye granitsy = Condensed Matter and Interphases.* 2022;24(1): 3–10. https://doi.org/10.17308/kcmf.2022.24/9049

Для цитирования: Агаева Р. М., Мамедов Ш. Г., Аждарова Д. С., Рагимова В. М., Алиев О. М. Синтез и изучение свойств синтетических аналогов минерала наффильдита с участием редкоземельных элементов. *Конденсированные среды и межфазные границы*. 2022;24(1): 3–10. https://doi.org/10.17308/kcmf.2022.24/9049

✉ Sharafat H Mammadov, e-mail: azxim@mail.ru

1. Introduction

In recent years, there has been a significant increase in interest in ternary and quaternary compounds with the participation of rare earth elements (REE), as well as copper, antimony, and bismuth, which have a wider range of physical properties. Due to their valuable physical properties, they have become promising targets of research for modern materials science [1–3].

Crystal chemical substantiation and obtaining new classes of compounds based on known structures is of great importance. Therefore, obtaining and studying the physicochemical properties of analogues of naffildite allows to expand the range of complex compounds. Therefore, the purpose of this work is to study the properties of synthetic analogues of naffildite with the participation of rare earth elements.

The crystal structure of naffildite was first determined in [4]. Naffildite crystallizes in the orthorhombic syngony and has the following unit cell parameters: a = 14.387 (7), b = 21.011 (5), c = 4.46 (6) Å, space group Pbnm or $Pbn2_1$, Z = 4.

The bases of the naffildite structure contain ten-element complex ribbons. These ten-element ribbons are connected on both sides with Pb, Bi and randomly spaced Pb, Bi. The latter consists of aikinite ribbons [5]. It should be noted that the authors of [6], when considering the crystal chemistry of homologues of stibnite Sb_2S_3 also referred to the naffildite structure. They found that stibnite ribbons are the main element of many natural and synthetic sulphosalts. Subsequently, in [9–11], it was established that the crystal structures of a number of synthetic compounds, in particular, $Pb_4Sb_6S_{13}$, $Pb_{4.75}Bi_{4.1}S_{11.2}$, $Pb_4Sb_4S_{11}$ and others are composed of complex combinations of semi-octahedral ribbons.

When considering the crystal chemistry of complex sulphides [12, 13], it was found that the structure of naffildite is connected on both sides with common sulphur atoms by four elemental ribbons of aikinite $[CuPb_2Bi_2S_6]_8$. Here Cu atoms play the role of a cementing cation. However, the monograph [13] lists only the unit cell parameters, interplanar distances, and intensities of diffraction lines of naffildite. Fig. 1a shows ribbon structures and representation of a naffildite structure with Pauling polyhedra is shown in Fig. 1b.

As can be seen from Fig. 1b, four of the lead atoms are arranged in eight-dimensional

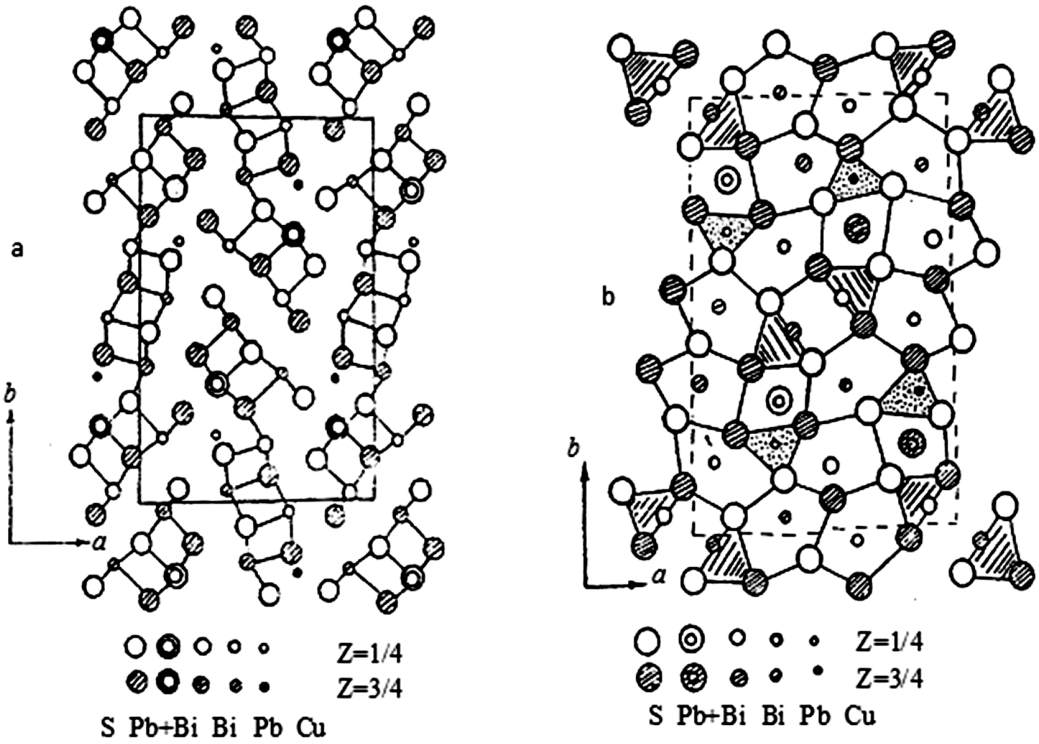

Fig. 1. The crystal structure of naffildite: a – ribbon representation; b – representation with a Pauling polyhedra

(trigonal prisms plus two hemi-octahedrons), four Pb atoms and four Bi atoms are arranged in seven-dimensional (hemi-octahedron plus trigonal prism) coordinations. Four Bi atoms are located in the plane at the centre of the hemi-octahedron and have a five-fold coordination. Two Pb atoms and two Bi atoms randomly fill polyhedra consisting of a hemi-octahedron and a trigonal prism which are parallel in a plane. Four Cu atoms are arranged in tetrahedra. They form a quadruple coordination and play the role of a cementing cation. Taking in consideration the aforementioned, the crystal chemical formula of naffildite can be represented as follows:

$$Cu_4Pb_{10}Bi_{10}S_{28} \rightarrow$$
$$\rightarrow {}^{VI}Cu_4\,{}^{VII}Pb_4\,{}^{VIII}Pb_4\,{}^{VII}(Pb, Bi)_4\,{}^{VI}Bi_4\,{}^{V}Bi_4\,S_{28}$$

Thus, the crystal structure of naffildite consists of several polyhedra with complex configurations. It should be noted that this complexity of the configuration of polyhedra allows us to obtain a synthetic homologous series of naffildite by the substitution of cations with the corresponding atoms.

It is known that the CN of lanthanides in complex sulphides varies from 6 to 9 [14], the coordination polyhedra in them are mainly octahedron, trigonal prism, one-, two- and tricapped trigonal prisms. Therefore, the possibility of obtaining new classes of compounds with substitution of Pb in a naffildite structure, which has sevenfold coordination with Eu^{2+} or Yb^{2+}cations (statistically arranged Pb, Bi atoms) with compensating Bi^{3+}cations, located in hemi-octahedra, substituting Sb^{3+} and Ln^{3+} with the naffildite structure, was proposed.

Earlier, we synthesised and studied the properties of synthetic lanthanum and neodymium-containing analogues of the mineral naffildite [15], berthierite [16, 17], aikinite, $CuPbBi_3S_6$ [18], and bournonite $CuPbSbS_3$ [19,20]. Based on this, this study presents the results of the synthesis, X-ray study, and physiochemical properties of analogues of naffildite with other rare earth elements.

2. Experimental

The starting ternary compounds ($CuSbS_2$, $CuBiS_2$, $LnSbS_3$ and $LnBiS_3$) were studied in detail in [1, 21, 22]. For the determination of the optimal mode of synthesis and growth of single crystals of $Cu_2LnSb_3S_7$ and $Cu_2LnBi_3S_7$ compounds, derived from the structure of naffildite, differential thermal (DTA), X-ray phase (XRD) and microstructural (MSA) analyses, as well as by determination of the microhardness and density were performed. DTA was performed using an NTR-70 Kurnakov thermograph in the temperature range of 298–1200 K. The heating rate was10 deg/min. Aluminium oxide was used as a standard [23].

X-ray diffraction patterns were recorded using a Bruker D2 PHASER diffractometer (CuK_α-radiation, Ni - filter); MSA was performed using an MIM-8 microscope. The microhardness was measured using a PMT-3 microhardness tester with the loads selected as a result of measuring the microhardness of each phase, and the density was determined by the pycnometric method.

Samples were synthesised from ternary sulphides (in the case of obtaining $Cu_2LaSb_3S_7$, $Cu_2CeSb_3S_7$, $Cu_2PrSb_3S_7$ and $Cu_2NdSb_3S_7$) in sealed quartz ampoules, preliminarily evacuated to a residual pressure of 10^{-3} mmHg at 950–1100 K for 8 hours. The rest of the antimony and bismuth-containing analogues, due to the peritectic nature of the formation, were synthesised through batches (2Cu + Ln + 3Sb(Bi) + 7S) from extra pure elements. After completion of the reaction, homogenizing annealing was carried out for a month at 600–700 K, depending on the composition.

3. Results and discussion

Phase diagram of $CuSbS_2$-$PrSbS_3$ system, plotted based on the results of physico-chemical analysis, is shown in Fig. 2. As can be seen, with a ratio of components of 2:1, a quaternary sulphosalt of composition $Cu_2PrSb_3S_7$ was formed in the $CuSbS_2$-$PrSbS_3$ system. This compound melts congruently at 985 K and divides the system into two subsystems: $CuSbS_2$-$Cu_2PrSb_3S_7$ and $Cu_2PrSb_3S_7$-$PrSbS_3$. Both subsystems are of the eutectic type. Coordinates of eutectic points: 15 mol. % $PrSbS_3$ and T = 700 K, 55 mol. % $PrSbS_3$ and T = 825 K. The solubility based on the original sulphides was limited and was 5 mol. % $PrSbS_3$ based on $CuSbS_2$ and 5 mol. % $CuSbS_2$ based on $PrSbS_3$.

The quaternary compound $Cu_2PrSb_3S_7$ is a phase of variable composition and exists in the range of compositions 32÷37 mol. % $PrSbS_3$.

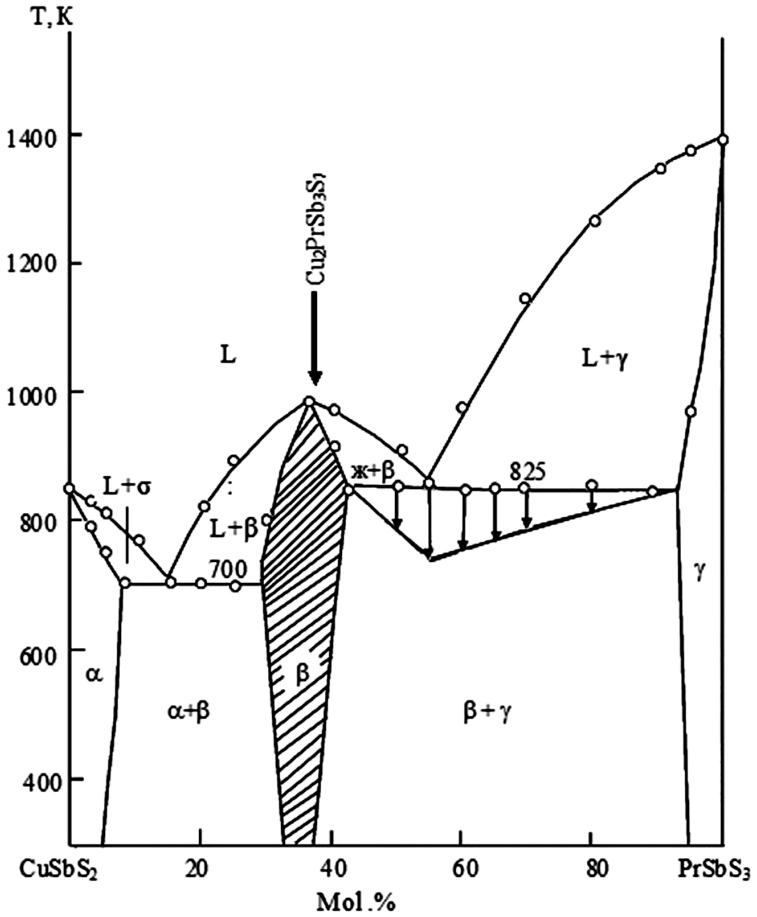

Fig 2. *T-x* diagram of the $CuSbS_2$ – $PrSbS_3$ system

The formation of a new phase in the system was also confirmed by microhardness measurement data. Depending on the composition in $CuSbS_2$ – $PrSbS_3$ system there are three sets of microhardness values 2300÷2450, 2100÷2200 and 2900÷3100 MPa related to microhardness α, β and γ-phases, respectively.

As we noted above, all systems in the La-Nd series have the same character, i.e., the quaternary compounds melt congruently. Other similar systems involving antimony and bismuth are also quasi-binary, in all cases with a component ratio of 2:1, naffildite-like compounds are formed. However, they melt incongruently.

The XRD data were in complete agreement with the DTA and MSA data and confirm the formation of a compound of $Cu_2LnSb_3(Bi)_3S_7$ type.

Crystallographic data and some physico-chemical properties of compounds of $Cu_2LnSb_3(Bi_3)S_7$ type are shown in Table 1 and the calculations of X-ray diffraction patterns for some compounds of this type are presented in Table 2.

The resulting quaternary compounds are isostructural with each other, crystallize in the orthorhombic syngony, and belong to the naffildite structural type. In the unit cell $Cu_2LnSb_3(Bi_3)S_7$ Z = 4, a Pbnm or $Pbnm2_1$ space group is located. As can be seen from Table 1, the parameters and volume of the elementary cell naturally decrease in the series of lanthanides with an increase in the charge of Ln^{3+}.

The temperature dependences of the electrical conductivity coefficients and thermal electromotive force of some compounds of the $Cu_2LnBi_3S_7$ (Ln = La, Nd, Sm, Gd, Er) type were investigated and shown in Fig. 3 and 4.

The measurement results showed that these crystals are characterised by a dependence inherent in impurity semiconductors. In the impurity region (315–343 K), the electrical conductivity gradually increases and, upon transition to the intrinsic region (450–525 K), increases abruptly. The band gap calculated from this region increases in the series $Cu_2LaSb_3S_7$ –

Table 1. Crystallographic and some physicochemical properties of compounds of the $Cu_2LnSb_3S_7$ and $Cu_2LnBi_3S_7$ types

Compound	Lattice parameters, Å			V, Å^3	Density, g/cm^3	Microhardness, MPa	ΔE, eV
	a	b	c				
$Cu_2LaSb_3S_7$	1.4490	21.422	3.902	1232.92	4.38	1950	0.53
$Cu_2CeSb_3S_7$	14.462	21.414	3.972	1230.08	4.46	2000	–
$Cu_2PrSb_3S_7$	14.441	21.460	3.931	1218.23	4.512	2010	–
$Cu_2NdSb_3S_7$	14.460	21.406	3.964	1226.98	4.64	2100	0.60
$Cu_2SmSb_3S_7$	14.392	21.362	3.940	1211.32	4.82	2200	0.73
$Cu_2GdSb_3S_7$	14.362	21.454	3.922	1208.45	4.78	2370	0.80
$Cu_2ErSb_3S_7$	14.303	21.284	3.884	1182.39	4.90	2350	–
$Cu_2YbSb_3S_7$	14.271	21.252	3.842	1152.86	4.96	2400	–
$Cu_2LuSb_3S_7$	14.264	21.206	3.804	1150.64	5.36	2450	–
$Cu_2LaBi_3S_7$	14.722	21.864	4.142	1333.23	5.70	1850	0.38
$Cu_2CeBi_3S_7$	14.704	21.806	4.104	1315.89	5.92	1900	–
$Cu_2NdBi_3S_7$	14.661	21.784	4.046	1292.19	6.16	1940	0.40
$Cu_2SmBi_3S_7$	14.606	21.706	4.022	1275.3	6.32	2080	0.45
$Cu_2GdBi_3S_7$	14.584	21.664	4.00	1263.79	6.54	2150	0.69
$Cu_2ErBi_3S_7$	14.522	21.606	3.486	1093.77	6.70	2200	0.86
$Cu_2LuBi_3S_7$	14.506	21.564	3.464	1083.56	6.83	2360	0.90

Table 2. Calculation of X-ray diffraction patterns of compounds $Cu_2GdSb_3S_7$, $Cu_2LuSb_3S_7$, and $Cu_2NdBi_3S_7$

$Cu_2GdSb_3S_7$				$Cu_2LuSb_3S_7$				$Cu_2NdBi_3S_7$			
d_{exp}	I/I_o	hkl	d_{calc}	d_{exp}	I/I_o	hkl	d_{calc}	d_{exp}	I/I_o	hkl	d_{calc}
7.184	20	200	7.182	7.134	10	200	7.132	7.336	18	200	7.331
4.373	10	320	4.372	5.918	10	230	5.918	5.110	18	230	5.109
3.980	8	330	4.979	4.340	8	320	4.338	4.174	10	150	4.176
3.684	30	250	3.684	4.066	8	150	4.065	4.054	10	330	4.054
3.577	15	060	3.575	3.638	15	250	3.645	3.662	15	400	3.664
3.440	10	031	3.434	3.537	15	060	3.535	3.631	15	060	3.633
3.280	5	221	3.278	3.356	10	201	3.358	3.432	10	131	3.434
3.193	5	260	3.192	3.208	7	221	3.201	3.269	34	430	3.272
3.062	100	141	3.062	3.166	20	280	3.167	3.172	100	141	3.172
2.984	30	440	2.984	3.130	100	147	3.139	3.041	75	440	3.042
2.898	5	241	2.896	2.954	30	440	2.958	2.798	30	450	2.805
2.794	60	331	2.793	2.941	10	241	2.939	2.369	20	470	2.373
2.649	28	401	2.648	2.861	45	331	2.861	2.334	40	271	2.338
2.310	8	511	2.304	2.601	30	401	2.602	2.280	25	560	2.281
2.240	30	560	2.239	2.550	8	161	2.547	2.120	5	650	2.120
2.122	12	1.10.0	2.122	2.271	10	511	2.269	2.093	8	601	2.092
2.034	12	611	2.034	2.226	40	560	2.220	2.050	15	720	2.057
1.958	80	002	1.961	2.120	25	371	2.118	2.023	10	002	2.023
1.875	35	132	1.875	2.100	6	0.10.0	2.098	1.860	30	312	1.862
1.827	8	142	1.827	2.009	8	611	2.007	1.848	35	711	1.853
1.689	12	690	1.689	1.900	10	002	1.902	1.774	25	830	1.778
1.619	8	362	1.618	1.838	6	202	1.837	1.716	8	352	1.718
1.574	5	452	1.597	1.819	30	222	1.811	1.581	8	691	1.583
1.530	10	940	1.530	1.776	8	142	1.776	1.335	26	113	1.333
1.479	5	901	1.478	1.748	20	491	1.747	1.310	10	692	1.310
				1.703	10	741	1.701				
				1.693	10	840	1.690				
				1.670	8	690	1.673				
				1.580	8	362	1.580				
				1.560	10	452	1.560				
				1.520	5	940	1.519				

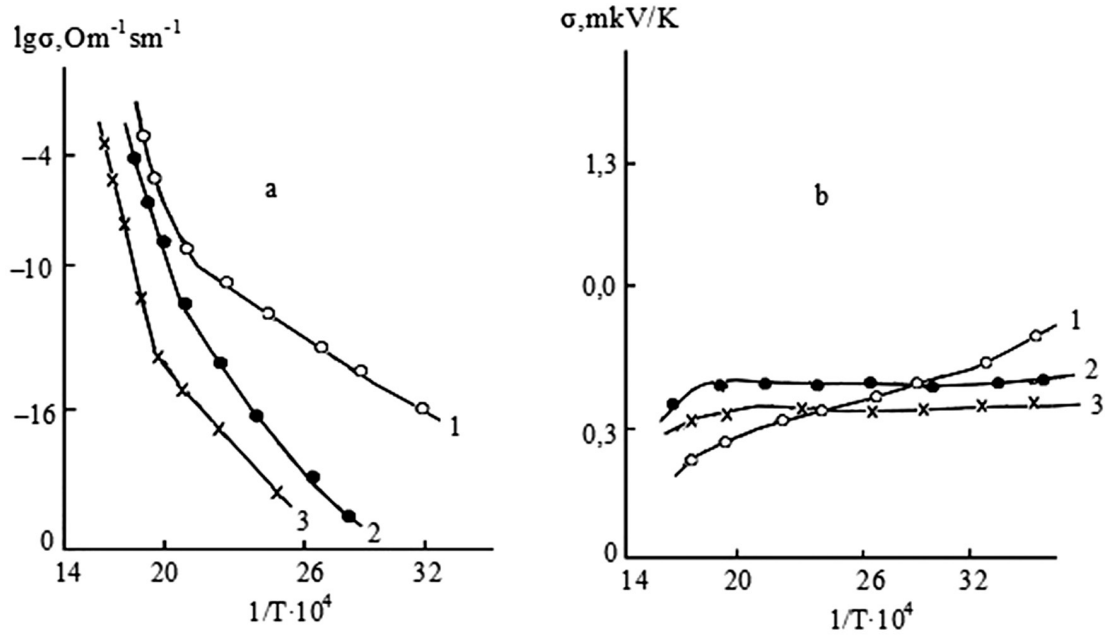

Fig. 3. Temperature dependences of electrical conductivity (a) and thermal electromotive force (b) of compounds of $Cu_2LaBi_3S_7$ (1), $Cu_2NdBi_3S_7$ (2), and $Cu_2GdBi_3S_7$ (3)

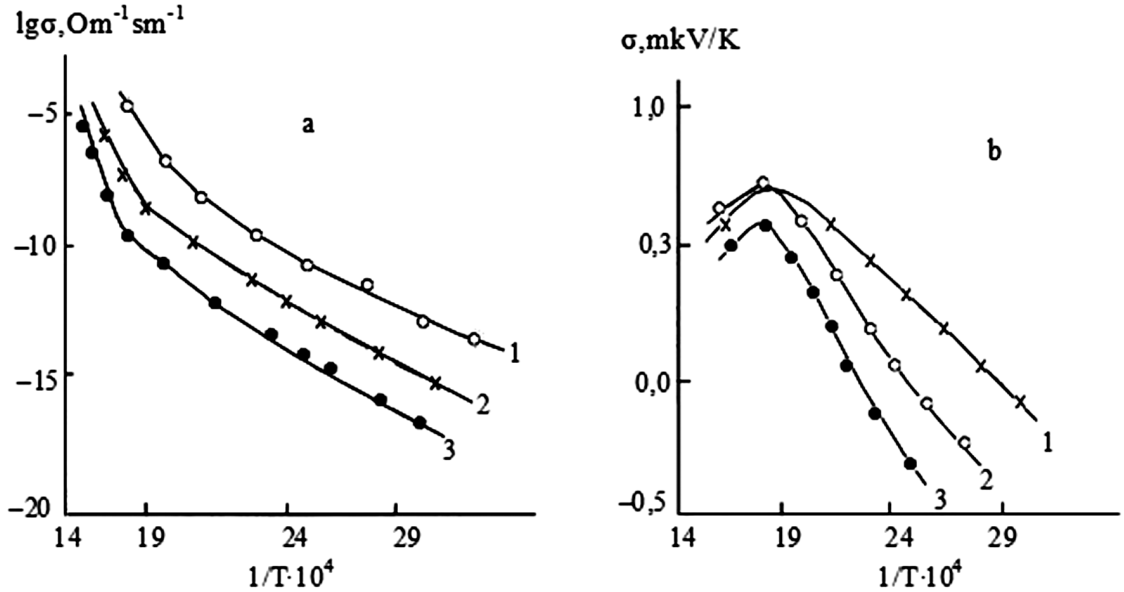

Fig. 4. Temperature dependences of electrical conductivity (a) and thermal electromotive force (b) of compounds of $Cu_2SmBi_3S_7$ (1), $Cu_2ErBi_3S_7$ (2), and $Cu_2LuBi_3S_7$ (3)

$Cu_2GdSb_3S_7$ from ΔE = 0.53 (for $Cu_2LaSb_3S_7$) to ΔE = 0.80 eV (for $Cu_2GdSb_3S_7$) and ΔE=0.38 eV (for $Cu_2LaBi_3S_7$) to ΔE = 0.90 eV (for $Cu_2Lubi_3S_7$).

The nature of the change of thermal electromotive force (α) for $Cu_2LaBi_3S_7$, $Cu_2NdBi_3S_7$, and $Cu_2GdBi_3S_7$ compounds is similar to a change in electrical conductivity, i.e. in its own region α decreases sharply. In the case of $Cu_2SmBi_3S_7$, $Cu_2ErBi_3S_7$, and $Cu_2LuBi_3S_7$ compounds with an increase in electrical conductivity, the thermal electromotive force also increases, and in the intrinsic conduction region it decreases, which was probably due to their complex band structure.

4. Conclusions

Technological conditions have been developed and compounds of the $Cu_2LnSb_3S_7$ and $Cu_2LnBi_3S_7$ types have been synthesised. It was

established that they are isostructural, crystallize in the orthorhombic syngony ($Cu_2LnSb_3S_7$ – a = 14.490÷14.264, b = 21.422÷21.206, c = 3.902–3.804 Å; $Cu_2LnBi_3S_7$ – a = 14.722÷14.506, b = 21.864÷21.564, c = 4.142÷3.464 Å; Z = 4, space group Pbnm or $Pbn2_1$) and belong to the naffildite structural type.

The crystal lattice parameters of the obtained compounds were calculated and some physicochemical and electrophysical properties were studied. It was established that these compounds are p-type semiconductors.

Author contributions

Mammadov Sh. H. – writing of the article and head of scientific research. Aliyev O. M. – idea for the scientific work and writing of the article. Azhdarova D. S. – scientific editing of the text, final conclusions. Agaeva R. M. – conducting research. Ragimova V. M. – conducting research.

Conflict of interests

The authors declare that they have no known competing financial interests or personal relationships that could have influenced the work reported in this paper.

References

1. Rustamov P. G., Aliev O. M., Eynullaev A. V., Aliev I. P. *Chalcolanthanates of rare elements*. Moscow: Nauka Publ., 1989. 238 p. (In Russ.)

2. Levine B. F., Bethea C. G., Lambrcht Y. G., Robbins M. Nonlinear optical properties of Zn_3AgInS_3 and Zn_5AgInS_7. *IEEE Journal of Quantum Electronics*. 2013;40(2): 258–259. https://doi.org/10.1109/JQE.1973.1077477

3. Frumar M., Kalat, Norak J. Growth and some physical properties of semiconducting $CuPbSbS_3$ crystals. *Journal of Crystal Growth*. 2011;62(3): 239–244. https://doi.org/10.1016/0022-0248(73)90011-0

4. Kohatsu I., Wuensch B. J. The crystal structure of nuffieldite, $Pb_2Cu(Pb, Bi)Bi_2S_7$. *Zeitschrift fur Kristallographie B*. 1973;138: 343–365. https://doi.org/10.1524/zkri.1973.138.1-4.3435

5. Kohatsu I., Wuensch B. J. The crystal structure of aikinite, $PbCuBiS_3$. *Acta Crystallographica Section B*. 1975;27(7): 1245–1252. https://doi.org/10.1107/S0567740871003819

6. Orlova A. Yu., Gainov R. R., Duglav A. V., Penkov I. N. Electronic structure and indirect spin-spin interactions in bournonite ($CuPbSbS_3$) according to antimony NQR data. *Letters to ZhETF*. 2013; 97(7): 479–484. (In Russ.). Available at: https://www.elibrary.ru/item.asp?id=20920410

7. Petrova I. V., Kaplunnik L. N., Bortnikov N. S., et al. Crystal structure of synthetic robinsonite. *Doklady Academii Nauk*. 1978;241(1): 88–90. (In Russ.). Available at: http://www.mathnet.ru/links/25023945c613505eda5b0c048a6f26b7/dan41834.pdf

8. Petrova I. V., Kuznetsova A. I., Belokoneva E. L., et al. On the crystal structure of boulangenite. *Doklady Academii Nauk*. 1979;242(20): 337–340. (In Russ.). Available at: http://www.mathnet.ru/php/archive.phtml?wshow=paper&jrnid=d an&paperid=41989&option_lang=rus

9. Petrova I. V., Bortnikov N. S., Pobedimskaya E. A., Belov N. V. Crystal structure of a new synthetic Pb, Sb sulfosalt. *Doklady Academii Nauk*. 1979;244(3): 607–609. (In Russ.). Available at: http://www.mathnet.ru/php/archive.phtml?wshow=paper&jrnid=dan&paperid=42281&option_lang=rus

10. Pobedimskaya E. A., Kaplunnik L. N., et al. *Crystal chemistry of sulfides*. Results of science and technology. Ser. Crystal chemistry. Moscow: 1983;17: 61–62. (In Russ.)

11. Kostov I., Mincheva-Stefanova I. *Sulfide minerals*. Moscow: Mir Publ.; 1984. 229 p. (In Russ.)

12. Eliseev A. A., Kuzmicheva G. M. On the implementation of the law of simple constant multiple ratios in the crystal chemistry of chalcogenides of rare earth elements. *Journal of Inorganic Chemistry*. 1979;24(1): 68–73. (In Russ.)

13. Agaeva R. M., Kasumov V. A., Aliev O. M. Synthesis and X-ray diffraction characterization of $Cu_2LnSb_3S_7$ (Ln = La, Nd). *Inorganic Materials*. 2002;38: 645–646. https://doi.org/10.1023/A:1016219820562

14. Agaeva R. M., Aliev O. M. State diagrams of $CuBiS_2$–$LnBiS_3$ (Ln = La, Nd) systems. *Inorganic Materials*. 2005;41: 920–922. https://doi.org/10.1007/S10789-005-0237-3

15. Gasimov V. A., Gasimova G. N., Aliev O. M. Synthesis and X-ray diffraction characterization of $FeNdSbS_4$, an analog of berthierite. *Inorganic Materials*. 2004;40: 1095–1096. https://doi.org/10.1023/b:inma.0000046476.39031.ae

16. Aliev O. M., Azhdarova D. S., Ragimova V. M., Maksudova T. F. Synthesis and physicochemical properties of the lanthanum-containing analogue of the berthierite mineral $FeSb_2S_4$. *Russian Journal of Inorganic Chemistry*. 2018;63: 383–386. https://doi.org/10.1134/S0036023618030026

17. Aliev O. M., Azhdarova D. S., Agaeva R. M., Maksudova T. F., Mamedov Sh. G. Phase relations along the Cu_2S (Sb_2S_3, $PbSb_2S_4$, $Pb_5Sb_4S_{11}$)–$PbCuSbS_3$ joins in the pseudoternary system Cu_2S-PbS-Sb_2S_3 and physical properties of $(Sb_2S_3)_{1-x}$ $(PbCuSbS_3)_x$ solid solutions.

2018;54: 1199–1204. https://doi.org/10.1134/S0020168518120014

18. Alieva R. A., Bayramova S. T., Ragimova V. M., Aliev O. M., Bagieva M. Phase diagrams of the $CuSbS_2$–MeS (Me – Sb, Eu, Yb) systems. *Inorganic Materials*. 2010;46: 703–706. https://doi.org/10.1134/S0020168510070022

19. Bayramova S. T., Bagieva M. R., Agapashaeva S. M., Aliev O. M. Phase relations in the $CuAsS_2$–MS (M — Pb, Eu, Yb) systems. *Inorganic Materials*. 2011;47: 231–234. https://doi.org/10.1134/S0020168511030046

20. Bayramova S. T., Bagieva M. R., Aliev O. M. Synthesis and properties of structural analogs of the mineral bournonite. *Inorganic Materials*. 2011;47: 345–348. https://doi.org/10.1134/S0020168511040054

21. Babanly M. B., Yusibov Yu. A., Abyshov V. T. *Three-component chalcogenides based on copper and silver*. Baku: BSU Publ.; 1993. 341 p. (In Russ.)

22. Lazarev V. B., Berul S. I., Salaov A. V. *Triple semiconductor connections in A^{I}-B^{V}-C^{VI} systems*. Moscow: Nauka Publ.; 1982. 150 p. (In Russ.)

23. Rzaguluyev V. A., Kerimli O. Sh., Azhdarova D. S., Mamedov Sh. G., Aliev O. M. Phase equilibria in Ag_8SnS_6–Cu_2SnS_3 и Ag_2SnS_3–$Cu_2Sn_4S_9$ systems. *Kondensirovannye sredy i mezhfaznye granitsy = Condensed Matter and Interphases*. 2019;21(4): 544–551. (In Russ., abstract in Eng.). https://doi.org/10.17308/kcmf.2019.21/2365

Information about the authors

Reikhan Agaeva, PhD in Chemistry, Associate Professor, Azerbaijan State Pedagogical University, Azerbaijan.
https://orcid.org/0000-0002-2924-3204
agayeva.reyhan@mail.ru

Sharafat H. Mammadov, PhD in Chemistry, Associate Professor, Senior Researcher, Nagiev Institute of Catalysis and Inorganic Chemistry of Azerbaijan National Academy of Sciences (Baku, Azerbaijan).
https://orcid.org/0000-0002-1624-7345
azxim@mail.ru

Dilbar S. Azhdarova, DSc in Chemistry, Nagiev Institute of Catalysis and Inorganic Chemistry of Azerbaijan National Academy of Sciences (Baku, Azerbaijan).
https://orcid.org/0000-0002-8119-733X
dilbarazhdarova@gmail.com

Valida M. Ragimova, PhD in Chemistry, Nagiev Institute of Catalysis and Inorganic Chemistry of Azerbaijan National Academy of Sciences (Baku, Azerbaijan).
https://orcid.org/0000-0001-6974-9966

Ozbek M. Aliyev, DSc in Chemistry, Professor, Nagiev Institute of Catalysis and Inorganic Chemistry of Azerbaijan National Academy of Sciences (Baku, Azerbaijan).
https://orcid.org/0000-0002-6411-108X
alievozbek@gmail.com

Received October 6, 2021; approved after reviewing November 15, 2021; accepted for publication February 15, 2022; published online March 25, 2022.

Translated by Valentina Mittova
Edited and proofread by Simon Cox

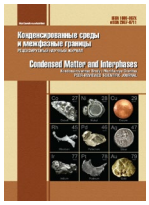

ISSN 1606-867X (Print)
ISSN 2687-0711 (Online)
Condensed Matter and Interphases
Kondensirovannye Sredy i Mezhfaznye Granitsy
https://journals.vsu.ru/kcmf/

Original articles

Research article
https://doi.org/10.17308/kcmf.2022.24/9050

A refined phase diagram of the GeTe-Bi_2Te_3 system

T. M. Alakbarova[1,2]✉, H.-J. Meyer[2], E. N. Orujlu[3], M. B. Babanly[3]

[1]*Azerbaijan State Oil and Industry University, 16/21 Azadlıq ave., Baku AZ-1010, Azerbaijan*

[2]*Section for Solid State and Theoretical Inorganic Chemistry, Institute of Inorganic Chemistry, University of Tübingen, D-72076, Tübingen, Germany*

[3]*Institute of Catalysis and Inorganic Chemistry after M.Nagiev of the Azerbaijan National Academy of Sciences, 113, H. Javid ave., Baku, Az1143, Azerbaijan*

Abstract

Updated phase diagram of the GeTe–Bi_2Te_3 system was constructed using differential thermal, X-ray diffraction analysis and scanning electron microscopy (SEM) results of alloys synthesized with specially developed technology. The refined version significantly differs from those reported so far. The presented phase diagram reflects six ternary compounds: $Ge_4Bi_2Te_7$, $Ge_3Bi_2Te_6$, $Ge_2Bi_2Te_5$, $GeBi_2Te_4$, $GeBi_4Te_7$, and $GeBi_6Te_{10}$.

The study determined that the first two compounds are formed as a result of solid-state reactions at temperatures of 750–800 K, and the latter four are formed as a result of peritectic reactions at 863, 854, 848, and 843 K, respectively. Wide homogeneity regions based on the initial binary compounds were also found. These regions reach 10 mol% at room temperature. The coordinates of eutectic point are 83 mol% Bi_2Te_3 and 838 K. It crystallises at 838 K. It was found that all the identified ternary compounds crystallise in a tetradymite-like layered structure. $Ge_4Bi_2Te_7$, $Ge_3Bi_2Te_6$, $Ge_2Bi_2Te_5$, and $GeBi_2Te_4$ compounds belong to the nGeTe·Bi_2Te_3 homologous series. Their crystal lattices are formed by the insertion of GeTe bilayers into the quintuple Bi_2Te_3 layers. $GeBi_4Te_7$ and $GeBi_6Te_{10}$ compounds are representatives of the GeTe·$m$$Bi_2Te_3$ homologous series and have a mixed-layer structure. The parameters of the crystal lattices of the compounds were determined by the Rietveld method based on their powder diffraction data.

Keywords: Germanium-bismuth tellurides, Phase diagram, Layered tetradymite-like structures, Solid solutions

Funding: The study was carried out within the framework of the scientific programme of the international laboratory "Advanced materials for spintronics and quantum computing", created on the basis of the Institute of Catalysis and Inorganic Chemistry of Azerbaijan National Academy of Sciences (Azerbaijan) and the Donostia International Physics Center (Spain) and partial financial support of the Science Development Foundation under the President of the Republic of Azerbaijan - grant EIF-GAT-5-2020-3(37)-12/02/4-M-02.

The study was also supported by the DAAD (Deutscher Akademischer Austauschdienst) within the framework of a research grants programme "Bi-nationally Supervised Doctoral Degree".

For citation: Alakbarova T. M., Meyer H.-J., Orujlu E. N., Babanly M. B. A refined phase diagram of the GeTe-Bi_2Te_3 system. *Kondensirovannye sredy i mezhfaznye granitsy = Condensed Matter and Interphases*. 2022;24(1): 11–18. 10.17308/kcmf.2022.24/9050

Для цитирования: Алекперова Т. М., Мейер Х-Ю., Оруджлу Э. Н., Бабанлы М. Б. Уточнение фазовой диаграммы системы GeTe–Bi_2Te_3. *Конденсированные среды и межфазные границы*. 2022;24(1): 11–18. 10.17308/kcmf.2022.24/9050

✉ Turkan Muzahim Alakbarova, e-mail: turkanbdu@hotmail.com

1. Introduction

In recent years, there has been a growth of interest in layered chalcogenides which serve as functional materials for various purposes [1-3]. Such valuable materials include ternary compounds of the $A^{IV}Te$-$B^{V}_2Te_3$ (A^{IV}-Ge, Sn, Pb; B^{V}-Sb, Bi) systems with a layered tetradymite-like structure. These compounds have long been the focus of research since they are thermoelectric materials with low thermal conductivity [2–8]. After the discovery of a new state of quantum matter - a topological insulator (TI) [9, 10], it was determined that compounds of the types $A^{IV}B^{V}_2Te_4$, $A^{IV}B^{V}_4Te_7$, $A^{IV}B^{V}_6Te_{10}$, etc. are three-dimensional TIs, which can have a variety of applications, including in spintronics, quantum computing, medicine, security systems, etc. [11-19]. In addition, it should be noted that Ge-B^{V}-Te alloys are widely used in optical storage devices and are currently considered to be the main class of materials with a reversible phase transition between amorphous and crystalline states [20–23].

The development of new methods for the directed synthesis of complex inorganic phases, in particular chalcogenide phases, is based on the data on the phase equilibrium and thermodynamic properties of the corresponding systems [15, 24]. The analysis of the existing literature regarding the phase equilibrium of $A^{IV}Te$-$B^{V}_2Te_3$ systems conducted in [15] showed that, despite the increased interest in the above mentioned ternary compounds, the phase diagrams of these systems are far from being perfect and need to be studied more thoroughly.

A specific feature of GeTe-$B^{V}_2Te_3$ systems, which makes them particularly interesting, is the fact that, besides the compounds of the GeTe·$mB^{V}_2Te_3$ homologous series, typical for all $A^{IV}Te$-$B^{V}_2Te_3$ systems, they also form compounds of the nGeTe·$B^{V}_2Te_3$ series [15, 25–29]. The information regarding the crystal structure and various physical properties of many of these ternary compounds is given in [15, 18, 25–31].

According to the available literature data, the quasi-binary system GeTe-Bi_2Te_3 has been investigated by a number of studies [25–27, 32]. The first phase diagram of the GeTe-Bi_2Te_3 system was constructed in 1965 [32]. According to [32], the system is characterized by the presence of compounds $Ge_3Bi_2Te_6$, $GeBi_2Te_4$, and $GeBi_4Te_7$ formed as a result of peritectic reactions, as well as by wide regions of solid solutions based on both of the initial binary compounds. [25–27] describe additional detailed XRD studies of the quasi-binary system GeTe-Bi_2Te_3 and present its compiled phase diagram taking into account the data from [32]. Besides the above listed ternary compounds, the phase diagram shows the presence of compositions of some other ternary compounds without specifying the nature and temperature of their formation.

Considering the above, we undertook a new study of the phase equilibrium in the GeTe–Bi_2Te_3 system using a specially developed technique for the synthesis of the samples. The resulting new version of the T-x diagram in the composition range of 0–50 mol% Bi_2Te_3 was presented in [33].

We have now completed our study of the phase equilibria in the GeTe-Bi_2Te_3 system and constructed its complete T-x diagram. The results are presented in this article.

2. Experimental

2.1. Materials and synthesis

The alloys of the studied system were synthesised in two stages. First, binary compounds GeTe and Bi_2Te_3 were synthesised by melting high purity elemental germanium (CAS 7440-56-4), bismuth (CAS 7440-69-9), and tellurium (CAS 13494-80-9) in evacuated (~10^{-2} Pa) quartz ampoules at temperatures of ~50 °C higher than their melting points. The binary compounds were identified using the differential thermal analysis (DTA) and the X-ray diffraction analysis (XRD) methods. Then, we obtained the alloys of the GeTe-Bi_2Te_3 system by fusing the initially synthesized and identified binary compounds in evacuated quartz ampoules with various ratios. The synthesized alloys was examined by means of the DTA and XRD techniques.

When designing the second stage of the synthesis, we took into account the previously published data [26, 34, 35], according to which bulk samples of layered tetradymite-like phases, obtained by the well-known fusion method, do not reach the equilibrium state even after being subjected to thermal annealing for a long time (2000-3000 h). Apparently, this is accounted for by the fact that, in contrast to standard bulk

phases, van der Waals phases obtained under nonequilibrium crystallisation conditions (i.e. standard cooling of the melt), practically do not change during further thermal annealing due to very low diffusion level between layers.

Taking this into account, in order to ensure a high degree of dispersion of the alloys containing layered phases, in [36–39] the fused samples were quenched from the liquid state by dropping ampoules into cold water followed by stepwise annealing.

In this study, we applied the same technique. After the fusion, the samples were quenched from a liquid state (950 K) in iced water and then subjected to thermal annealing at 800 K for 1000 h.

2.2. Research methods

In our study, we used DTA, XRD, and SEM methods.

The DTA was performed using a DSC NETZSCH 404 F1 Pegasus differential scanning calorimeter and a multi-channel DTA device based on an electronic TC-08 Thermocouple Data Logger. Powder diffraction patterns of the initial compounds and intermediate alloys were recorded on a Bruker D8 diffractometerwith CuK_α-radiation within an angle range of 2θ = 10÷80°. The diffraction patterns were indexed and the lattice parameters were calculated using Topas 4.2 software by the *Le Bail method*. The EDX (energy dispersive X-ray spectroscopy) analysis was performed on a HITACHI SU8030 scanning electron microscope with a Bruker-EDX detector system.

3. Results and discussion

XRD study of annealed alloys with compositions oF > 50 mol. % Bi_2Te_3 showed that samples correspond to $GeBi_4Te_7$ and $GeBi_6Te_{10}$ stoichiometric compositions, as well as with sample with 90 mol.% Bi_2Te_3 composition were single phased. Powder diffraction patterns of the mentioned alloys are given in Fig. 1a-c. An analysis of the powder diffraction patterns showed that they were completely indexed in

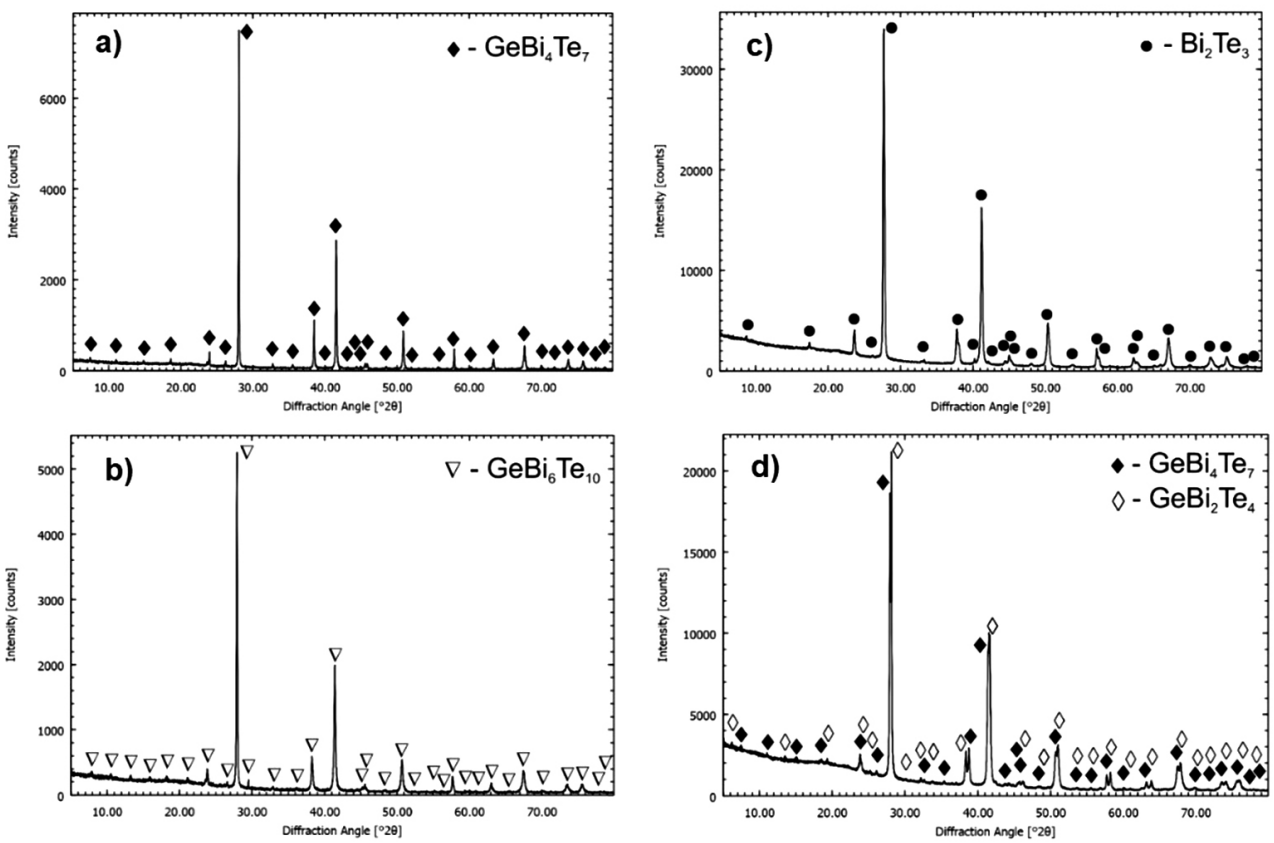

Fig. 1. X-ray powder diffraction patterns of $GeBi_4Te_7$ (a), $GeBi_6Te_{10}$ (b), 90 mol% Bi_2Te_3 (c), and 57.5 mol% Bi_2Te_3 (d)

a tetradymite-like hexagonal structure. The lattice parameters calculated by the Rietveld method are given in Table 1. The table also gives the crystallographic parameters of the synthesised GeTe and Bi_2Te_3, as well as of other ternary compounds of the GeTe-Bi_2Te_3 system according to the data obtained in our earlier study [33].

The XRD data also confirmed the phase compositions of the alloys from two-phase regions $GeBi_2Te_4$–$GeBi_4Te_7$, $GeBi_4Te_7$–$GeBi_6Te_{10}$, and $GeBi_6Te_{10}$–β. As an example, Fig. 1d shows the diffraction pattern of an alloy with a 57.5 mol% Bi_2Te_3 composition. As we can see, the sample consists of a two-phase mixture $GeBi_2Te_4$+$GeBi_4Te_7$.

The results of SEM correlated with the XRD data. Fig. 2 demonstrates the SEM images of compounds $GeBi_2Te_4$, $GeBi_4Te_7$, and $GeBi_6Te_{10}$. These results confirm that all the samples are single-phase and have a layered structure. Fig. 3 and Table 2 show the results of the elemental microanalysis of one of these compounds, namely $GeBi_6Te_{10}$, which appeared in the phase diagram of the GeTe-Bi_2Te_3 system for the first time. As can be seen from Table 2, the elemental composition

Table 1. Crystallographic parameters of the phases in the GeTe–Bi_2Te_3 system

Composition	Crystal system, space group, and lattice parameters, Å
GeTe	Trigonal, *R*3*m*, *a* = 4.1628(3), *c* = 10.6675(8)
$Ge_4Bi_2Te_7$	Trigonal, *R*3*m*, *a* = 4.2638(2), *c* = 73.271(3)
$Ge_3Bi_2Te_6$	Trigonal, *R*3*m*, *a* = 4.2730(3), *c* = 62.634(4)
$Ge_2Bi_2Te_5$	Trigonal, *P*-3*m1*, *a* = 4.2986(2), *c* = 17.335(3)
$GeBi_2Te_4$	Trigonal, *R*-3*m*, *a* = 4.3176(3), *c* = 41.259(5)
$GeBi_4Te_7$	Trigonal, *P*-3*m1*, *a* = 4.3556(2), *c* = 23.928(4)
$GeBi_6Te_{10}$	Trigonal, *R*-3*m*, *a* = 4.3572(3), *c* = 101.911(2)
90 mol. % Bi_2Te_3	Trigonal, *R*-3*m*, *a* = 4.3693(2), *c*= 30.2132(2)

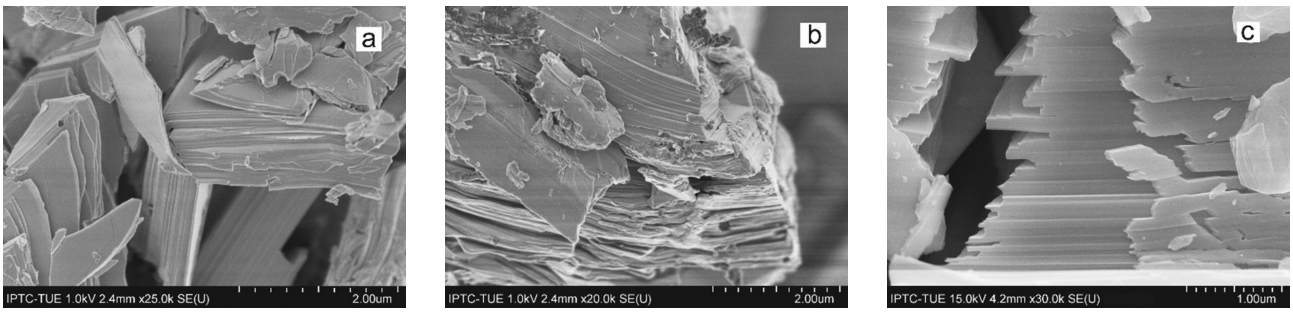

Fig. 2. SEM images of compounds $GeBi_2Te_4$(a), $GeBi_4Te_7$, (b) and $GeBi_6Te_{10}$ (c)

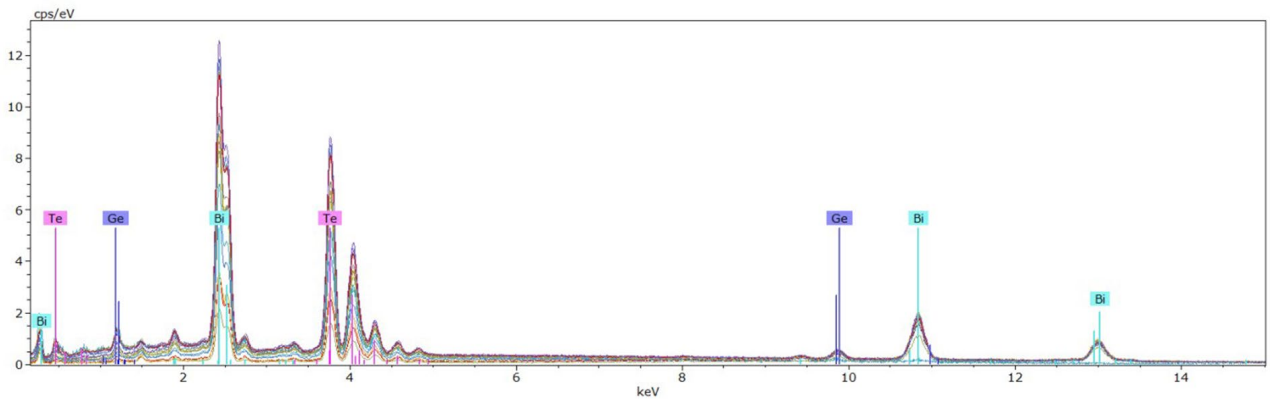

Fig. 3. EDX spectrum of a single crystal $GeBi_6Te_{10}$

corresponds to the stoichiometry of the said compound.

Based on the DTA data and the results of XRD and SEM, we constructed a T-*x* diagram of the system GeTe-Bi_2Te_3 (Fig. 4). A part of the phase diagram in the region of 0–50 mol% Bi_2Te_3 composition was adopted from [33]. The diagram presented in Fig. 4 shows the presence of six new ternary compounds, four of which are formed as a result of the following peritectic reactions:

$L+\alpha_1 \leftrightarrow Ge_2Bi_2Te_5$ (p_1, 863 K) (1)

$L+ Ge_2Bi_2Te_5 \leftrightarrow GeBi_2Te_4$ (p_2, 854 K) (2)

$L+ GeBi_2Te_4 \leftrightarrow GeBi_4Te_7$ (p_3, 848 K) (3)

$L+ GeBi_4Te_7 \leftrightarrow GeBi_6Te_{10}$ (p_4, 843 K) (4)

At the peritectic points, the compositions are the following: 52 (p_1), 60 (p_2), 73 (p_3), and 77 mol% Bi_2Te_3 (p_4) respectively.

The system has eutectic equilibrium (E) with the coordinates of the eutectic point being 83 mol% Bi_2Te_3 and 838 K.

The data on the GeTe - $GeBi_2Te_4$ subsystem is presented and discussed in detail in [33]. A characteristic feature of the phase equilibria in this system is the incongruent nature of melting

Table 2. Elemental composition of $GeBi_6Te_{10}$ according to EDX

Element	Series [wt %]	Non standard C [wt %]	Standard C [wt %]	Atom C [at %]	Error (3 sigma) [wt %]
Germanium	K-series	2.51	2.69	5.65	0.28
Bismuth	L-series	43.84	47.07	34.33	3.33
Tellurium	L-series	46.79	50.24	60.02	4.10
	Total	93.14	100.00	100.00	

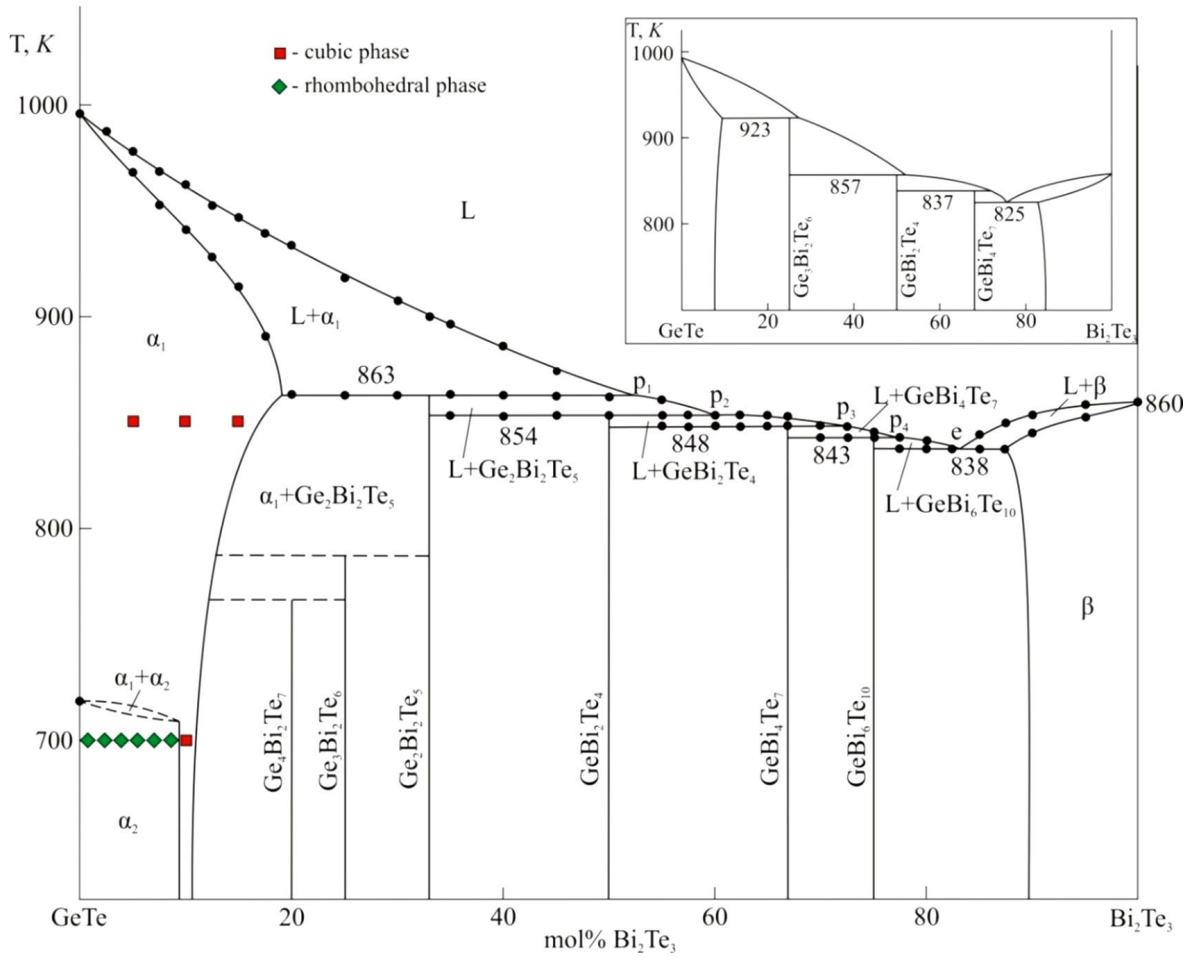

Fig. 4. Phase diagram of the GeTe-Bi_2Te_3 system. A *T–x* diagram based on the data from [32] is given in the right-hand upper corner.

of the compounds and small difference (5–8°) in the temperatures of peritectic reactions. We registered thermal effects with similar temperatures on the DTA curves of the samples weighing 0.05–0.1 g. For heavier samples these peaks overlap forming one large peak. Fig. 5 demonstrates the DTA heating curves for the samples with a 55 mol% Bi_2Te_3 composition weighing 0.5 and 0.1 g. It is obvious that the sample weighing 0.5 g has 1 endothermic peak covering the temperature range of 848–860 K, while the thermogram of the sample weighing 0.1 g clearly shows three endothermic effects at 848, 854, and 860 K. According to Fig. 4, the first two endothermic effects correspond to peritectic reactions (2) and (1), and the third effect corresponds to the end of melting.

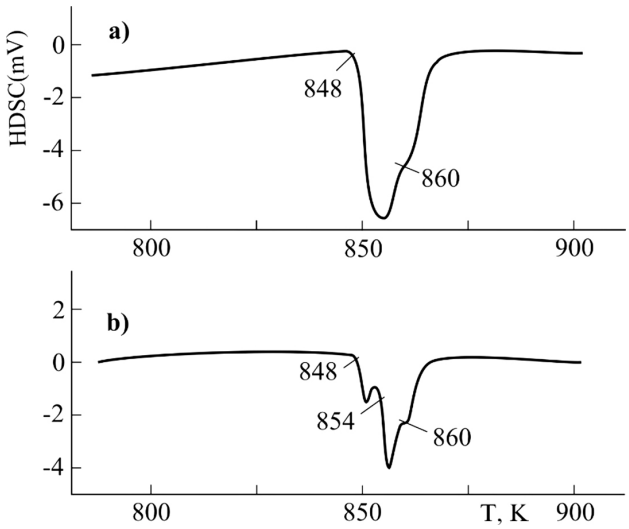

Fig. 5. DTA heating curves of the samples of 55 mol% Bi_2Te_3 weighing 0.5 (a) and 0.1 g (b)

An updated version of the GeTe-Bi_2Te_3 phase diagram differs significantly from that presented in [25, 32] in the number of ternary compounds and the nature and temperature of their formation (Fig. 4). We assume that this may be due to the nonequilibrium of the samples obtained in [25, 32], since the homogenization is hindered due to their layered structure.

3. Conclusions

Based on the results of DTA, XRD, and SEM analyses of carefully homogenized alloys synthesized by means of a specially developed technique, a new version of the phase diagram of the GeTe-Bi_2Te_3 system was constructed. It shows the presence of six ternary compounds, $Ge_4Bi_2Te_7$, $Ge_3Bi_2Te_6$, $Ge_2Bi_2Te_5$, $GeBi_2Te_4$, $GeBi_4Te_7$, and $GeBi_6Te_{10}$, in the system formed as a result of solid-phase (the first two compounds) and peritectic reactions. The study also revealed wide homogeneity regions based on Bi_2Te_3 and both modifications of GeTe. The constructed phase diagram differs significantly from the ones presented in earlier studies.

It was found that all the identified ternary compounds crystallise in a tetradymite-like layered structure. The first three compounds belong to the nGeTe·$B^V_2Te_3$ homologous series, and the rest of them belong to the GeTe·$m$$B^V_2Te_3$ series. The parameters of the crystal lattices of the identified ternary compounds were calculated using the Rietveld method based on their powder diffraction patterns. We do not exclude the possibility of existence of other representatives of both homologous series, although we did not observe any in the synthesised samples.

Author contributions

All authors made an equivalent contribution to the preparation of the publication.

Conflict of interests

The authors declare that they have no known competing financial interests or personal relationships that could have influenced the work reported in this paper.

References

1. Liu X., Lee S., Furdyna J. K., Luo T., Zhang Y. H. *Chalcogenide: From 3D to 2D and Beyond.* Elsevier; 2019. 398 p.

2. Scheer R., Schock H-W., *Chalcogenide Photovoltaics: Physics, Technologies, and Thin Film Devices.* Wiley-VCH; 2011. 384 p.

3. Ahluwalia G. K. *Applications of Chalcogenides: S, Se, and Te.* Springer; 2016. 461 p.

4. Shevelkov A. V. Chemical aspects of the design of thermoelectric materials. *Russian Chemical Reviews.* 2008;77(1): 1–19. https://doi.org/10.1070/RC2008v077n01ABEH003746

5. Kohri H., Shiota I., Kato M., Ohsugi I. J., Goto T. Synthesis and thermoelectric properties of Bi_2Te_3–GeTe pseudo-binary system. *Advances in Science and Technology.* 2006;46: 168–173. https://doi.org/10.4028/www.scientific.net/AST.46.168

6. Rosenthal T., Schneider M. N., Stiewe C., Döblinger M., Oeckler O. Real structure and thermoelectric properties of GeTe-Rich germanium

antimony tellurides. *Chemistry of Materials*. 2011;23(19): 4349–4356. https://doi.org/10.1021/cm201717z

7. Wu D., Xie L., Xu X., He J. High thermoelectric performance achieved in GeTe–Bi_2Te_3 pseudo-binary via Van der Waals gap-induced hierarchical ferroelectric domain structure. *Advansed Functional Materials*. 2019;29(18): 1806613. https://doi.org/10.1002/adfm.201806613

8. Cao Y., Li, Z., Wu J., Huang X., Zhang S. Electrical properties of GeTe-based ternary alloys. *Journal of Wuhan University of Technology-Mater. Sci. Ed.* 2018;33(2): 472–475. https://doi.org/10.1007/s11595-018-1847-2

9. Moore J. E. The birth of topological insulators. *Nature*. 2010;464: 194–198. https://doi.org/10.1038/nature08916

10. Kane C. L., Moore J. E. Topological insulators. *Physics World*. 2011;24(02): 32–36. https://doi.org/10.1088/2058-7058/24/02/36

11. Eremeev S. V., Landolt G., Aliyev Z. S., Babanly M. B., Amiraslanov I. R. Atom-specific spin mapping and buried topological states in a homologous series of topological insulators. *Nature Communications*. 2012;3: 635. https://doi.org/10.1038/ncomms1638

12. Cava R. J., Ji H., Fuccillo M. K., Gibson Q. D., Horb Y. S. Crystal structure and chemistry of topological insulators, *Journal of Materials Chemistry C*. 2013;1: 3176–3189. https://doi.org/10.1039/C3TC30186A

13. Papagno M., Eremeev S., Fujii J., Aliev Z.S. Multiple coexisting dirac surface states in three-dimensional topological insulator $PbBi_6Te_{10}$. *ACS Nano*. 2016;10(3): 3518–3524. https://doi.org/10.1021/acsnano.5b07750

14. Pacile D., Eremeev S. V., Caputo M., Pisarra M., De Luca O., Grimaldi I., Fujii J., Aliev Z. S., Babanly M. B., Vobornik I., Agostino R. G., Goldoni A., Chulkov E. V., Papagno M. Deep insight into the electronic structure of ternary topological insulators: A comparative study of $PbBi_4Te_7$ and $PbBi_6Te_{10}$. *Physica Status Solidi Rapid Research Letters*. 2018;12(12): 1800341-8. https://doi.org/10.1002/pssr.201800341

15. Babanly M. B., Chulkov E. V., Aliev Z. S., Shevelkov A. V., Amiraslanov I. R. Phase diagrams in materials science of topological insulators based on metal chalcogenides. *Russian Journal of Inorganic Chemistry*. 2017;62(13): 1703–1729. https://doi.org/10.1134/S0036023617130034

16. Nurmamat M., Okamoto K., Zhu S., Menshchikova T. V., Rusinov I. P., Korostelev V. O., Miyamoto K., Okuda T., Miyashita T., Wang X., Ishida Y., Sumida K., Schwier E. F., Ye M., Aliev Z. S., Babanly M. B, Amiraslanov I. R., Chulkov E. V., Kokh K. A., Tereshchenko O., Shimada K., Shin S., Kimura A. Topologically non-trivial phase-change compound $GeSb_2Te_4$. *ACS Nano*. 2020; 14(7): 9059–9065. https://doi.org/10.1021/acsnano.0c04145

17. Okamoto K., Kuroda K., Aliyev Z. S., Babanly M. B., Amiraslanov I. R. Observation of a highly spin-polarized topological surface state in $GeBi_2Te_4$. *Physical Review B*. 2012;86(19): 195304–195308. https://doi.org/10.1103/PhysRevB.86.195304

18. Sterzi A., Manzoni G., Crepaldi A., Cilento F., Zacchigna M., Leclerc M., Parmigiani F. Probing band parity inversion in the topological insulator $GeBi_2Te_4$ by linear dichroism in ARPES. *Journal of Electron Spectroscopy and Related Phenomena*. 2018;225: 23–27. https://doi.org/10.1016/j.elspec.2018.03.004

19. Peng R., Ma Y., Wang H., Huang B., Dai Y. Stacking-dependent topological phase in bilayer MBi_2Te_4 (M = Ge, Sn, Pb). *Physical Review B*. 2020;101(11): 115427. https://doi.org/10.1103/PhysRevB.101.115427

20. Siegrist T., Merkelbach P., Wuttig M. Phase change materials: challenges on the path to a universal storage device. *Annual Review of Condensed Matter Physics*. 2012;3: 215–237. https://doi.org/10.1146/annurev-conmatphys-020911-125105

21. Tominaga J. Topological memory using phase-change materials. *MRS Bulletin*. 2018;43(05): 347–351. https://doi.org/10.1557/mrs.2018.94

22. Jones R. O. Phase change memory materials: Rationalizing the dominance of Ge/Sb/Te alloys. *Physical Review B*. 2020;101(2): 024103. https://doi.org/10.1103/physrevb.101.024103

23. Liu, Y., Li, X., Zheng, H., Chen, N., Wang, X., Zhang, X., … Zhang, S. High-Throughput screening for phase-change memory materials. *Advansed Functional Materials*. 2021;31(21): 2009803. https://doi.org/10.1002/adfm.202009803

24. Babanly M. B., Mashadiyeva L. F., Babanly D. M., Imamaliyeva S. Z., Taghiyev D. B., Yusibov Y. A. Some issues of complex investigation of the phase equilibria and thermodynamic properties of the ternary chalcogenide systems by the EMF method. *Russian Journal of Inorganic Chemistry*. 2019;13: 1649–1671. https://doi.org/10.1134/S0036023619130035

25. Shelimova L. E., Karpinskii O. G., Zemskov V. S. Structural and electrical properties of layered tetradymite-like compounds in the GeTe-Bi_2Te_3 and GeTe-Sb_2Te_3 systems. *Inorganic Materials*. 2000;36(3): 235–242. https://doi.org/10.1007/BF02757928

26. Shelimova L. E., Karpinskii O. G., Kosyakov V. I. Homologous series of layered tetradymite-like compounds in Bi-Te and GeTe-Bi_2Te_3 systems. *Journal of Structural Chemistry*. 2000;41(1): 81–87. https://doi.org/10.1007/BF02684732

27. Shelimova L. E., Karpinskii O. G., Konstantinov P. P. Crystal structures and thermoelectric properties of layered compounds in the ATe-Bi_2Te_3 (A = Ge, Sn, Pb) systems. *Inorganic Materials*. 2004;40(5): 451–460. https://doi.org/10.1023/B:INMA.0000027590.43038.a8

28. Jung C. S., Kim S. H., Im H. S., Park K., Park J., Ahn J-P., Yoo S. J., Kim J-G., Kim J. N., Shim J. H. In situ

temperature-dependent transmission electron microscopy studies of pseudobinary mGeTe·Bi_2Te_3 (m = 3–8) nanowires and first-principles calculations. *Nano Letters*. 2015;15(6): 3923–3930. https://doi.org/10.1021/acs.nanolett.5b00755

29. Rohr F. V., Schilling A., Cava R. J. Single-crystal growth and thermoelectric properties of $Ge(Bi,Sb)_4Te_7$. *Journal of Physics: Condensed Matter*. 2013;25(7): 075804. https://doi.org/10.1088/0953-8984/25/7/075804

30. Urban P., Simonov A., Weber T., O. Oeckler. Real structure of $Ge_4Bi_2Te_7$: refinement on diffuse scattering data with the 3D-ΔPDF method. *Journal of Applied Crystallography*. 2015;48: 200–211. https://doi.org/10.1107/S1600576714027824

31. Eremeev S. V., Rusinov I. P., Echenique P. M., Chulkov E. V. Temperature-driven topological quantum phase transitions in a phase-change material $Ge_2Sb_2Te_5$. *Scientific Reports*. 2016;6: 38799. https://doi.org/10.1038/srep38799

32. Abrikosov N. X, Danilova-Dobryakova G. T. Study of the GeTe-Bi_2Te_3 phase diagram. *Izvestiya Akademii Nauk SSSR, Neorganicheskie Materialy*. 1965;1: 57–61. (In Russ.)

33. Alakbarova T. M., Meyer H-J., Orujlu E. N., Amiraslanov I. R., Babanly M. B. Phase equilibria of the GeTe–Bi_2Te_3 quasi-binary system in the range 0–50 mol% Bi_2Te_3. *Phase Transitions*. 2021;94(5): 366–375. https://doi.org/10.1080/01411594.2021.1937625

34. Abrikosov N. K., Bankina V. F., Poretskaya L. V., Shelimova, L. E., Skudnova, E. V. *Semiconducting II–VI, IV–VI, and V–VI Compounds*. Springer US; 1969. 252 p.

35. Abrikosov, N. K., Bankina, V. F. Study of phase diagram of the system Bi–Te. *Journal of Inorganic Chemistry USSR*. 1958: 659–667. (In Russ.)

36. Hasanova G. S., Aghazade A. I., Imamaliyeva S. Z., Yusibov Y. A., Babanly M. B. Refinement of the phase diagram of the Bi-Te system and the thermodynamic properties of lower bismuth tellurides. *JOM*. 2021;73(5): 1511–1521. https://doi.org/10.1007/s11837-021-04621-1

37. Hasanova G. S., Aghazade A. I., Babanly D. M., Imamaliyeva S. Z, Yusibov Y. A., Babanly M. B. Experimental study of the phase relations and thermodynamic properties of Bi–Se system. *Journal of Thermal Analysis and Calorimetry*. 2021. https://doi.org/10.1007/s10973-021-10975-0

38. Gasanova G. S., Agazade A. I., Babanly D. M., Tagiev D. B, Yusibov Yu. A., Babanly M. B. Thermodynamic properties of bismuth selenides. *Russian Journal of Physical Chemistry A*. 2021;95(5): 920–925. https://doi.org/10.1134/S0036024421050137

39. Hasanova G. S., Aghazade A. I., Yusibov Y. A., Babanly M. B. Thermodynamic properties of the BiTe and Bi_8Te_9. *Physics and Chemistry of Solid State*. 2020;21(4): 714–719. https://doi.org/10.15330/pcss.21.4.714-719

Information about authors

Turkan M. Alakbarova, Postdoctoral student, Azerbaijan State Oil and Industry University (Baku, Azerbaijan).
https://orcid.org/0000-0003-4913-4520
turkanbdu@hotmail.com

Hans-Jürgen Meyer, Professor, Section for Solid State and Theoretical Inorganic Chemistry, Institute of Inorganic Chemistry, University of Tübingen (Tübingen, Germany).
https://orcid.org/0000-0003-2450-4011
juergen.meyer@uni-tuebingen.de

Elnur N. Orujlu, Postdoctoral Student, Research Fellow, Institute of Catalysis and Inorganic Chemistry, Azerbaijan National Academy of Sciences (Baku, Azerbaijan).
https://orcid.org/0000-0001-8955-7910;
elnur.oruclu@yahoo.com

Mahammad B. Babanly, DSc in Chemistry, Professor, Associate Member of the Azerbaijan National Academy of Sciences, Deputy-director of the Institute of Catalysis and Inorganic Chemistry, Azerbaijan National Academy of Sciences, Baku State University (Baku, Azerbaijan).
https://orcid.org/0000-0001-5962-3710
babanlymb@gmail.com

Received December 10, 2021; approved after reviewing January 15, 2022; accepted for publication February 15, 2022; published online March 25, 2022.

Translated by Yulia Dymant
Edited and proofread by Simon Cox

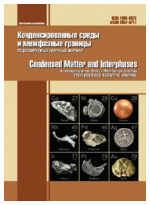

ISSN 1606-867X (Print)
ISSN 2687-0711 (Online)
Condensed Matter and Interphases
Kondensirovannye Sredy i Mezhfaznye Granitsy
https://journals.vsu.ru/kcmf/

Original articles

Research article
https://doi.org/10.17308/kcmf.2022.24/9051

Preparation and characterisation of cobalt and cobalt-zinc ferrites for magnetorheological materials

Yu. S. Haiduk[1]✉, E. V. Korobko[2], D. A. Kotsikau[1], I. A. Svito[1], A. E. Usenka[1], V. V. Pankov[1]

[1]*Belarusian State University,*
4 Nezavisimosty pr., Minsk 220030, Belarus

[2]*A. V. Luikov Heat and Mass Transfer Institute of NAS of Belarus,*
15 P. Brovki ul., Minsk 220072, Belarus

Abstract

The aim of this study was to study the structure, morphology, magnetic, and magnetorheological properties of cobalt and cobalt-zinc ferrite powders to be used as a functional component of magnetorheological fluids.

Ferrites of cobalt $CoFe_2O_4$ and cobalt-zinc $Co_{0.65}Zn_{0.35}Fe_2O_4$ were obtained by combined hydrolysis of inorganic metal salt in aqueous solutions followed by thermal treatment of the precipitates. The ferrites were studied by means of X-ray phase analysis, scanning electron microscopy, IR spectroscopy, and magnetometry.

The synthesised ferrites are polydispersed powders with the size of primary particles of 300–400 nm and the size of the coherent scattering regions of 22–33 nm. They demonstrate a high shear stress in magnetorheological suspensions, which is 2.5 times higher than that of the nanosized particles. High-temperature annealing results in a significant increase in the specific magnetisation of the powders, as well as the shear stress in suspensions prepared on their basis. Doping cobalt ferrite with zinc leads to an increase in the specific magnetisation and rheological characteristics.

The studied materials have a high shear stress in suspensions (~ 2.5 kPa at 650 mT) and can be used as functional fillers for magnetorheological materials.

Keywords: Cobalt ferrite, Cobalt-zinc ferrite, Magnetorheological materials

For citation: Haiduk Yu. S., Korobko E. V., Kotsikau D. A., Svito I. A., Usenka A. E., Pankov V.V. Preparation and characterisation of cobalt and cobalt-zinc ferrites for magnetorheological materials. *Kondensirovannye sredy i mezhfaznye granitsy = Condensed Matter and Interphases*. 2022;24(1): 19–28. https://doi.org/10.17308/kcmf.2022.24/9051

Для цитирования: Гайдук Ю. С., Коробко Е. В., Котиков Д. А., Свито И. А., Усенко А. Е., Паньков В. В. Получение и характеризация ферритов кобальта и кобальта-цинка для магнитореологических материалов *Конденсированные среды и межфазные границы*. 2022;24(1): 19–28. https://doi.org/10.17308/kcmf.2022.24/9051

✉ Yulyan S. Haiduk, e-mail: j_hajduk@bk.ru

1. Introduction

Magnetic fluids (MF) and magnetorheological fluids (MRF) belong to the category of magnetically controllable materials. They differ in the degree of the magnetorheological effect, which is much stronger in MRFs than in MFs. MFs usually contain nanosized magnetic particles, whose concentration in the composition does not exceed a few vol%. The concentration of magnetic particles in MRFs can reach up to 50 vol%, and their size usually exceeds 0.1 μm [1]. MRFs are used as an active medium for damping devices designed for the protection of vehicles, industrial equipment, buildings, and structures from vibrations and other mechanical influences, as well as for shaft hermitization, production of prostheses, and production of recoil devices and return systems for artillery, etc. [2].

The most common way to gain the magnetorheological response of a suspension is to increase the magnetisation of micro- and nanosized magnetic particles reducing the coercivity, as well as to obtain anisometric particles (for instance, needle-like particles). In order to do this, it is necessary to enhance the existing methods for synthesising magnetic materials. A promising solution is to combine micro- or nanoparticles rather than to use them separately. It is known that micron particles demonstrate stronger magnetorheological effect, and their combination with nanoparticles stabilises the suspension preventing or slowing down the aggregation and sedimentation processes. A combined effect of several factors (the morphology of the particles, their magnetisation, the coercive force, and the mass fraction in the suspension) can lead to a synergistic effect, which in turn results in an emergent viscosity effect.

Cobalt and cobalt-zinc ferrites synthesised by means of chemical coprecipitation [3–6], the sol-gel method [7], electrostatic spraying [8] and other methods are being actively studied as promising ferrimagnetic materials. Zinc ferrite has a cubic spinel lattice with normal distribution of cations in the spinel sublattices, while cobalt ferrite has a reverse structure. Structural deviations result in a nonequilibrium distribution of cations in the lattice and cause a change in the magnetic properties [9–11]. In addition, changing the distribution of the cations in the ferrite lattice by forming solid solutions between certain ferrite compositions, we can alter the magnetic properties of the material to a certain degree. Thus, the introduction of a non-magnetic Zn^{2+} ion to the lattice of cobalt ferrite with a strong preference for tetrahedral positions will cause the migration of Fe^{3+} ions into the octahedral positions, leading to an increase in the magnetic moment.

In our earlier study [12], we developed a technique that allows controlling the magnetic properties of cobalt-zinc ferrite by substituting for cobalt ions in the structure of Co-Zn spinel with a non-magnetic double charge cation, namely zinc. We found that an increase in the magnetisation and a decrease in the coercivity occurs until the concentration of zinc reaches $x = 0.35$ ($Co_{0.65}Zn_{0.35}Fe_2O_4$). The ferrites obtained by spray-drying followed by annealing in the inert component matrix (NaCl) consisted of particles that are uniform in size (~ 50 nm), some of them being in a superparamagnetic state. The powder had specific magnetisation of about ~ 45 $A \cdot m^2 kg^{-1}$ and demonstrated a shear stress of ~ 1 kPa in a suspension based on industrial oil, with the magnetic field induction being 600 mT [12].

The aim of this study was to study the structure, morphology, magnetic, and magnetorheological properties of cobalt and cobalt-zinc ferrite powders to be used as a functional components of magnetorheological materials, namely magnetorheological fluids. To increase the average size of the particles, their specific magnetisation, and, as a result, the shear stress in ferrite suspensions, we used the method of chemical precipitation from aqueous solutions followed by high-temperature treatment of the precipitates in air.

2. Experimental

The $CoFe_2O_4$ ferrite powder was obtained from solutions of the metal salts followed by high-temperature annealing. Samples of $CoSO_4 \cdot 7H_2O$ weighing 36.54 g and $Fe(NO_3)_3 \cdot 9H_2O$ weighing 52.54 g were dissolved in 1 l of distilled water. An ammonia solution was poured into the resulting salt solution with vigorous stirring. The pH level of the resulting suspension was monitored (pH = 11.0). The suspension was heated to 90 °C. The precipitate was washed by magnetic

decantation, after which it was heat treated at 740 ºC for 8 h in air and ground in an agate mortar.

To obtain $Co_{0.65}Zn_{0.35}Fe_2O_4$ samples, powders of $CoSO_4 \cdot 7H_2O$ (16.25 g), $ZnCl_2$ (4.26 g), and $Fe(NO_3)_3$ (49.81 g) were dissolved in 1.5 l of distilled water. The solution was stirred with magnetic stirrer for 5 min to reach complete homogenisation. An ammonia solution was poured into the resulting salt solution under vigorous stirring and the pH level of the formed suspension was monitored using indicator paper (pH = 11.0). The suspension was heated to 90 °C. The precipitate was washed by magnetic decantation [12], after which it was heat treated at 740 ºC for 8 h and ground in an agate mortar.

X-ray studies were performed using a DRON-3 diffractometer (CoK_α-radiation, λ = 0.1790 nm) within an angle range of 2θ = 6–90°. The sizes of coherent scattering regions (CSR) were determined by the broadening of diffraction reflections (Scherrer method).

The radiodensity was calculated using the formula:

$$d_x = \frac{8M}{a^3 N_A}, \quad (1)$$

where M is formal molecular weight; a is the lattice parameter, and Å; N_A is Avogadro number.

The degree of crystallinity of the samples was determined using the ratio:

$$\left(1 - \frac{I_{\text{background}}}{I_{311}}\right) \times 100\,\%, \quad (2)$$

where I_{311} is the intensity of the reflex of the spinel, corresponding to the crystallographic direction 311; $I_{\text{background}}$ is the intensity of the background line of the x-ray diffraction pattern.

Dislocation density δ (number of lines per 1 m²) was calculated using the formula:

$$\delta = \frac{1}{D^2}. \quad (3)$$

IR-spectra were recorded using an AVATAR FTIR-330 spectrometer (Thermo Nicolet) in the wavenumber region (ν) 400–700 cm^{-1} with a resolution of ±1 cm^{-1}. The spectra were registered in adiffuse scattering mode using the Smart Diffuse Reflectance accessory.

The surface structure of polycrystalline and film samples was studied by means of scanning electron microscopy using a LEO 1420. Simultaneously, the ratio of the concentration of metal atoms in ferrite powders and the features of their distribution on the surface of the particles were determined by energy dispersive X-ray spectroscopy (EDX-analysis).

The magnetic characteristics were studied using a Cryogen Free Measurement System from Cryogenic Ltd, where hysteresis loops were recorded at temperatures of 10 and 300 K and magnetic field induction B_{max} = 8 T. The weight of the samples, not including the capsule, was 0.04134 g for $CoFe_2O_4$ and 0.0685 g for $Co_{0.65}Zn_{0.35}Fe_2O_4$.

The dependence of the shear stress (τ) of the suspensions on the magnetic induction of the applied magnetic field was measured using a Physics MCR 301 AntonPaar rotational viscometer in constant shear rate mode (Mobil 22 binder, shear rate γ = 200 s^{-1}, T = 20° C). Powder suspensions in the binder were prepared using a UZDM–2 ultrasonic disperser with a frequency of 44 kHz.

3. Results and discussion

Fig. 1 demonstrates the XRD spectra of the $CoFe_2O_4$ and $Co_{0.65}Zn_{0.35}Fe_2O_4$ ferrites, obtained by means of coprecipitation followed by thermal treatment in air (740 °C, 8 h), and the XRD spectrum of the $Co_{0.65}Zn_{0.35}Fe_2O_4$ ferrite, obtained in [12] by spray-drying followed by thermal treatment in air (740 °C, 8 h) for comparison.

By analysing the XRD spectra we can say that in all the three cases the formation of the spinel ferrite structure (space group *Fd3m*) is completed under the set thermal treatment conditions. The diffraction peaks demonstrate high intensity and slight broadening, which indicates the formation of a highly ordered crystal lattice. The peaks positions and their relative intensities indicate the presence of a single phase with a spinel structure. The structural parameters of the crystal lattice are given in Table 1.

The size of the coherent scattering regions corresponding to the physical sizes of crystallites was 36 and 31 nm for $CoFe_2O_4$ and $Co_{0.65}Zn_{0.35}Fe_2O_4$ obtained by coprecipitation, which is significantly greater than that of the sample obtained by spray-drying (20 nm). This is accounted for by the fact that the annealing of ferrite in the

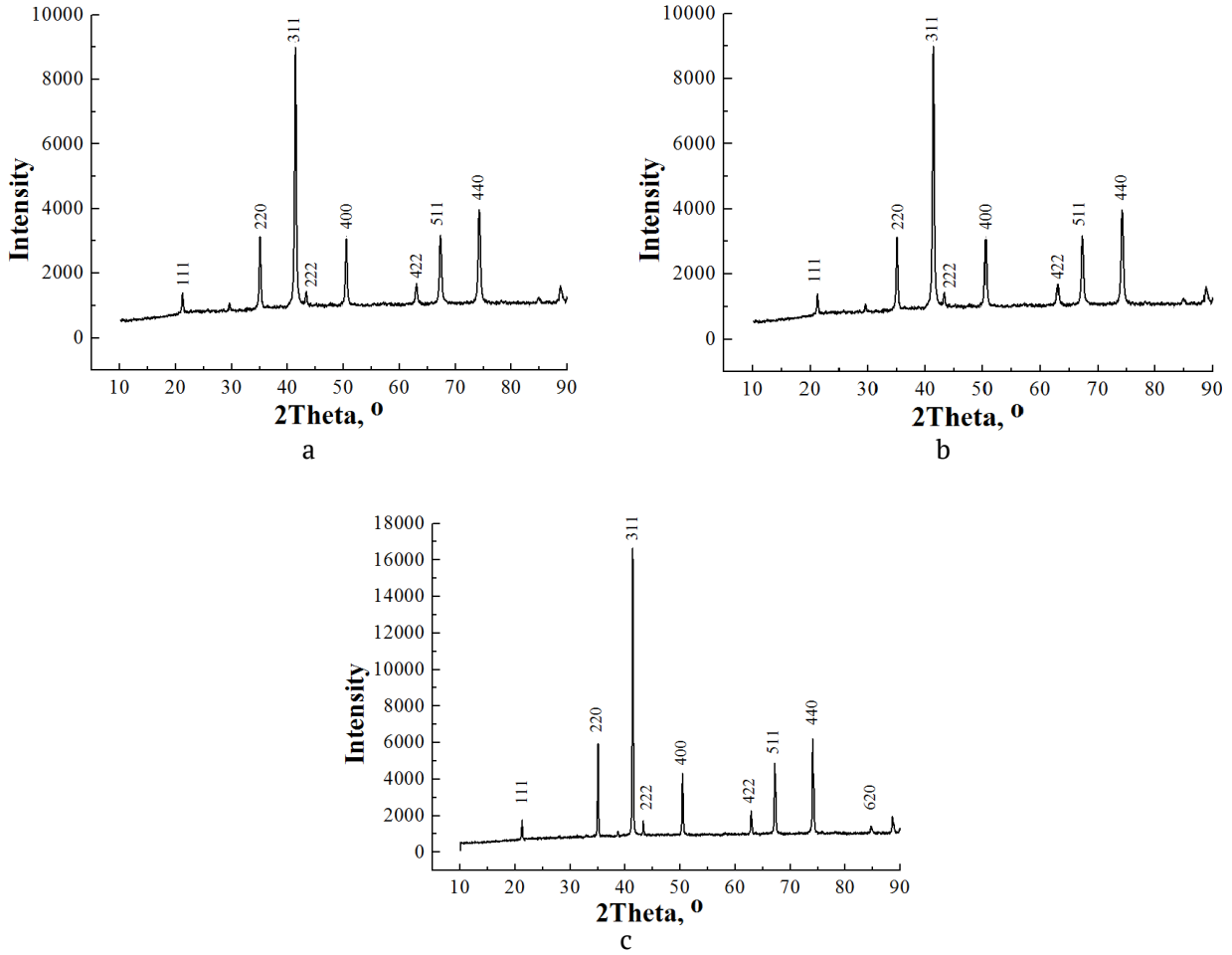

Fig. 1. XRD spectra: a) $Co_{0.65}Zn_{0.35}Fe_2O_4$ (spray-drying); b) $CoFe_2O_4$ (coprecipitation), c) $Co_{0.65}Zn_{0.35}Fe_2O_4$ (coprecipitation)

Table 1. The structural parameters of the crystal lattice: lattice constant *a*, unit cell volume *V*, size of the CSR *D*, dislocation density δ, radiodensity d_x, degree of crystallinity d_c for $Co_{0.65}Zn_{0.35}Fe_2O_4$ powders (spray-drying) (1), $CoFe_2O_4$ (coprecipitation) (2), $Co_{0.65}Zn_{0.35}Fe_2O_4$ (coprecipitation) (3)

Sample	a, Å	*V*, nm³	*D*, нм	$\delta\times10^2$ nm^{-2}	d_x, g/cm³	d_c, %
1	8,3998	592,626	20	0,2500	5,310	85
2	8,3898	590,554	22	0,2066	5,279	88
3	8,4037	593,488	33	0,0918	5,293	94

inert sodium chloride medium hinders the growth of crystallites. The samples obtained by coprecipitation also demonstrate higher crystallinity and lower dislocation density.

Fig. 2. shows fragments of SEM micrographs of the studied $CoFe_2O_4$ and $Co_{0.65}Zn_{0.35}Fe_2O_4$ powders, which demonstrate a high degree of agglomeration of the particles. Agglomerates larger than 1 μm appear either due to the surface properties of the particles, or due to the fact that the thermal treatment conditions induced the first stage of the sintering accompanied by the formation of small bridges between the particles. The primary particles have the size of 300 – 400 nm and a specific shape with pronounced facets. $Co_{0.65}Zn_{0.35}Fe_2O_4$ particles are more crystallized because the temperature of the synthesis and sintering of zinc ferrite is much lower than that of cobalt ferrite.

A comparison of the size of crystallites (coherent scattering regions), calculated by the diffractometry method (Table 1), and the size of

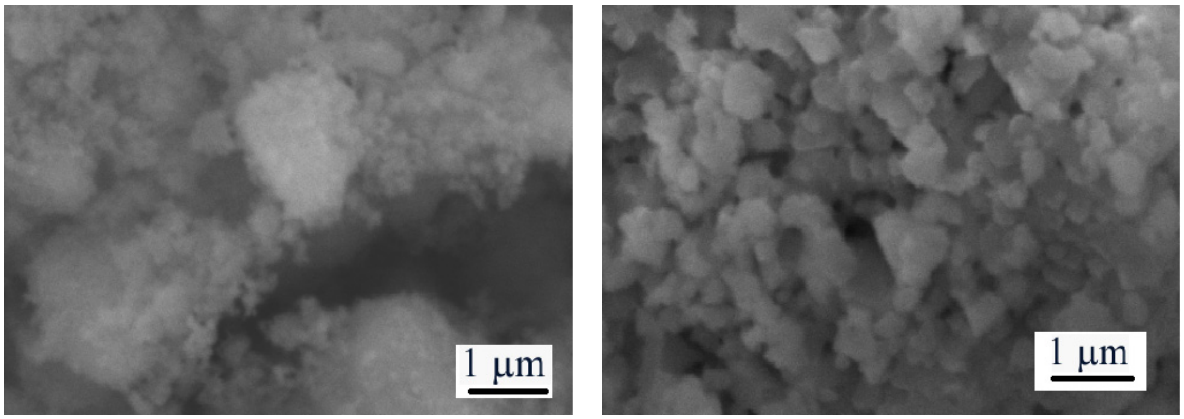

a b

Fig. 2. SEM micrographs: a) $CoFe_2O_4$ (coprecipitation); b) $Co_{0.65}Zn_{0.35}Fe_2O_4$ (coprecipitation)

the particles demonstrated that after annealing at 740 °C some particles include several crystallites and are multidomain. It is known that the critical size for the transition of a single-domain particle to a multidomain at 300 K is around 40 nm (for cobalt ferrite, for instance) [13]. In the region of transition to the ferromagnetic state, following the growth of the particles crystallites spontaneously break up into several domains in order to reduce high magnetisation energy of a single-domain particle.

Fig. 3 shows the IR absorption spectra of the $CoFe_2O_4$ and $Co_{0.65}Zn_{0.35}Fe_2O_4$ powders.

In the region of characteristic frequencies both $CoFe_2O_4$ and $Co_{0.65}Zn_{0.35}Fe_2O_4$ spectra demonstrate pronounced combined vibrational bands of Me–O (at 414 and 567 cm^{-1}). The band at 414 cm^{-1} usually refers to the octahedral vibrations of the metal $Me_{octa} \leftrightarrow O$, and the band at 567 cm^{-1} corresponds to the internal stretching vibrations of the metal in the site $Me_{tetra} \leftrightarrow O$ [5]. The said absorption bands are also observed in the spectrum of $Co_{0.65}Zn_{0.35}Fe_2O_4$ obtained by spray-drying [12]. All the bands have a high degree of resolution, which may reflect a high ordering of the crystal structure.

A wide absorption band at 1600 cm^{-1} [12], corresponding to vibrations of adsorbed water [11], is much less prominent in the $CoFe_2O_4$ sample (Fig. 3a) and practically absent in the $Co_{0.65}Zn_{0.35}Fe_2O_4$ sample (Fig. 3b). The spectrum of $Co_{0.65}Zn_{0.35}Fe_2O_4$ obtained by spray-drying also demonstrated absorption at 2100–2300 cm^{-1}, 1500–1600 cm^{-1}, and near 1000 cm^{-1} (presumably explained by the absorption of CO_2 molecules and NO_3^- ions). The corresponding absorption

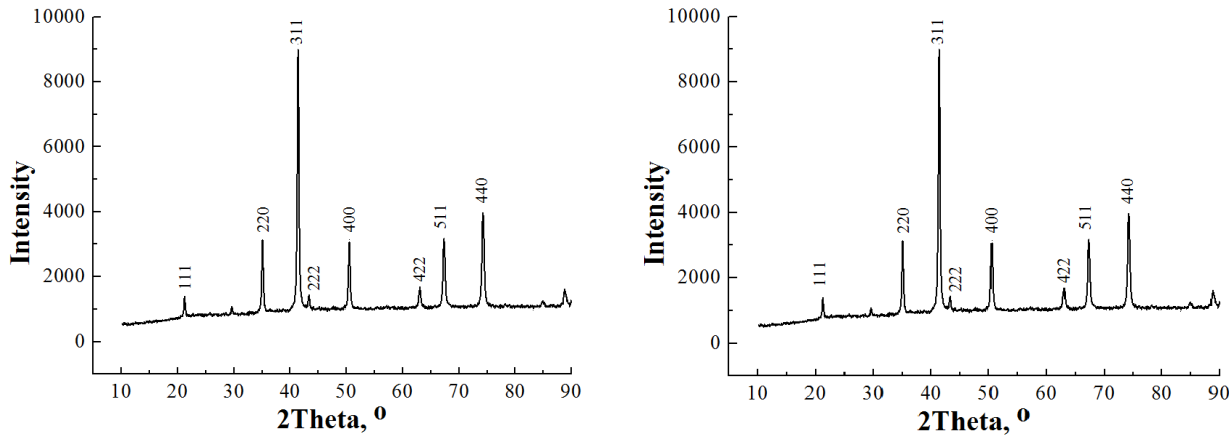

Fig. 3. IR absorption spectrum: a) $CoFe_2O_4$; b) $Co_{0.65}Zn_{0.35}Fe_2O_4$

bands are much less prominent in the spectrum of $CoFe_2O_4$ (Fig. 3a) and absent in the spectrum of the $Co_{0.65}Zn_{0.35}Fe_2O_4$ sample obtained by coprecipitation (Fig. 3b).

Fig. 5 shows the change in magnetisation for $CoFe_2O_4$ and $Co_{0.65}Zn_{0.35}Fe_2O_4$ obtained by coprecipitation depending on the magnetic field induction. Both powders exhibited ferrimagnetic behaviour. The specific magnetisation of the $Co_{0.65}Zn_{0.35}Fe_2O_4$ powder obtained in this study exceeds the specific magnetisation of cobalt-zinc ferrites of the same composition obtained using other methods, namely the sol-gel method (60÷80 A·m^2 kg^{-1}) [14, 15] and coprecipitation from aqueous solutions of inorganic salts (40÷70 A·m^2 kg^{-1}) [16], (60 ÷ 90 A·m^2 kg^{-1}) [17].

In our earlier article we demonstrated that with an increase in the zinc content in the cobalt-zinc ferrite, an increase in the saturation magnetisation was noted. Thus, for the $Co_{0.65}Zn_{0.35}Fe_2O_4$ powder the magnetisation was M_s = 42.6 A·m^2 kg^{-1}, and for the $CoFe_2O_4$ powder it was M_s = 25.0–26.0 A·m^2 kg^{-1}. When the concentration of Zn^{2+} ions increased from 0 to 0.35, the total magnetisation ($M_{oct.}M_{tet.}$) for $Co_{1-x}Zn_xFe_2O_4$ also increased due to the displacement of iron ions to the octahedral positions of the spinel by the zinc ions. The increase in the magnetisation of the ferrite is accompanied by an increase in interlattice AB superexchange interactions [12]. When the number of substituting Zn^{2+} ions is large enough (x > 0.35), the antiferromagnetic interaction of Fe^{3+} ions located in neighbouring positions in the octahedral sublattice begins. Therefore, the BB interaction leads to a decrease in the total magnetic moment [12].

It was also established earlier, that doping cobalt ferrite with zinc ions results in a decrease in the coercive force for the same particle sizes [7, 12]. This is explained by the reduction of the magnetic anisotropy of doped powders. Particles of the critical size, i.e. particles on the border of the ferromagnetic state, have the highest coercive force. For cobalt ferrite, the size of such particles is ~ 40 nm. With the further growth of the particles the coercive force decreases. This dependence can be accounted for by the domain structure, the critical size of the particles, and the degree of the anisotropy of the surface and intercrystalline boundaries. The coercivity of 0.27 kOe obtained at 300 K is much lower than the theoretically calculated coercivity of cobalt (5.3 kOe) [13], which indicates the ferrimagnetic state of the particles.

The magnetic parameters of the powders calculated based on the magnetic hysteresis loops of $CoFe_2O_4$ and $Co_{0.65}Zn_{0.35}Fe_2O_4$ are given in Table 2.

The shape of the magnetisation curves shown in Fig. 4 is similar to the shape described in the literature and is characterized by their significant rectangularity [18]. Table 2 shows that the value of M_s slightly decreases with the growth of temperature, while the adjusted residual magnetisation M_r/M_s and the coercivity H_c decrease significantly. This happens due to the influence of thermal fluctuations of the magnetisation of individual particles [18–20]. For $CoFe_2O_4$ M_r/M_s = 0.83 at low temperatures, which, according to the Stoner-Wohlfarth model, indicates the presence of cubic anisotropy, while for $Co_{0.65}Zn_{0.35}Fe_2O_4$ it is not observed (M_r/M_s < 0.5) [12]. The uncharacteristic kinks on the magnetisation curves (Fig. 4a) can result from the interaction between the hard and soft anisotropy regimes, the polydispersity of the powder, the shape of the particles, and their interaction [12].

Table 2 demonstrates that the coercivity of the zinc-containing ferrite is much lower than

Table 2. The parameters of the magnetisation curves of $CoFe_2O_4$ and $Co_{0.65}Zn_{0.35}Fe_2O_4$ powders (saturation magnetisation M_s, adjusted remanent magnetisation M_r/M_s, coercivity H_c)

	$CoFe_2O_4$			$Co_{0.65}Zn_{0.35}Fe_2O_4$		
T, K	M_s, A·m^2 kg^{-1}	M_r/M_s	H_c, kOe	M_s, A·m^2 kg^{-1}	M_r/M_s	H_c, kOe
10	83.3	0.77	12.5	123.6	0.44	1.35
100	83.5	0.74	8.0	122.4	0.39	1.1
200	80.7	0.60	3.1	112.5	0.23	0.5
300	73.2	0.37	0.27	97.9	0.12	0.1

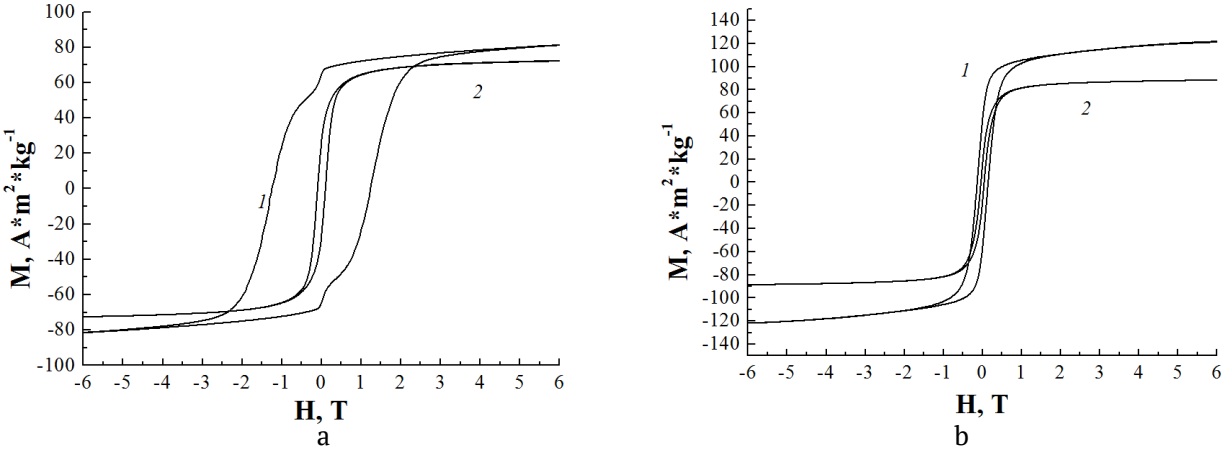

Fig. 4. Curves of the dependence of the magnetisation on the magnetic field strength at different temperatures *1* – 10 K, *2* – 300 K: a) $CoFe_2O_4$; b) $Co_{0.65}Zn_{0.35}Fe_2O_4$

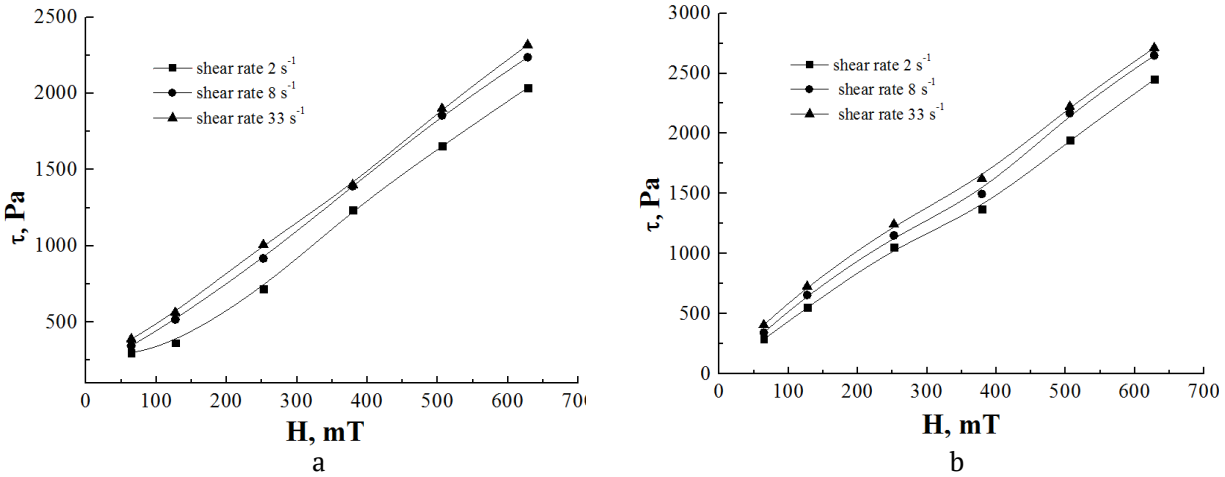

Fig. 5. Dependence of the shear stress of MRF containing 20 wt% of ferrite powder in Mobil 22 on the magnetic field induction at shear rates of 2, 8, and 33 s^{-1}: a) $CoFe_2O_4$; b) $Co_{0.65}Zn_{0.35}Fe_2O_4$

that of $CoFe_2O_4$. This is associated primarily with the characteristic constant of the material anisotropy and the introduction of zinc ions into the ferrite structure [12]. The presence of inhomogeneities, impurities, and crystal lattice defects preventing the remagnetisation of the sample, also increase H_c. These factors are associated with the method of synthesising the sample. $Co_{0.65}Zn_{0.35}Fe_2O_4$, powder obtained in this study has H_c = 0.1 kOe at 300 K, while the coercivity of the sample obtained by spray-drying in sodium chloride medium was 0.4 kOe [12]. With regard to MRFs, it is advisable to use ferrites with lower coercivity in order to increase the magneto-control of the composition.

The comparison of M_s for $Co_{0.65}Zn_{0.35}Fe_2O_4$ obtained by spray-drying followed by annealing in the NaCl medium in [12] and for the sample obtained by coprecipitation followed by annealing in air under the same conditions (Table 2) demonstrated a significant increase in the specific magnetisation for the coprecipitation method. The high-temperature annealing of the $Co_{0.65}Zn_{0.35}Fe_2O_4$ powder in air results in the formation of larger particles with a higher degree of crystallinity as compared to the annealing in the NaCl matrix. The surface layer of the particles with random spin orientation has much less effect on the magnetic properties of the particles than in the former case, which is why the specific magnetisation is much higher. Therefore, the suggested annealing conditions proved to be optimal for obtaining high magnetisation of $Co_{0.65}Zn_{0.35}Fe_2O_4$. In this case, we minimised the

negative effect of the non-magnetic surface layer of the particles, while the particles retained their individuality at the nano scale without sintering.

The $CoFe_2O_4$ and $Co_{0.65}Zn_{0.35}Fe_2O_4$ powders obtained by coprecipitation have high oil absorption and form fairly stable suspensions in the industrial Mobil 22 oil. This makes it possible to use them as functional fillers for magnetorheological materials, including magnetorheological suspensions based on carbonyl iron in synthetic oil. In the latter case, the ferrite additives would perform the modifying and stabilising functions. Fig. 5 shows the dependences of the shear stress of an MRF on the magnetic field induction at different shear rates for the MRF containing 20 wt% of ferrite powder in the industrial Mobil 22 oil.

A high value of shear stress (over 2500 Pa) at 650 mT indicated that the studied powders can be considered promising materials for the above listed applications. It should be noted that the previously studied $Co_{0.65}Zn_{0.35}Fe_2O_4$ powder obtained by spray-drying at 650 mT demonstrated the shear stress of ~ 1000 Pa [12]. Such a significant increase in the shear stress for the obtained samples is explained by the conditions of the synthesis, namely the high-temperature annealing. Comparing the $Co_{0.65}Zn_{0.35}Fe_2O_4$ powders obtained by spray-drying [12] and coprecipitation, we can see that besides the increase in the particle size and the degree of crystallinity (from 85 to 97 %) the annealing results in a change in the shape of the particles from spherical to faceted. Such morphological changes influence the rheological behaviour of the powders in the suspension resulting in an increase in the shear stress. At the same time, the density and the oil absorption of the particles can also increase.

4. Conclusions

In this paper we proposed a new technique for synthesising cobalt and cobalt-zinc ferrites based on the method of coprecipitation from aqueous solutions of the corresponding salts. The technique involves high-temperature annealing of the precipitates in air which results in highly crystalline polydispersed powders with high specific saturation magnetisation (97.9 $A \cdot m^2 \cdot kg^{-1}$ at 300 K).

The synthesised ferrites are polydispersed powders with the size of primary particles of 300–400 nm and the size of the coherent scattering regions of 30–35 nm. They demonstrate high shear stress in magnetorheological suspensions, which is 2.5 times higher than that of the nanosized particles.

In our study, we also obtained suspensions of the ferrite powders with the industrial Mobil 22 oil (20 wt%) for the analysis of the dependences of the shear stress on the magnetic field induction. The high shear stress (2.5 kPa) with a relatively low magnetic field induction (from 600 mT and above) allowed us to consider the obtained materials as being promising for use as functional fillers for magnetorheological materials, including magnetorheological suspensions of damping devices.

Author contributions

Haiduk Yu. S. – writing the article, synthesising the materials, conducting research, interpreting the results. Korobko E. B. – conducting research (magnetorheological measurements), interpreting the results, scientific editing. Kotsikau D. A. – conducting research (IR spectroscopy), scientific editing. Svito I. A. – conducting research (magnetic measurements), interpreting the results. Usenko A. E. – scientific leadership, interpreting the results. Pankov V. V. – scientific leadership, research concept, interpreting the results, final conclusions.

Conflict of interests

The authors declare that they have no known competing financial interests or personal relationships that could have influenced the work reported in this paper.

References

1. Vekas L. Ferrofluids and magnetorheological fluids. *Advances in Science and Technology*. 2008;54(1):127–136. https://doi.org/10.4028/www.scientific.net/AST.54.127

2. Belyaev E. S., Ermolaev A. I., Titov E. Yu., Tumakov S. F. *Magnetorheological fluids: technologies of creation and application*. N. Novgorod; Nizhegorod. state tech. un-t them. R. E. Alekseeva. 2017. 94 p. (In Russ.). http://www.vntr.ru/lib/vntr18-VOL7.pdf

3. Mayekar J., Dhar V., Radha S. Synthesis, Characterization and magnetic study of zinc ferrite nanoparticles. *International Journal of Innovative*

Research in Science, Engineering and Technology. 2016;5(5): 83678371. https://doi.org/10.15680/IJIRSET.2016.0505268

4. Rani B. J., Ravina M., Saravanakumar B., Ravi G., Ganesh V., Ravichandran S., Yuvakkumar R. Ferrimagnetism in cobalt ferrite ($CoFe_2O_4$) nanoparticles. *Nano-Structures & Nano-Objects*. 2018;14: 84–91. https://doi.org/10.1016/j.nanoso.2018.01.012

5. Manouchehri S., Ghasemian Z., Shahbazi-Gahrouei D., Abdolah M. Synthesis and characterization of cobalt-zinc ferrite nanoparticles coated with DMSA. *Chem Xpress*. 2013;2(3):147–152. https://www.tsijournals.com/articles/synthesis-and-characterization-of-cobaltzinc-ferritenanoparticles-coated-with-dmsa.pdf

6. Lopez. P. P. J., Gonzalez - Bahamon L. F., Prado J., Caicedo J. C., Zambrano G., Gomez M. E., Esteve J. Study of magnetic and structural properties of ferrofluids based on cobalt–zinc ferrite nanoparticles. *Journal of Magnetism and Magnetic Materials*. 2012;324(4): 394–402. https://doi.org/10.17586/2220-8054-2016-7-4-624-628

7. Singhal S., Namgyal T., Bansal S., Chandra K. Effect of Zn substitution on the magnetic properties of cobalt ferrite nano particles prepared via sol-gel route. *Journal of Electromagnetic Analysis and Applications*. 2010;2(6): 376–381. http://dx.doi.org/10.4236/jemaa.2010.26049

8. Gaikwad R. S., Chae S.-Y., Mane R. S., Han S.-H., Joo O.-S. Cobalt ferrite nanocrystallites for sustainable hydrogen production application. *International Journal of Electrochemistry*. 2011: 1–6. https://doi.org/10.4061/2011/729141

9. Ladole C. A. Preparation and characterization of spinel zinc ferrite $ZnFe_2O_4$. *International Journal of Chemical Science*. 2012;10(3): 12301234. https://www.tsijournals.com/articles/preparation-and-characterization-of-spinel-zinc-ferrite-znfe2o4.pdf

10. Raghuvanshi S., Kane S. N., Tatarchuk T. R., Mazaleyrat F. Effect of Zn addition on structural, magnetic properties, antistructural modeling of $Co_{1-x}Zn_xFe_2O_4$ nano ferrite. *AIP Conference Proceedings 1953*. 2018: 030055. https://doi.org/10.1063/1.5032390

11. Sawadzky G. A., Van der Woude F., Morrish A. H. Cation distributions in octahedral and tetrahedral sites of the ferrimagnetic spinel $CoFe_2O_4$. *Journal of Applied Physics*. 1968;39(2): 1204–1206. https://doi.org/10.1063/1.1656224

12. Haiduk Yu. S, Korobko E. V., Shevtsova K.A., Kotikov D. A., Svito I.A., Usenka A. E., Ivashenko D. V., Fakhmi A., Pankov V. V. Synthesis, structure and magnetic properties of cobalt-zinc nanoferrite for magnetorheological liquids. *Kondensirovannye sredy i mezhfaznye granitsy = Condensed Matter and Interphases*. 2020;22(1): 28–38. https://doi.org/10.17308/kcmf.2020.22/2526

13. Chinnasamy C. N., Jeyadevan B., Shinoda K., Tohji K., Djayaprawira D. J., Takahashi M., Joseyphus R. J., Narayanasamy A. Unusually high coercivity and critical single-domain size of nearly monodispersed $CoFe_2O_4$ nanoparticles. *Applied Physics Letters*. 2003;83(14): 2862–2864. https://doi.org/10.1063/1.1616655

14. Lin Q., Xu J., Yang F., Lin J., Yang H., He Y. Magnetic and mössbauer spectroscopy studies of zinc-substituted cobalt ferrites prepared by the sol-gel method. *Materials*. 2018;11(10): 1799. https://doi.org/10.3390/ma11101799

15. Liu Y., Zhu X. G., Zhang L., Min F. F., Zhang M. X. Microstructure and magnetic properties of nanocrystalline $Co_{1-x}Zn_xFe_2O_4$ ferrites. *Materials Research Bulletin*. 2012;47: 4174–4180. https://doi.org/10.1016/j.materresbull.2012.08.076

16. Ranjani M., Jesurani S., Priyadharshini M., Vennila S. Sol-gel synthesis and characterization of zinc substituted cobalt ferrite magnetic nanoparticles. International *Journal of Advanced Research*. 2016;5(6): 882 886. https://doi.org/10.17577/IJERTV5IS060665

17. Copolla P., da Silva F. G., Gomide G., Paula F. LO, Campos A.F. C., Perzynski R., Kern C., Depeyrot G., Aquino R. Hydrothermal synthesis of mixed zinc–cobalt ferrite nanoparticles: structural and magnetic properties. *Journal of Nanoparticle Research*. 2016;18(138): 1 – 15. https://doi.org/10.1007/s11051-016-3430-1

18. Praveena K., Sadhana K. Ferromagnetic properties of Zn substituted spinel ferrites for high frequency applications. *International Journal of Scientific and Research Publications*. 2015;5(4): 121. Available at: http://www.ijsrp.org/research-paper-0415.php?rp=P403877

19. Komogortsev S. V., Patrusheva T.N., Balaev D. A., Denisova E. A., Ponomarenko I. V. Cobalt ferrite nanoparticles based on mesoporous silicon dioxide. *Pis'ma* v *Zhurnal teoreticheskoi fiziki*. 2009;35(19): 6–11. (In Russ.). https://www.elibrary.ru/item.asp?id=20326999

20. Komogortsev S. V., Iskhakov R. S., Balaev A. D., Kudashov A. G., Okotrub A. V., Smirnov S. I. Magnetic properties of Fe_3C ferromagnetic nanoparticles encapsulated in carbon nanotubes *Physics of the Solid State*. 2007;49(4): 734-738. https://doi.org/10.1134/s1063783407040233

Information about the authors

Yulyan S. Haiduk, PhD in Chemistry, Senior Researcher, Belarusian State University (Minsk, Belarus).
https://orcid.org/0000-0003-2737-0434
j_hajduk@bk.ru

Evguenia V. Korobko, DSc in Technical Sciences, Professor, Head of Laboratory, A. V. Luikov Heat and Mass Transfer Institute of the National Academy of Sciences of Belarus (Minsk, Belarus).
https://orcid.org/0000-0002-2870-9658
evkorobko@gmail.com

Dzmitry A. Kotsikau, PhD in Chemistry, Associate Professor, Belarusian State University (Minsk, Belarus).
https://orcid.org/0000-0002-3318-7620
kotsikau@bsu.by

Ivan A. Svito, PhD in Physics and Mathematics, Senior Researcher, Belarusian State University (Minsk, Belarus).
https://orcid.org/0000-0002-4510-0190
ivansvito184@gmail.com

Alexandra E. Usenka, PhD in Chemistry, Associate Professor, Department of Physical Chemistry, Belarusian State University (Minsk, Belarus).
https://orcid.org/0000-0002-2251-6193
usenka@bsu.by

Vladimir V. Pankov, DSc in Chemistry, Professor, Head of the Department of Physical Chemistry, Belarusian State University (Minsk, Belarus).
https://orcid.org/0000-0001-5478-0194
pankov@bsu.by

Received September 9, 2021; approved after reviewing October 1, 2021; accepted for publication December 15, 2021; published online March 25, 2022.

Translated by Yulia Dymant
Edited and proofread by Simon Cox

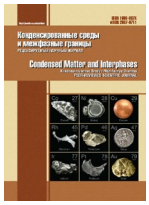

ISSN 1606-867X (Print)
ISSN 2687-0711 (Online)
Condensed Matter and Interphases
Kondensirovannye Sredy i Mezhfaznye Granitsy
https://journals.vsu.ru/kcmf/

Original articles

Research article
https://doi.org/10.17308/kcmf.2022.24/9052

Formation of a solvate of manganese(III) acetylacetonate with chloroform

V. P. Zlomanov✉, R. S. Eshmakov, I. V. Prolubshchikov

Lomonosov Moscow State University,
1 Leninskie Gory, Moscow 119991, Russian Federation

Abstract

Metal acetylacetonates are coordination compounds consisting of the acetylacetonate anion ($CH_3COCHCOCH_3$, indicated as acac) and metal ions. Typically, both oxygen atoms of the anion bind with the metal and form a six-membered chelate ring. The simplest complexes have the formulas $M(acac)_3$ and $M(acac)_2$. Many complexes are soluble in organic solvents, and such solutions are used for the synthesis of catalysts. The processes of formation of solvates of acetylacetonates of various metals have not been studied properly. It should be noted that the determination of the composition and properties of solvates is important for understanding the peculiarities of the extraction processes of metal acetylacetonates. Manganese(III) acetylacetonate $Mn(acac)_3$, for example, is also widely used. The recrystallisation of the complex is most commonly conducted from solutions in chloroform, and in this case, the corresponding solvates may be formed, which can affect the structure and properties of $Mn(acac)_3$. There are no data on the synthesis conditions and the composition of the solvates of manganese(III) acetylacetonate with chloroform. Therefore, the purpose of this work is to study the possibilities of its formation and to establish the composition of such solvates.

The formation of the solvate in solution was established using Fourier IR spectroscopy by the shift of the absorption band of the C-H chloroform bond. The composition of the $Mn(acac)_3 \cdot 2CHCl_3$ solvate was determined using gravimetric analysis.

Keywords: Manganese, Acetylacetonate, Solvate, Gravimetric analysis, IR spectroscopy

For citation: Zlomanov V. P., Eshmakov R. S., Prolubshchikov I. V. Formation of a solvate of manganese(III) acetylacetonate and chloroform. *Kondensirovannye sredy i mezhfaznye granitsy = Condensed Matter and Interphases.* 2022;24(1): 29–32. https://doi.org/10.17308/kcmf.2022.24/0000 https://doi.org/10.17308/kcmf.2022.24/9052

Для цитирования: Зломанов В. П., Эшмаков Р. С., Пролубщиков И. В. Образование сольвата ацетилацетоната марганца(III) с хлороформом. *Конденсированные среды и межфазные границы*. 2022;24(1): 29–32. https://doi.org/10.17308/kcmf.2022.24/9052

✉ Vladimir P. Zlomanov, e-mail: zlomanov1@mail.ru

1. Introduction

Manganese(III) acetylacetonate – $[Mn(C_5H_7O_2)_3]$ – is used as the source material for the synthesis of electrolytes [1] and catalysts [2–8]. Regardless of the synthesis method, $Mn(acac)_3$ is most frequently recrystallised from solutions in chloroform. In this case, the corresponding solvates may be formed, which can affect the structure and properties of $Mn(acac)_3$. The processes of formation of solvates of acetylacetonates of various metals have not been studied properly. There are some data on the formation of solvates of acetylacetonates of trivalent chromium, iron, and scandium with chloroform [9, 10]. However, there are no such data for $Mn(acac)_3$. The purpose of this work was to study the possibilities of formation of solvates of manganese(III) acetylacetonates with chloroform using gravimetry and Fourier IR spectroscopy.

2. Experimental

2.1. Synthesis

To evaluate the possibility of the formation of solvates, we used chloroform as a solvent since it dissolves manganese(III) acetylacetonate well. A saturated solution of $Mn(acac)_3$ in chloroform was prepared at room temperature. The solution was filtered and left in air until a crystal haze formed. After that, the crystals were separated by decantation. Oversaturation was created through evaporation of chloroform, which allowed regulating the rate of formation and growth of nuclei of new phases, including possible solvates. The crystallisation took from one to several days. Upon cooling, big shiny black crystals of the $Mn(acac)_3$ solvate with chloroform were isolated at first and then decomposed after drying (for more than 24 hours) in air, which manifested in surface clouding and the transformation of crystals into powder.

2.2. Gravimetric determination of the composition of a $Mn(acac)_3$ solvate with chloroform

The composition of the $Mn(acac)_3 \cdot nCHCl_3$ solvate obtained through the recrystallisation of $Mn(acac)_3$from chloroform was determined using gravimetry. To do that, we poured the saturated solution of manganese(III) acetylacetonate in chloroform into a weighed 50-ml flask and left it in air. Once the free solvent evaporated and signs of decomposition (loss of shine, colour changed from black to dirty green) of the first few crystals appeared, we recorded the weight of the flask and calculated the weight of the solvate. Two weeks later, when the decomposition of the solvate was almost complete (the weight stopped changing), we heated the flask with the substance up to 100 °C for 10 minutes using a heat gun in order to remove the last traces of solvent. After that, the weight was recorded again. The flasks were weighed on scales with an accuracy of 0.01 g. Over the whole period of the experiment the substance in the open flask was kept in a dark and dry place with almost fixed temperature (23±1 °C).

The weight of the flask with the substance at the beginning of decomposition, in other words, the weight of the flask with the solvate, was M = 34.17±0.01 g. At the end of decomposition, after being heated with a heat gun the weight of the flask with crystals (manganese(III) acetylacetonate without chloroform) was m = 31.45±0.01 g. The weight of the empty flask is m_F = 27.48±0.01 g. If we express the composition of the solvate by the formula $Mn(acac)_3 \cdot nCHCl_3$, then, using the obtained data, we can calculate the number n of chloroform molecules in the solvate as follows:

$$n = \frac{(M-m)*M(Mn(acac)_3)}{(m-m_F)*M(CHCl_3)} =$$

$$= \frac{(34.17-31.45)*352.265}{(31.45-27.48)*119.378} = 2.022,$$

$$\Delta n = \left(\frac{\Delta M+\Delta m}{M-m} + \frac{\Delta m+\Delta m_F}{m-m_F}\right)*n =$$

$$= \left(\frac{0.01+0.01}{34.17-31.45} + \frac{0.01+0.01}{31.45-27.48}\right)*2.022 \pm 0.03,$$

that is, n = 2.02±0.03, while the composition of the solvate, therefore, can be expressed by the formula $Mn(acac)_3 \cdot 2CHCl_3$, in other words, trivalent manganese acetylacetonate forms solvates with chloroform with the ratio of 1:2 as well as the corresponding derivatives of iron(III), chromium(III), and scandium (III).

2.3. Fourier IR spectroscopy

To establish the possibility of the formation of solvates, we analysed the IR spectra of

solutions using Perkin Elmer Frontier FT-IR. The transmission spectrum of the $Mn(acac)_3$ solution in chloroform was recorded in a potassium bromide cuvette. The device was calibrated using a cuvette with pure chloroform.

A bright band was observed at ~3000 cm^{-1} in the IR transmission spectrum of the $Mn(acac)_3$ solution in chloroform relative to chloroform (Fig. 1). It corresponds to the vibrations of the C-H bond in $CHCl_3$ [11]. Its intensity should not be considered significant, since it should be subtracted from the background when recording the spectrum. $Mn(acac)_3$ does not have such intense absorption bands in this region [12–14]. The considered band is also shifted in relation to the spectrum of pure chloroform. The observed band is associated with the interaction of chloroform molecules with $Mn(acac)_3$ molecules, in other words, it indicates the formation of $Mn(acac)_3$ solvates with $CHCl_3$.

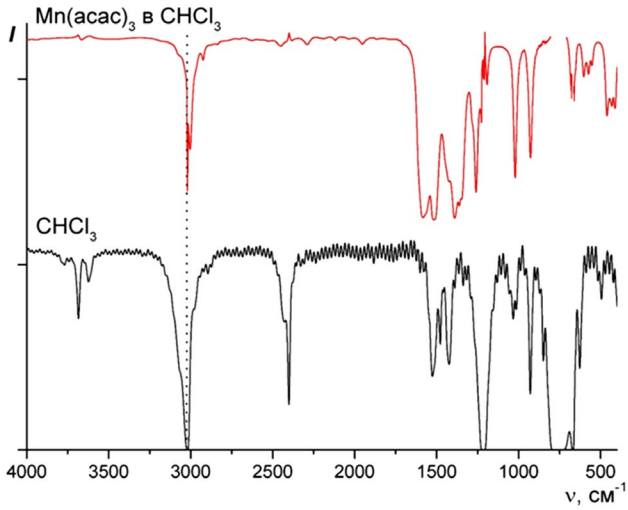

Fig. 1. IR transmission spectra of pure chloroform (relative to air) and a solution of $Mn(acac)_3$ in chloroform (relative to chloroform). The intensities of the spectra are normalised

3. Conclusions

As a result of our work, through the use of Fourier IR spectroscopy, it was found that manganese(III) acetylacetonate forms a solvate with chloroform in solution, and it was also found through the use of gravimetry that the composition of the crystal solvate is expressed by the formula $Mn(acac)_3 \cdot 2CHCl_3$. The obtained results are the first steps in the study of the solvation of manganese(III) acetylacetonate. For a more extended picture and a better understanding of the influence of the processes occurring in the solution on the structure of the complex, its solvates should be studied with a number of other solvents, and not only their composition, but also the structure should be established.

The latter task is very difficult, but it is highly interesting as part of the studied issue.

Author contributions

All authors made an equivalent contribution to the preparation of the publication.

Conflict of interests

The authors declare that they have no known competing financial interests or personal relationships that could have influenced the work reported in this paper.

References

1. Sleightholme A. E. S., Shinkle A. A., Liu Q., Li Y., Monroe C. W., Thompson L. T. Non-aqueous manganese acetylacetonate electrolyte for redox flow batteries. *Journal of Power Sources*. 2011;196(13): 5742–5745. https://doi.org/10.1016/j.jpowsour.2011.02.020

2. Hirano M., Yakabe S., Clark J. H., Morimoto T. Synthesis of sulfoxides by the oxidation of sulfides with sodium chlorite catalysed by manganese(III) acetylacetonate in acetone in the presence of alumina. *Journal of the Chemical Society, Perkin Transactions 1*. 1996;22: 2693–2698. https://doi.org/10.1039/P19960002693

3. Dewar M. J. S., Nakaya T. Oxidative coupling of phenols. *Journal of the American Chemical Society*. 1968;90(25): 7134–7135. https://doi.org/10.1021/ja01027a051

4. Van Gorkum R., Bouwman E., Reedijk J. Fast Autoxidation of ethyl linoleate catalyzed by [$Mn(acac)_3$] and bipyridine: A possible drying catalyst for alkyd paints. *Inorganic Chemistry*. 2004;43(8): 2456–2458. https://doi.org/10.1021/ic0354217

5. Sharma R. K., Yadav M., Monga Y., Gaur R., Adholeya A., Zboril R., Varma R. S., Gawande M. B. Silica-based magnetic manganese nanocatalyst – Applications in the oxidation of organic halides and alcohols. *ACS Sustainable Chemistry & Engineering*. 2016;4(3): 1123–1130. https://doi.org/10.1021/acssuschemeng.5b01183

6. Ban H. T., Kase T., Murata M. Manganese-based transition metal complexes as new catalysts for olefin polymerizations. *Journal of Polymer Science, Part A:*

Polymer Chemistry. 2001;39(21): 3733–3738. https://doi.org/10.1002/pola.10021

7. Park Y. J., Kim J. G., Kim M. K., Chung H. T., Kim H. G. Preparation of $LiMn_2O_4$ thin films by a sol–gel method. *Solid State Ionics*. 2000;130(3-4): 203–214. https://doi.org/10.1016/S0167-2738(00)00551-8

8. Shimizu Y., Murata T. Sol–gel synthesis of perovskite-type lanthanum manganite thin films and fine powders using metal acetylacetonate and poly(vinyl alcohol). *Journal of the American Ceramic Society*. 1997;80(10): 2702–2704. https://doi.org/10.1111/j.1151-2916.1997.tb03178.x

9. Steinbach J. F., Burns J. H. Chloroform-bearing chelates. *Journal of the American Chemical Society*. 1958;80(8): 1839–1841. https://doi.org/10.1021/ja01541a018

10. Clarke F. R., Steinbach J. F., Wagner W. F. Halomethane solvates of tervalent acetylacetonates. *Journal of Inorganic and Nuclear Chemistry*. 1964;26(7): 1311–1316. https://doi.org/10.1016/0022-1902(64)80215-3

11. Grinvald I. I., Kalagaev I. Yu., Petukhov A. N., Grushevskaya A. I., Kapustin R. V., Vorotyntsev I. V. Association of haloforms in condensed and gas phases. Ir spectroscopy and Dft calculations. *Journal of Structural Chemistry*. 2018;59(2): 313–320. https://doi.org/10.1134/S0022476618020087

12. Pinchas S., Silver B. L., Laulicht I. Infrared absorption spectra of the ^{18}O-labeled acetylacetonates of Cr(III) and Mn(III). *Journal of Chemical Physics*. 1967;46(4): 1506–1510. https://doi.org/10.1063/1.1840881

13. Lawson K. E. The infrared absorption spectra of metal acetylacetonates. *Spectrochimica Acta*. 1961;17(3): 248–258. https://doi.org/10.1016/0371-1951(61)80071-4

14. Diaz-Acosta I., Baker J., Hinton J. F., Pulay P. Calculated and experimental geometries and infrared spectra of metal tris-acetylacetonates: vibrational spectroscopy as a probe of molecular structure for ionic complexes. Part II. *Spectrochimica Acta, Part A*. 2003;59(2): 363-377. https://doi.org/10.1016/S1386-1425(02)00166-X

Information about the authors

Vladimir P. Zlomanov, DSc in Chemistry, Professor at the Department of Inorganic Chemistry of the Faculty of Chemistry, Lomonosov Moscow State University (Moscow, Russian Federation).

https://orcid.org/0000-0002-0327-4715
zlomanov1@mail.ru

Rodion S. Eshmakov, 6th year student of the Faculty of Chemistry, Lomonosov Moscow State University (Moscow, Russian Federation).

https://orcid.org/0000-0002-6002-6515
rodion.eshmakov@chemistry.msu.ru

Igor V. Prolubshchikov, 4th year student of the Faculty of Chemistry, Lomonosov Moscow State University (Moscow, Russian Federation).

https://orcid.org/0000-0003-0735-1658
prolubshikoviv@gmail.com

Received November 15, 2021; approved after reviewing December 10, 2021; accepted February 15, 2022; published online March 25, 2022.

Translated by Marina Strepetova
Edited and proofread by Simon Cox

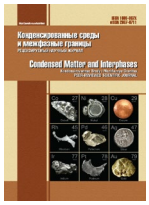

ISSN 1606-867X (Print)
ISSN 2687-0711 (Online)
Condensed Matter and Interphases
Kondensirovannye Sredy i Mezhfaznye Granitsy
https://journals.vsu.ru/kcmf/

Original articles

Research article
https://doi.org/10.17308/kcmf.2022.24/9053

The influence of the physicochemical nature of the components of the V_2O_5/GaAs, MnO_2/GaAs, V_2O_5/InP, MnO_2/InP, TiO_2/InP, and SnO_2/InP heterostructures and the oxidation conditions on the surface morphology of the synthesised films

A. S. Kovaleva[1]✉, B. V. Sladkopevtsev[1], A. A. Samsonov[1], S. I. Alferova[2], D. G. Kovalev[1], S. A. Titov[1], N. D. Pryakhin[1], I. Ya. Mittova[1]

[1]Voronezh State University,
[1]Universitetskaya pl., Voronezh, 394018, Russian Federation

[2]Voronezh State Pedagogical University,
86 ul. Lenina, Voronezh, 394043, Russian Federation

Abstract

The formation of oxide functional films on the surface of semiconductors is a serious technological challenge, which is even more complicated in the nanometre thickness range. It is necessary to form films with specified values of thickness, resistivity, and a certain surface morphology for practical applications. Such films are used in micro- and optoelectronics, environmental monitoring, and alternative energy devices. The goal of this work is to establish the features of the surface morphology of thin films formed as a result of the thermal oxidation of the MnO_2/GaAs, V_2O_5/GaAs, V_2O_5/InP, MnO_2/InP, TiO_2/InP, and SnO_2/InP heterostructures depending on the physicochemical nature of the components and the oxidation conditions.

The synthesis of thin films on the InP and GaAs surfaces was carried out by thermal oxidation under the influence of magnetron-deposited layers of chemostimulator-modifiers. The thickness of the formed films and their composition were determined by laser ellipsometry, X-ray phase analysis, and infra-red spectroscopy. The scanning tunnel and atomic force microscopy were used to determine the morphological characteristics of the films and their dependence on the type of semiconductor substrate, the nature of the chemostimulator-modifier, and the conditions of the thermal oxidation.

The application to the GaAs and InP surfaces of the most effective chemostimulator-modifiers (V_2O_5 and MnO_2) of thermal oxidation and higher temperatures of the oxidation process contributed to the formation of smoother and nanostructured films.

Keywords: Gallium arsenide, Indium phosphide, Heterostructure, Thermal oxidation, Surface morphology, Grain size

Acknowledgements: The research results were partially obtained using the equipment of the Centre for Collective Use of Scientific Equipment of Voronezh State University. URL: http://ckp.vsu.ru

For citation: A. S. Kovaleva, B. V. Sladkopevtsev, A. A. Samsonov, S. I. Alferova, D. G. Kovalev, S. A. Titov, N. D. Pryakhin, I. Ya. Mittova The influence of the physicochemical nature of the components of the V_2O_5/GaAs, MnO_2/GaAs, V_2O_5/InP, MnO_2/InP, TiO_2/InP, and SnO_2/InP heterostructures and the oxidation conditions on the surface morphology of the synthesised films. *Kondensirovannye sredy i mezhfaznye granitsy = Condensed Matter and Interphases.* 2022;24(1): 33–44. https://doi.org/10.17308/kcmf.2022.24/9053

Для цитирования: Ковалева А. С., Сладкопевцев Б. В., Самсонов А. А. Алферова С. И., Ковалев Д. Г., Титов С. А., Пряхин Н. Д., Миттова И. Я. Влияние физико-химической природы компонентов гетероструктур MnO_2/GaAs, V_2O_5/GaAs, V_2O_5/InP, MnO_2/InP, TiO_2/InP и SnO_2/InP и режима процесса оксидирования на морфологию поверхности синтезированных пленок. *Конденсированные среды и межфазные границы*. 2022;24(1): 33–44. https://doi.org/10.17308/kcmf.2022.24/9053

✉ Anastasia S. Kovaleva, e-mail: nkovaleva.vsu@yandex.ru

1. Introduction

The synthesis of new materials for electronics has always been important. They have been used to create competitive optoelectronic [1], environmental monitoring [2], and alternative energy [3] devices. The challenges of import substitution and miniaturisation require new highly rapid, environmentally friendly, and cost-effective methods and approaches to create efficient devices based on MIS (metal-insulator-semiconductor) and SIS (semiconductor-insulator-semiconductor) structures [4–7]. Thermal oxidation is one of the most common methods used to create nanosized functional oxide films on the surface of semiconductors [8]. This technological challenge becomes more complicated in the nanometre thickness range since in many processes the regular growth of films begins at a sufficiently developed stage (at a thickness of more than 100 nm) and the dependence of film properties on their surface morphology and structure is the most pronounced in the nanometre thickness range.

The intrinsic thermal oxidation of the A^3B^5 semiconductors leads to the formation of low quality films, which can be improved by changing the process mechanism from intrinsic to chemically stimulated [8, 9]. Nanoscale layers of oxide-chemostimulators, formed by the method of reactive magnetron sputtering contribute to a change in the mechanism of the oxidation of GaAs and InP semiconductors from intrinsic to transit or catalytic, which allows accelerating the process of film growth, purposefully changing their composition, surface morphology, and structure and, consequently, their properties [9].

In [10–13], it was established that nanosized layers of V_2O_5 [10, 11] applied to the InP and GaAs surfaces contribute to catalytic oxidation, whereas the application of nanosized layers of MnO_2 [12, 13] mainly promote transit oxidation. Coated layers of SnO_2 [14, 15] and TiO_2 [16, 17] do not exhibit chemical stimulating properties in the processes of InP thermal oxidation, although they are thermodynamically capable of transferring oxygen to semiconductor components; however, they modify the composition of the film.

The investigation of the surface morphology of films formed as a result of thermal oxidation of heterostructures based on A^3B^5 semiconductors is necessary in order to track the dynamics of changes in their characteristics compared to reference samples, to understand the dependence of the surface morphology of synthesised objects on the physicochemical nature of the substrate and deposited oxide, the oxidation conditions, and the characteristics of films. Such data are necessary to optimise the formation of low-dimensional composite structures based on A^3B^5 semiconductors, primarily MIS structures. It is assumed that the created oxide films can compete with SiO_2 when manufacturing ohmic contacts, anti-reflective coatings for mirrors of heterolasers on GaAs and InP substrates, and in other aspects of functional electronics [4, 7].

Therefore, the goal of this work is to establish the features of the surface morphology of thin films formed as a result of thermal oxidation of the V_2O_5/GaAs(100), V_2O_5/GaAs(111), MnO_2/GaAs(100), MnO_2/GaAs(111), V_2O_5/InP, MnO_2/InP, TiO_2/InP, and SnO_2/InP heterostructures depending on the physicochemical nature of the components and the oxidation conditions.

2. Experimental

As semiconductor substrates, we used pre-prepared (100) and (111) oriented AGChT (tellurium-doped, electronic) gallium arsenide with a concentration of the main charge carriers of at least $8\cdot10^{18}$ cm^{-3}, and (100) oriented FIE-1A (tin-doped, electronic) indium phosphide with a concentration of the main charge carriers of at least $5\cdot10^{16}$ cm^{-3}.

When studying the mechanisms of processes on the surface and in layers of nanometre thickness, it is necessary to pay special attention to the standardisation of the surface morphology of the substrates, which dictates a thorough pretreatment of monocrystals. Before thin-film heterostructures were formed, the used substrates were treated with the following etchers: a) to clean and polish the surface of indium phosphide, we used a peroxide-sulphuric acid polishing solution H_2SO_4:H_2O_2:H_2O = 2:1:1, etching time was 10 min; b) to clean and polish the surface of gallium arsenide, we used concentrated hydrofluoric acid (ω(HF) = 49%), etching time was 10 min. The gallium face of GaAs(111) was determined by the method described in [18]. We needed to determine the gallium face of such a

substrate since it is more preferable for growing films on it: the film's microstructure would be less defective.

A thin nanosized (~35 nm) oxide layer performing a chemically stimulating (modifying) function was deposited by reactive magnetron sputtering of vanadium target (99.99% purity) with a diameter of 50 mm (2 inch) in an oxygen-argon atmosphere (V_2O_5 layers) using an Angstrom engineering CoVap II installation. The initial evacuation of atmospheric air from the vacuum chamber was carried out with a fore vacuum pump, and the subsequent deep evacuation (p_{res} ~ 10^{-6} Torr) was conducted by a Varian Turbo 301 turbomolecular pump. In the process of developing a technique for sputtering a vanadium target in an oxygen-argon atmosphere, the optimal composition of the gas mixture was established for the reactive deposition of vanadium pentoxide layers Ar:O_2 – 3:1. Nanoscale layers of the SnO_2 modifier (Sn target with 99.99 % purity) and TiO_2 (Ti target with a purity of at least 99.8%) were deposited in similar way. The MnO_2 layers (a compressed target of manganese dioxide powder with a purity of at least 99.8 %) were deposited in an Ar atmosphere.

The first step in the study of various characteristics is to determine the composition of layers formed by magnetron sputtering on the surface of semiconductors. For HSs with V_2O_5, the deposited layer mainly consisted of vanadium pentoxide but in addition to it, the diffraction patterns showed a peak corresponding to V_2O_3, which can be explained by the specifics of the magnetron sputtering process. However, its relative content was low; therefore, we designated the synthesised HSs as V_2O_5/A^3B^5 [10]. A similar situation was characteristic of HSs with MnO_2: the magnetron-sputtered layer on A^3B^5 mostly consisted of MnO_2 with a relatively small inclusion of Mn_2O_3, therefore, we designated the synthesised HSs as MnO_2/A^3B^5 [12,13]. Magnetron sputtering of tin dioxide on the InP surface resulted in the formation of a layer of SnO_2, without the formation of undesirable phases [14]. The titanium dioxide layer formed by magnetron sputtering only contained TiO_2 phases in structural modifications of anatase and rutile [19].

The thermal oxidation of synthesised heterostructures V_2O_5/GaAs(100), V_2O_5/GaAs(111), MnO_2/GaAs(100), MnO_2/GaAs(111), V_2O_5/InP, MnO_2/InP, TiO_2/InP, and SnO_2/InP was carried out in a flowing quartz reactor of a horizontal resistive heating furnace MTP-2M-50-500 (TRM-10 sensor unit, adjustment accuracy ±1 °C) in flowing oxygen (the volume flow rate of 30 l/h) in the temperature range from 500 to 550 °C. The oxidation time varied between 20–180 minutes.

For practical applications, it is necessary to form films with specified values of thickness, resistivity, and a certain stable and reproducible surface morphology. MnO_2/GaAs and V_2O_5/GaAs heterostructures with (100) and (111) oriented substrates were thermally oxidised in various conditions until the target film thickness of up to ~250 nm was reached. The formation of films with a thickness of about 200 nm was necessary to compare them with SiO_2 films of similar thickness, which are widely used to manufacture ohmic contacts, to protect side edges of mesastripes, and to create anti-reflective coatings for mirrors of Fabry-Perot heterolaser resonators on GaAs and InP substrates in a system of GaInAsP isolattice solid solutions covering the wavelength range of 0.8–1.8 μm [3]. A necessary requirement for the formed films is certain values of electrical strength, breakdown voltages, adhesion to the substrate, and surface roughness. The study of films of the nanoscale thickness range is natural due to the further miniaturisation of micro- and optoelectronic objects [6, 7].

The thicknesses of the deposited layers of chemostimulator oxides and films grown as a result of thermal oxidation were controlled by laser (LE, LEF-754, wavelength of 632.8 nm, ±1 nm accuracy) and spectral ellipsometry (SE, Ellips-1891, wavelength range of 250–1100 nm, the measurement accuracy of the ellipsometric parameters $\Psi\delta = 0.05°$ and $\delta\Delta = 0.1°$). To interpret the measurement results, we used a single-layer model "external medium–film–substrate" with sharp interfaces between the media [20–22].

By increasing the growth rate of the film thickness as compared to the intrinsic oxidation (acceleration of the process), it is possible to judge whether the selected substance is a chemostimulator. A relative increase in the

growth rate of oxide film b during the thermal oxidation of HS was calculated by formula (1):

$$b = \frac{\Delta d_{Me_x O_y / A^3B^5}}{\Delta d_{A^3B^5}}, \quad (1),$$

where $\Delta d A^3B^5$ is a change in the thickness of the oxide film during the intrinsic oxidation of the semiconductor (standard) and $\Delta d_{Me_xO_y/}A^3B^5$ is a change in the thickness of the oxide film during the thermal oxidation of the HS with a deposited chemostimulator layer minus the thickness of the latter [13].

To characterise the heterostructures and thin films formed on the semiconductor surface, a set of instrumental methods was used. The phase composition of the samples was studied by X-ray phase analysis (XPA) using a ARL X'tra diffractometer (Thermo Scientific, Cu$K_{\alpha 1}$ with λ = 1.540562 Å). Data on the chemical bonds in the synthesised films were obtained by transmission infrared spectroscopy (IRS) using a VERTEX 70 IR-Fourier spectrometer (frequency range of 400–1400 cm^{-1}). The surface morphology of the samples and reference samples was studied by atomic force microscopy (AFM) using a Solver P47 Pro scanning probe microscope by NT-MDT corporation in the semi-contact mode at various points of the surface with an HA_NC Etalon cantilever and by scanning tunnelling microscopy (STM) using the NTK UMKA in the DC mode. These methods were complementary since the surface of dielectrics could not be studied by the STM method, and one of our tasks was to form dielectric oxide films.

3. Results and Discussion

The results of film thickness measurements (LE, SE) on GaAs monocrystal samples of various orientations with nanoscale layers of MnO_2 and V_2O_5 chemostimulators at 500 and 530 °C in the time intervals from 20 to 180 minutes are given in Table 1.

Films with a thickness of less than 100 nm were synthesised most quickly on the V_2O_5/GaAs(111) HS, which allows us to conclude that the time of film formation depends on the substrate orientation when the V_2O_5 HS is used as a chemostimulator. For the GaAs(111) orientation of the substrate, there was the largest bond angle between the surface atoms and the plane of the substrate surface (90°), which determined the bond availability for oxygen [18]. This contributed to a higher rate of interaction between the plane and the oxidiser. No such dependence was found for the MnO_2/GaAs heterostructure.

When comparing the thicknesses of the formed films for similar InP-based HSs (Table 2), it was obvious that there was a maximum acceleration when using the magnetron-formed layer of V_2O_5 as a chemostimulator. The layers of tin and titanium dioxides had the opposite effect; they slowed down the process of film formation during the oxidation of the heterostructure but acted as modifiers of the composition of oxide films (Table 3), which was necessary for the formation of films with the desired properties [14].

Films formed by thermal oxidation of the V_2O_5/GaAs(100) HSs consisted of vanadium oxides in various oxidation states (V_2O_5 and VO_2) (Fig. 1a). This was related to the decomposition of V_2O_5 in flowing oxygen during thermal oxidation and the active interaction of vanadium pentoxide with substrate components. The VO_2 phases on the X-ray pattern of the sample with the substrate orientation (111) was not observed (Fig. 1b).

Table 1. Thicknesses of nanoscale films (LE, SE) formed by thermal oxidation of HSs on GaAs with deposited layers of V_2O_5 and MnO_2 in various conditions and the relative change in film thickness calculated by formula (1)

Sample	TO mode	Film thickness, nm		Relative change in film thickness, times
		LE	SE	
V_2O_5/GaAs(100)	T=500 °C, t=50 min	83	81	2.18
V_2O_5/GaAs(111)	T=500 °C, t=25 min	88	86	2.41
MnO_2/GaAs(100)	T=500 °C, t=60 min	77	74	1.91
MnO_2/GaAs(111)	T=500 °C, t=70 min	72	74	1.68
GaAs	T=500 °C, t=60 min	27	27	–

Table 2. Thicknesses of films (LE) formed by thermal oxidation of HSs based on InP at 530 °C for 60 min and the relative change in film thickness calculated by formula (1)

Sample	TO mode	Film thickness, nm	Relative change in film thickness, times
SnO_2(68 nm)/InP	*T*=530 °C, *t*=60 min	82	0.389
TiO_2(35 nm)/InP		53	0.48
V_2O_5(21 nm)/InP		115	2.61
MnO_2(21 nm)/InP		76	1.5
InP		41	–

Table 3. Identified phases for GaAs-based HSs after thermal oxidation for 50 and 20 minutes, respectively, at 500 °C

Sample, TO mode	Interplane distance, d_{hkl}	Defined phase
V_2O_5/GaAs(100) (50 min)	4.3743; 3.1498	V_2O_5
	3.3510	VO_2
	3.2607; 1.4553	As_2O_5
	2.1903	Ga_2O_3
	2.0628	GaAs
V_2O_5/GaAs(111) (20 min)	4.3876; 2.7577	V_2O_5
	2.0644	GaAs
	1.4531	As_2O_5
	2.1770	Ga_2O_3

No arsenates were found in the films since the conditions of thermal oxidation were not severe enough, however, gallium and arsenic oxides were present as had been expected (see Table 3). The XPA and IR methods also confirmed the absence of vanadium oxide consumption, i.e., the process of thermal oxidation of the studied HSs in various conditions had a catalyst regeneration cycle, which in our case was vanadium oxide (V) [8–10].

The presence of arsenic in the films in the form of As_2O_5 indicated the binding of the substrate components at the internal interface, which prevented the accumulation of underoxidised arsenic. A change in the orientation of GaAs at a constant temperature of thermal oxidation (500 °C) led to changes in the qualitative phase composition of the films. The X-ray pattern of the film grown by thermal oxidation of the V_2O_5/GaAs(100) HS had 2 reflections corresponding to As_2O_5, while the X-ray pattern of the film formed by the oxidation of V_2O_5/GaAs(111) had no second As_2O_5 peak, which indicated a more efficient binding of oxygen components in case of the (100) oriented substrate.

In case of the transition to other HSs, in which indium phosphide acted as a substrate, the composition of the films became somewhat more complicated. The formed films consisted of vanadium oxides in various oxidation states (V_2O_5; V_2O_3; VO_2), indium oxide (In_2O_3), and indium phosphate ($InPO_4$) (Table 4) [11]. The qualitative difference from similar gallium arsenide-based HSs was primarily that their X-ray pattern had peaks corresponding to indium phosphate, one of the target oxidation products for this particular semiconductor, formed as a result of the secondary interaction of the corresponding oxides. Using the data about the composition of the film formed on the SnO_2/InP HS, we can draw a conclusion about the modifying properties of SnO_2 [14]. The presence of peaks corresponding to the $Sn_3(PO_4)_2$ compound indicates an interaction between the SnO_2 layer deposited on the surface with the oxidation products of the substrate components, in particular phosphorus, and, as a consequence, a change in the composition of the film and its surface. Additional studies of the TiO_2/InP sample by IR spectroscopy revealed absorption bands

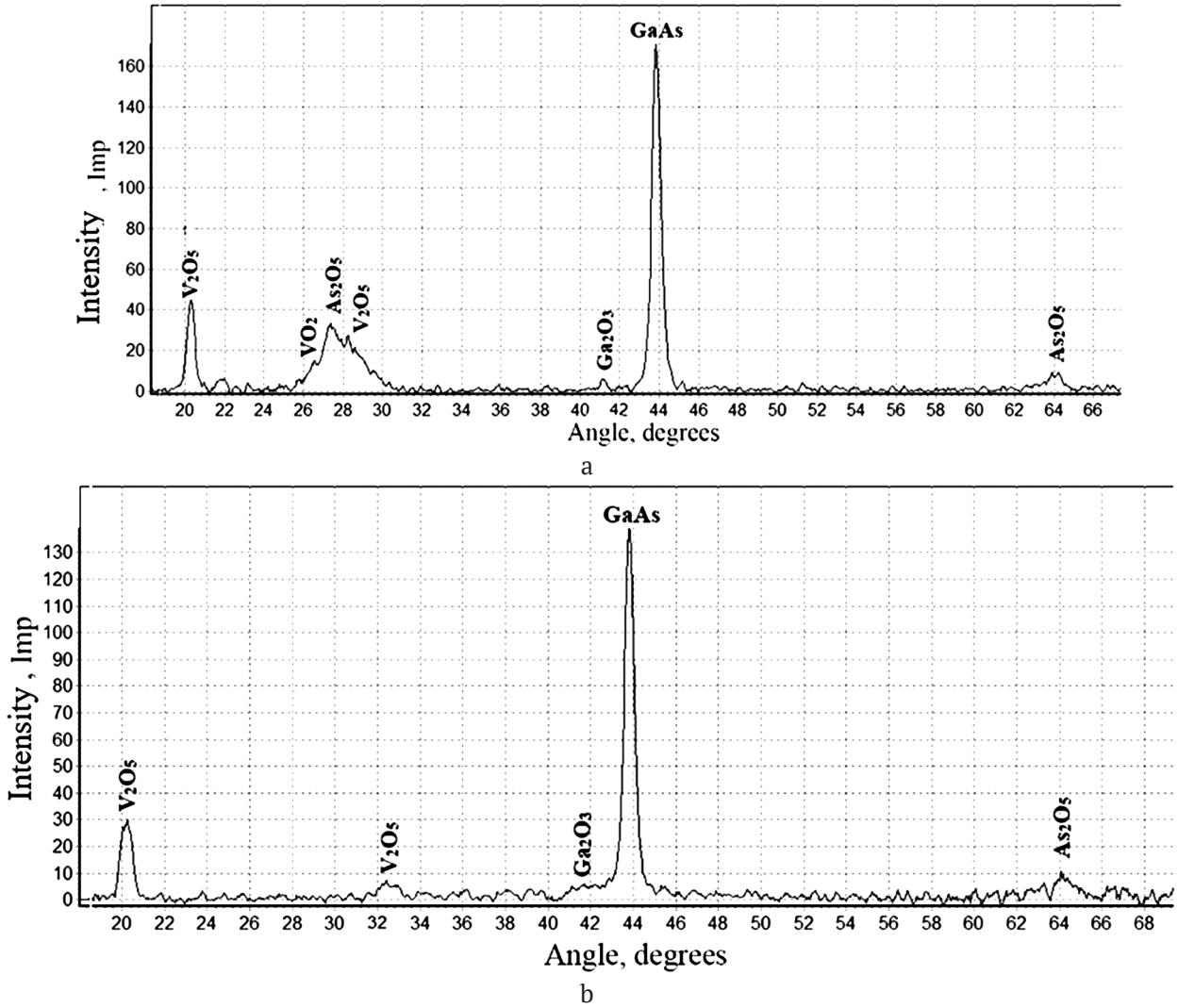

Fig. 1. XRD patterns of V_2O_5/GaAs(100) (a) and V_2O_5/GaAs(111) (b) heterostructures after thermal oxidation at a temperature of 500 °C for 50 minutes and 20 minutes, respectively

of the $Ti(PO_3)_3$, TiP_2O_7, $Ti_4(P_4O_{12})_3$, $InPO_4$, and $In(PO_3)_3$ compounds [23,24], which also indicates the modifying effect of titanium dioxide layers.

The surface morphology of the synthesised nanosized films reflected the different nature of the effect of the deposited oxides. Thermal oxidation of HSs of V_2O_5/GaAs (relief height within 10 nm) and MnO_2/GaAs (relief height of 70 nm) for 50 and 60 minutes, respectively (Fig. 2), led to the formation of films with a pronounced grain structure with an average lateral grain size of 360 nm for MNO_2/GaAs(100) and 150 nm for V_2O_5/GaAs(100). The ordered arrangement of grains was most pronounced on the surface of the V_2O_5/GaAs(100) sample.

Films formed with a thickness of more than 130 nm had noticeable differences in the data of laser and spectral ellipsometry, which can be associated with a greater development of the surface of the films with an increase in the oxidation time (according to AFM data, the maximum relief height reached 200 nm for the MnO_2/GaAs(100) sample with an oxide film thickness of 232 nm according to the averaged LE and SE data (Fig. 3)). The films were characterised by a grain structure with an average diameter of the grain of 300 nm. There was a similar tendency to the formation of a more developed surface (relief height of 87 nm at a film thickness of 164 nm, average diameter of the grain of 250 nm) with an increase in the oxidation time for the V_2O_5/GaAs(100) sample.

After 60 minutes of thermal oxidation of the V_2O_5/InP HS at 530 °C (the thickness of the formed

Table 4. Identified phases for the Me_xO_y/InP HSs after TO at 500 and 530 °C, 60 minutes

Sample, TO mode	Interplane distance, d_{hkl}	Defined phase
SnO_2/InP (530 °C)	5.5324	$In(PO_3)_3$
	3.6897; 3.5745	$Sn_3(PO_4)_2$
	3.0299	$InSn_4$
	2.932	InP
	1.4814	In_2O_3
	1.5074	$InPO_4$
	1.4668	P_2O_5
TiO_2/InP (500 °C)	2.9305; 1.4652	InP
	2.9213; 1.5256	In_2O_3
	1.5157; 1.4815; 1.3976	TiO_2
	1.5109; 1.4863	Ti_2O_3
V_2O_5/InP (500 °C)	4.999; 1.729	In_2O_3
	3.414; 4.392	V_2O_5
	1.468; 2.935	InP
	2.480; 2.244	V_2O_3
	2.013	VO_2
	1.451; 3.709	$InPO_4$
MnO_2/InP (500 °C)	4.999; 1.729	In_2O_3
	3.108; 2.005	MnO_2
	1.468; 2.935	InP
	2.494; 2.110	Mn_2O_3
	1.451; 3.709	$InPO_4$

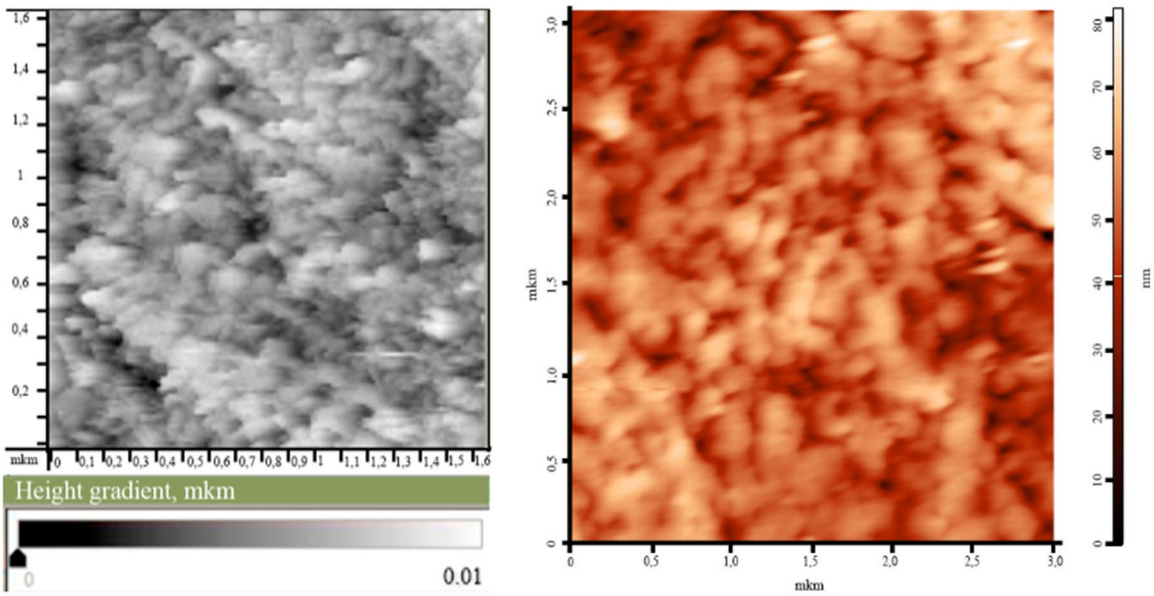

a b

Fig. 2. STM image of the surface of the V_2O_5(35 nm)/GaAs(100) samples (TO 500 °C, 50 min) (a) and AFM image of the surface of the MnO_2 (34 nm)/GaAs(100) sample (TO 500 °C, 60 min) (b). The scanning areas are 1.6×1.6 and 3×3 μm^2, respectively. The thickness of oxide films (LE) is 83 nm and 77 nm, respectively

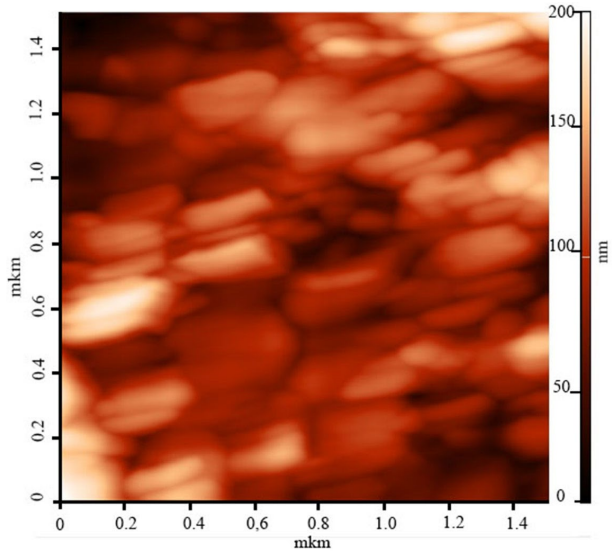

Fig. 3. AFM image of the surface of the MnO_2/GaAs(100) sample (TO 500 °C, 180 min). The scanning area is 1.5×1.5 μm². The thickness of the oxide film (LE, SE) is 232 nm

film of 120 nm) (Fig. 4), the surface of the formed film became rough with pronounced structural elements (lines, bends, grains of an average size of 30 nm). After 60 minutes of oxidation of the MnO_2/InP HS at 530 °C (film thickness of 76 nm), the relief height did not exceed 20 nm, and the surface was characterised by a grain structure with an average size of 55 nm [13].

When potential chemostimulators, which are able to modify the composition of the growing films (SnO_2, TiO_2 [14]), were applied on InP, which resulted in the formation of phosphates of the introduced element (see Table 4), fairly coarse-grained films with a grain diameter of 100–700 nm, depending on the synthesis mode, and a relief height of 20-40 nm were formed at 500–550 °C in 60 minutes (Fig. 5).

The comparison of the morphology of TiO_2/InP samples which were thermally oxidised at temperatures of 500 °C (Fig. 6a) and 530 °C (Fig. 6b) for 60 minutes showed that at higher temperatures the film surface had a more pronounced grain structure but with a smaller height difference.

Table 5 summarises the data that illustrate the effect of the substrate type on the surface morphology of the films grown by thermal oxidation of the corresponding HSs.

It can be seen that films formed on InP generally have a more uniform relief than those

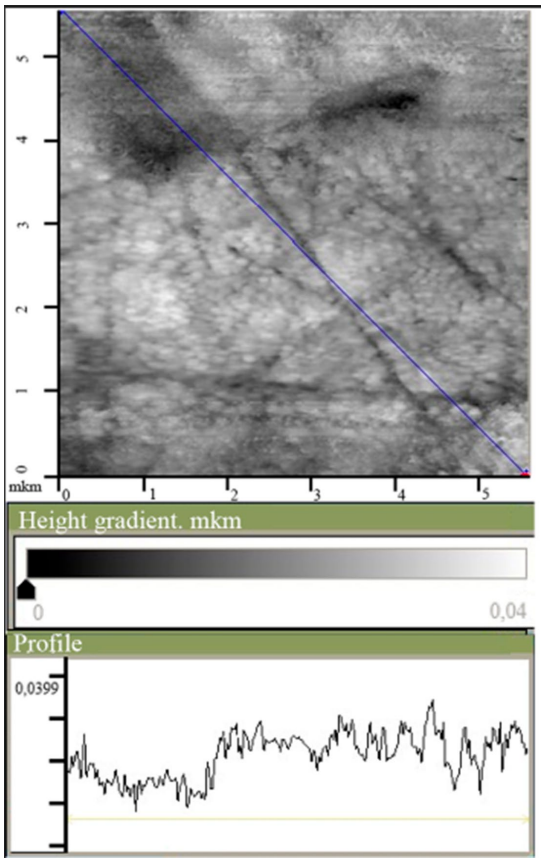

Fig. 4. STM image and surface profile of the V_2O_5/InP sample (TO 530 °C, 60 min). The scanning area is 5.5×5.5 μm². The thickness of the oxide film (LE) is 120 nm

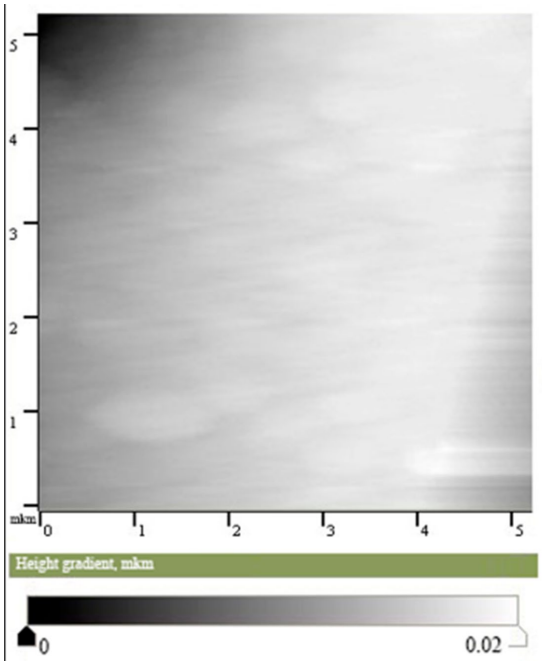

Fig. 5. STM image of the surface of the SnO_2/InP sample (TO 550 °C, 60 min). The scanning area is 5.2×5.2 μm². The thickness of the oxide film (LE) is 90 nm

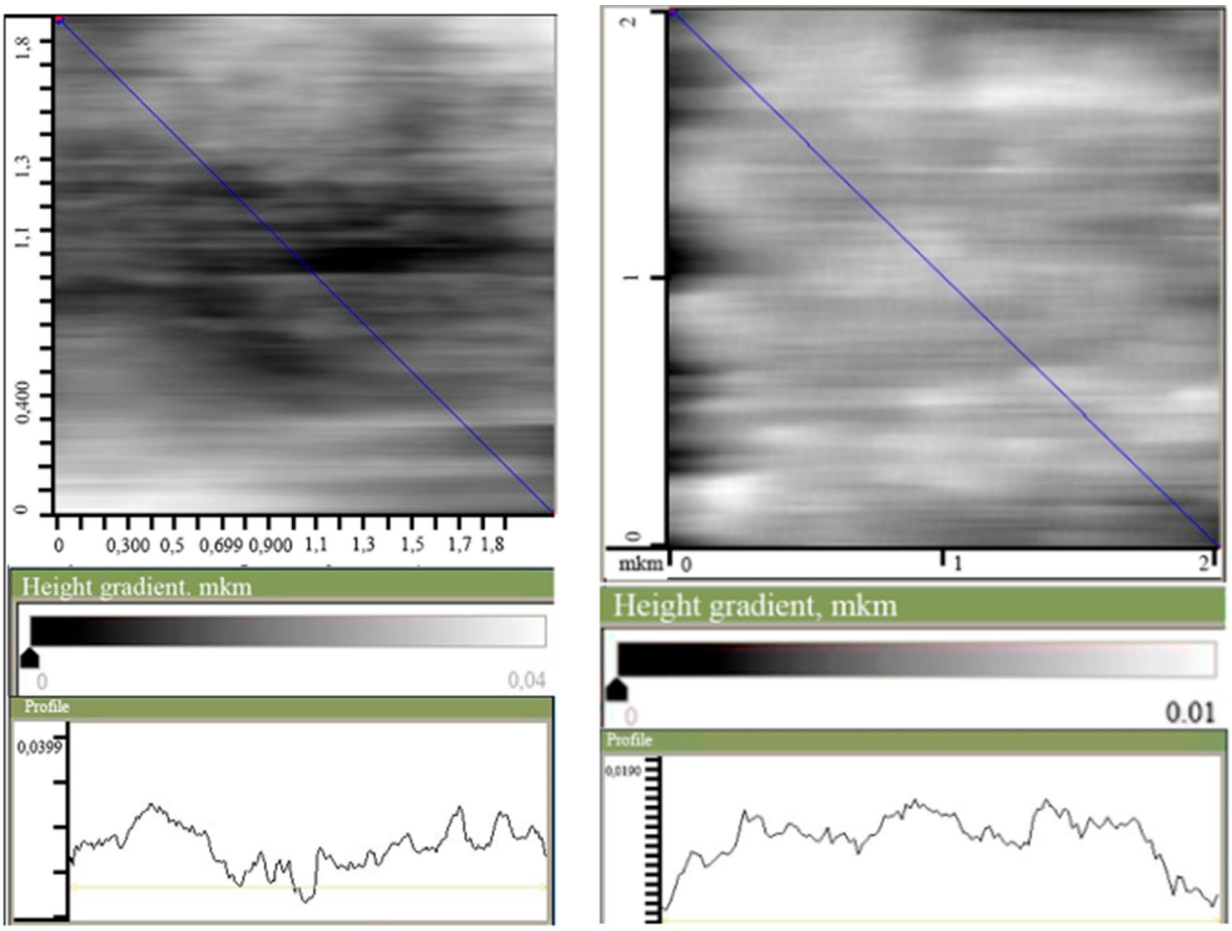

a b

Fig. 6. STM image and the surface profile of the TiO_2/InP samples (TO 500 °C, 60 min) (a) and TiO_2/InP (TO 530 °C, 60 min) (b). The scanning areas are 2×2 μm². The thickness of the formed films (LE) is 50 nm and 55 nm, respectively

Table 5. Surface characteristics (STM, AFM) of Me_xO_y/InP and Me_xO_y/GaAs HSs depending on the type of substrate

Sample	TO mode	Scanning area, μm²	Relief height, nm	Average grain size, nm
V_2O_5/InP	550 °C, 60 min	5.5×5.5	40	30
V_2O_5/GaAs(100)	500 °C, 50 min	1.6×1.6	9	150
MnO_2/InP	530 °C, 60 min	5.2×5.2	20	50
MnO_2/GaAs(100)	500 °C, 60 min	3×3	70	360

formed on GaAs; they also have smaller grains. Such films have a thickness corresponding to the nanoscale range and a nanodispersed structure. The TiO_2/InP HS (Table 6) can be used as an example to trace the effect of temperature at the same duration of the process on the surface morphology of the films. As the table shows, a higher temperature contributes to the smoothing of the surface relief, however, the grain size in the lateral direction increases more than twice.

The physicochemical nature of the oxides in the deposited layers has the most significant effect on film structuring (Table 7). HSs with oxide layers, which perform the functions of a modifier and have a noticeable chemostimulating effect on the process of thermal oxidation (V_2O_5, MnO_2) [10–13], for the same semiconductor (InP) produce nanosized and nanostructured films. In

Table 6. Surface characteristics (STM, AFM) of Me_xO_y/InP HSs depending on the thermal oxidation mode

Sample	TO mode	Scanning area, μm²	Relief height, nm	Average grain size, nm
TiO_2/InP	500 °C , 60 min	2×2	25	90
TiO_2/InP	530 °C, 60 min	2×2	12	250

Table 7. Surface characteristics (STM, AFM) of Me_xO_y/InP HSs depending on the type of chemostimulator

Sample	TO mode	Scanning area, μm²	Relief height, nm	Average grain size, nm
SnO_2/InP	550 °C, 60 min	5.2×5.2	20	400
TiO_2/InP	530 °C, 60 min	2×2	12	250
V_2O_5/InP	550 °C, 60 min	5.5×5.5	40	30
MnO_2/InP	530 °C, 60 min	5×5	20	50

the case of the solely modifying effect on the composition of the formed films (SnO_2/InP, TiO_2/InP), even at a relatively small height of the relief, the films are coarse-grained, with a lateral grain size of up to 400 nm.

4. Conclusion

The targeted selection of compounds, orientations of the A^3B^5semiconductor substrate, and the oxidation conditions make it possible to vary the thickness and surface morphology of the films. The introduction of the most effective chemostimulator-modifiers (V_2O_5, MnO_2) of thermal oxidation on the surface of GaAs and InP, as compared to less efficient chemostimulator-modifiers (SnO_2, TiO_2), causes the formation of smoother films with a nanodispersed surface structure. The smoothing of the surface relief of oxide films is also promoted by a higher temperature of the oxidation process.

Author contributions

All authors made an equivalent contribution to the preparation of the publication.

Conflict of interests

The authors declare that they have no known competing financial interests or personal relationships that could have influenced the work reported in this paper.

References

1. Oktyabrsky S., Peide Ya. *Fundamentals of III-V Semiconductor MOSFETs*. Boston: Springer-Verlag; 2010. 445 p. https://doi.org/10.1007/978-1-4419-1547-4

2. Alferov Zh. I., Zubov F. I., Cirlin G. E., Zhukov A. E., Shchavruk N. V., Pavlov A. Yu., Ponomarev D. S., Klochkov A. N., Khabibullin N. A., Maltsev P. P. The first terahertz quantum-cascade laser fabricated in Russia. *Nano- and Microsystem Technology*. 2017;19(5): 259–265. https://doi.org/10.17587/nmst.19.259-265

3. Sheng S. Li. *Semiconductor physical electronics*. New York: Springer-Verlag; 2006. 708 p. https://doi.org/10.1007/0-387-37766-2

4. Ünlü H., Horing N. J. M., Dabowski J. *Low-dimensional and nanostructured materials and devices*. Springer Science LCC; 2015. 674 p. https://doi.org/10.1007/978-3-319-25340-4

5. Khan S. B., Akhtar K. *Photocatalysts: Applications and attributes*. IntechOpen; 2019. 143 p. https://doi.org/10.5772/intechopen.75848

6. Mittova I. Ya., Sladkopevtsev B. V., Mittova V. O. Nanoscale semiconductor and dielectric films and magnetic nanocrystals - new directions of development of the scientific school of Ya. A. Ugai "Solid state chemistry and semiconductors". Review. *Kondensirovannye sredy i mezhfaznye granitsy = Condensed Matter and Interphases*. 2021;23(3): 309–336. https://doi.org/10.17308/kcmf.2021.23/3524

7. Moshnikov V. A., Alexandrova O. A. *Nanostructured oxide materials in modern micro-, nano- and optoelectronics*. Saint Petersburg: SPbGETU «LETI» Publ.; 2017. 266 p. (In Russ.)

8. Mittova I. Ya. Influence of the physicochemical nature of chemical stimulators and the way they are introduced into a system on the mechanism of the thermal oxidation of GaAs and InP. *Inorganic Materials*. 2014;50(9): 874–881. https://doi.org/10.1134/s0020168514090088

9. Tomina E. V., Mittova I. Ya., Sladkopevtsev B. V., Kostryukov V. F., Samsonov A. A., Tretyakov N. N. Thermal oxidation as a method of formation of nanoscale functional films on $A^{III}B^{V}$ semiconductors: chemostimulated influence of metal oxides: overview. *Kondensirovannye sredy i mezhfaznye granitsy = Condensed Matter and Interphases*. 2018;20(2): 184–

203. (In Russ., abstract in Eng.) https://doi.org/10.17308/kcmf.2018.20/522

10. Mittova I. Ya., Tomina E. V., Lapenko A. A., Sladkopevtsev B. V. Catalytic action of vanadium and its oxide (V) in the processes of oxidation of $A^{III}B^{V}$ semiconductors. *Nanosystems: Physics, Chemistry, Mathematics*. 2012;3(2): 116–138. (In Russ.) Available at: https://www.elibrary.ru/item.asp?id=17881315

11. Tretyakov N. N., Mittova I. Ya., Sladkopevtsev B. V., Agapov B. L., Pelipenko D. I., Mironenko S. V. Surface morphology, composition, and structure of nanofilms grown on InP in the presence of V_2O_5. *Inorganic Materials*. 2015;51(7): 655–660. https://doi.org/10.1134/S002016851507016X

12. Mittova I. Ya., Sladkopevtsev B. V., Tomina E. V., Samsonov A. A., Tretyakov N. N., Ponomarenko S. V. Preparation of dielectric films via thermal oxidation of MnO_2/GaAs. *Inorganic Materials*. 2018;54(11): 1085–1092. https://doi.org/10.1134/S0020168518110109

13. Tretyakov N. N., Mittova I. Ya., Sladkopevtsev B. V., Samsonov A. A., Andreenko S. Yu. Effect of a magnetron-sputtered MnO_2 layer on the thermal oxidation kinetics of InP and the composition and morphology of the resultant films. *Inorganic Materials*. 2017;53: 65–71. https://doi.org/10.1134/S0020168517010174

14. Mittova I. Ya., Kostryukov V. F., Ilyasova N. A., Sladkopevtsev B. V., Samsonov A. A. Modification of nanoscale thermal oxide films formed on indium phosphide under the influence of tin dioxide. *Nanosystems: Physics, Chemistry, Mathematics*. 2020;11(1): 110–116. https://doi.org/10.17586/2220-8054-2020-11-1-110-116

15. Bersirova O. L., Bruk L. I., Dikusar A. I., Karaman M. I., Sidelnikova S. P., Simashkevich A.V., Sherban D. A., Yapontseva Yu. S. Thin films of titanium and tin oxides and semiconductor structures on their basis obtained by pyrolytic pulverization: Preparation, characterization, and corrosion properties. *Surface Engineering and Applied Electrochemistry*. 2007;43(6): 443-452. https://doi.org/10.3103/S1068375507060075

16. Diebold U. The surface science of titanium dioxide. *Surface Science Reports*. 2003;48(5-8): 53-229. https://doi.org/10.1016/S0167-5729(02)00100-0

17. Khoroshikh V. M., Bilous V. A. Titanium dioxide films for photocatalysis and medicine. *FIP FIP PSE*. 2009;7(3): 223-238. (In Russ.) Available at: http://dspace.nbuv.gov.ua/bitstream/handle/123456789/7978/07-Khoroshikh.pdf?sequence=1

18. Sangwal K. *Etching of crystals: Theory, experiment, a. application*. Amsterdam: North-Holland Physics Publishing; 1987. 496 p.

19. Acosta D. R., Martínez A., Magaña C. R., Ortega J. M. Electron and Atomic Force Microscopy studies of photocatalytic titanium dioxide thin films deposited by DC magnetron sputtering. *Thin Solid Films*. 2005;490(2): 112–117. https://doi.org/doi:10.1016/j.tsf.2005.04.067

20. Kostryukov V. F., Mittova I. Ya., Shvets V. A., Tomina E. V., Sladkopevtsev B. V., Tret'yakov N. N. Spectral ellipsometry study of thin films grown on GaAs by chemically stimulated thermal oxidation. *Inorganic Materials*. 2014;50(9): 882–887. https://doi.org/10.1134/S0020168514090052

21. Shvets V. A., Rykhlitskii, S. V., Mittova, I. Ya., Tomina E. V. Analysis of the optical and structural properties of oxide films on InP using spectroscopic ellipsometry. *Technical Physics*. 2013;58: 1638–1645. https://doi.org/10.1134/S1063784213110248

22. Spesivtsev E. V., Rykhlitskii S. V., Shvets V. A. Development of methods and instruments for optical ellipsometry at the Institute of Semiconductor Physics of the Siberian Branch of the Russian Academy of Sciences. *Optoelectronics Instrumentation and Data Processing*. 2011;47(5): 419-425. https://doi.org/10.3103/S8756699011050219

23. Nakamoto K. *Infrared and Raman spectra of inorganic and coordination compounds*. New York: John Wiley; 1986. 479 p.

24. Vorobyev N. I. *Atlas of infrared spectra of phosphates. Double condensed phosphates*. Minsk: Foundation for Fundamental Research Publ.; 1993. 250 p. (In Russ.)

Information about authors

Anastasia S. Kovaleva, 2nd year master's degree student, Voronezh State University (Voronezh, Russian Federation).
https://orcid.org/0000-0002-0350-8518
nkovaleva.vsu@yandex.ru

Boris V. Sladkopevtsev, PhD in Chemistry, Associate Professor at the Department of Materials Science and Nanosystem Technologies, Voronezh State University (Voronezh, Russian Federation).
https://orcid.org/0000-0002-0372-1941
dp-kmins@yandex.ru

Alexey A. Samsonov, PhD in Chemistry, Lead Engineer at the Department of Materials Science and Nanosystem Technologies, Voronezh State University (Voronezh, Russian Federation).
https://orcid.org/0000-0002-9338-815X
samsonjr@mail.ru

Svetlana I. Alferova, PhD in Chemistry, Associate Professor at the Department of Chemistry, Voronezh State Pedagogical University (Voronezh, Russian Federation).
https://orcid.org/0000-0001-7304-5988
alferovasvet53@mail.ru

Danila G. Kovalev, 2nd year master's degree student, Voronezh State University (Voronezh, Russian Federation).
https://orcid.org/0000-0003-2265-1579
dkovalev754@gmail.com

Sergey A. Titov, student, Voronezh State University (Voronezh, Russian Federation).
https://orcid.org/0000-0001-6322-8174
donatedmaster@mail.ru

Nikita D. Priakhin, student, Voronezh State University (Voronezh, Russian Federation).
https://orcid.org/0000-0002-8453-2412
revan19_91@mail.ru

Irina Ya. Mittova, DSc in Chemistry, Professor at the Department of Materials Science and Nanosystems Technologies, Voronezh State University (Voronezh, Russian Federation).
https://orcid.org/0000-0001-6919-1683
imittova@mail.ru

Received December 15, 2021; approved after reviewing December 21, 2021; accepted February 15, 2022; published online March 25, 2022.

Translated by Irina Charychanskaya
Edited and proofread by Simon Cox

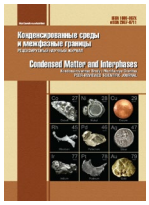

ISSN 1606-867X (Print)
ISSN 2687-0711 (Online)
Condensed Matter and Interphases
Kondensirovannye Sredy i Mezhfaznye Granitsy
https://journals.vsu.ru/kcmf/

Original articles

Research article
https://doi.org/10.17308/kcmf.2022.24/9054

The interconnection of efficiency and the degree of aggregation of nanofiller in polymer nanocomposites

G. V. Kozlov, I. V. Dolbin✉

Kh. M. Berbekov Kabardino-Balkarian State University,
173 Chernyshevski ul., Nalchik 360004, Russian Federation

Abstract

The rule of mixtures was the first theoretical model, used for a description of the elastic modulus of multicomponent systems, including those of polymer nanocomposites. However, the use of nominal magnitudes of the characteristics of system components in such an approach led to overestimated values of their elastic modulus. Therefore, various modified versions of the rule of mixtures are currently used for this purpose, which significantly complicate its application and do not indicate the physical factors leading to overestimated theoretical results.

In this study, a modified rule of mixtures was proposed, taking into account the decrease in the effective (actual) elastic modulus of the nanofiller in a polymer matrix of the nanocomposite compared to the nominal value determined only by the aggregation of the nanofiller. It is known that the aggregation process is the main negative factor reducing the final properties of nanomaterials, while other factors (for example, the interfacial adhesion level, nanofiller orientation, etc.) depend on the degree of aggregation. The physical sence of the aggregation process is a decrease in the relative proportion of nanofiller-polymer matrix interfacial regions, i.e., the effectiveness of a nanofiller as a reinforcing element of a nanocomposite is determined by its ability to generate high-modulus interfacial regions.

The rule of mixtures modified in this way correctly describes the dependence of the elastic modulus of the nanocomposite on the content of the nanofiller, regardless of the type of the latter (carbon nanotubes, graphene, etc.). Therefore, the nanofiller efficiency indicator can serve as a complex parameter that is characteristic of the nanocomposite quality.

Keywords: The rule of mixtures, Nanocomposite, Carbon nanotubes, Graphene, Aggregation, Elastic modulus, Interfacial regions

For citation: Kozlov G. V., Dolbin I. V. The interconnection of efficiency and the degree of aggregation of nanofiller in polymer nanocomposites. *Kondensirovannye sredy i mezhfaznye granitsy = Condensed Matter and Interphases.* 2022;24(1): 45–50. https://doi.org/10.17308/kcmf.2022.24/9054

Для цитирования: Козлов Г. В., Долбин И. В. Взаимосвязь эффективности и степени агрегации нанонаполнителя в полимерных нанокомпозитах. *Конденсированные среды и межфазные границы.* 2022;24(1): 45–50. https://doi.org/10.17308/kcmf.2022.24/9054

✉ Igor V. Dolbin, e-mail: i_dolbin@mail.ru

1. Introduction

It is known [1], that the rule of mixtures was the first mathematical apparatus used for the description of the properties of polymer composites. Since the simplest initial version of this rule rarely provides a correct description of the properties of composites, in particular, their elastic modulus, a large number of modified versions of the rule of mixtures, taking into account the orientation and anisotropy of the nanofiller, its efficiency, etc., have been developed [2]. The most commonly used modification of the rule of mixtures for anisotropic fillers is as follows [2]:

$$E_c = \left(\eta_0 E_{ef} - E_m\right)\varphi_n + E_m, \quad (1)$$

where E_c, E_{ef}, and E_m are the elastic modulus of the composite, the effective modulus of the filler, and the elastic modulus of the matrix polymer, respectively, η_0 is the fibre orientation factor, φ_n is the volume content of the filler.

It should be noted that value of E_{ef} refers to the actual elastic modulus of the filler in the polymer matrix of the composite, which decreases compared to the nominal value of this parameter due to the aggregation of the filler and other factors. Obviously, the complex parameter $\eta_0 E_{ef}$ is the actual elastic modulus of the filler in the polymer matrix. Therefore, the purpose of this study was the determination of the effectiveness of a nanofiller in the reinforcing process of polymer nanocomposites based on the example of two types of these nanomaterials, filled with anisotropic 1D (carbon nanotubes) and 2D (graphene oxide) nanofillers.

2. Experimental

In the case of polyamide-6/carbon nanotube nanocomposites, single-walled carbon nanotubes (CNTs) functionalized with carboxylic acid (CNT-COOH) supplied by Carbon Solutions, Inc. (USA) were used as a nanofiller. Nanotubes of this brand have specific end groups for chemical functionalization - they contain 3-4% carboxylic acid groups and have a relative carbon purity of 80-90%. All other necessary chemical reagents were obtained from Aldrich (USA) and used as supplied [3].

The following procedure was used to obtain nanocomposites based on polyamide-6 (PA-6) by *in situ* polymerization. Carbon nanotubes and caprolactam were loaded into a flask, and the mixture was sonicated at 353 K for 2 h to obtain a homogeneous CNTs dispersion. Then the flask was placed in an oil bath heated to 373 K, and 6-aminocaproic acid was added to the suspension. The suspension was heated for 6 h at 523 K with mechanical stirring in a nitrogen atmosphere. Then, the resulting mixture was poured into water, where a very rigid polymeric nanomaterial was deposited. The precipitate was cut into small pieces and washed with hot water at 353 K for an hour to remove the unreacted monomer and low molecular weight oligomers [3].

Fibres of PA-6/CNT nanocomposites were obtained by the extrusion of the material heated to 523 K in a nitrogen atmosphere through a hole with a diameter of 0.40 mm and subsequent cooling to room temperature in air. Mechanical tests for uniaxial tension of the fibres obtained by this method using samples with the diameter of ~ 1 mm and length of ~ 40 mm were performed using an Instron Universal Testing Machine (UTM, model 4455, USA) at a temperature of 293 K and a strain rate of ~ 10^{-3} s^{-1} [3].

Poly(ethylene terephthalate) (PET) manufactured by Toray Saehan with a weight-average molecular weight was used as a matrix polymer for polymer/graphene oxide nanocomposites. $\overline{M}_w = 1.92 \cdot 10^5$. The graphene oxide (GO), prepared according to the modified Hummers method, was used as a nanofiller. The functionalization of GO was performed using S_N2-type reaction with alkyl bromide, which easily reacts with hydroxyl and carboxyl groups on the surface of GO [4].

PET/GO nanocomposites were obtained by mixing the components (PET and GO) in 0-chlorophenyl and the subsequent sonication of the mixture for 1 h. After that, PET/GO nanocomposite films were obtained by pouring these solutions with different nanofiller contents onto a horizontal substrate. Then the solvent was slowly evaporated at room temperature during the day, and finally the films were dried under vacuum at a temperature of 343 K during the day. The content of graphene oxide in the studied nanocomposites varied within 0.5–3.0 wt%. % [4].

The mechanical properties of PET/GO nanocomposites under uniaxial tension were

measured using an Instron-5543 universal testing machine using a 1 kN load cell at a temperature of 293 K and a slider speed of 3 mm/min [4].

3. Results and discussion

In the case of polymer nanocomposites, the rule of mixtures (equation (1)) can be rewritten as follows:

$$E_n = \left(\eta_{ef} E_{nan} - E_m\right)\varphi_n + E_m, \quad (2)$$

where E_n is the elastic modulus of the nanocomposite, E_{nan} is the nominal modulus of the nanofiller, taken for the considered nanomaterials equal to 750 GPa [3], η_{ef} is the efficiency indicator of the nanofiller when increasing the elastic modulus of the nanocomposite.

It should be noted that the most significant difference between equations (1) and (2) is the use of the nominal, rather than the effective value of the elastic modulus of the nanofiller E_{nan} in the last equation. In turn, this means that the efficiency indicator η_{ef} takes into account all factors leading to a decrease in the nominal value of the elastic modulus of the nanofiller (orientation, anisotropy, aggregation, etc.).

The fact that nanofiller aggregation is the strongest factor affecting the properties of nanocomposites is well known [5]. In this study, for the characterization of this process, we used the aggregation parameter χ defined as follows [6]:

$$\chi = \frac{\varphi_n}{\varphi_n + \varphi_{if}}, \quad (3)$$

where φ_{if} is the relative proportion of interfacial regions estimated using the following percolation relation [7]:

$$\frac{E_n}{E_m} = 1 + 11\left(\varphi_n + \varphi_{if}\right)^{1,7}, \quad (4)$$

where is the ratio En/Em is commonly referred to as reinforcement degree of the nanocomposite.

Attention should be paid to the physical meaning of the parameter χ, which is determined according to equation (3). As is known [8], the interfacial regions are the same reinforcing element of the nanocomposite structure as the nanofiller itself [8]. Thus, the parameter χ is determined by the growth of the actual proportion of the reinforcing element of the nanocomposite structure ($\varphi_n + \varphi_{if}$) relative to the nominal φ_n. In other words, the degree of aggregation of a nanofiller is determined by its ability to generate interfacial regions.

In turn, the value of φ_n is determined according to the well-known formula [7]:

$$\varphi_n = \frac{W_n}{\rho_n}, \quad (5)$$

where W_n is the weight content of the nanofiller, ρ_n is its density, which for carbon nanotubes was estimated as follows [7]:

$$\rho_n = 188\left(d_{CNT}\right)^{1/3}, \text{ kg/m}^3, \quad (6)$$

where d_{CNT} is the outer diameter of the carbon nanotube, specified in nanometers.

For graphene oxide, the value of ρ_n is taken as being equal to 1600 kg/m^3 [9]. The dependence of the nanofiller efficiency indicator η_{ef} on the reciprocal value of aggregation parameter χ is shown in Fig. 1. It was linear and demonstrated an increase in the efficiency of the nanofiller as the degree of its aggregation decreased. This dependence can be analytically expressed by the following equation:

$$\eta_{ef} = 2{,}8 \cdot 10^{-3} \chi^{-1}. \quad (7)$$

It should be noted that the proposed model is adequate for nanofillers with very different forms of aggregation. For carbon nanotubes, which initially form bundles of collinearly arranged individual nanotubes, the emergence of ring-shaped formations in the polymer matrix is realized, structurally similar to macromolecular coils of branched polymer chains [10]. It should be noted that the emergence of such formations is a common effect for 1D nanofillers [11, 12]. Separate plates of graphene oxide in a polymer matrix form “packages” (tactoids) consisting of several collinearly stacked plates, the number of which varies from 1 to 100 [13]. Nevertheless, the various structural forms of nanofiller aggregation described above are correctly interpreted within the formalism of the proposed model (Fig. 1 and equation (7)).

For the studied PA-6/CNT and PET/GO nanocomposites, the calculation according to equations (3) and (4) showed an increase of χ in the interval 0.0143–0.330 at $\varphi_n \leq 0.02$ (Fig. 1), which, according to equation (7), leads to the

variation of η_{ef} = 0.195–0.009. Such a variation η_{ef} suggests for a hypothetical nanocomposite with E_{nan} = 1000 GPa, E_m = 2.5 GPa and φ_n = 0.02 change in magnitude E_n according to equation (2) from 2.68 to 6.40 GPa or a variation in the reinforcement degree E_n/E_m from 1.07 to 2.56, i.e., an increase of about 2.4 times, and this estimate clearly demonstrates the strong effect of nanofiller aggregation on the properties of polymer nanocomposites.

A comparison of the experimentally obtained dependences of the reinforcement degree E_n/E_m on the volume content of the nanofiller φ_n for PA-6/CNT and PET/OG nanocomposites, which were calculated according to the rule of mixtures (equations (2) and (7)), is shown in Fig. 2. As can be seen, in both cases, a good agreement between theory and experiment was obtained. Their average discrepancy was 6 %. This correspondence was obtained only by using the actual value of the elastic modulus of the nanofiller $\eta_{ef}E_{nan}$, instead of its nominal value E_{nan}. The same figure shows the theoretical curve calculated according to the base case, i.e., equation (1), which does not take into account nanofiller aggregation at h_0 = 0.38 [14] for a random orientation of anisotropic nanofillers. This curve provides overestimated values of the reinforcement degree and does not reflect the actual shape of the dependence $E_n/E_m(\varphi_n)$ for PET/GO nanocomposites. It should be noted that the calculation according to the basic equation is in good agreement with the experimental data with low φ_n (< 0.002), where aggregation is negligible. The obtained correspondence means that the main factor influencing the properties of nanocomposites is the aggregation of the nanofiller, characterized by the parameter χ, and other factors (orientation, anisotropy, etc.) are only derivatives of the main process – aggregation. For example, the authors of [15] showed that the formation of ring-shaped structures of carbon nanotubes in a polymer matrix leads to a change in their anisotropy, namely, a decrease in the radius of these structures determines a decrease in the actual level of anisotropy of this nanofiller. Finally, it should be mentioned, that the change E_n/E_m with φ_n for the studied nanocomposites (Fig. 2), the authors of [3, 4] also explained by the increase in the degree of aggregation of the nanofiller as its content increased, without provision of any quantitative estimates to confirm this assumption.

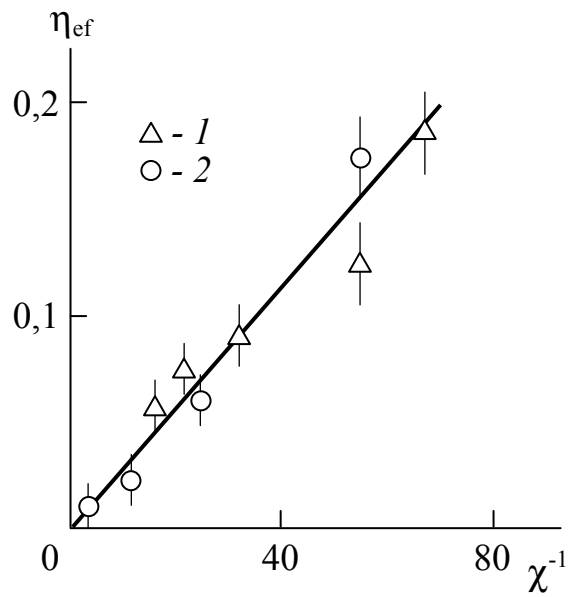

Fig. 1. The dependence of efficiency indicator of nanofiller η_{ef} on the reciprocal value of aggregation parameter c for nanocomposites PA-6/CNT (*1*) and PET/GO (*2*)

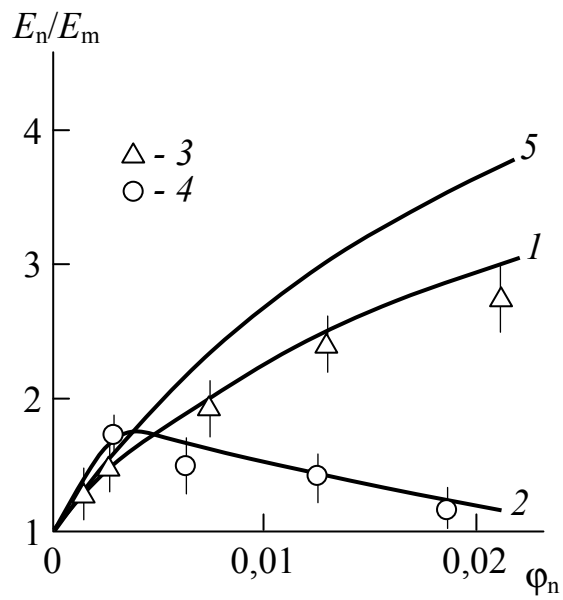

Fig. 2. Comparison of dependences of the reinforcement degree E_n/E_m on the volume content of the nanofiller φ_n for nanocomposites PA-6/CNT (*1*, *3*) and PET/GO (*2*, *4*) calculated according to the rule of mixtures (the equations (2) and (7)) (*1*, *2*) and those experimentally obtained (*3*, *4*). *5* – calculation according to the basic equation (1) at η_0 = 0.38

4. Conclusions

Thus, the fundamental novelty of the obtained results consists of the following postulates. The effectiveness of a nanofiller in improving the properties of polymer nanocomposites is determined only by the degree of its aggregation. Other factors (orientation, anisotropy, etc.) are derivatives of this main process. The physical meaning of the aggregation parameter is the ratio of the nominal and actual content of the reinforcing component in the structure of the nanocomposite, i.e., the efficiency of the nanofiller is determined by its ability to generate high-modulus interfacial regions. The rule of mixtures provides a correct description of the elastic modulus (or reinforcement degree) only when using the actual (effective) elastic modulus of the nanofiller, and not its nominal value. The nanofiller efficiency indicator can serve as a complex characteristic of the quality of the resulting polymer nanocomposites.

Author contributions

All authors made an equivalent contribution to the preparation of the publication.

Conflict of interests

The authors declare that they have no known competing financial interests or personal relationships that could have influenced the work reported in this paper.

References

1. Ahmed S., Jones F.R. A review of particulate reinforcement theories for polymer composites. *Journal of Materials Science*. 1990;25(12): 4933–4942. https://doi.org./10.1007/bf00580110

2. Krenchel H. *Fibre Reinforcement*. Copenhagen: Academic Forlag; 1964. 326 p.

3. Gao J., Itkis M. E., Yu A., Bekyarova E., Zhao B., Haddon R. C. Continuous spinning of a single-walled carbon nanotube – nylon composite fiber. *Journal of the American Chemical Society*. 2005;127(11): 3847–3854. https://doi.org/10.1021/ja0446193

4. Shim S. H., Kim K. T., Lee J. U., Jo W. H. Facile method to functionalize graphene oxide and its application to poly (ethylene terephthalate)/graphene composites. *ACS Applied Materials & Interfaces*. 2012;4(16): 4184–4191. https://doi.org/10.1021/am300906z

5. Šupová M., Martynková G. S., Barabaszová K. Effect of nanofillers dispersion in polymer matrices: A Review. *Science of Advanced Materials*. 2011;3(1): 1–25. https://doi.org/10.1166/sam.2011.1136

6. Kozlov G. V., Mikitaev A. K. *Structure and properties of nanocomposites polymer/organoclay*. Saarbrücken: LAP LAMBERT Academic Publishing GmbH and Comp.; 2013. 318 p.

7. Mikitaev A. K., Kozlov G. V., Zaikov G. E. *Polymer Nanocomposites: Variety of Structural Forms and Applications*. New York: Nova Science Publishers, Inc.; 2008. 319 p.

8. Coleman J. N., Cadek M., Ryan K. P., Fonseca A., Nady J. B., Blau W. J., Ferreira M. S. Reinforcement of polymer with carbon nanotubes. The role of an ordered polymer interfacial regions. Experiment and modeling. *Polymer*. 2006;47(23): 8556–8561. https://doi.org/10.1016/j.polymer.2006.10.014

9. Xu Y., Hong W., Bai H., Li Ch., Shi G. Strong and ductile poly (vinyl alcohol)/graphene oxide composite films with layred structure. *Carbon*. 2009;47(15): 3538–3543. https://doi.org/10.1016/j.carbon.2009.08.022

10. Schaefer D. W., Justice R. S. How nano are nanocomposites? *Macromolecules*. 2008;43(24): 8501–8517. https://doi.org/10.1021/ma070356w

11. Bridge B. Theoretical modeling of the critical volume fraction for percolation conductivity in fibre-loaded conductive polymer composites. *Journal of Materials Science Letters* . 1989;8(2): 102–103. https://doi.org/10.1007/BF00720265

12. Lim G.-H., Ahn K., Bok S., Nam J., Lim B. Curving silver nanowires using liquid droplets for highly stretchable and durable percolation networks. *Nanoscale*. 2017;14(26): 8937–8946. https://doi.org/10.1039/C7NR02615C

13. Jang B. Z., Zhamu A. Processing of nanographene platelets (NGPs) and NGP nanocomposites: a review. *Journal of Materials Science*. 2008;43(21): 5092-5101. https://doi.org/10.1007/s10853-008-2755-2

14. Coleman J. N., Cadek M., Ryan K. P., Fonseca A., Nady J. B., Blau W. J., Ferreira M. S. Reinforcement of polymers with carbon nanotubes. The role of an ordered polymer interfacial region. Experiment and modeling. *Polymer*. 2006;47(22): 8556–8561. https://doi.org/10.1016/j.polymer.2006.10.014

15. Aygubova A. Ch., Karnet Yu. N., Kozlov G. V., Magomedov G. M. Effective length of a nanofiller and the degree of reinforcement of polymer/carbon nanotubes (nanofibers) nanocomposites. *International Journal of Nanomechanics Science and Technology*. 2016;7(4): 349–354. https://doi.org/10.1615/nanomechanicsscitechnolintj.v7.i4.60

Information about authors

Georgy V. Kozlov, Research Fellow, Kh. M. Berbekov Kabardino-Balkarian State University (Nalchik, Russian Federation).
https://orcid.org/0000-0002-9503-9113
i_dolbin@mail.ru

Igor V. Dolbin, PhD in Chemistry, Associate Professor of the Department of Organic Chemistry and High-Molecular Compounds, Kh. M. Berbekov Kabardino-Balkarian State University (Nalchik, Russian Federation).
https://orcid.org/0000-0001-9148-2831
i_dolbin@mail.ru

Received July 5, 2021; approved after reviewing September 2, 2021; accepted for publication February 15, 2022; published online March 25, 2022.

Translated by Valentina Mittova
Edited and proofread by Simon Cox

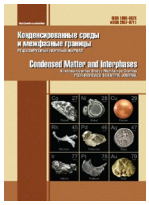

ISSN 1606-867X (Print)
ISSN 2687-0711 (Online)
Condensed Matter and Interphases
Kondensirovannye Sredy i Mezhfaznye Granitsy
https://journals.vsu.ru/kcmf/

Original articles

Research article
https://doi.org/10.17308/kcmf.2022.24/9055

Characteristics of the formation and composition of $Al_xGa_{1-x}N$/AlN/por-Si/Si(111) heterostructures grown using a porous silicon buffer layer

A. S. Lenshin[1,2]✉, P. V. Seredin[1], D. S. Zolotukhin[1], A. N. Beltyukov[3], A. M. Mizerov[4], I. A. Kasatkin[5], A. O. Radam[1], E. P. Domashevskaya[1]

[1]*Voronezh State University,*
1 Universitetskaya pl., Voronezh 394018, Russian Federation

[2]*Voronezh State University of Engineering Technologies,*
19 pr. Revolyutsii, Voronezh 394036, Russian Federation

[3]*Udmurt Federal Research Centre of the Ural Branch of the Russian Academy of Sciences,*
34 T. Baramzina ul., Izhevsk 426067, Russian Federation

[4]*Alferov Federal State Budgetary Institution of Higher Education and Science Saint Petersburg National Research Academic University of the Russian Academy of Sciences,*
Building 3, letter A, 8 Khlopin ul., Saint Petersburg 194021, Russian Federation

[5]*Saint Petersburg State University,*
7/9 Universitetskaya naberezhnaya, Saint Petersburg 199034, Russian Federation

Abstract

In this work, we studied the efficiency of introducing nanoporous silicon as a buffer layer in the growth of $Al_xGa_{1-x}N$/AlN/Si(111) on a single-crystal silicon by molecular beam growth technology. We also considered its influence on the morphological characteristics and atomic composition of the surface layers of heterostructures. As determined by X-ray diffraction, microscopic, and X-ray photoelectron methods, the heterostructure grown on Si(111) *n*-type monocrystalline silicon wafer with nanoporous por-Si buffer layer has a more homogeneous epitaxial layer, and the surface morphology of the layer is also more homogeneous.

Keywords: Porous silicon buffer layer, Heterostructures, Epitaxy

Funding: This study was supported by Russian Science Foundation grant No. 19-72-10007. This work was partially supported by the Ministry of Science and Higher Education of the Russian Federation within the framework of government order for higher education institutions, project No. FZGU-2020-0036.

Acknowledgements: Scanning electron microscopy studies were carried out at the Centre for Collective Use of Voronezh State University. XPS studies were carried out using the equipment of the Centre for Collective Use "Centre for Physical and Physico-Chemical Methods of Analysis, Study of the Properties and Characteristics of Surfaces, Nanostructures, Materials, and Products" of the Udmurt Federal Research Centre of the Ural Branch of the Russian Academy of Sciences. X-ray diffraction studies were carried out using the equipment of the Research Centre for X-ray Diffraction Studies of Saint Petersburg State University.

For citation: Lenshin A. S, Zolotukhin D. S., Beltyukov A. N., Seredin P. V., Mizerov A. M., Kasatkin I. A., Radam A. O., Domashevskaya E. P. Characteristics of the formation and composition of $Al_xGa_{1-x}N$/AlN/por-Si/Si(111) heterostructures grown using a porous silicon buffer layer. *Kondensirovannye sredy i mezhfaznye granitsy = Condensed Matter and Interphases.* 2022;24 (1): 51–59. https://doi.org/10.17308/kcmf.2022.24/9055

✉ Alexander S. Lenshin, e-mail: lenshinas@mail.ru

Для цитирования: Леньшин А. С, Золотухин Д. С., Бельтюков А. Н., Середин П. В., Мизеров А. М., Касаткин И. А., Радам А. О., Домашевская Э. П. Особенности роста и состава гетероструктур $Al_xGa_{1-x}N$/AlN/Si, выращенных с использованием буферного слоя пористого кремния. *Конденсированные среды и межфазные границы*. 2022;24(1): 51–58. https://doi.org/10.17308/kcmf.2022.24/9055

1. Introduction

The integration of III-N technology with existing silicon technology is highly promising for creating new types of microwave and optoelectronic devices. The use of silicon substrates for the growth of III-N heterostructures is advantageous due to their commercial availability and the high level of Si technology. The main problem of integrating the two technologies is the considerable mismatch of crystal lattice parameters and thermal expansion coefficients. This results in a large number of defects, uncontrolled fluctuations of solid solution composition, as well as peeling and cracking of heterostructures. An equally important problem in the production of high-power microwave nitride transistors is the heat removal from devices, which have a power dissipation of dozens of watts [1–5].

The latest way to solve these problems is to introduce various transition buffer layers into the III-N/Si(111) heterostructure. These are multi-period superlattices, layers of alternating 2D–3D morphology, or layers with gradually changing composition [6–7]. The thickness of the buffer layers can reach several tens of micrometres. The main methods for growing heterostructures for various devices are metalorganic vapour-phase epitaxy (MOVPE) and molecular beam epitaxy (MBE).

The aim of this study was to determine how introducing por-Si nanoporous silicon as a buffer layer in the growth of AlxGa1-xN/AlN/por-Si/Si(111) heterostructure influenced the structural-morphological characteristics and atomic composition of the surface layers. For this purpose, we used X-ray diffraction, microscopic, and X-ray photoelectron methods.

2. Experimental. Obtaining heterostructures by molecular beam epitaxy, structural and morphological research methods

We obtained $Al_xGa_{1-x}N$/AlN/Si(111) heterostructures of two types, with a buffer por-Si layer and without it. They were grown simultaneously on a monocrystalline silicon Si(111) wafer by nitrogen-plasma-assisted molecular beam epitaxy (PA MBE) on a Veeco Gen 200 unit [7]. We used standard Si(111) wafers of monocrystalline silicon of KDB grade (boron-doped p-type silicon) as substrates for the growth of $Al_xGa_{1-x}N$/AlN heterostructure layers. First, we formed nanoporous layers with a thickness of about 20 nm and an average pore diameter of less than 3 nm on half of the wafer surface using the original technique described in [8]. Immediately before growing the heterostructure, the wafers were annealed and nitrided for 30 min [9] in the growth chamber of the unit.

The formation of all the layers composing the heterostructures took place under metal enriched conditions. The growth rate was controlled and limited by the nitrogen flow, it was F_N~0.05 μm/h. An AlN buffer layer was formed on the substrate surface to prevent etching of the silicon substrate with liquid Ga and the formation of Ga-Si eutectic. After that, the growth of the main $Al_xGa_{1-x}N$ layer took place. Figure 1 shows the expected design set by the technological growth regime and the expected thickness of the layers of an $Al_xGa_{1-x}N$/AlN/Si heterostructure with a buffer layer of nanoporous silicon.

The morphology of the grown heterostructures was examined with a JEOL JSM 6380 LV scanning electron microscope (SEM) and a SOLVER P47 PRO atomic force microscope (AFM). Statistical analysis of the surface morphology was performed using the NOVA software.

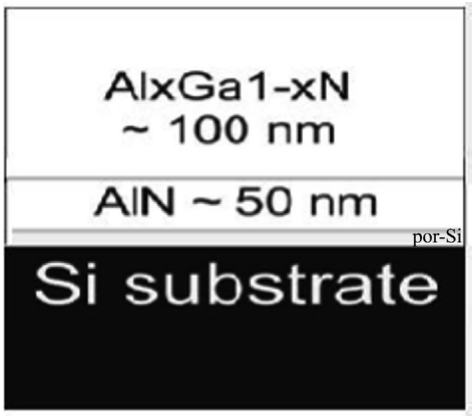

Fig. 1. The design of $Al_xGa_{1-x}N$/AlN/Si heterostructure with nanoporous silicon buffer layer

The samples were studied by X-ray photoelectron spectroscopy (XPS) on a SPECS spectrometer. The depth of the XPS analysis of the sample surface is 1–2 nm.

When processing the measurement results, Shirley algorithms were used to determine the background line and subtract the background values. To determine the binding energy of the heterostructure elements, we used the C1*s* line of natural hydrocarbon impurities of the sample surface not subjected to special cleaning as a reference line, the binding energy *E*b[C1*s*] = 285 eV. The core levels of the elements and their chemical state were determined using the X-ray photoelectron spectra database of the US National Institute of Standards [10].

The HR XRD data were obtained at 305 K on a Bruker D8 Discover diffractometer with a Ge220 monochromator.

3. Results and discussion

3.1. X-ray diffraction data

Figure 2 shows the results of X-ray diffraction in the ω–2θ geometry using the characteristic radiation of copper. It can be seen from the experimental data that the (111) diffraction line of the Si(111) silicon substrate is the most intense on the scans of both heterostructures. In addition, both scans show high-intensity reflexes (0002) from the basic plane of the hexagonal unit cell, which belong to the $Al_xGa_{1-x}N$ solid solution with a hexagonal structure. The fact that the diffractogram of the heterostructure with por-Si sublayer (dotted curves in Fig. 2) shows only the reflection from the basic plane (0002) suggests the monocrystalline state of the epitaxial film.

The diffractogram of the heterostructure grown on the c-Si(111) substrate without a porous sublayer (solid curves in Fig. 2) shows the reflection from the plane (11–20) of the $Al_xGa_{1-x}N$ solid solution. This reflection may be due to growth of $Al_xGa_{1-x}N$ solid solution columns in the <11–20> direction. Similar reflections were not observed in the ω-2θ scan of the heterostructure with a porous sublayer, indicating greater homogeneity and perfection of its crystalline structure.

3.2. Sample morphology studied by scanning electron and atomic force microscopy.

Fig. 3. shows SEM images of the surface of heterostructures obtained on monocrystalline silicon substrates (a) and using a buffer sublayer of porous silicon (b).

The surface of the samples exhibits sub-micron inhomogeneities caused by the columnar

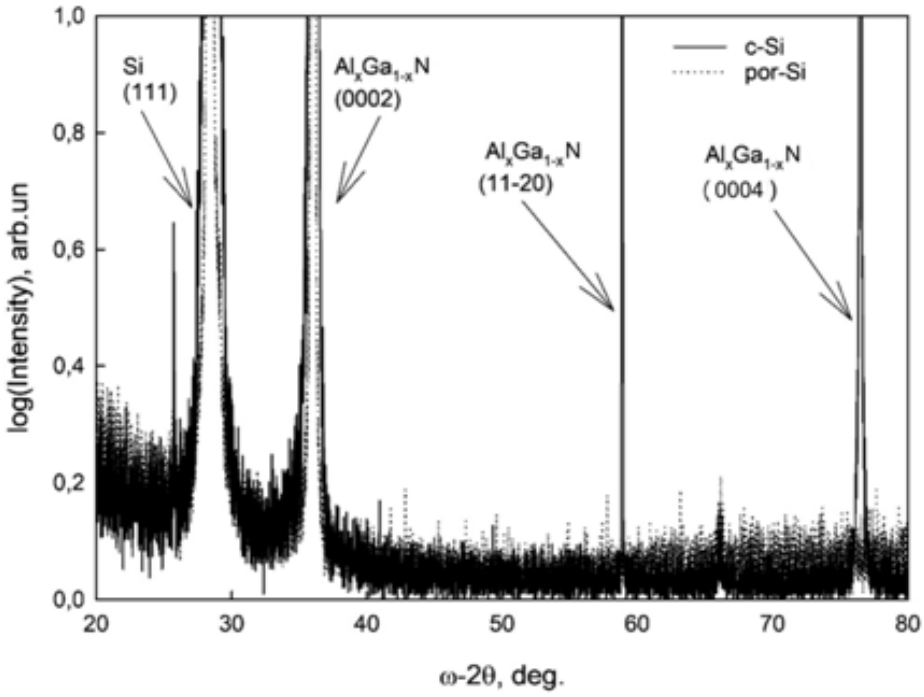

Fig. 2. XRD patterns of $Al_xGa_{1-x}N$/AlN heterostructures grown on c-Si(111) (dotted line) and por-Si/c-Si(111) (solid line) wafers

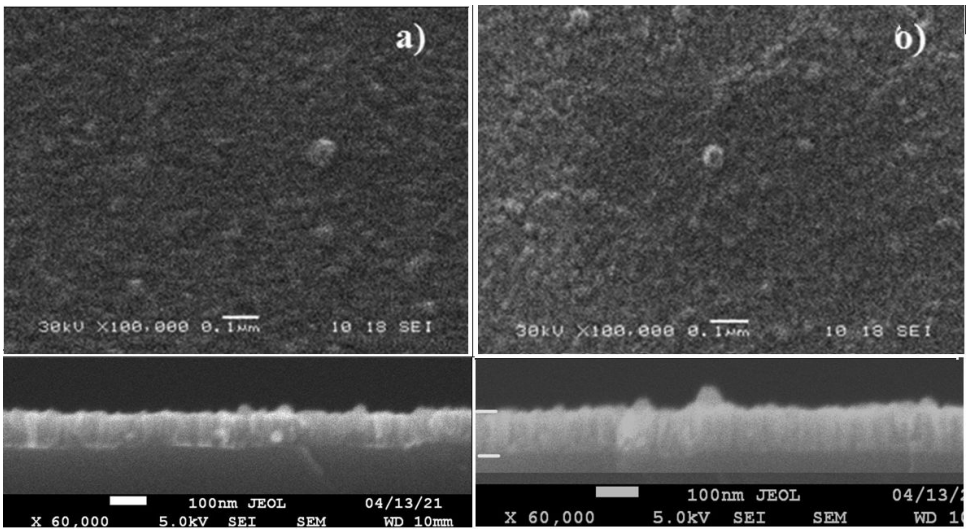

Fig. 3. SEM images of the surface and chipping of heterostructures: a) on the $Al_xGa_{1-x}N$/AlN/Si(111) monocrystalline silicon wafer; b) on the $Al_xGa_{1-x}N$/AlN/por-Si/Si(111) wafer with por-Si buffer layer

film structure observed in SEM images of the chipped samples. We had observed a similar columnar film structure in $In_xGa_{1-x}N$/Si(111) heterostructures [11–12]. We compared the morphology of the two types of heterostructures, with and without the por-Si sublayer, and saw that the heterostructure grown on a porous layer had a smaller spread in the sizes of the surface inhomogeneities. So, its film structure was more homogeneous compared to the heterostructure grown without the buffer layer. This conclusion confirmed the above XRD data.

The analysis of the profile SEM images showed that the actual thickness of the heterostructure layers coincided with those specified in the technological procedure. The lateral size distribution of surface inhomogeneities caused by the columnar structure of the film was determined by analysing AFM images (Figure 4).

Fig. 4 shows the AFM surface images and size distribution profiles of two $Al_xGa_{1-x}N$/AlN/Si(111) heterostructures grown directly on a c-Si(111) wafer and with a preformed buffer layer of porous silicon. The samples with the por-Si buffer layer have a smaller spread in the size of inhomogeneities compared to the heterostructure grown on crystalline silicon (Fig. 4a). The average inhomogeneity size on the surface of the samples grown with the por-Si buffer layer is ~100 nm. $Al_xGa_{1-x}N$/AlN/Si samples grown on crystalline silicon show two maxima of nanocolumn size distribution of ~65 and 130 nm (Fig. 4c).

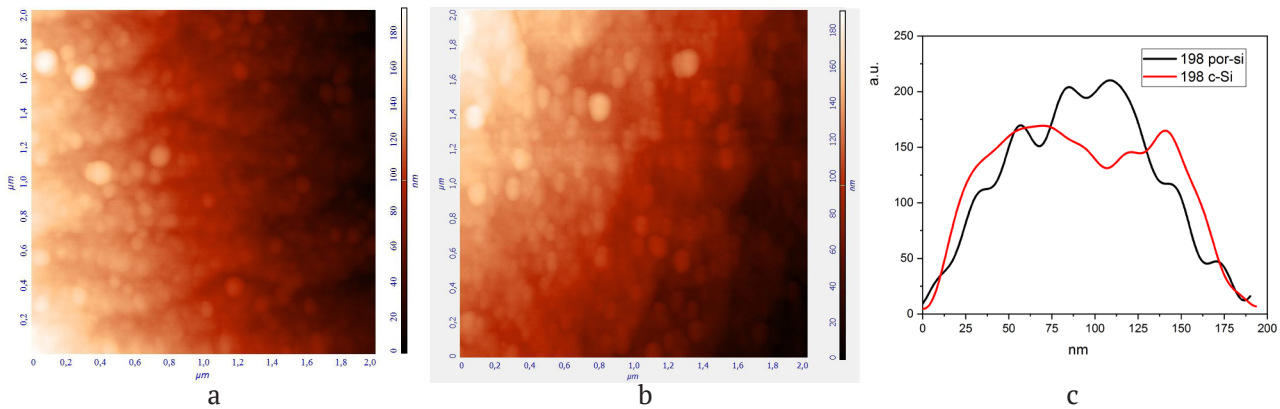

a b c

Fig. 4. AFM surface images of $Al_xGa_{1-x}N$/AlN/Si heterostructures grown: on the monocrystalline c-Si(111) wafer (a), on the por-Si/s-Si(111) wafer with a porous sublayer (b), and size distribution profiles of inhomogeneities on their surface (c)

3.3. Atomic composition of the surface of heterostructures as determined by X-ray photoelectron spectroscopy (XPS).

Figures 5 and 6 show XPS images of Al 2p, Ga 2p, and N1s core levels for heterostructures grown directly on monocrystalline silicon c-Si(111) (Fig. 5) and with a porous sublayer (Fig. 6). Table 1 shows the values of the binding energy determined with an accuracy of 0.05 eV and the half width values based on XPS study of the core levels for the two heterostructures.

XPS spectra analysis showed that on the surface of both heterostructures Al and Ga atoms formed chemical bonds with nitrogen. The binding energy (and half-width) of the core level spectra of all three elements in the $Al_xGa_{1-x}N$ solid solution were practically identical. The values were close to the binding energy of aluminium and gallium in nitrides [10]. In addition, the Al 2p spectra demonstrated the contribution of the low-intensity component of oxidised aluminium Al_2O_3 (*E*b = 75.5 eV), formed on the surface of the samples when exposed to air. The Ga 2p**3**/2 spectrum showed no similar component, but that may be due to the nitrogen N KLL Auger line superimposed on the low-energy part of the gallium spectrum. The binding energy values of the N1s nitrogen spectra correspond to Al and Ga nitrides [10]. In addition, a low-energy hydride component was observed in the nitrogen spectra, apparently it was due to the residual reagents on the surface of heterostructures (NH_3 type bonds, *E*b = 398.7 eV [10]).

By analogy with studies [13,14], the aluminium content of the film can be calculated using relation (1):

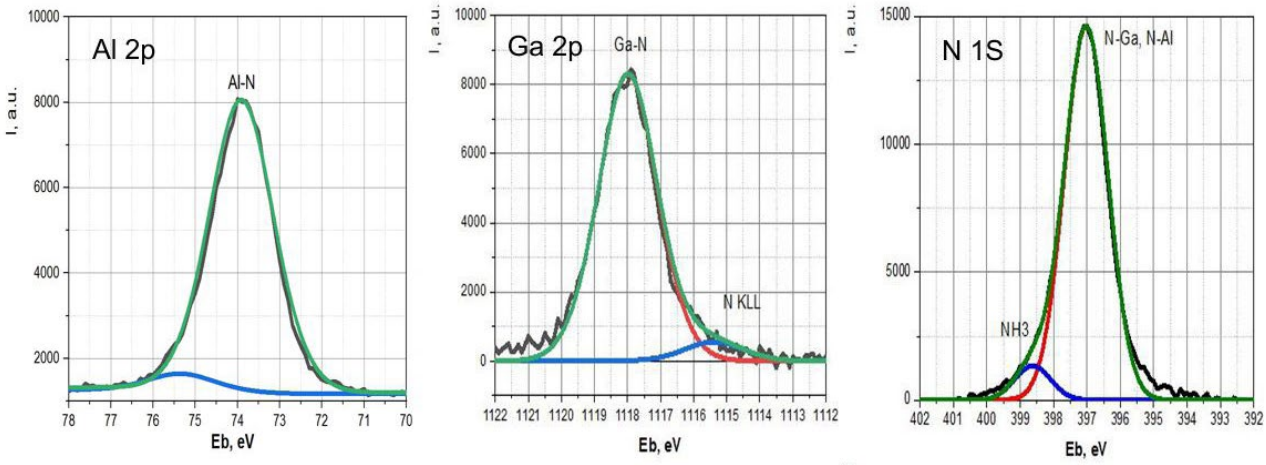

Fig. 5. XPS of Al 2p, Ga 2p**3/2,** and N1s in $Al_xGa_{1-x}N$/AlN/Si(111) heterostructures, grown on the monocrystalline silicon Si(111) wafer

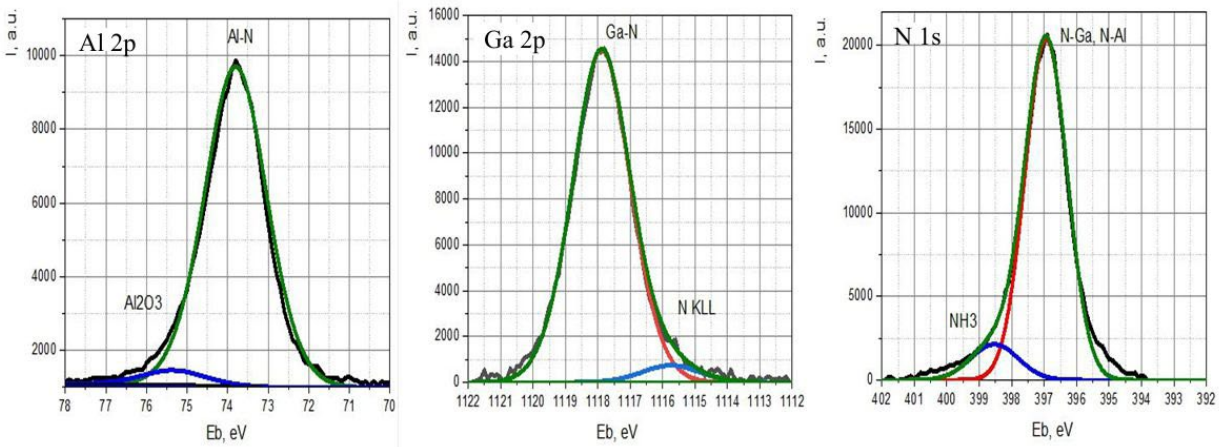

Fig. 6. XPS of Al 2p, Ga 2p**3/2**, and N1s in $Al_xGa_{1-x}N$/AlN/por-Si/Si(111) heterostructures grown on monocrystalline silicon wafer with a buffer layer of porous silicon

Table 1. Binding energy and half-width values by XPS of Al 2p, Ga 2p3/2, and N 1S core levels for heterostructures grown on c-Si(111) and on por-Si/c-Si(111)

	Binding energy, eV/ Half-width, eV					
	Al2p		Ga2p3/2		N1s	
$Al_xGa_{1-x}N$/AlN /c-Si	73.80	1.64	1117.92	2.10	396.97	1.55
$Al_xGa_{1-x}N$/AlN /por-Si/c-Si	73.91	1.72	1117.87	2.15	396.93	1.56
AlN [10]	73.90		1117.80			
GaN [10]						
GaN [10]					397.0	
AlN [10]					397.30	

$$x_{Al} = \frac{I_{Al_2p_3} / F_{Al_2p_3}}{(I_{Al_2p_3} / F_{Al_2p_3} + I_{Ga_2p_3} / F_{Ga_2p_3})}, \quad (1)$$

where I is the integral intensity of the photoelectron maxima of the corresponding lines in the spectrum and F is the sensitivity factor ($F_{Ga2}p_3$ = 2.75 and $F_{Al2}p_3$ = 0.54). Based on relation (1), we determined the Al atom concentration values in solid solution. They were x_{a_cryst} = 0.49 for samples of $Al_xGa_{1-x}N$/AlN/Si(111) grown directly on monocrystalline silicon and x_{a_por} = 0.54 for samples of $Al_xGa_{1-x}N$/AlN/Si/por-Si/Si(111) grown using a porous buffer layer. It coincided quite well with the expected technological values of *x*-0.50 specified during synthesis. The slight difference in the values of *x* of the two heterostructures may be due to their minor structural and morphological differences.

4. Conclusions

For the first time, $Al_xGa_{1-x}N$/AlN/por-Si/Si (111) heterostructures were formed by nitrogen-plasma-assisted molecular beam epitaxy using a buffer layer of por-Si porous silicon.

X-ray diffraction and electron microscopy methods showed that the formation of $Al_{0.54}Ga_{0.46}N$ solid solution on a buffer layer of porous silicon results in a more homogeneous size distribution and orientation in the basic direction of the solid solution nanocolumns compared to the similar solid solution $Al_{0.49}Ga_{0.51}N$, grown simultaneously on the same plate of monocrystalline silicon without porous layer under the same technological conditions.

The slight shift of ~ 5 % towards Al demonstrated by the surface composition of the solid solution on the substrate with a buffered porous layer may be due to the more homogeneous structural and morphological characteristics of this heterostructure.

Author contributions

Lenshin A. S. – scientific guidance, research concept, sample synthesis, text writing, and final conclusions. Zolotukhin D. S. – text writing, final conclusions. Beltyukov A. N. – measurements, text writing. Seredin P. V. – measurements, text writing. Mizerov A. M. – sample synthesis, text writing. Kasatkin I. A. –measurements, text writing. Radam A. O. – measurements. Domashevskaya E. P. – text editing, final conclusions.

Conflict of interests

The authors declare that they have no known competing financial interests or personal relationships that could have influenced the work reported in this paper.

References

1. Ho V. X., Al Tahtamouni T. M., Jiang H. X., Lin J. Y., Zavada J. M., Vinh N.Q. Room-temperature lasing action in GaN quantum wells in the infrared 1.5 μm region. *ACS Photonics*. 2018;5: 1303–1309. https://doi.org/10.1021/acsphotonics.7b01253

2. Laurent T., Manceau J.-M., Monroy E., Lim C. B., Rennesson S., Semond F., Julien F. H., Colombelli R. Short-wave infrared (λ = 3 μm) intersubband polaritons in the GaN/AlN system. *Applied Physics Letters*. 2017;110: 131102. https://doi.org/10.1063/1.4979084

3. Ajay A., Lim C. B., Browne D. A., Polaczynski J., Bellet-Amalric E., den Hertog M. I., Monroy E. Intersubband absorption in Si- and Ge-doped GaN/AlN heterostructures in self-assembled nanowire and 2D layers. *Physica Status Solidi B*. 2017;254: 1600734. https://doi.org/10.1002/pssb.201600734

4. Gkanatsiou A. A., Lioutas Ch. B., Frangis N., Polychroniadis E. K., Prystawko P., Leszczynski M. Electron microscopy characterization of AlGaN/GaN

heterostructures grown on Si (111) substrates. *Superlattices and Microstructures*. 2017;103: 376–385. https://doi.org/10.1016/j.spmi.2016.10.024

5. Oh J-T., Moon Y-T., Jang J-H., Eum J-H., Sung Y-J., Lee S. Y., Song J-O., Seong T-Y. High-performance GaN-based light emitting diodes grown on 8-inch Si substrate by using a combined low-temperature and high-temperature-grown AlN buffer layer. *Journal of Alloys and Compounds*. 2018;732: 630–636. https://doi.org/10.1016/j.jallcom.2017.10.200

6. Sugawara Y., Ishikawa Y., Watanabe A., Miyoshi M., Egawa T. Observation of reaction between a-type dislocations in GaN layer grown on 4-in. Si(111) substrate with AlGaN/AlN strained layer superlattice after dislocation propagation. *Journal of Crystal Growth*. 2017;468: 536–540. https://doi.org/10.1016/j.jcrysgro.2016.11.010

7. Mizerov A. M., Timoshnev S. N., Sobolev M. S., Nikitina E. V., Shubina K. Yu., Berezovskaia T. N., Shtrom I. V., Bouravleuv A. D. Features of the initial stage of GaN growth on Si(111) substrates by nitrogen-plasma-assisted molecular-beam epitaxy. *Semiconductors*. 2018;52(12), 1529-1533. https://doi.org/10.1134/S1063782618120175

8. Kukushkin S. A., Mizerov A. M., Osipov A. V., Redkov A. V., Timoshnev S. S. Plasma assisted molecular beam epitaxy of thin GaN films on Si(111) and SiC/Si(111) substrates: Effect of SiC and polarity issues. *Thin Solid Films*. 2018;646: 158–162. https://doi.org/10.1016/j.tsf.2017.11.037

9. Lenshin A. S., Kashkarov V. M., Domashevskaya E. P., Bel'tyukov A. N., Gil'mutdinov F. Z. Investigations of the composition of macro-, micro- and nanoporous silicon surface by ultrasoft X-ray spectroscopy and X-ray photoelectron spectroscopy. *Applied Surface Science*. 2015;359: 550–559. https://doi.org/10.1016/j.apsusc.2015.10.140

10. *NIST X-ray Photoelectron Spectroscopy Database*. Available at: https://srdata.nist.gov/xps/

11. Seredin P. V., Goloshchapov D. L., Lenshin A. S., Mizerov A. M., Zolotukhin D. S. Influence of por-Si sublayer on the features of heteroepitaxial growth and physical properties of InxGa1-xN/Si(111) heterostructures with nanocolumn morphology of thin film. *Physica E: Low-dimensional Systems and Nanostructures*. 2018;104: 101–110. https://doi.org/10.1016/j.physe.2018.07.024

12. Seredin P. V., Lenshin A. S., Mizerov A. M., Leiste H., Rinke M. Structural, optical and morphological properties of hybrid heterostructures on the basis of GaN grown on compliant substrate por-Si(111). *Applied Surface Science*. 2019;476: 1049–1060. https://doi.org/10.1016/j.apsusc.2019.01.239

13. Fang Z. L., Li, Q. F. Shen X. Y., Cai J. F., Kang J. Y., Shen W. Z., Modified InGaN/GaN quantum wells with dual-wavelength green-yellow emission. *Journal of Applied Physics*. 2014;115(4): 043514. https://doi.org/10.1063/1.4863208

14. Seredin P. V., Lenshin A. S., Zolotukhin D. S., Goloshchapov D. L., Mizerov A. M., Arsentyev I. N., Beltyukov A. N. Investigation into the influence of a buffer layer of nanoporous silicon on the atomic and electronic structure and optical properties of $A^{III}N$/por-Si heterostructures grown by plasma-activated molecular-beam epitaxy. *Semiconductors*. 2019;53 (7): 993–999. https://doi.org/10.1134/S1063782619070224

Information about the authors

Alexander S. Lenshin, DSc in Physics and Mathematics, leading researcher at the Department of Solid State Physics and Nanostructures, Voronezh State University; Associate Professor, Voronezh State University of Engineering Technologies (Voronezh, Russian Federation).

https://orcid.org/0000-0002-1939-253X
lenshinas@phys.vsu.ru

Pavel V. Seredin, DSc in Physics and Mathematics, Head of the Department of Solid State Physics and Nanostructures, Voronezh State University (Voronezh, Russian Federation).

https://orcid.org/0000-0002-6724-0063
paul@phys.ru

Dmitry S. Zolotukhin, PhD student at the Department of Solid State Physics and Nanostructures, Voronezh State University (Voronezh, Russian Federation).

https://orcid.org/0000-0002-9645-9363
zolotuhin@phys.vsu.ru

Artemy N. Beltyukov, PhD in Physics and Mathematics, Senior Researcher at the Udmurt Federal Research Center of the Ural Branch of the Russian Academy of Sciences (Izhevsk, Russian Federation).

https://orcid.org/0000-0002-7739-7400
beltukov.a.n@gmail.com

Andrey M. Mizerov, PhD in Physics and Mathematics, Leading Researcher at the Laboratory of Nanoelectronics, Alferov Federal State Budgetary Institution of Higher Education and Science Saint Petersburg National Research Academic University of the Russian Academy of Sciences (Saint Petersburg, Russian Federation).

https://orcid.org/0000-0002-9125-6452
andreymizerov@rambler.ru

Igor A. Kasatkin, PhD in Geology and Mineralogy, leading specialist in high resolution X-ray diffractometry, Saint Petersburg State University, Research Centre for X-ray Diffraction Studies (Saint Petersburg, Russian Federation).

https://orcid.org/0000-0001-9586-5397
igor.kasatkin@spbu.ru

Ali O. Radam, PhD student at the Department of Solid State Physics and Nanostructures, Voronezh State University (Voronezh, Russian Federation).
https://orcid.org/0000-0002-1072-0816
radam@phys.vsu.ru

Evelina P. Domashevskaya, DSc in Physics and Mathematics, Professor at the Department of Solid State Physics and Nanostructures, Voronezh State University (Voronezh, Russian Federation).
https://orcid.org/0000-0002-6354-4799
ftt@phys.ru

Received October19, 2021; approved after reviewing November 29, 2021; accepted for publication December 15, 2021; published online March 25, 2022.

Translated by Anastasiia Ananeva
Edited and proofread by Simon Cox

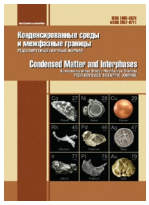

ISSN 1606-867X (Print)
ISSN 2687-0711 (Online)
Condensed Matter and Interphases
Kondensirovannye Sredy i Mezhfaznye Granitsy
https://journals.vsu.ru/kcmf/

Original articles

Research article
https://doi.org/10.17308/kcmf.2022.24/9056

Corrosion inhibition of steel by selected homologues of the class 3-alkyl-5-amino-1H-1,2,4-triazoles in acidic media

D. V. Lyapun, A. A. Kruzhilin✉, D. S. Shevtsov, Yu. V. Aseeva, Kh. S. Shikhaliev

[1]*Voronezh State University,*
1 Universitetskaya pl., Voronezh 394018, Russian Federation

Abstract

The use of hydrochloric acid in the treatment of the bottomhole formation zone leads to the significant corrosion of metals, as well as hydrogen and chloride stress cracking of pump compressor pipes. In order to solve this problem, corrosion inhibitors are added to a hydrochloric acid solution. This article presents the results of a study of the anticorrosive activity of a number of derivatives of the class of 3-alkyl-5-amino-1H-1,2,4-triazole under the conditions of hydrochloric acid corrosion of low-carbon steel.

During the study, selected 3-alkyl-5-amino-1H-1,2,4-triazoles were synthesized. Their structure was confirmed and proved using NMR spectroscopy and HPLC/MS spectrometry. Regularities of the anticorrosive action of the investigated compounds have been established using polarization electrochemical studies and gravimetric direct corrosion tests. Corrosion rates, inhibition coefficients and degrees of protection have been calculated for all inhibitors. The probable mechanism of the inhibitory action of the studied compounds has been substantiated using quantum chemical calculations based on the density functional theory using the Gaussian program.

It was shown that the structure of the alkyl substituents has the greatest effect on the inhibitory activity of the studied compounds. The mechanism was proposed for the adsorption of the inhibitor, which explained the increase in protective properties with an increase in the length of the alkyl substituent. The high hydrophobicity of the aliphatic fragment, not involved in the chemisorption process, additionally prevents the acid solution from contacting the metal surface, while the heterocyclic moiety ensures the sorption of the inhibitor on the metal surface.

As a result, it was shown that derivatives of the homologous series of 3-alkyl-5-aminotriazole are suitable as inhibitors of acid corrosion of ST-3 steel. The minimum length of a hydrocarbon radical at which significant inhibitory activity was observed is 7 carbon atoms. Protection degrees of 65–85% were achieved when 3-heptyl-5-amino-1H-1,2,4-triazole additives at a concentration of at least 2 g/L were added to the hydrochloric acid solution.

Keywords: Metal corrosion, Steel, corrosion inhibitors, Heterocyclic compounds, Aminotriazoles, Physicochemical research methods, Drilling equipment

Funding: The study was supported by the Russian Foundation for Basic Research, project no. 20-33-80017.

Acknowledgements: Analytical studies were carried out using equipment of Shared Knowledge Center “NRC “Kurchatov Institute” – IREA”.

For citation: Lyapun D. V., Kruzhilin A.A., Shevtsov D. S., Aseeva Yu. V., Shikhaliev Kh. S. Corrosion inhibition of carbon steel by selected homologues of the class 3-alkyl-5-amino-1H-1,2,4-triazoles in acidic media. *Kondensirovannye sredy i mezhfaznye granitsy = Condensed Matter and Interphases*. 2022;24(1): 59–68. https://doi.org/10.17308/kcmf.2022.24/9056

Для цитирования: Ляпун Д. В., Кружилин А. А., Шевцов Д. С., Асеева Ю. В., Шихалиев Х. С. Ингибирование коррозии стали некоторыми гомологами класса 3-алкил-5-амино-1H-1,2,4-триазолов в кислой среде. *Конденсированные среды и межфазные границы*. 2022;24(1): 59–68. https://doi.org/10.17308/kcmf.2022.24/9056

✉ Alexey A. Kruzhilin, e-mail: kruzhilin.alexey@gmail.com

1. Introduction

The intensification of production in oil fields is currently one of the priority areas for the development of the oil industry. At the same time, a large share of carbonate reservoirs in oil and gas reserves, relatively low production and low oil recovery in such oil fields make this group of reservoirs especially promising in terms of the use of new technologies for intensifying production. There are a large number of methods for influencing the bottomhole zone of wells in carbonate reservoirs. Hydrochloric acid technologies and their modifications are widespread in oil fields; they play a huge role in intensifying oil production. Their use is so high that, according to the total effect of additional oil produced from the deposit, they are equated with methods of enhanced oil recovery.

The use of hydrochloric acid in the treatment of the bottomhole formation zone leads to significant corrosion of metals, as well as hydrogen and chloride stress cracking of pump compressor pipes. As a result of corrosion, pipelines quickly become unusable, and this affects the economic effect of acid treatments. In order to solve this problem, corrosion inhibitors are added to the hydrochloric acid solution.

Various organic and inorganic compounds are used as such additives. However, many currently known corrosion inhibitors are non-biodegradable, contributing to a significant pollution of waste water and soil, and therefore, recently, research into the search for and synthesis of environmentally friendly and harmless compounds of natural origin, promising as anti-corrosion agents, are being intensified [1–2].

To date, a wide range of heterocyclic compounds exhibiting anticorrosive properties for steel have been studied. These compounds include, for example, aminopyrazoles [3], aminopyridines [4], pyrimidines [5–6], thiazoles [7], benzimidazoles [8-9], etc., however, various triazole derivatives are undoubted and undeniable leaders. In particular, the effect of benzotriazole (BTA) on ferrous and non-ferrous metals has been studied in detail [10–12]. This substance is a fairly versatile inhibitor for various environments. However, the BTA has some drawbacks: the indicators of degree of protection and the coefficients of inhibition of acid corrosion of steel are very low. It is also known that it is moderately hepatotoxic, is a mutagen, and the semi-lethal dose is ~560 mg/kg [13].

Fatty acids, which are mostly environmentally friendly, biodegradable compounds involved in the metabolism of many organisms, can be used for the production of various organic compounds, including corrosion inhibitors for both ferrous and non-ferrous metals. For example, fatty acid hydrazides and thiosemicarbazides [14] and Schiff bases of fatty acids of soybean oil [15] inhibit steel corrosion. Heterocyclic corrosion inhibitors for steel based on carboxylic acids, such as imidazoles [16] and 3-alkyl-5-mercapto-1,2,4-triazoles [17] are known. At the same time, it is known that the simplest representative of the class of aminotriazoles, amitrol, possesses low toxicity (LD_{50}=1100 mg/kg) [18].

Therefore, the synthesis of heterocyclic inhibitors of the class of 5-amino-3-alkyl-1,2,4-triazoles based on carboxylic acids for the investigation of their anti-corrosion properties under the conditions of acid corrosion of steel is an important and urgent task. The goal of this study was the investigation of anti-corrosion activity of derivatives of the class of 3-alkyl-5-amino-1H-1,2,4-triazole under the conditions of hydrochloric acid corrosion of low-carbon steel.

2. Experimental

2.1. Synthesis of starting compounds

General procedure for the synthesis of 3-alkyl-5-amino-1H-1,2,4-triazoles.

The corresponding carboxylic acid was added in portions with stirring to a mixture of 100 ml of toluene with aminoguanidine carbonate (0.2 M), 0.21 M. The mixture was carefully heated to 50–70°C and, after the evolution of carbon dioxide had ceased, it was boiled with a Dean-Stark apparatus and a reflux condenser. After the separation of water in the trap ceased, the reaction mass was cooled and the solvent was decanted. The residue was ground and washed on the filter with toluene, dried, and recrystallized from a boiling mixture of isopropyl alcohol and petroleum ether. The precipitate formed after cooling was filtered, washed with petroleum ether, and dried at 60°C.

3-methyl-5-amino-1H-1,2,4-triazole (**b**). Yield 65–70%, mp 148–150 °C. White powder. ^{1}H NMR spectrum: 2.02 (s, 3H, CH_3); 5.73 (s, 2H, NH_2); 11.50 (s, H, NH). Determined, m/z: 99.0672 $[M+H]^+$. $C_3H_6N_4+H^+$. Calculated, m/z: 99.0665.

3-ethyl-5-amino-1H-1,2,4-triazole (**c**). Yield 57–63%, mp 139–141 °C. White powder. ^{1}H NMR spectrum: 1.02 (t, 3H, J=7.5, CH_3); 2.40 (q, J=7.5, 2H, CH_2); 5.70 (s, 2H, NH_2); 11.49 (s, H, NH). Determined, m/z: 113.0816 $[M+H]^+$. $C_4H_8N_4+H^+$. Calculated, m/z: 113.0822.

3-butyl-5-amino-1H-1,2,4-triazole (**d**). Yield 55–57%, mp 124–126 °C. White powder. ^{1}H NMR spectrum: 0.87 (t, J=7.5, 3H, CH_3); 1.29–1.37 (m, 2H, CH_2); 1.44-1.51 (m, 2H, CH_2); 2.38 (t, J=7.3, 2H, CH_2); 5.61 (s, 2H, NH_2); 11.49 (s, H, NH). Determined, m/z: 141.1127 $[M+H]^+$. $C_6H_{12}N_4+H^+$. Calculated, m/z: 141.1135.

3-pentyl-5-amino-1H-1,2,4-triazole (**e**). Yield 55–64%, mp 124–127 °C. White powder. ^{1}H NMR spectrum: 0.86 (t, J=7.5, 3H, CH_3); 1.29-1.38 (m, 4H, $2CH_2$); 1.52-1.59 (m, 2H, CH_2); 2.38 (t, J=7.3, 2H, CH_2); 5.56 (s, 2H, NH_2); 11.49 (s, H, NH). Determined, m/z: 155.1299 $[M+H]^+$. $C_7H_{14}N_4+H^+$. Calculated, m/z: 155.1292.

3-heptyl-5-amino-1H-1,2,4-triazole (**f**). Yield 60–64%, mp 120–124 °C. White powder. ^{1}H NMR spectrum: 0.85 (t, J=7.5, 3H, CH_3); 1.25-1.36 (m, 8H, $4CH_2$); 1.52-1.59 (m, 2H, CH_2); 2.38 (t, J=7.3, 2H, CH_2); 5.55 (s, 2H, NH_2); 11.49 (s, H, NH). Determined, m/z: 183.1301 $[M+H]^+$. $C_9H_{18}N_4+H^+$. Calculated, m/z: 183.1605.

2.2. Methods for structure proof of compounds

Control of the individuality of the reagents and the obtained compounds and the course of the reaction, was carried out using thin layer chromatography (hereinafter referred to as TLC) on Silufol UV-254 plates. Chloroform was used as the eluent; the development of chromatograms was carried out in UV light and iodine vapour. ^{1}H NMR spectra were recorded using a Bruker AC-300 (operating frequency 300 MHz) in pulsed Fourier mode in a DMSO-d6; The assignment of the signals was carried in relation to the residual signals of the proton of the deuterium solvent. Mass spectra were recorded using an MX-1321 spectrometer with direct injection of the sample into the ion source at 100–150 °C and an accelerating voltage of 70 eV. The melting point was determined using a PTP-M device.

2.3. Electrochemical research

Polarization curves were obtained on an electrode made of ST-3 steel (with an area of 1.0 cm^2) in an electrochemical cell with undivided electrode spaces using an IPC-PRO potentiostat. The working electrode was preliminarily cleaned with K2000 sandpaper and degreased with ethyl alcohol. Electrode potentials (E) was measured relative to the silver chloride electrode, connecting the space of the electrochemical cell and the reference electrode through an electrolytic bridge based on agar-agar and sodium nitrate, and recalculated to the scale of a standard hydrogen electrode (potential was +202 mV relative to SHE). A platinum grid was used as an auxiliary electrode.

The test substances were introduced into the acid until the required concentration was obtained. The electrodes were placed in the prepared solution and kept until the onset of a stationary state for 30 min. After the open-circuit potential (E_{cor}) was established, polarization curves with a potential scan rate of 0.2 mV/s in the anode and cathode directions were obtained. Polarization curves were recorded until the current density reached 0.1 A cm^{-2}.

2.4. Calculation of the corrosion rate using the polarization resistance method

The rate of corrosion in current units was determined by the polarisation resistance technique as summarized by Mansfeld [19].

The studies were carried out using a three-electrode cell with undivided cathode and anode spaces without mixing under natural aeration conditions, the reference electrode was silver chloride (potential +202 mV relative to SHE), and the auxiliary electrode was a platinum grid. The reference electrode was separated from the cell by an electrolytic bridge based on agar-agar and $NaNO_3$.

The working electrode was preliminarily cleaned with P2000 sandpaper, degreased with ethyl alcohol (96%), and washed with distilled water. The electrodes were placed in the prepared solution and kept until the onset of a stationary state for 30 min. When the steady state was

reached, the electrode was polarized in the range of ±30 mV from the value E_{cor} in potentiodynamic mode with a scanning rate of 0.2 mV/s.

Polarization resistance R_r was determined as the slope of the polarization curve at the point E_{cor} in the coordinates ΔE - i, where ΔE is the difference between the current electrode potential and the open-circuit potential (E–E_{cor}). Next, the dependence was plotted with the coordinates $2.3 \cdot R_p \cdot i - \Delta E$. Coefficients b_a and b_c (Tafel slopes of the cathode and anode segments of the polarization curve) were determined using the TableCurve 2D program as the approximation parameters of the equation:

$$2.3 \cdot R_p \cdot I = \\ = \frac{b_a \cdot b_c}{b_a + b_c}[\exp(\frac{E - E_{cor}}{b_{1a}}) - \exp(-\frac{E - E_{cor}}{b_{2c}})]. \quad (1)$$

The corrosion current was calculated taking into account the obtained coefficients according to the equation:

$$I_{cor} = \frac{B}{R_p}. \quad (2)$$

For the comparison of the data obtained in various studies, the values of the corrosion current density (i_{cor}) calculated using the expression will be presented further:

$$i_{cor} = \frac{I_{cor}}{S}, \quad (3),$$

where S is the geometric area of the electrode. For the convenience of further comparison of the obtained data, the ratio of the corrosion current density of each test sample to the current density of the background experiment was calculated ($i^0_{cor} \approx 6.8$ mA/cm^2):

$$i_{cor(relative)} = \frac{i_{cor}}{i^0_{cor}} \times 100\%. \quad (4)$$

Measurements for each concentration of the substance were made at least 5 times until reproducible data were obtained with subsequent statistical processing of the measurement results.

2.5. Gravimetric direct corrosion tests

Corrosion tests were carried out on steel plates (20×40 mm, thickness 1.2 mm). Each sample was preliminarily polished with K 1000 fine-grained sandpaper, after which it was washed with distilled water, ethanol, and dried with filter paper. The experiments were carried out in a 24% HCl solution (for 7 days) under natural aeration without stirring for three samples in parallel (for each inhibitor concentration). After testing, the plates were washed with distilled water and treated with compositions in accordance with GOST 9.907-83.

The corrosion rate was determined according to the weight loss of the samples and was calculated using the formula:

$$k_{inh} = \frac{\Delta m}{S \cdot t} \quad (5)$$

where $\Delta m = m_0 - m$ (m_0 is the weight of the sample before the start of the experiment, m is the weight of the sample after test, g), S is the total surface area of the plate, m^2.

For each solution, the corrosion rate k_0 without inhibitor additive was determined ($k_{0(medium)} \approx 16.9 \pm 0.5$ g/m^2 day is the average value of the corrosion rate without the addition of an inhibitor, obtained over the course of the studies). The effectiveness of the inhibitory action of aminotriazole derivatives was evaluated according to the value of the inhibition coefficient:

$$\gamma = \frac{k_0}{k_{inh}} \quad (6)$$

and the degree of protection:

$$Z = [\frac{(k_0 - k_{inh})}{k_0}] \cdot 100\%, \quad (7)$$

where k_0 and k_{inh} are the corrosion rates in the background solution and in the solution with the inhibitor, respectively.

2.6. Quantum-chemical calculations

All molecules of the synthesized compounds were fully optimized using the density functional theory (DFT) with the B3LYP functional using the 6-31G (d, p) basis in the Gaussian program [20]. The optimized geometry shows non-negative frequencies, resulting in the molecules being positioned at minimum energy on the potential energy surface. Determination of the energies of HOMO and LUMO molecular orbitals, their difference HLG (HOMO-LUMO-gap), as well as the ionization potential (*IP*), electron affinity (*EA*), electronegativity (χ), absolute hardness (η),

and absolute softness (σ) for all molecules were carried out at the same level of theory.

According to the density functional theory, the absolute hardness (η) is defined as [21]

$$\eta = \frac{1}{2}\frac{\partial \mu}{\partial N} = \frac{1}{2}\frac{\partial^2 E}{\partial N^2}, \quad (8)$$

where μ is the chemical potential, N is the number of electrons, and E – energy. R. G. Pearson proposed a working definition of absolute hardness as

$$\eta = \frac{IP - EA}{2}, \quad (9)$$

where IP and EA are ionization potential and electron affinity. Also, according to Koopmans' theorem IP and EA are defined as

$$IP = -E_{\text{HOMO}};\ EA = -E_{\text{LUMO}}, \quad (10)$$

E_{HOMO} and E_{LUMO} are the energies of the highest occupied and lowest unoccupied molecular orbitals.

Electronegativity (χ) is also defined in terms of HOMO and LUMO energies as

$$\chi = \frac{IP + EA}{2}. \quad (11)$$

According to formulas described above (9, 11), the hardness is a measure of the resistance to changes in the electron cloud of a chemical system and is an important parameter in the reaction chemistry. Absolute softness (σ) is inversely proportional to hardness. It is generally accepted [21] that in the homologous series of organic compounds, the most reactive substances have a higher softness value in comparison with their homologues. This idea makes possible the theoretical evaluation and comparison of the degree of binding of inhibitors of the same class of organic compounds with metal and, as a result, estimate their probable inhibitory ability.

3. Results and discussion

Along with the inhibitors synthesized in the study (Fig. 1), Amitrol, a commercially available 3H-5-amino-1H-1,2,4-triazole **a**, was also studied in corrosion tests. Solutions with inhibitor concentrations of 1 g/l and 2 g/l were studied.

As a result of potentiodynamic studies, it was found that the addition of 3-H-5-amino-1H-1,2,4-triazole **a** to the acid solution up to 2 g/l slightly changed the shape and position of the anodic and cathodic parts of the polarization curves. (Fig. 2). However, for the cathode sections, insignificant decrease in the current density at all studied concentrations of the inhibitor (C_{inh}) was revealed. The addition of 3-methyl-5-amino-1H-1,2,4-triazole up to 2 g/l had a similar effect on the nature of the polarization curves. Thus, for 3-methyl- and 3H-5-amino-1H-1,2,4-triazoles, we can assume an insignificant inhibitory effect due to inhibition of the cathodic reduction half-reaction of the oxidizer.

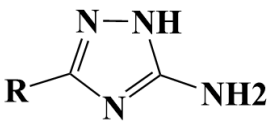

R: H (a), CH_3 (b), C_2H_5 (c), C_4H_9 (d), C_5H_{11} (e), C_7H_{15} (f)

Fig. 1. Structure of the studied derivatives of 1,2,4-triazole

The addition of 3-ethyl-5-amino-1H-1,2,4-triazole to the acid solution up to 2 g/l slightly changed the shape and position of the anodic and cathodic segments of the polarization curves relative to the control measurement without amino-1H-1,2, 4-triazole. The nature of the polarization curves for 3-butyl-5-amino-1H-1,2,4-triazole and 3-pentyl-5-amino-1H-1,2,4-triazole was similar to the results for 3-ethyl derivatives. Thus, the presence of an inhibitory effect according to potentiodynamic measurements for compounds **b-e** is unlikely.

With the addition of 3-heptyl-5-amino-1H-1,2,4-triazole at a concentration of 1 g/L, the polarization curves were hardly distinguishable from the control curves; only a slight decrease in current densities was observed in all parts of the curve. With an increase in concentration to 2 g/l, a significant, up to 1 order of magnitude, decrease in the density of the anode and cathode current was observed at a given value of the electrode potential. At the same time, the open-circuit potential was slightly different from the control value. Such a course of the polarization curve

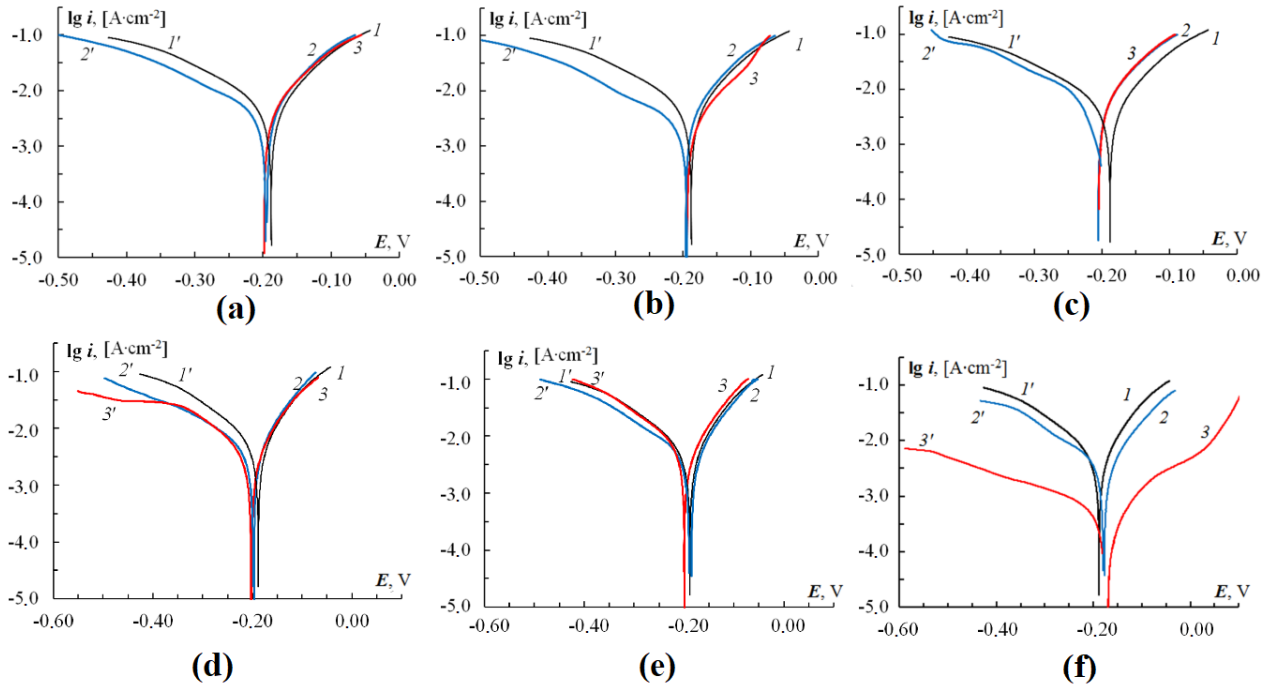

Fig. 2. Anodic (*1-3*) and cathodic (*1′-4′*) polarization curves of ST-3 steel in HCl (24 %) at C_{inh} (g/L): *1, 1′* – 0.0; *2, 2′* – 1.0; *3, 3′* – 2.0, obtained by the addition of 3-H-5-amino-1H-1,2,4-triazole (**a**), 3-methyl-5-amino-1H-1,2,4-triazole (**b**), 3-ethyl-5-amino-1H-1,2,4-triazole (**c**), 3-buthyl-5-amino-1H-1,2,4-triazole (**d**), 3-pentyl-5-amino-1H-1,2,4-triazole (**e**), 3-heptyl-5-amino-1H-1,2,4-triazole (**f**)

indicates the presence of a noticeable inhibitory effect of 3-heptyl-5-amino-1H-1,2,4-triazole in relation to steel in concentrated hydrochloric acid.

The results of direct corrosion tests in general correlated with electrochemical studies. Degrees of protection Z for compounds **a-e** did not exceed 10-15%, which for the direct tests can be considered as evidence of the absence of an inhibitory effect. The introduction of 3-heptyl-5-amino-1H-1,2,4-triazole **f** into a hydrochloric acid solution significantly reduced the corrosion of the studied steel plates (protection degree *Z* ~ 65% at an inhibitor concentration of 2 g/l). Calculations carried out using the polarization resistance method also confirmed this trend

Table 1. Corrosion rate and degree of protection data calculated by polarization resistance method and direct corrosion tests

No.	Inhibitor	C_{inh}, g/l	C_{inh}, g/l	γ	*Z*, %	$I_{cor\ (abs)}$, mA/cm^2	$i_{cor\ (rel)}$
a	5-amino-1H-1,2,4-triazole	1.00	14.19	1.19	16.04	6.2±0.9	8.8 %
		2.00	14.19	1.19	16.04	6.8±0.9	0.0 %
b	3-methyl-5-amino-1H-1,2,4-triazole	1.00	15.41	1.10	8.82	6.8±0.7	0.0 %
		2.00	15.20	1.11	10.06	6.6±0.6	2.9 %
c	3-ethyl-5-amino-1H-1,2,4-triazole	1.00	13.93	1.21	17.57	7.6±1.2	–11.7 %
		2.00	13.87	1.22	17.93	9.8±0.8	–44.1 %
d	3-butyl-5-amino-1H-1,2,4-triazole	1.00	12.37	1.37	26.80	7.7±0.9	–13.2 %
		2.00	12.28	1.38	27.34	6.3±1.3	7.3 %
e	3-pentyl-5-amino-1H-1,2,4-triazole	1.00	14.55	1.16	13.91	8.5±0.1	–24.9 %
		2.00	13.24	1.28	21.66	8.6±0.8	–26.5 %
f	3-heptyl-5-amino-1H-1,2,4-triazole	1.00	9.86	1.71	41.66	7.1±0.7	–4.4 %
		2.00	5.74	2.94	66.04	0.8±0.5	89.0 %

(Table 1). With an inhibitor concentration of 2 g/l, the average degree of protection for the heptyl derivative **f** was ~90%. For all other compounds, the degrees of protection calculated as a result of electrochemical studies indicate the absence of an inhibitory effect or the intensification of the course of electrode processes in their presence (at i_{cor} (rel) < 0)

The analysis of the results of quantum chemical calculations for the molecules of studied corrosion inhibitors (Table 2) demonstrated the absence of significant change of the orbital characteristics with an increase in the length of the aliphatic fragment. The main electron density is distributed over the molecular orbitals of the heterocyclic fragment and the exocyclic amino group of the inhibitors. This finding shows that the heterocyclic matrix, as well as the amino group with high probability ate the main centre of triazole molecules involved in adsorption and binding to the metal surface (Fig. 3). Thus, correlating the results of corrosion tests and quantum chemical calculations, we can conclude that the structure of the alkyl substituent, and not the electronic structure of the molecule as a whole, has the greatest effect on the inhibitory activity of the studied compounds, since the distribution of electron densities in the molecules of inhibitors practically does not change with changes in the structure of the side aliphatic substituent.

As can be seen from the test results, effective protection of steel from acid corrosion in

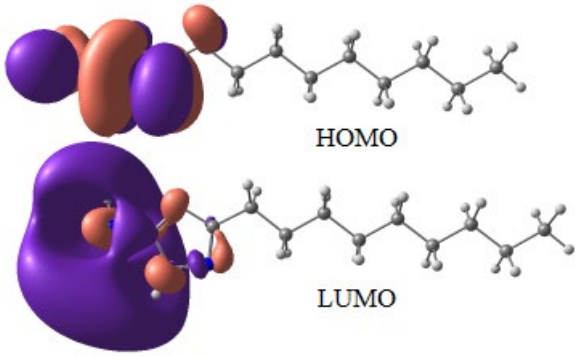

Fig. 3. HOMO and LUMO visualization of the 3-heptyl-5-amino-1H-1,2,4-triazole molecule

Table 2. Optimized structures, calculated HOMO, LUMO energies, HOMO-LUMO gap (HLG), Ionization Potential (*IP*), Electron Affinity (*EA*), Electronegativity (χ), Absolute Hardness (η) and Softness (σ) in eV at B3LYP/6-311+G (d,p) level of theory

No.	Structure	HOMO	LUMO	HLG	*IP*	*EA*	χ	η	σ
a	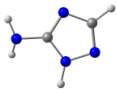	−6.62	−0.54	6.08	6.62	0.54	3.58	3.04	0.33
b	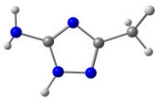	−6.43	−0.50	5.93	6.43	0.50	3.46	2.96	0.34
c	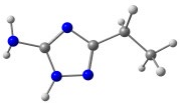	−6.42	−0.49	5.93	6.42	0.49	3.46	2.96	0.34
e	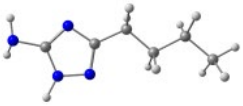	−6.41	−0.50	5.91	6.41	0.50	3.46	2.96	0.34
e	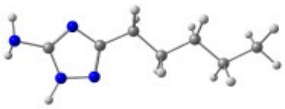	−6.41	−0.50	5.91	6.41	0.50	3.46	2.96	0.34
f	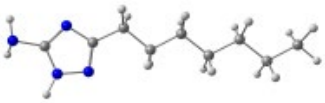	−6.41	−0.50	5.91	6.41	0.50	3.46	2.95	0.34

hydrochloric acid is possible by increasing the length of the aliphatic substituent in the homologous series of 3-alkyl-5-amino-1H-triazoles to 7 carbon atoms.

This feature of steel passivation can be explained by an increase in the lyophilic nature of the inhibitor molecule. Probably, the introduction of hydrophobic substituents into the cycle reduces the interaction of the organic molecule with the solvent and increases its adsorption capacity.

As a result, most probably the formation of protective triazole layers on the metal surface occurs under the considered conditions. (Fig. 4). Probably, a self-organization mechanism occurs, in which the inhibitor molecule is oriented on the metal surface according to the "head-tail" principle, when the heterocyclic moiety provides self-organization and binding of the inhibitor to the metal surface, and the lateral hydrophobic aliphatic substituent of the molecule prevents contact of the acid solution with a metal surface. This mechanism explains the increase in the protective properties of inhibitors with an increase in the length, and, consequently, in the hydrophobic properties of the alkyl substituent.

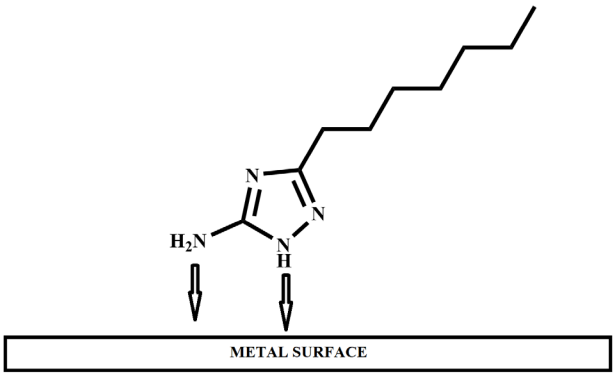

Fig. 4. Schematic diagram of the formation of protective layers by the example of 3-heptyl-5-amino-1H-1,2,4-triazole

Earlier in the study [22], the mechanism of formation of such layers was also studied in detail for copper chloride corrosion. It was shown that when copper was protected with 3-alkyl-5-aminotriazoles, inhibitory activity was observed already when 3-butyl-1H-5-aminotriazole was introduced into the system at concentrations of at least 0.001 M.

The results obtained in this study do not contradict the results of earlier studies, as well as literature data.

Thus, it was found that inhibitory activity under the condition of hydrochloric acid corrosion of steel is probable for compounds of the homologous series of 3-alkyl-5-aminotriazole. The minimum length of the hydrocarbon fragment, at which a significant protective effect is observed, is 7 carbon atoms.

4. Conclusions

The study performed using polarization methods and direct corrosion tests allowed establishing that derivatives of the homologous series of 3-alkyl-5-aminotriazole are suitable as inhibitors of chloride acid corrosion on ST-3 steel.

The minimum length of the hydrocarbon radical, at which significant anti-corrosion properties are observed, is 7 carbon atoms. In this case, the minimum concentration of inhibition is 1 g/L. However, high degrees of protection of 65-85% are achieved when 3-heptyl-5-amino-1H-1,2,4-triazole is added to the hydrochloric acid solution at a concentration of at least 2 g/l.

Author contributions

All authors made an equivalent contribution to the preparation of the publication.

Conflict of interests

The authors declare that they have no known competing financial interests or personal relationships that could have influenced the work reported in this paper.

References

1. Cano E., Pinilla P., Polo J. L., Bastidas J. M. Copper corrosion inhibition by fast green, fuchsin acid and basic compounds in citric acid solution. *Materials and Corrosion*. 2003; 54(4): 222–228. https://doi.org/10.1002/maco.200390050

2. Moretti G., Guidi F., Grion G. Tryptamine as a green iron corrosion inhibitor in 0.5 M deaerated sulphuric acid. *Corrosion science*. 2004; 46(2): 387–403. https://doi.org/10.1016/S0010-938X(03)00150-1

3. Gad Allah A. G., Moustafa H. Quantum mechanical calculations of amino pyrazole derivatives as corrosion inhibitors for zinc, copper and α-brass in acid chloride solution. *Journal of Applied Electrochemistry*. 1992; 22(7): 644–648. https://doi.org/10.1007/BF01092613

4. Mostafa S. I., Abd El-Maksoud S. A. Synthesis and characterization of some transition metal complexes of 2-amino-3-hydroxypyridine and its application in corrosion inhibition. *Monatshefte fuer Chemie/Chemical Monthly*. 1998;129(5): 455–466. https://doi.org/10.1007/PL00000102

5. Nandeesh L. S., Sheshadri B. S. Inhibitory effect of 2-mercapto pyrimidine on corrosion of copper single crystal planes in 0.1 M H_2SO_4. *Proceedings of the Indian Academy of Sciences - Chemical Sciences*. 1991;103(6): 763–775. Available at: https://www.ias.ac.in/article/fulltext/jcsc/103/06/0763-0775

6. Habib U., Badshah A., Flörke U., Qureshi R. A., Mirza B. Khan A. Synthesis of (2,4-diamino-5-(3′,4′,5′-trimethoxybenzyl) pyrimidine) copper (II) complex at 20–25 °C and its structural characterization. *Journal of Chemical Crystallography*. 2009;39(8): 607–611. https://doi.org/10.1007/s10870-009-9547-7

7. Zor S. Sulfathiazole as potential corrosion inhibitor for copper in 0.1 M NaCl. *Protection of Metals and Physical Chemistry of Surfaces*. 2014;50(4): 530–537. https://doi.org/10.1134/S2070205114040200

8. Madkour L. H., Elshamy I. H. Experimental and computational studies on the inhibition performances of benzimidazole and its derivatives for the corrosion of copper in nitric acid. *International Journal of Industrial Chemistry*. 2016;7(2): 195–221. https://doi.org/10.1007/s40090-015-0070-8

9. Zhang D-Q., Gao L-X., Zhou G-D. Synergistic effect of 2-mercapto benzimidazole and KI on copper corrosion inhibition in aerated sulfuric acid solution. *Journal of Applied Electrochemistry*. 2003;33(5): 361–366. https://doi.org/10.1023/A:1024403314993

10. Finšgar M. and Milosev I., Inhibition of copper corrosion by 1,2,3-benzotriazole: a review, *Corrosion Science*. 2010; 52: 2737–2749. doi:10.1016/j.corsci.2010.05.002

11. Kuznetsov Yu. I., Agafonkina M. O., Shikhaliev Kh. S., Andreeva N. P., Potapov A. Yu., Adsorption and passivation of copper by triazoles in neutral aqueous solution. *International Journal of Corrosion and Scale Inhibition*. 2014;3(2): 137–148. https://doi.org/10.17675/2305-6894-2014-3-2-137-148

12. Khiati Z., Othman A. A., Sanchez-Moreno M., Bernard M.-C., Joiret S., Sutter E. M. M., Vivier V. Corrosion inhibition of copper in neutral chloride media by a novel derivative of 1,2,4-triazole. *Corrosion Science*. 2011;53: 3092–3099. https://doi.org/10.1016/j.corsci.2011.05.042

13. Stupnišek-Lisac E., Gazivoda A., Madžarac M. Evaluation of non-toxic corrosion inhibitors for copper in sulphuric acid. *Electrochimica Acta*. 2002;47: 4189–4194. https://doi.org/10.1016/S0013-4686(02)00436-X

14. Quraishi M. A., Jamal D. Fatty acid triazoles: Novel corrosion inhibitors for oil well steel (N-80) and mild steel. *Journal of the American Oil Chemists' Society*. 2000;77: 1107–1111. https://doi.org/10.1007/s11746-000-0174-6

15. Graiver D., Dacomba R., Khawaji M., Jaros A., Berglund K., Narayan R. Steel-corrosion inhibitors derived from soybean oil. *Journal of the American Oil Chemists' Society*. 2012;89: 1895–1903. https://doi.org/10.1007/s11746-012-2077-z

16. Aiad I. A., Hafiz A. A., El-Awady M. Y., Habib A. O. Some imidazoline derivatives as corrosion inhibitors. *Journal of Surfactants and Detergents*. 2010;13: 247–254. https://doi.org/10.1007/s11743-009-1168-9

17. Quraishi M. A., Jamal D., Saeed M. T. Fatty acid derivatives as corrosion inhibitors for mild steel and oil-well tubular steel in 15% boiling hydrochloric acid. *Journal of the American Oil Chemists' Society*. 2000;77: 265–268. https://doi.org/10.1007/s11746-000-0043-3

18. Gaines T. B., Kimbrough R. D., Linder R. E. The toxicity of amitrole in the rat. *Toxicology and Applied Pharmacology*. 1973;26(1): 118–129. https://doi.org/10.1016/0041-008x(73)90092-6

19. Mansfeld F. Tafel slopes and corrosion rates obtained in the pre-Tafel region of polarization curves. *Corrosion Science*. 2005;47(12): 3178–3186. https://doi.org/10.1016/J.CORSCI.2005.04.012

20. Frisch M. J., Trucks G. W., Schlegel H. B., Scuseria G. E., Robb M. A., Cheeseman J. R., Scalmani G., Barone V., Petersson G. A., Nakatsuji H. Gaussian16 Revision B.01. *Gaussian Inc. Wallingford CT*. 2016. Режим доступа: https://gaussian.com/g16main/

21. Parr R. G., Pearson R. G. Absolute hardness: companion parameter to absolute electronegativity. *Journal of the American Oil Chemists' Society*. 1983;105(26): 7512–7516. https://doi.org/10.1021/ja00364a005

22. Shevtsov D. S., Shikhaliev Kh. S., Stolpovskaya N. V., Kruzhilin A. A., Potapov A. Yu., Zartsyn I. D., Kozaderov O. A., Lyapun D. V., Prabhakar C., Tripathi A. 3-Alkyl-5-amino-1,2,4-triazoles synthesized from the fatty acids of sunflower oil processing waste as corrosion inhibitors for copper in chloride environments. *International Journal of Corrosion and Scale Inhibition*. 2020;9(2): 726–744. https://doi.org/10.17675/2305-6894-2020-9-2-21

Information about authors

Denis V. Lyapun, Engineer, Department of Organic Chemistry, Voronezh State University (Voronezh, Russian Federation).

https://orcid.org/0000-0002-5187-124X

dshef@yandex.ru

Alexey A. Kruzhilin, PhD in Chemistry, Researcher, Department of Organic Chemistry, Voronezh State University (Voronezh, Russian Federation).
https://orcid.org/0000-0003-2262-0131
kruzhilin.alexey@gmail.com

Dmitry S. Shevtsov, Engineer, Department of Physical Chemistry, Voronezh State University (Voronezh, Russian Federation).
https://orcid.org/0000-0003-4480-787X
shevtsov@chem.vsu.ru

Yuliya V. Aseeva, postgraduate student of the Department of Organic Chemistry, Voronezh State University (Voronezh, Russian Federation).
https://orcid.org/0000-0002-5342-7898
tdyva3@gmail.com

Khidmet S. Shikhaliev, DSc in Chemistry, Professor, Head of the Department of Organic Chemistry, Voronezh State University (Voronezh, Russian Federation).
https://orcid.org/0000-0002-6576-0305
chocd261@chem.vsu.ru

Received December 2, 2021; approved after reviewing January 27, 2022; accepted for publication February 15, 2022; published online March 25, 2022.

Translated by Valentina Mittova
Edited and proofread by Simon Cox

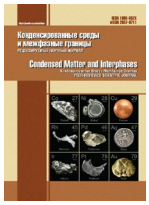

ISSN 1606-867X (Print)
ISSN 2687-0711 (Online)
Condensed Matter and Interphases
Kondensirovannye Sredy i Mezhfaznye Granitsy
https://journals.vsu.ru/kcmf/

Original articles

Research article
https://doi.org/10.17308/kcmf.2022.24/3685

Specifics of the formation of regular opal structures from spherical silica particles in various colloidal solutions

V. A. Maslov[1], S. B. Kravtsov[1], I. A. Novikov[1], V. A. Usachev[2], P. P. Fedorov[1]✉, V. B. Tsvetkov[1], E. G. Yarotskaya[1]

[1] *Prokhorov General Physics Institute of the Russian Academy of Sciences, 38 Vavilova str., Moscow 119991, Russian Federation.*

[2] *Bauman Moscow State Technical University 5 2nd Baumanskaya ul., app. 1, Moscow 105005, Russian Federation*

Abstract

Photonic crystal opal matrices are bulk spatial periodic structures based on amorphous spherical silica particles whose size is compatible with the wavelengths of the visible light spectrum. These structures are very promising and can be used as matrices for new functional materials.

The article studies the formation of a regular opal structure on dielectric substrates by means of the evaporation of droplets and layers of colloidal solutions based on water and ethanol with various concentrations of spherical SiO_2 particles with a diameter of about 250 nm synthesised using the Stöber method.

Keywords: Opal structures, Evaporation-induced self-assembly method, Tetraethoxysilane, Sedimentation, Lyophilic medium, Iridescence

Acknowledgements: The authors are grateful to D. V. Kalinin for his recommendations on the synthesis of monodisperse spherical silica particles and formation of regular opal structures based on them; to N. E. Kononenko for valuable advice regarding the distillation of TEOS, to V. Yu. Khramov for taking part in the discussion of the results of our study; and to I. V. Maslov for their help in arranging for the equipment and materials for our experiments. The authors are also grateful to the employees of ITMO University, M. A. Baranov and A. N. Sergeev, for obtaining the SEM images of the opal structures.

For citation: Maslov V. A., Kravtsov S. B., Novikov I. A., Usachev V. A., Fedorov P. P., Tsvetkov V. B., Yarotskaya E. G. Specifics of the formation of regular opal structures from spherical silica particles in various colloidal solutions. *Kondensirovannye sredy i mezhfaznye granitsy = Condensed Matter and Interphases.* 2022;24(1): 69–75. https://doi.org/10.17308/kcmf.2022.24/3685

Для цитирования: Маслов В. А., Кравцов С. Б., Новиков И. А., Усачев В. А., Федоров П. П., Цветков В. Б., Яроцкая Е. Г. Особенности формирования регулярной опаловой структуры из сферических частиц кремнезема в различных коллоидных растворах. Конденсированные среды и межфазные границы. 2022;24(1): 69–75. https://doi.org/10.17308/kcmf.2022.24/3685

✉ Pavel P. Fedorov, e-mail: ppfedorov@yandex.ru

1. Introduction

An opal matrix is a face-centred cubic lattice (FCC) formed by densely packed spheres of amorphous silicon dioxide (SiO_2) with similar diameters and the size of 0.1–1.0 μm. The space between the SiO_2 spheres is occupied by a void sublattice, which can be filled with other materials. Such structures serve as a basis for photonic crystals with the electromagnetic band gap blocking the waves with wavelengths compatible with the parameters of the periodic structure. By filling the voids between the structural elements of an opal matrix with various substances, we can create periodic nanocomposites of optically active materials to be used in optoelectronics, semiconductor engineering, opal-semiconductor based photonic media, magnetic recording systems, etc. [1–11].

In order to obtain regular opal structures, first we need to synthesise spherical particles of silica, whose size should not vary by more than a few percent. In this regard, the Stöber method is considered to be the most appropriate [12]. This method is based on the hydrolysis of tetraethoxysilane (TEOS) in an aqueous-alcoholic medium in the presence of ammonium hydroxide serving as a catalyst. This method was first described by *G. Kolbe* in 1956 [13] and then elaborated by *W. Stober* et al. The method allows for the synthesis of SiO_2 particles of almost ideal spherical shape in a wide range of diameters: from tens of nanometres to several micrometres. The size and sphericity of the particles depend on the purity and concentrations of the reagents, the temperature, and the composition of the colloidal solution, which is most commonly based on ethyl alcohol. The next important and equally difficult task is to obtain ordered 2D and 3D microstructures with linear dimensions of up to several millimetres. The most popular method for the creation of such structures is the method of natural sedimentation in alcoholic colloidal solutions. In this case the particles deposit on a flat horizontal substrate at a rate determined according to Stokes' law [1]. It takes several weeks to obtain opal layers of several millimetres.

The evaporation-induced self-assembly method proved to be quite effective for alcoholic media [8, 9]. This method involves the deposition of spherical silica particles on an inclined or vertical substrate during the evaporation of the alcoholic suspension. Although opal films obtained during the formation of a regular structure in alcoholic media are more perfect than bulk samples, the number of cracks and dislocations in the obtained samples is still very large. In fact, there are hardly any 1 mm^2 regions with no dislocations. The film obtained using this method demonstrated a mesh of horizontal and vertical bands [10], which the authors explained by the fluctuations in the temperature and the concentration of particles in the solutions being evaporated under conditions which are difficult to control.

D. V. Kalinin et al. developed a promising technique for obtaining regular structures from spherical submicron silica particles [1, 5]. The technique involves packing the particles in a droplet or a 0.1–0.5 mm thin layer in a lyophilic medium based on dimethyl sulfoxide. To increase the mobility of the silica spheres, a plasticiser (namely isopropanol) is added to the quite viscous suspension. During its formation in the suspension, the structure demonstrates plasticity, which significantly enhances the regularity of packing and reduces the chance of microcracks resulting from the shrinkage of the film during drying. This method can be used to obtain 3D opal structures with the width of tens of layers of SiO_2 particles over an area of 1–2 cm^2.

The existing literature does not provide enough comparative data on the formation of regular opal structures by submicron silica particles from various suspensions depending on the concentrations of the solutions. Therefore, the purpose of our study was to compare the suspensions most commonly used by other researchers as the media for obtaining regular opal structures based on ethyl alcohol and water. In our study, we investigated the possibility of using a 50% aqueous solution of ethanol as a solvent, because there is very little information about it in the literature. To maintain the accuracy of our experiments, we used silica particles synthesised by means of the Stöber method in the laboratory.

2. Experimental

The starting materials for the synthesis of spherical silica particles were: 95% ethanol by Alfa-him, 25% ammonia (P.A.), tetraethoxysilane by

various Russian and international manufacturers (P.A. and E.P.), and distilled water.

For the distillation of TEOS, a special unit was assembled consisting of a three-neck flask and a refrigerator made of heat-resistant glass. To enhance the accuracy of the fractionation of the reagents, the flask was placed on a specially designed electrical furnace regulated by means of a RIF-101 based precision temperature controller. To control the temperature, we used a platinum-rhodium thermocouple placed at the inlet of the refrigerator. Each TEOS composition was divided into 4–5 fractions in the range of 165–173 °C. Each fraction was used separately in the experiments. The best results were obtained when the most volatile fraction of TEOS was used.

To prevent the formation of moisture during the distillation process, we passed argon through the system and used a tube with calcined calcium chloride. The silica particles were synthesised in a 50–200 ml glassware by mixing the components at 20 °C. The solution was stirred on a MM-5 magnetic stirrer or a Meos Praha T2 vibrating plate for 1–2 hours, after which the particles were formed within an interval of 8–24 hours without any mechanical influences. The synthesised spherical silica particles were separated from the alcoholic solution in a centrifuge (Elecon R10-01 or TsUM-1) with the rotation speed of 1500–2000 rpm, which was reconfigured for 50 ml test tubes. The obtained precipitates containing the minimum amount of moisture were put into containers with: a) ethyl alcohol (C_2H_5OH), b) 1:1 aqueous-alcoholic solution, and c) distilled water - in order to obtain suspensions with the concentration of silica particles from 15 to 0.5 wt%.

The layers and droplets of the suspensions with various concentrations of silica particles were put on a 24×24×0.17 mm glass plate (microscope slides) using a glass rod, a pipette, or a brush. The relative change in the weight of the substrate before and after the application of the suspension was registered by means of VLA-200 analytical scales with an accuracy of 0.2 mg. We also registered the time of evaporation of the colloidal solution and the area of drop spreading. This helped us to calculate the thickness of the solution layer and the film of the silica spheres after drying out the suspension. Either visually or via an MBS-2 microscope, we observed the presence of an interference pattern from the film (iridescence), when the SiO_2 spheres were regularly packed at a reflection angle of about ~5°. We also determined the crack density of the film on a BIOLAM transmission microscope at 50× and 200× magnifications. The surface structure of the films was studied using a Carl Zeiss EVO LS 10 electron microscope.

3. Results and discussion

In our study, we determined, as did the authors of [7, 11], that the reproducibility of the experiments on the synthesis of monodisperse silica particles heavily depends on the quality of TEOS. The use of TEOS of different manufacturers under identical conditions resulted in silica particles of different shape and size, which could hardly be used to obtain ordered regular structures. The diameters of the silica particles differed by 2–4 times (Fig. 1).

Only the use of TEOS purified from high-temperature fractions resulted in reproducible monodisperse silica particles. In our further analysis, we used 250±10 nm particles. Table 1 presents the characteristics of the films of spherical silica particles formed from an alcoholic suspension depending on the concentration of SiO_2. We determined that the height of the droplets decreases with smaller concentrations of the suspension. The average thickness of the silica films also decreases significantly: it is about 5 μm for the 10% suspension, and about 1 μm for the

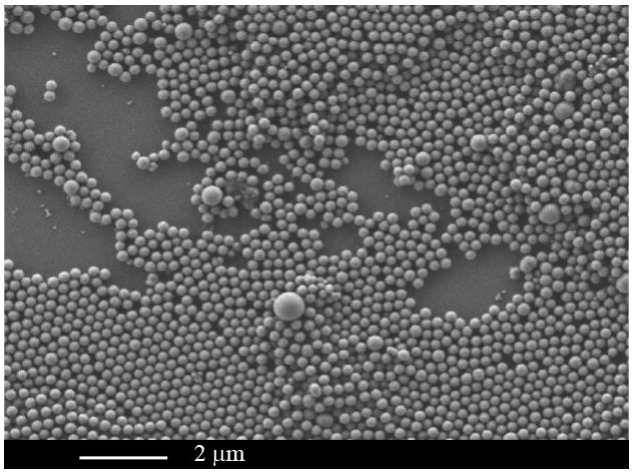

Fig. 1. SiO_2 spheres of various diameters obtained when using the commercial reagent of TEOS (evaporation-induced self-assembly in a 10% alcoholic suspension)

2.5% suspension. Since for all the compositions with the concentration of the suspension of over 1% we clearly observed iridescence (both visually and via a microscope with the reflection angle of about ~ 5°), we can conclude that submicron SiO_2 particles are regularly packed in dried droplets of alcoholic suspension. The defects include radial beam-like cracks in the direction from the periphery to the centre. The results of our study are consistent with the results obtained in [11]. The latter study modelled the process of particles packing using various methods and demonstrated the identity of the formation of the SiO_2 film from alcoholic suspensions by means of the evaporation-induced self-assembly method and the droplet evaporation method.

Our study demonstrated the difference between the formation of regular opal structures in a layer or in a droplet of an alcoholic suspension depending on the concentration of silica particles. The structure of the iridescent layer with the silica particles the concentration in the suspension of over 10 % is not uniform, as shown in [6]. The periphery of the film is significantly thinner, which indicates the maximum iridescence, which then decreases towards the centre (Fig. 2).

Droplets of the alcoholic suspension with the concentration of SiO_2 particles below 10 wt% demonstrated larger drop spreading with the thickness being significantly more uniform. The thickening of the outer ring in the droplet's periphery is almost imperceptible,

Table 1. Characteristics of the films of spherical silica particles formed from the alcoholic suspension depending on the concentration of SiO_2

Solvent C_2H_5OH	Silica concentration, wt%									
	15	10		5		3		1		0.5
Droplet weight, mg	6.7	11	5.5	8.8	4.4	8	4	1	2.6	5
Droplet area, cm^2	0.8	2.5	0.8	4.0	2.2	3.8	2.3	1.2	2.1	3
Suspension density, g/cm^3	0.9	0.85	0.85	0.82	0.82	0.8	0.8	0.79	0.79	0.79
Droplet height, μm	93	50	80	26	24	26	22	10	16	12
Height of the SiO_2 nanosphere layer, μm		5.6		1.3		1.2				
Film iridescence	+	+	+	+	+	+	+	слаб.	слаб.	? -

Table 2. Characteristics of the films of spherical silica particles formed from the aqueous suspension depending on the concentration of SiO_2

Solvent H_2O	Silica concentration, wt%					
	15	10	5	2.5	1	0.5
Droplet weight, mg	15.8	16.3	15.8	12.8	15.8	15.0
Droplet area, cm^2	0.5	0.7	0.7	0.8	1.1	0.6
Suspension density, g/cm^3	1.06	1.04	1.02	1.01	1.0	1.0
Droplet height, μm	300	224	220	170	145	135
Film iridescence	+	+	+	слаб.	-	-

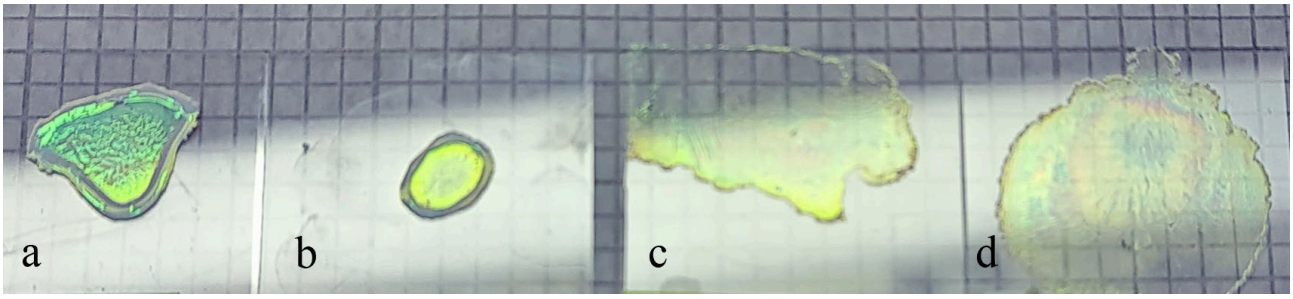

Fig. 2. Films of spherical SiO_2 particles obtained by the evaporation of the droplets of the alcoholic suspension of SiO_2 with various concentrations of submicron silica spheres (see Table 1): a – SiO_2 concentration: 15 %; b – SiO_2 concentration: 10 %; c – SiO_2 concentration: 5 %; d – SiO_2 concentration: 3 %

Таблица 3. Характеристики пленок из сферических частиц кремнезема, сформированных из водно-спиртовой суспензии, в зависимости от концентрации SiO_2

Solvent C_2H_5OH(50%)+H_2O(50%)	Silica concentration, wt%								
	15	10		5		3	2.5	1	0.5
Droplet weight, mg	15.8	16.3	14.1	15.8	16.3	13.8	14.8	15.6	15
Droplet area, cm^2	0.55	0.7	0.7	0.7	0.9	0.8	0.85	1.0	0.9
Suspension density, g/cm^3	0.96	0.94	0.94	0.92	0.92	0.91	0.9	0.9	0.9
Droplet height, μm	300	250	210	240	195	190	190	170	185
Height of the SiO_2 nanosphere layer, μm			1.2		1.1		0.2		
Film iridescence	+	+	+	+	+	+	+	слаб	?

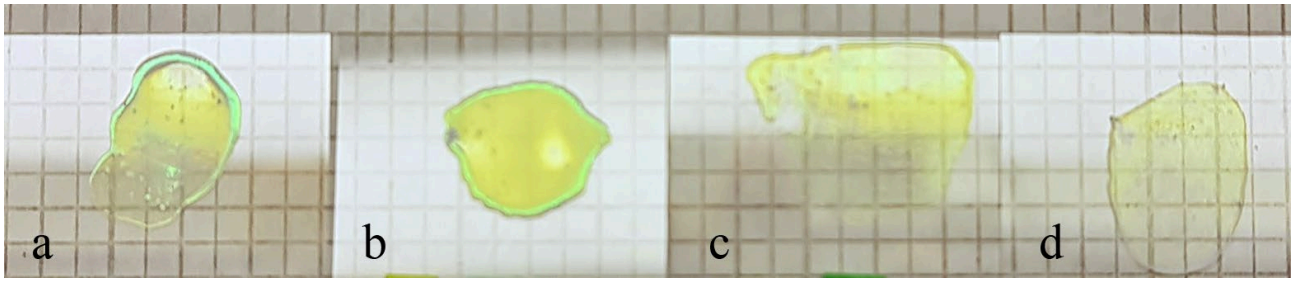

Fig. 3. Films of spherical SiO_2 particles obtained by the evaporation of the droplets of the 50 %C_2H_5OH – 50 % H_2O suspension with various concentrations of submicron silica spheres: a – SiO_2 concentration: 10 %; b – SiO_2 concentration: 5 %; c – SiO_2 concentration: 2.5 %; d – SiO_2 concentration: 1 %

and the homogeneity of the films increases over the spreading area. Table 2 presents the characteristics of the films of spherical silica particles formed from an aqueous suspension depending on the concentration of SiO_2.

The study demonstrated that it takes 4-6 hours for a droplet to evaporate, and the homogeneity of the films is higher than that of the films obtained from alcoholic compositions with larger concentrations (> 10 wt%). The iridescence, which is less bright than the iridescence in alcoholic suspensions, is only observed in thick suspensions with concentrations of SiO_2 of over 5 %.

Using aqueous-alcoholic suspensions (with a 50% concentration of C_2H_5OH), we obtained films similar to those formed during the evaporation of the alcoholic suspension (Fig. 3).

Table 3 presents the characteristics of the films of spherical silica particles formed from an aqueous-alcoholic suspension depending on the concentration of SiO_2. The average evaporation time was 25–30 minutes, which is several times more than the time required for the evaporation of alcoholic suspensions, but is an order of magnitude less than the time required for the evaporation of an aqueous suspension. The thickness of the iridescent films with a minimum concentration of SiO_2 is lower than the thickness

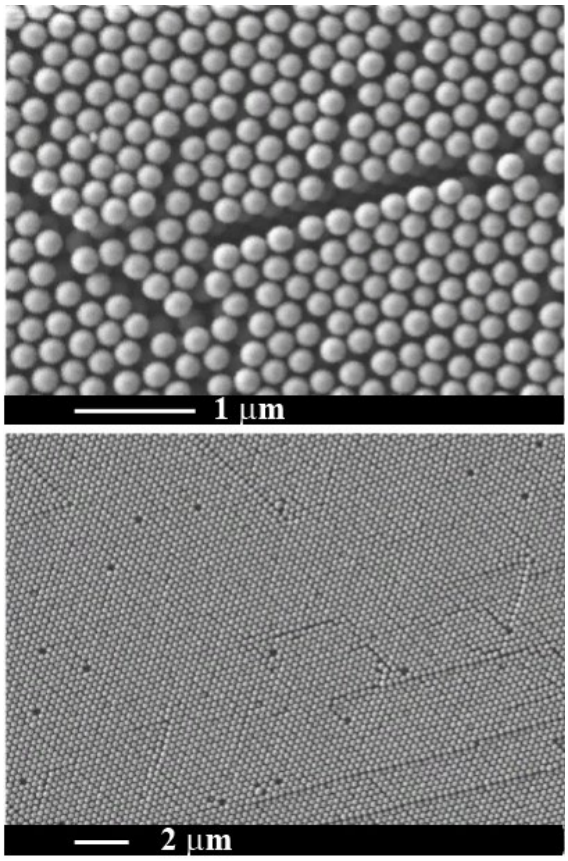

Fig. 4. Regular structure of the layer of 250±10 nm silica spheres obtained during the evaporation of a 10% aqueous-alcoholic (50%) suspension on a horizontal substrate

of films obtained from alcoholic suspensions, and the spread of the droplets of the suspension with concentrations of 2.5 and 1 % is more uniform (Fig. 3).

Fig. 4 shows the image of a film consisting of silica spheres obtained during the evaporation of an aqueous-alcoholic suspension layer on a horizontal glass substrate.

4. Conclusions

The films consisting of submicron silica spheres obtained by means of evaporation of colloidal aqueous, alcoholic, and aqueous-alcoholic (50%) solutions of various concentrations are characterised by concentric and radial banding. [10] suggests that this (as well as a series of horizontal and vertical bands appearing when using the evaporation-induced self-assembly method) is caused by a single reason: then change in the concentration of silica particles in the suspension. Comparing the surface of the films obtained under identical conditions by means of the evaporation-induced self-assembly method on an inclined substrate and the droplet evaporation of the suspension on a horizontal substrate, we can see that in the latter case there are much fewer bands or other defects. We suppose that using aqueous-alcoholic suspensions of spherical silica particles in order to obtain opal layers on a horizontal substrate is a promising method that can be used to enhance the regularity and the quality of films.

Author contributions

All authors made an equivalent contribution to the preparation of the publication.

Conflict of interests

The authors declare that they have no known competing financial interests or personal relationships that could have influenced the work reported in this paper.

References

1. Deniskina N. D., Kalinin D. V., Kazantseva L. K. *Noble opals, natural and synthetic*. Novosibirsk: Nauka Publ.; 1987. (in Russ.)

2. Samoilovich M. I., Ivleva L. I., Tsvetkov M. Yu., Klescheeva S. M. Single crystal SBN: Yb / Opal matrix (SiO_2):Er composite as a nanophotonic structure. In: *Nanostructured thin films and nanodispersion hardened coatings*. 2004. pp. 279–284. (in Russ.)

3. Kalinin D. V., Serdobintseva V. V., Plekhanov A. N., Sobolev N. V. The mechanism of formation of noble opal regular structures occurred in the form of films on the surface of solids. *Doklady Akademii Nauk*. 2005;402(2): 227–229. (In Russ.). Available at: https://elibrary.ru/item.asp?id=9149524

4. Sinitskii A. S., Knotko A. V., Tret'yakov Yu. D. Synthesis of SiO_2 photonic crystals via self-organization of colloidal particles. *Inorganic Materials*. 2005;41(11): 1178–1184. https://doi.org/10.1007/s10789-005-0283-x

5. Kalinin D. V., Serdobintseva V. V., Shabanov V. F. Growing single crystal opal films from lyophilic suspensions of monodispersie spherical silica particles. *Doklady Physics*. 2007;52(10): 536–539. https://doi.org/10.1134/S1028335807100060

6. Kamashev D. V. *Influence of synthesis conditions on the morphology and properties of supramolecular structures of silica*. Yekaterinburg: URAN, Komi Scientific Center, Institute of Geology; 2007. pp. 34–59. (In Russ.)

7. Tsvetkov M. Yu. Cand. in phys. and math. sci. diss. Abstr. Irkutsk: Abstract of the Ph.D. thesis. *Opal matrix-based nanocomposites as photonic media*. Shatura, 2008. 119 p. (in Russ.). Available at: https://www.dissercat.com/content/nanokompozity-na-osnove-opalovykh-matrits-kak-fotonnye-sredy

8. Basiev T. T., Orlovskii Yu. V., Osiko V. V., Samoilovich M. I., Alimov O. K. Conversion of luminescence of laser dyes in opal matrices to stimulated emission. *Quantum Electronics*. 2008;38(7): 665–669. https://doi.org/10.1070/QE2008v038n07ABEH013714

9. *Photonic crystals and nanocomposites: structure formation, optical and dielectric properties*. Shabanov V. F., Zyryanov V. Ya. (Eds.) Novosibirsk: SO RAN Publ.; 2009. pp. 9–41. (in Russ.)

10. Molchanov S. P., Lebedev-Stepanov P. V., Klimonskiy S. O., Sheberstov K. R., Tretyakov S. Yu., Alfimov M. V. Self-assembly of ordered layers of silica microspheres on a vertical plate. *Nanotechnologies in Russia*. 2010;5(5-6): 299–303. https://doi.org/10.1134/S1995078010050034

11. Lebedev-Stepanov P. V., Kadushnikov R. M., Molchanov S. P., Ivanov A. A., Mitrokhin V. P., Vlasov K. O., Rubin N. A., Yurasik G. A., Nazarov V. G., Alfimov M. V. Self-assembly of nanoparticles in the microvolume of a colloidal solution: physics, modeling, experiment. *Nanotechnologies in Russia*. 2013;8(3-4): 137–162. https://doi.org/10.1134/S1995078013020110

12. Stober W., Fink A., Bohn E. J. Controlled growth of monodisperse silica spheres in the micron size range. *Journal of Colloid and Interface Science*. 1968;26(1): 62–69. https://doi.org/10.1016/0021-9797(68)90272-5

13. Kolbe G. *Das komplexchemiche Verhalten der Kieselsaure*. Dissertation. Jena: Friedrich-Schiller Universitat; 1956.

Information about the authors

Vladislav A. Maslov, Senior Researcher, Prokhorov General Physics Institute of the Russian Academy of Sciences (Moscow, Russian Federation).
https://orcid.org/0000-0002-8793-6033
iofran.tarusa1@yandex.ru

Sergey B. Kravtsov, Researcher, Prokhorov General Physics Institute of the Russian Academy of Sciences (Moscow, Russian Federation).
https://orcid.org/0000-0003-0558-1222
habbot@yandex.ru

Ivan A. Novikov, Researcher, Prokhorov General Physics Institute of the Russian Academy of Sciences (Moscow, Russian Federation).
https://orcid.org/0000-0003-4898-4662
i.novikov@niigb.ru

Vadim A. Usachev, PhD in Technical Sciences, Department Head, Bauman Moscow State Technical University (Moscow, Russian Federation).
https://orcid.org/0000-0002-8962-3532
vau@bmstu.ru

Pavel P. Fedorov, DSc in Chemistry, Professor, Chief Researcher, Prokhorov General Physics Institute of the Russian Academy of Sciences (Moscow, Russian Federation).
https://orcid.org/0000-0002-2918-3926
ppfedorov@yandex.ru

Vladimir B. Tsvetkov, DSc in Physics and Mathematics, Deputy Director for Research, Prokhorov General Physics Institute of the Russian Academy of Sciences (Moscow, Russian Federation).
https://orcid.org/0000-0002-1483-3308
tsvetkov@lsk.gpi.ru

Evgeniya G. Yarotskaya, PhD in Chemistry, Prokhorov General Physics Institute of the Russian Academy of Sciences (Moscow, Russian Federation).
https://orcid.org/0000-0001-6704-1964
yar461@yandex.ru

Received November 25, 2021; approved after reviewing December 15, 2021; accepted for publication February 15, 2022; published online March 25, 2022.

Translated by Yulia Dymant
Edited and proofread by Simon Cox

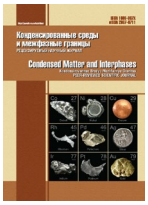

ISSN 1606-867X (Print)
ISSN 2687-0711 (Online)
Condensed Matter and Interphases
Kondensirovannye Sredy i Mezhfaznye Granitsy
https://journals.vsu.ru/kcmf/

Original articles

Research article
https://doi.org/10.17308/kcmf.2022.24/9057

Effect of the morphology and composition of trimetallic PtCuAu/C catalysts on the activity and stability of the methanol oxidation reaction

V. S. Menshchikov✉, S. V. Belenov, A. Yu. Nikulin

Southern Federal University,
105/42 Bolshaya Sadovaya str., Rostov-on-Don 344006, Russian Federation

Abstract

A study on the influence of the method for obtaining trimetallic PtCuAu/C catalysts on their activity in the oxidation of methanol has been carried out.

The structural characteristics of the obtained trimetallic catalysts have been studied by X-ray diffraction and transmission electron microscopy. The nanoparticles of the material obtained by the galvanic synthesis method had a size twice as large (~ 6 nm) than the nanoparticles of the material obtained by the co-deposition of metal precursors. According to the results from the accelerated stress testing of catalysts, it was found that the material obtained by the galvanic method of substitution of copper atoms with gold had a higher residual activity in the oxidation of methanol than the commercial Pt/C analogue.

This study shows the potential of obtaining and using multicomponent platinum-containing nanoparticles deposited on a carbon carrier as effective catalysts for use in methanol fuel cells.

Keywords: methanol fuel cells, catalysis, trimetallic catalysts, galvanic replacement

Funding: The reported study was supported by the Russian Foundation for Basic Research, project no. 19-33-90140.

Acknowledgements: The authors are grateful to LLC “Systems for Microscopy and Analysis” (Skolkovo, Moscow) for conducting TEM and EDX studies.

For citation: Menshchikov V. S., Belenov S. V., Nikulin A. Yu. Effect of the morphology and composition of trimetallic PtCuAu/C catalysts on the activity and stability of the methanol oxidation reaction. *Kondensirovannye sredy i mezhfaznye granitsy = Condensed Matter and Interphases*. 2022;24(1): 76–87. https://doi.org/10.17308/kcmf.2022.24/9057

Для цитирования: Меньщиков В. С., Беленов С. В., Никулин А. Ю. Влияние структуры триметаллических катализаторов на активность и стабильность в реакции окисления метанола. *Конденсированные среды и межфазные границы*. 2022;24(1): 76–87. https://doi.org/10.17308/kcmf.2022.24/9057

✉ Vladislav S. Menshikov, e-mail: men.vlad@mail.ru

1. Introduction

The study of the methanol oxidation reaction (MOR) is of great practical importance for the commercialization of direct methanol fuel cells (DMFC). Despite numerous studies in the field of DMFC, their widespread use is hindered by several factors: the slow methanol oxidation reaction, the poisoning of the catalytic layer by intermediate oxidation products, and the high cost of the catalysts themselves containing noble metals. These problems are relevant for both an anode catalyst of methanol oxidation [1] and a cathode oxygen reduction catalyst. At the same time, another important problem of cathode catalysts is the crossover of methanol into the cathode space [2]. Pt nanoparticles deposited on a finely dispersed carbon carrier are one of the most common catalysts; however, the rather high cost of this metal, combined with its low tolerance to intermediate oxidation products, remains the main problem preventing the widespread use of Pt as an anode and/or cathode in DMFC.

The mechanism of methanol oxidation in an acidic medium can be represented as a sequence of several stages [3].

1. Electro adsorption of methanol molecules on a Pt electrode followed by the formation of intermediate products such as -CHO, -COOH, -CO, etc.

2. The formation of Pt-OH on the catalyst surface because of water decomposition followed by the participation of hydroxyl groups in the oxidation of intermediate products.

3. Removal of formed CO_2.

Among the intermediate products of methanol oxidation, CO is the most harmful. CO molecules are chemisorbed on the surface of the Pt catalyst, which leads to blocking of active surface areas and reduces the activity of the catalyst. One of the possible ways to solve this problem is to change the electronic structure of the metal by doping the Pt catalyst with various noble (Pd, Ru, Au) and some transitional *d*-metals (Cu, Ni, Fe, Co, etc.), which contribute to the removal of CO from the surface, facilitating its oxidation to CO_2 [4–6]. PtRu alloys are well-known catalysts with a lower sensitivity to CO compared to pure Pt [7–8]. However, due to the relatively high cost of the Ru doping component, the most relevant are catalysts doped with transition *d*-metals, such as PtNi [9], PtCu [10], PtCo [10–11].

Thus, the authors of [10] showed that the obtained PtCo/C and PtCu/C catalysts demonstrated higher activity in the oxidation reaction, compared to PtRu/C. At the same time, the authors of the study noted that in the process of standardization (activation) of the surface, the doping component can be dissolved from the catalyst surface, and copper ions passing into the electrolyte can distort the results of experimental studies.

It was shown in [4] that the doping of platinum with copper atoms increased the catalytic activity in the reactions of methanol oxidation and oxygen reduction by 5 and 2 times, respectively, compared to Pt/C. The positive influence of the doping component on the activity of Pt catalysts can be explained by two effects. The first is a bifunctional mechanism of catalysis, in which the high rate of methanol oxidation is determined by the easier adsorption of OH groups on the surface of the doping component, which in turn led to the faster oxidation of chemisorbed CO molecules on neighbouring areas of the Pt surface [12]. The second is the electronic effect associated with the electronic interaction of the atoms of the doping component with Pt atoms. This effect leads to a decrease in the binding energy of adsorbed particles with the catalyst surface. As we mentioned earlier, the main disadvantage of bimetallic PtCu/C catalysts is the possible selective dissolution of the doping component during their functioning [10]. Over the past two years, the preparation and modification of bimetallic PtCu/C catalysts has been an urgent task for researchers around the world. In addition, more and more groups are focusing on the preparation and study of trimetallic nanoparticles (NP) containing Cu: PtCuNi [13], PtCuAu [14], PtPdCo [15], PtCuCo [16], etc. Earlier, it was shown [18–19] that the substitution of Cu atoms by Au atoms on the surface of a platinum-containing catalyst promotes not only an increase in the activity in MOR and the oxygen reduction reaction (ORR), but also a decrease in the selective dissolution of the doping component in the electrochemical cell. However, the question of the relationship between the structure, activity, and stability of trimetallic catalysts remains unclear.

The purpose of this study was the investigation of the relationship between the structure, activity in MOR and the stability of trimetallic PtCuAu/C catalysts obtained by various methods.

2. Experimental

Synthesis of trimetallic PtCuAu/C catalysts was carried out by two different methods. In the first case, the preparation of the catalyst was performed in two stages. At the first stage, a PtCu/C material with a solid solution structure and theoretical Pt:Cu ratio of 1:1 was obtained [18–19]. For this, the required amount of precursors of $H_2PtCl_6 \cdot 6H_2$ (Aurat, Russia, mass fraction of patina – 37.6%) and $CuSO_4 \cdot 5H_2O$ (analytical grade) were added to the water–ethylene glycol suspension of the Vulcan-XC72 carbon carrier in such a way that the mass fractions of metals will be 30 wt%. Pt and 10 wt%. Cu. Then, with constant stirring, an excess of 0.5 M $NaBH_4$ solution was added for joint reduction of Pt and Cu. This synthesis method is described in more detail in [20–21]. Further, after filtration and drying, a part of the PtCu/C catalyst obtained in the first stage was used in the second stage of synthesis. For this, a water–ethylene glycol solution was added to a weighed portion of the PtCu/C material, the resulting suspension was dispersed by ultrasound, and the calculated amount of the gold precursor $HAuCl_4 \cdot 4H_2O$ (Aurat, Russia, mass fraction of gold 49.04%) was added with constant stirring. The amount of gold precursor was calculated in such a way that at full reduction, the gold content in the resulting material was 5 at% of the metal phase. In this case, after the addition of the gold precursor, galvanic substitution of Cu atoms by Au atoms from the catalyst surface occurred. After keeping the suspension under constant stirring for 30 min the resulting suspension was filtered, washed several times with water and isopropyl alcohol, and then dried over P_2O_5. The resulting catalyst was labelled as PtCuAu/C_G.

Another method for the synthesis of the PtCuAu/C catalyst is based on the reduction of three metal with a $NaBH_4$ solution in water-ethylene glycol suspension [18–19]. In this case, the theoretical calculation of the mass fractions of metals corresponded to the PtCuAu/C_G material. This catalyst was labelled as PtCuAu/C_A.

The mass fraction of metals was determined by thermogravimetry based on the weight of the unburned residue. For this, the test sample was placed in a pre-calcined crucible with a constant weight and heat treated in a muffle furnace in an air atmosphere at 800 °C for 40 min. It should be considered that the unburned residue consists of Pt, Au, and CuO. The metal ratios of Pt:Cu and Pt:Cu:Au in the obtained catalysts was determined by X-ray fluorescence analysis (XRF) using a RFS-001 spectrometer (Research Institute of Physics, Southern Federal University, Russia). The conditions of the analysis were following X-ray tube voltage, 50 kV; current, 150 μA; anode material, molybdenum; spectrum acquisition time, 300 s. Registration and processing of X-ray fluorescence spectra was carried out using the UniveRS software (Southern Federal University, Russia) [22].

The phase composition of the materials and the average crystallite size were determined by powder X-ray diffraction at room temperature using ARL X'TRA diffractometer (CuK_α), within an angle range of 2θ from 15 to 55 degrees, with a step of 0.02 degrees and a registration rate of 2 degrees per minute. The average crystallite size was determined using the Scherrer formula [23]:

$$D = \frac{K\lambda}{\mathrm{FWHM} \cdot \cos\theta},$$

where K = 0.98 is the Scherrer constant, λ is the wavelength of monochromatic radiation in Å, FWHM is the full width of the peak at half maximum (in radians), D is the average crystallite size, nm; θ is the reflection angle in radians.

The study by transmission electron microscopy (TEM) was performed using a microscope JEM-2100 (JEOL). Samples of materials weighing 0.5 mg were placed in 1 ml of heptane, the resulting suspension was homogenized in ultrasound for 2–3 min and applied to a nickel mesh coated with a thin layer of amorphous carbon. The materials were studied by transmission electron microscopy (TEM), high-resolution transmission electron microscopy (HRTEM), and scanning transmission electron microscopy (STEM) using an energy dispersive X-ray (EDX) microanalysis of the elemental composition. The electrochemical behaviour of the catalysts was studied at room temperature on a rotating disk electrode in a three-electrode cell by cyclic voltammetry using

a VersaSTAT 3 potentiostat. A saturated silver chloride electrode with a potential of 0.208 V was used as a reference electrode. Later in the study, all potentials were recalculated relative to the potential of a reversible hydrogen electrode. For the application of the studied catalyst to the working electrode, catalytic ink was prepared according to the procedure described in [24]. For the preparation, a catalyst sample weighing 0.0060 g was placed in a mixture of 900 μL of isopropanol and 100 μL of 0.5% Nafion alcohol solution (DuPont). The resulting suspension was stirred on a magnetic stirrer for 10 min, and then dispersed by ultrasound for the same time, while monitoring the temperature of the catalytic ink, which did not rise above 25 °C [25–26]. The mixing procedure was repeated, and then a 6 μL aliquot of ink was applied to the end of the disk electrode, dried at 700 rpm at room temperature, while the surface of the disk electrode was preliminarily polished and degreased according to the manufacturer's recommendations.

The surface of the catalytic layer was standardized in 0.1 M $HClO_4$ saturated with Ar for 30 min in the potential range of 0.04–1.20 V with a potential sweep rate of 200 mV/s. After standardization, the electrolyte was replaced with freshly prepared 0.1 M $HClO_4$ (Sigma Aldrich) to exclude the influence of dissolved copper ions on the values of the measured characteristics. After that, the cell was again saturated with argon and the electrochemical surface area (ESA) was measured with a potential sweep rate of 20 mV/s. ESA values were calculated based on the electrochemical adsorption and desorption of hydrogen [27] using the formula:

$$\mathrm{ESA} = \frac{Q_{\mathrm{H}}}{R \cdot m},$$

where $Q_{\mathrm{H}} = \frac{(Q_{\mathrm{ad}} + Q_{\mathrm{des}})}{2}$ is the average amount of electricity used for the electrochemical adsorption and desorption of hydrogen; R is the amount of electricity used for the adsorption/desorption of a monolayer of atomic hydrogen, which is 210 μC/cm^2; m is the weight of platinum on the electrode (the weight of platinum was calculated based on the weight of the catalytic layer deposited on the working electrode, taking into account the mass fraction of metals). This approach for the calculation of the ESA value is successfully used not only for Pt/C, but also for bimetallic catalysts [28]. In addition, for bimetallic catalysts, a good correlation between the ESA values measured independently by the adsorption/desorption of an atomic hydrogen monolayer and by the estimation of the area based on the oxidation of a chemisorbed CO monolayer was shown [18–19].

The activity of catalysts in MOR was evaluated in 0.1 M $HClO_4$ with the addition of 0.5 M CH_3OH with a potential sweep rate of 20 mV/s. At the same time, for the estimation of the activity in MOR, the generally accepted characteristics of cyclic voltammograms [29], are: Q_{CH3OH} is the amount of electricity used for the oxidation of methanol in the forward potential sweep; I_{Max} is the maximum current density in the forward potential sweep. For the assessment of the tolerance of catalysts to intermediate products of methanol oxidation, chronoamperograms were recorded under similar conditions at a potential of 0.87 for 30 min. The potential of 0.87 V corresponds to the potential of the direct peak of methanol oxidation. An increase in the polarizing potential is impractical due to the formation of passivating oxide compounds on the surface of the electroactive catalyst particles, which, along with the adsorption of the oxidation product, carbon monoxide, can be the cause of the observed current drop in the chronoamperograms. For the assessment of the tolerance, the following coefficients were calculated: $K = \frac{I_{\mathrm{initial}}}{I_{\mathrm{final}}} \cdot 100\%$ is the degree of residual current after 30 min, where I_{initial} and I_{final} are the initial and final current densities on the chronoamperogram, respectively, and $\delta = \frac{100}{I_0} \cdot (dI/dt)_{t>500}$ is the coefficient of long-term CO poisoning [30], taking into account the slope of the curve, where I_0 is the current density at the beginning of polarization inversely extrapolated from the linear decay of the current, $(dI/dt)_{t>500}$ is the slope of the linear attenuation of the current.

For the assessment of the stability of the obtained catalysts, we chose the mode of multiple cycling (1000 cycles) in the potential range of 0.4–1.6 V with a potential sweep rate of 100 mV/s [31]. Upon completion of stress testing in

the electrochemical cell, 0.5 M CH_3OH was added to the electrolyte and cyclic voltammograms and chronoamperograms were reordered. The stability of the catalysts in MOR was evaluated by comparing the parameters characterizing the activity and tolerance of materials. All potentials in this study are shown relative to a reversible hydrogen electrode (RHE).

3. Results and discussion

2.1. Study of the composition and structure of PtCuAu/C materials

The mass fraction of metals in the obtained catalysts turned out to be close to the calculated value (40 wt%) and amounted to 34–37 wt%. Table 1). The wide reflection maximum within an angle range of 2θ about 41° on the X-ray diffraction pattern of the PtCu/C catalyst (Fig. 1a) was shifted to the region of large values of angles 2θ (Fig. 1), as compared to the platinum phase (2θ = 39.8°), which was due to the formation of a solid PtCu solution. With the subsequent galvanic substitution of part of the copper for gold, a smaller shift of the Pt (111) maximum was observed in the X-ray diffraction pattern, compared to the PtCu/C material, which may be due to the formation of a PtCuAu solid solution, since the lattice parameter of gold (3.83 Å) is larger than that of platinum and copper. The similar position of the maximum was demonstrated for the PtCuAu/C_A material obtained by the co-reduction of precursors. For this material, additional weak peaks of the gold phase were also observed in the region of angles 2θ around 38° and 44°, corresponding to Au (111) and Au (200). These maxima indicate the presence of a separate Au phase in the PtCuAu/C_A material and, accordingly, the incomplete incorporation of gold into the composition of the

Table 1. Composition and structural characteristics of the obtained catalysts and commercial Pt/C material

Materials	Composition (XRF)	M-Loading (M), ω %	Average Size of Crystallites D_{Av}, nm (XRD)	Crystal lattice parameter, Å	Average Size of Nanoparticles D_{Av} (NPs), nm (TEM)
PtCu/C	Pt_1Cu_1	37±1	1.9 ± 0.3	3.79	–
PtCuAu/C_G	$Pt_1Cu_{0.51}Au_{0.10}$	34±1	2.0 ± 0.3	3.82	6.5
PtCuAu/C_A	$Pt_1Cu_{0.49}Au_{0.10}$	36±1	2.6 ± 0.3	3.83	2.9
JM20	Pt	40±1	2.0 ± 0.2	3.94	3.6*

* TEM for Pt/C from literature [37]

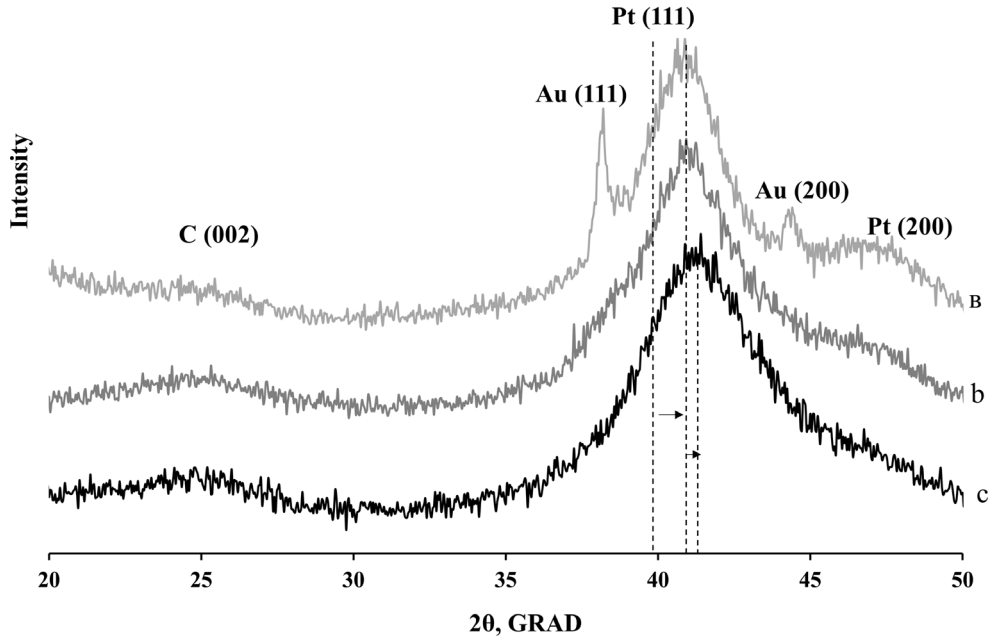

Fig. 1. X-ray diffraction patterns of catalysts: (a) PtCu/C, (b) PtCuAu/C_G, and (c) PtCuAu/C_A

PtCu solid solution. It should be noted that peaks corresponding to the phases of pure copper and its oxides were not revealed in the diffraction patterns of the studied catalysts. Nevertheless, the presence of amorphous structures cannot be ruled out [32]. The average crystallite size for the obtained catalysts, determined using the Scherrer equation, was in the range of 1.9–2.6 nm.

According to the TEM results (Fig. 2), the obtained PtCuAu/C_G and PtCuAu/C_A catalysts were characterized by a uniform distribution of metal NP over the surface of the carbon carrier. For the determination of the average size and size distribution of metal NP, TEM photographs were processed; the size of at least 400 particles was determined for each material. It was found that the average nanoparticle size for the PtCuAu/C_G material was 6.5 nm (Table 1), which is much higher than for the PtCuAu/C_A catalyst, the average particle size of which was 2.7 nm. The PtCuAu/C_A sample was characterized by a narrow size distribution of nanoparticles, while the PtCuAu/C_G sample was characterized by a wide size distribution of NP, from 2 to 12 nm (see histograms in Fig. 2). It should be noted that the average size of NP according to the TEM data for the studied catalysts turned out to be larger than the average size of crystallites calculated using the Scherrer equation (Table 1) [33], which indicates the polycrystalline nature of the particles. Probably, the larger size of NP for the PtCuAu_G catalyst is associated with the larger size of nanoparticles of the initial PtCu/C catalyst, which is due to the peculiarities of the boron hydride synthesis technique. Thus, it was shown in [34] that the PtCu/C material obtained under similar conditions has an average NP size of about 5.5 nm. Probably, the galvanic substitution of gold leads only to an insignificant enlargement of PtCu NP.

The actual composition of the obtained materials turned out to be close to that calculated based on the loading of precursors (Table 1). For the EDX analysis of the elemental composition of individual areas of the surface of PtCuAu/C materials, elemental mapping was used. According to EDX data, the most metal nanoparticles

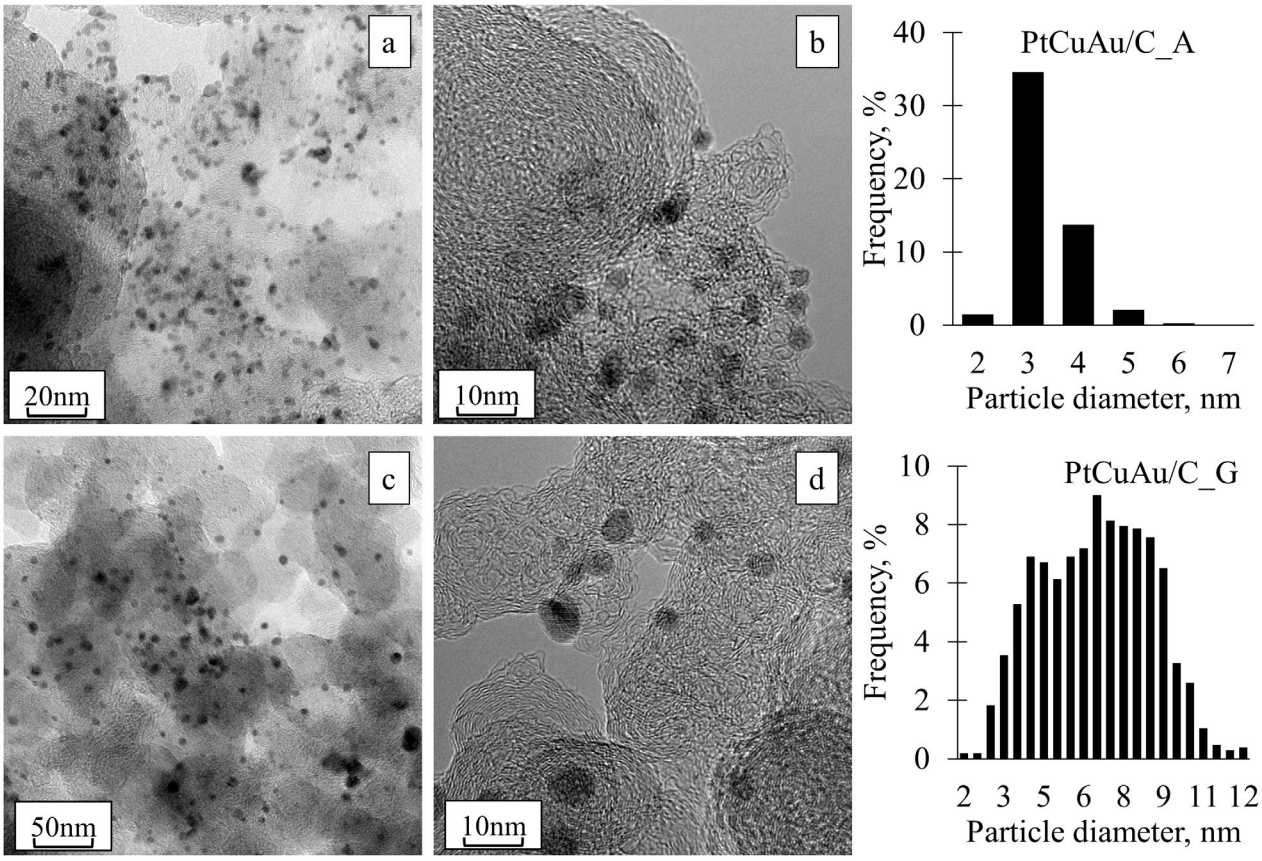

Fig. 2. TEM photographs and histograms of the nanoparticle size distribution obtained on their basis, for samples a,b – PtCuAu/C_A; (c, d) PtCuAu/C_G. 1000 particles of each material were selected for analysis

contained Pt, Cu, and Au atoms. The intensity of the signal from gold atoms was significantly lower, which was due to its lower atomic fraction in the material compared to other metals. For a more detailed analysis, the stencil grid, consisting of ellipses applied to the localizations of Pt (red) and gold (yellow), was transferred to photographs showing the localizations of other metals (Fig. 3). It can be seen from the Figure that all three components were not always included in the composition of the same nanoparticles. For example, in the PtCuAu/C_G material, in addition to trimetallic PtCuAu nanoparticles, bimetallic CuAu nanoparticles were present, since for the yellow ellipses a mismatch in the localization of gold and platinum atoms was revealed. For the PtCuAu/C_A material, the presence of CuAu nanoparticles was not typical (Fig. 3b, Fig. 3c).

2.2. Study of activity and stability of PtCuAu/C catalysts

Electrochemical standardization of the electrodes was carried out before measuring the activity of catalysts by cyclic voltammetry [18–21]. At the stage of electrochemical standardization of the obtained PtCuAu/C catalysts, no peaks of copper dissolution typical for the dissolution of copper from its own phase or the solid solution phase [35–36] were found in cyclic voltammograms in the potential ranges of 0.25–0.45 V and 0.70–0.80 V relative to RHE. Probably, this was due to the absence of the copper phase on the surface of the nanoparticles or on the carbon carrier and indicated a rather complete incorporation of copper into the solid solution. On the other hand, the absence of copper dissolution peaks in cyclic voltammograms does not disprove the possibility of the presence of X-ray amorphous copper oxide.

After standardization of the surface of the materials, cyclic voltammograms were recorded (Fig. 4), the hydrogen region of which was used to determine the ESA value of the catalyst based on the electrochemical adsorption/desorption of hydrogen atoms. The ESA values for PtCu/C and

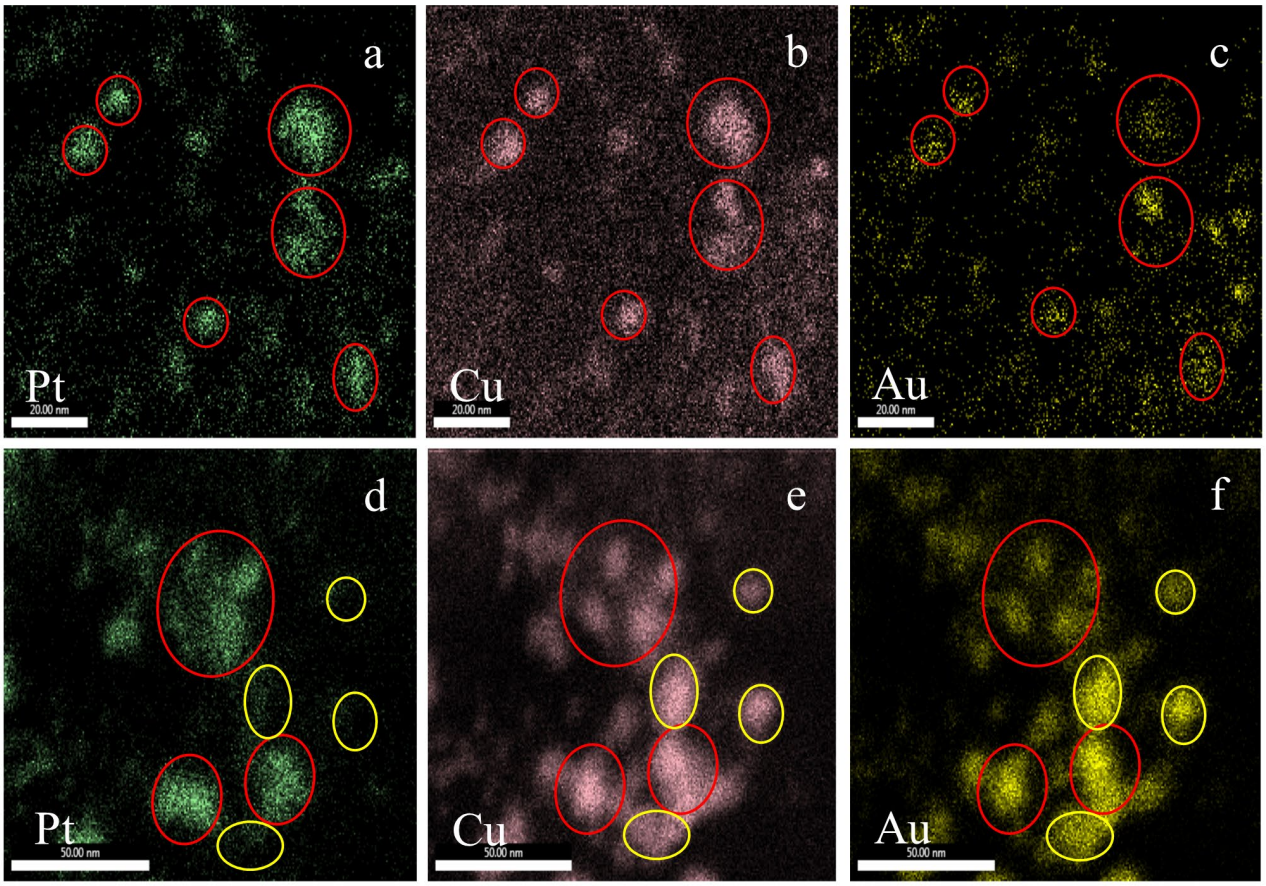

Fig. 3. EDX mapping of a,b,c - PtCuAu/C_A and d,e,f - PtCuAu/C_G catalysts

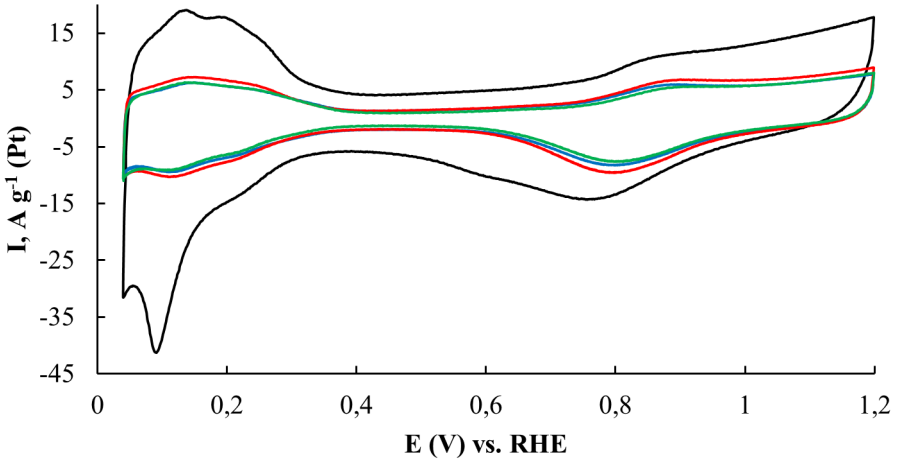

Fig. 4. Cyclic voltammograms of catalysts. Electrolyte is 0.1 M $HClO_4$, Ar atmosphere. The potential sweep rate is 20 mV s^{-1}

Table 2. Values of electrochemically active surface and catalyst activity in methanol

Materials	Q_{CH3OH}, C/g(Pt) 10^5	ESA, m^2/g(Pt)	I_{max}, A/g(Pt)	*I* chronoamperograms, A/g(Pt)		Long-term poisoning rate CO δ, %/s
				$I_{initial}$	I_{final}	
PtCu/C	43	28 ± 3	380	220	48	0.0435
PtCuAu/C_G	59	32 ± 3	572	395	77	0.0481
PtCuAu/C_A	52	31 ± 3	516	331	75	0.0495
JM20	42	77 ± 8	350	320	127	0.0327

PtCuAu/C materials were noticeably inferior to the ESA value calculated for the commercial Pt/C analogue (Table 2). In the case of the PtCuAu/C_G sample, the lower ESA value can be explained by the significantly larger size and wide size distribution of nanoparticles compared to the commercial Pt/C material. At the same time, the particle size of the PtCuAu/C_A material according to TEM slightly differs from that for the Pt/C catalyst. Possibly, the lower ESA value was due to the substitution of a proportion of the platinum atoms on the surface of the catalyst nanoparticles for gold atoms, which are not characterized by reversible adsorption/desorption of hydrogen, as well as to a higher degree of NP agglomeration due to the used synthesis technique [34]. It should be noted that the ESA value of the PtCuAu/C_G material differs slightly

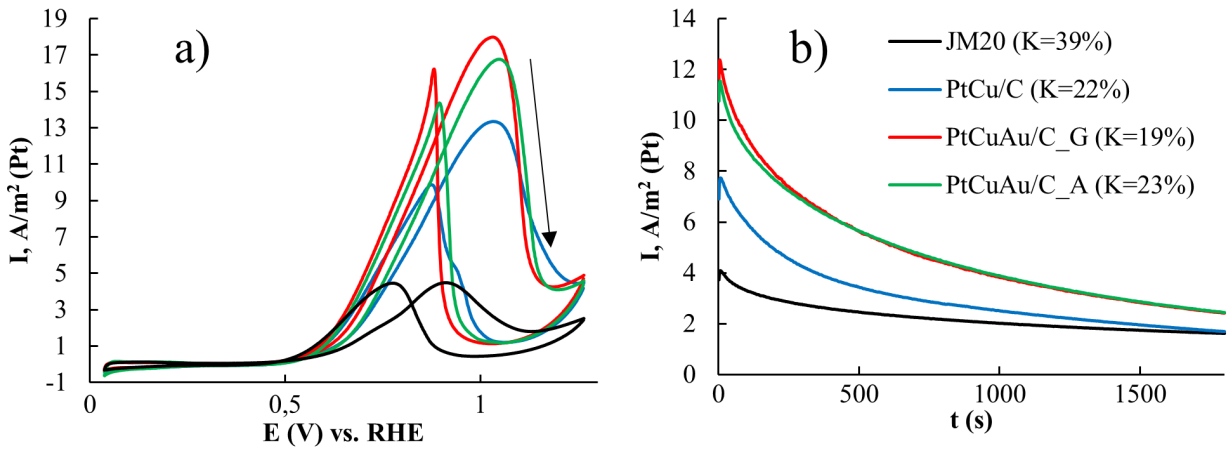

Fig. 5. (a)-cyclic voltammograms and (b) – chronoamperograms at a potential of 0.87 V. Electrolyte is 0.1 M $HClO_4$ + 0.5 M CH_3OH, Ar atmosphere

from the ESA value of the PtCu/C catalyst from which it was obtained. This fact indicates that in the process of galvanic substitution of copper atoms by gold, surface defects do not occur.

The activity of the catalysts in MOR was studied by the method of cyclic voltammograms after the addition of 0.5 M CH_3OH to the electrolyte (Fig. 5a). The PtCuAu/C_G and PtCuAu/C_A materials demonstrated the highest activity in MOR, both per platinum weight in the catalyst and per ESA value (Table 2). At the same time, for the PtCuAu/C_G catalyst, the maximum specific current and the amount of electricity used for the oxidation of methanol in the forward potential sweep among the studied materials were observed. According to the results of chronoamperometric measurements at the potential $E = 0.87$ V (Fig. 5b, Table 2), the PtCuAu/C_G and PtCuAu/C_A catalysts demonstrate both the highest initial and final specific currents recorded after 30 min at a constant potential compared to PtCu/C and Pt/C materials. At the same time, PtCu/C and both PtCuAu/C catalysts were characterized by a larger relative drop in currents with time (Fig. 5b), reflected in the value of the K coefficient (Figs. 5b, 6b). The long-term CO poisoning coefficient (δ) considers the current decay with time and will have the lowest value for catalysts for which the difference between the initial and final currents is close. Indeed, the CO poisoning coefficient was the lowest for the commercial Pt/C material. Probably, the lowest value of the coefficient for the Pt/C sample was since already after 500 sec of the experiment, the current reached a practically constant value, which indicates a high tolerance of the catalyst to the intermediate products of methanol oxidation. Accelerated stress testing of PtCu/C and PtCuAu/C catalysts in a three-electrode cell revealed that the highest current value per platinum weight after 30 min of the experiment was observed for the Pt/C catalyst (Table 2). Thus, doping of platinum with copper and gold atoms led to an increase in the catalytic activity in the methanol oxidation reaction, but at the same time caused a decrease in the tolerance of materials to poisoning by intermediate products.

The study of catalyst stability in accelerated stress testing showed that bi- and trimetallic catalysts degrade less than the commercial Pt/C analogue. This was clearly seen by comparison of ESA values after completion of the tests (Table 3). Thus, ESA decreased by 18% for PtCuAu/C_G, by 38% for PtCuAu/C_A, and by 33% for PtCu/C. At the same time, for the commercial Pt/C (JM20) catalyst, the reduction in ESA was 78%. The fact that after the completion of stress testing, both the weight and specific activity in MOR turned out to be the highest for the PtCuAu/C_G catalyst is even more important (Fig. 6a, Table 3). The same catalyst, PtCuAu_G, demonstrated the highest tolerance to methanol conversion products (Fig. 6b, Table 3). The tendency towards a decrease in the poisoning coefficient, observed for bi- and trimetallic materials after stress testing also should be mentioned.

4. Conclusions

Based on the results of evaluation of the catalytic activity, stability, and tolerance to intermediate products of methanol oxidation of the obtained catalysts by cyclic voltammetry and chronoamperometry, it was found that, despite the lower values of ESA compared to commercial Pt/C analogue, bi- and trimetallic catalysts have the highest activity in MOR.

It was established that a small addition of gold can increase the activity of the initial PtCu/C catalyst in MOR. The tolerance to the intermediate products of methanol oxidation for

Table 3. Values of electrochemically active surface and catalyst activity in methanol after stress testing

Materials	Q_{CH3OH}, C/g(Pt)·10^5	ESA, m^2/g(Pt)	I_{max}, A/g(Pt)	*I* chronoamperograms, A/g(Pt)		Long-term poisoning rate CO δ, %/s
				$I_{initial}$	I_{final}	
PtCu/C	21	19 ± 2	235	216	11	0.0333
PtCuAu/C_G	37	26 ± 3	370	284	71	0.0394
PtCuAu/C_A	19	19 ± 3	216	207	14	0.0353
JM20	4	17 ± 8	50	86	3	0.0499

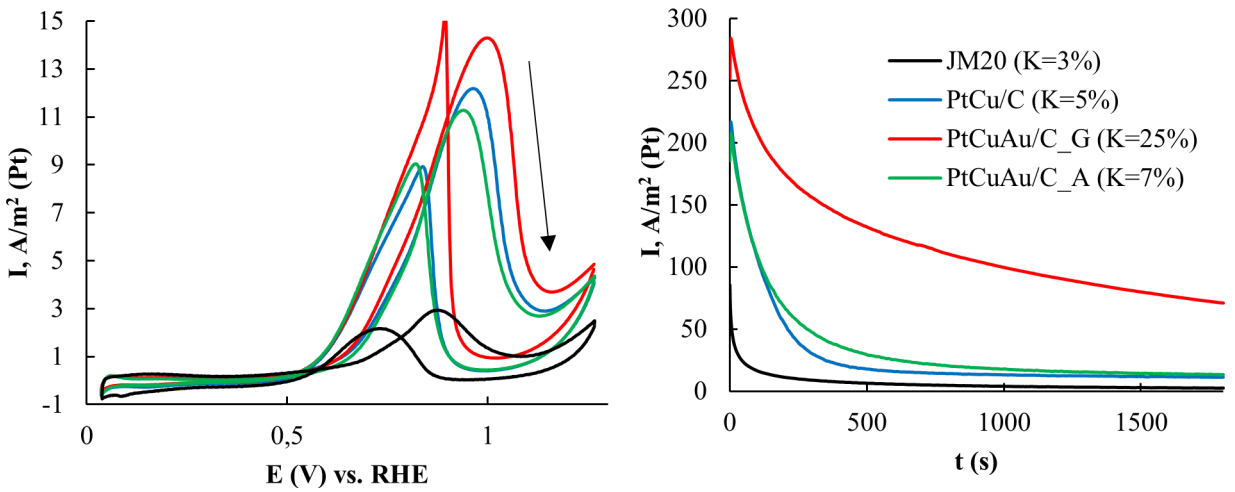

Fig. 6. (a)-cyclic voltammograms and (b)- chronoamperograms at a potential of 0.87 V after stress testing in an electrochemical cell. Electrolyte is 0.1 M $HClO_4$ + 0.5 MCH_3OH, Ar atmosphere

the obtained catalysts turned out to be lower than that of the Pt/C material, which may be due to the lowest ESA values. With a smaller ESA value of the material, the same amount of methanol was oxidized over a smaller surface area and the amount of oxidized methanol was greater per unit surface area. This results in higher surface poisoning compared to materials with higher ESA values. However, after the completion of stress testing, the activity and tolerance for the obtained trimetallic catalysts turned out to be an order of magnitude higher than for the Pt/C (JM20) material. Among the studied catalysts, the PtCuAu/C_G catalyst demonstrated the highest activity and tolerance in MOR after stress testing, which was 7.5 times higher than the Pt/C (JM20) material. The trimetallic PtCuAu/C_A and PtCuAu/C_G catalysts obtained by different synthesis methods demonstrated comparable activity in MOR; however, after stress testing, the PtCuAu/C_G material significantly outperformed the PtCuAu/C_A catalyst in terms of activity. This fact may be related to the large size of trimetallic nanoparticles for PtCuAu/C_G compared to PtCuAu/C_A, which ensures greater stability of this material according to the results of stress testing. For example, in [14], the PtCuAu/C material exhibits an activity 4.5 times higher than the commercial Pt/C. Thus, trimetallic catalysts are of interest for further study and testing in MEA. An important issue that needs to be addressed for testing is the prevention of copper dissolution during the MEA operation. One of the ways to solve this problem, along with the substitution of atoms copper by gold, is the pre-treatment of obtained catalysts in acids.

Author contributions

All authors made an equivalent contribution to the preparation of the publication.

Conflict of interests

The authors declare that they have no known competing financial interests or personal relationships that could have influenced the work reported in this paper.

References

1. Alias M. S., Kamarudin S. K., Zainoodin A. M., Masdar M. S. Active direct methanol fuel cell: An overview. *International Journal of Hydrogen Energy*. 2020;45(38): 19620–19641. https://doi.org/10.1016/j.ijhydene.2020.04.202

2. Gwak G., Kim D., Lee S., Ju H. Luo Y., Zhao J. Studies of the methanol crossover and cell performance behaviors of high temperature-direct methanol fuel cells (HT-DMFCs). *International Journal of Hydrogen Energy*. 2018;43(30): 13999–14011. https://doi.org/10.1016/j.ijhydene.2017.11.029

3. Hamnett A. Mechanism and electrocatalysis in the direct methanol fuel cell. *Catalysis Today*. 1997;38(4): 445–457. https://doi.org/10.1016/S0920-5861(97)00054-0

4. Wu M., Wu X., Zhang L., Abdelhafiz A., Chang I., Qu C., Jiang Y., Zeng J., Alamgir F. Cu@Pt catalysts prepared by galvanic replacement of polyhedral copper nanoparticles for polymer electrolyte membrane fuel cells. *Electrochimica Acta*. 2019;306: 167–174. https://doi.org/10.1016/j.electacta.2019.03.111

5. Qian J., Wei W., Huang X., Tao Y., Chen K., Tang X. A study of different polyphosphazene-coated carbon nanotubes as a Pt–Co catalyst support for methanol oxidation fuel cell. *Journal of Power Sources*. 2012;210: 345–349. https://doi.org/10.1016/j.jpowsour.2012.03.012

6. Fang B., Liu Z., Bao Y., Feng L. Unstable Ni leaching in MOF-derived PtNi-C catalyst with improved performance for alcohols fuel electro-oxidation. *Chinese Chemical Letters*. 2020;31(9): 2259–2262. https://doi.org/10.1016/j.cclet.2020.02.045

7. Mansor M., Timmiati S, Lim K, Wong W, Kamarudin S. K., Kamarudin N. H. N. Recent progress of anode catalysts and their support materials for methanol electrooxidation reaction. *International Journal of Hydrogen Energy*. 2019;44: 14744-69. https://doi.org/10.1016/j.ijhydene.2019.04.100

8. An X.-S., Fan Y.-J., Chen D.-J., Wang Q., Zhou Z.-Y., Sun S.-G. Enhanced activity of rare earth doped PtRu/C catalysts for methanol electro-oxidation. *Electrochimica Acta*. 2011;56(24): 8912–8918. https://doi.org/10.1016/j.electacta.2011.07.106

9. Sulaiman J, Zhu S, Xing Z, Chang Q, Shao M. Pt-Ni octahedra as electrocatalysts for ethanol electro-oxidation reaction. *ACS Catalysis*. 2017;7: 5134–5141. https://pubs.acs.org/doi/10.1021/acscatal.7b01435

10. Page T, Johnson R, Hormes J, Noding S, Rambabu B. A study of methanol electro-oxidation reactions in carbon membrane electrodes and structural properties of Pt alloy electrocatalysts by EXAFS. *Journal of Electroanalytical Chemistry*. 2000;485: 34–41. https://doi.org/10.1016/S0022-0728(00)00090-5

11. Baronia R, Goel J, Tiwari S, Singh P. Efficient electro-oxidation of methanol using PtCo nanocatalysts supported reduced graphene oxide matrix as anode for DMFC. *International Journal of Hydrogen Energy*. 2017;42:10238–10247. https://doi.org/10.1016/j.ijhydene.2017.03.011

12. Markovic N, Gasteiger H, Ross P, Jiang X, Villegas I., Weaver M.J. Electro-oxidation mechanisms of methanol and formic acid on Pt–Ru alloy surfaces. *Electrochimica Acta*. 1995;40: 91-8. https://doi.org/10.1016/0013-4686(94)00241-R

13. Wang X., Zhang L., Wang F., Yu J., Zhu H. Nickel-introduced structurally ordered PtCuNi/C as high performance electrocatalyst for oxygen reduction reaction. *Progress in Natural Science: Materials International*. 2020;30(6): 905–911. https://doi.org/10.1016/j.pnsc.2020.10.017

14. Wang X., Zhang L., Gong H., Zhu Y., Zhao H., Fu Y. Dealloyed PtAuCu electrocatalyst to improve the activity and stability towards both oxygen reduction and methanol oxidation reactions. *Electrochimica Acta*. 2016;212: 277–285. https://doi.org/10.1016/j.electacta.2016.07.028

15. Sarkar A., Murugan A. V., Manthiram A. Rapid microwave-assisted solvothermal synthesis of methanol tolerant Pt-Pd-Co nanoalloy electrocatalysts. *Fuel Cells*. 2010;10(3): 375–383. https://doi.org/10.1002/fuce.200900139

16. Srivastava R., Mani P., Hanh N., Strasser P. Efficient oxygen reduction fuel cell electrocatalysis on voltammetrically dealloyed Pt-Cu-Co nanoparticles. *Angewandte Chemie - International Edition*. 2007;46(47): 8988–8991. https://doi.org/10.1002/anie.200703331

17. Khatib F. N., Wilberforce T., Ijaodola O., Ogungbemi E., El-Hassan Z., Durrant A., Thompson J., Olabi A.G., Material degradation of components in polymer electrolyte membrane (PEM) electrolytic cell and mitigation mechanisms: *Renewable and Sustainable Energy Reviews*. 2019;111: 1–14. https://doi.org/10.1016/j.rser.2019.05.007

18. Belenov S. V., Men'shchikov V. S., Nikulin A. Y., Novikovskii N. M. PtCu/C materials doped with different amounts of gold as the catalysts of oxygen electroreduction and methanol electrooxidation. *Russian Journal of Electrochemistry*. 2020;56(8): 660–668. https://doi.org/10.1134/S1023193520080029

19. Belenov S. V., Menschikov V. S., Nevelskaya A. K., Rezvan D. V. Influence of PtCuAu's nanoparticle structure on its activity in methanol oxidation reaction. *Nanotechnol Russia*. 2019;14(11-12): 557–564. https://doi.org/10.1134/S1995078019060028

20. Alekseenko A. A., Guterman V. E., Volochaev V. A., Belenov, S. V. Effect of wet synthesis conditions on the microstructure and active surface area of Pt/C catalysts. *Russ. J. Inorganic Materials*. 2015;51(12): 1258–1263. http://dx.doi.org/10.1134/S0020168515120018

21. Guterman V. E., Belenov S. V., Pakharev A. Yu., Min M., Tabachkova N. Yu., Mikheykina E. B., Vysochina L. L., Lastovina T. A. Pt-M/C (M = Cu, Ag) electrocatalysts with an inhomogeneous distribution of metals in the nanoparticles. *International Journal of Hydrogen Energy*. 2016;41(3): 1609–1626. https://doi.org/10.1016/j.ijhydene.2015.11.002

22. Brugeman S. A., Zekhtor M. Yu., Novikovskiy N. M. *Universal Roentgen Spectra (UniveRS)*. Certificate of state registration of the computer program no. 2010615318 (Russia). 2010.

23. Langford J. I., Wilson A. J. C. Scherrer after Sixty Years: A Survey and Some New Results in the Determination of Crystallite Size. *Journal of Applied Crystallography*. 1978;11: 102–103. https://doi.org/10.1107/S0021889878012844

24. Guterman, V. E., Belenov, S. V., Lastovina, T. A., Fokina, E. P., Prutsakova, N. V., Konstantinova, Y. B. Microstructure and electrochemically active surface area of PtM/C electrocatalysts. *Russian Journal of Electrochemistry*. 2011;47(8) 997–1004. https://doi.org/10.1134/S1023193511080052

25. Groger O., Gasteiger H. A., Suchsland J. P. Review—Electromobility: Batteries or Fuel Cells? *Journal of The Electrochemical Society*. 2015;162(14): 2605–2623. http://dx.doi.org/10.1149/2.0211514jes

26. Garsany Y., Ge J., St-Pierre J., Rocheleau R., Swider-Lyons K. Analytical procedure for accurate comparison of rotating disk electrode results for the oxygen reduction activity of Pt/C. *Journal of The Electrochemical Society*. 2014;161(5): 628–640. http://dx.doi.org/10.1149/2.036405jes

27. Banham D., Ye S. Current status and future development of catalyst materials and catalyst layers for proton exchange membrane fuel cells: An industrial perspective. *ACS Energy Letters*. 2017;2(3): 629–638. https://doi.org/10.1021/acsenergylett.6b00644

28. Zhang C., Zhang Y., Xiao H., Zhang J., Li L., Wang L., Bai Q., Liu M., Wang Z, Sui N. Superior catalytic performance and CO tolerance of PtCu/graphdiyne electrocatalyst toward methanol oxidation reaction. *Colloids and Surfaces A: Physicochemical and Engineering Aspects*. 2021;612: 125960. https://doi.org/10.1016/j.colsurfa.2020.125960

29. Menshikov V. S., Novomlincky I. N., Belenov S. V., Alekseenko A. A., Safronenko O. I., Guterman V. E. Methanol, ethanol, and formic acid oxidation on new platinum-containing catalysts. *Catalysts*. 2021;11(2): 158–176. https://doi.org/10.3390/catal11020158

30. Guo J. W., Zhao T. S., Prabhuram J., Chen R., Wong C. W. Preparation and characterization of a PtRu/C nanocatalysts for direct methanol fuel cell. *Electrochimica Acta*. 2005;51(4): 754–763. https://doi.org/10.1016/j.electacta.2005.05.056

31. Shao Y., Yin G., Gao Y. Understanding and approaches for the durability issues of Pt-based catalysts for PEM fuel cell. *Journal of Power Sources*. 2007;171(2): 558–566. https://doi.org/10.1016/j.jpowsour.2007.07.004

32. Pryadchenko V. V., Srabionyan V. V., Kurzin A. A., Bulat N. V., Shemet D. B., Avakyan L. A., Belenov S. V., Volochaev V. A., Zizak I., Guterman V. E., Bugaev L. A. Bimetallic PtCu nanoparticles in PtCu/C electrocatalysts: structural and electrochemical characterization. *Applied Catalysis A: General*. 2016;525: 226–236. https://doi.org/10.1016/j.apcata.2016.08.008

33. Guterman V. E., Belenov S. V., Alekseenko A. A., Lin R., Tabachkova N. Y., Safronenko O. I. Activity and stability of Pt/C and Pt-Cu/C. *Electrocatalysts*. 2018;9(5): 550–562. https://doi.org/10.1007/s12678-017-0451-1

34. Guterman V. E., Belenov S. V., Alekseenko A. A., Volochaev V. A., Tabachkova N. Y. The relationship between activity and stability of deposited platinum-carbon electrocatalysts. *Russian Journal of Electrochemistry*. 2017;53(5): 531–539. https://doi.org/10.1134/S1023193517050081

35. Zhu H., Li X., Wang F. Synthesis and characterization of Cu@Pt/C core-shell structured catalysts for proton exchange membrane fuel cell. *International Journal of Hydrogen Energy*. 2011;36(15) 9151–9154. https://doi.org/10.1016/j.ijhydene.2011.04.224

36. Wang Y., Zhou H., Sun P., Chen T. Exceptional methanol electro-oxidation activity by bimetallic concave and dendritic Pt-Cu nanocrystals catalysts. *Journal of Power Sources*. 2014;245(1): 663–670. https://doi.org/10.1016/j.jpowsour.2013.07.015

37. Na H., Choi H., Oh J. W., Jung Y. S., Cho Y. S. Enhanced CO oxidation and cyclic activities in three-dimensional platinum/indium tin oxide/carbon black electrocatalysts processed by cathodic arc deposition. *ACS Applied Materials and Interfaces*. 2019;11(28): 25179–25185. https://doi.org/10.1021/acsami.9b06159

Information about the authors

Vldislav S. Menshikov, PhD student, Researcher at the Department of Electrochemistry, Southern Federal University (Rostov-on-Don, Russian Federation).

https://orcid.org/0000-0002-0531-2156
men.vlad@mail.ru.

Sergey V. Belenov, PhD in Chemistry, Research Fellow at the Department of Electrochemistry, Southern Federal University (Rostov-on-Don, Russian Federation).

https://orcid.org/0000-0003-2980-7089
serg1986chem@mail.ru

Aleksey Y. Nikulin, Researcher at the Department of Electrochemistry, Southern Federal University (Rostov-on-Don, Russian Federation;).

chemistnik@yandex.ru

Received August 22, 2021; approved after peer reviewing December 7, 2021; accepted for publication February 15, 2022; published online March 25, 2022.

Translated by Valentina Mittova
Edited and proofread by Simon Cox

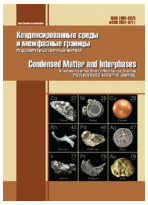

ISSN 1606-867X (Print)
ISSN 2687-0711 (Online)
Condensed Matter and Interphases
Kondensirovannye Sredy i Mezhfaznye Granitsy
https://journals.vsu.ru/kcmf/

Original articles

Research article
https://doi.org/10.17308/kcmf.2022.24/9058

The kinetics of cathodic hydrogen evolution on titanium disilicide in a sulphuric acid solution

V. V. Tretyakova, V. V. Panteleeva✉, A. B. Shein

Perm State University,
15 Bukirev str., Perm 614990, Russian Federation

Abstract

The kinetics and mechanism of hydrogen evolution reaction on the $TiSi_2$ electrode in x M H_2SO_4 + (0.5 – x) M Na_2SO_4 (x = 0.5; 0.35; 0.20; 0.05) solutions were studied using the methods of polarisation and impedance measurements.

The cathodic polarisation curves of $TiSi_2$ were characterised by a Tafel section with a slope of 0.116–0.120 V at E ranging from –0.30 to –0.48 V (SHE). The value of hydrogen evolution overpotential at i = 1 A/cm^2 for $TiSi_2$ was 0.90–0.96 V. The kinetic parameters of the hydrogen evolution reaction on silicide were close to the theoretical values for the slow stage of charge transfer.

Based on the measurements of the differential capacitance of the $TiSi_2$ electrode (at f = 10 kHz), depending on the cathodic polarisation and acidity of the electrolyte, it was concluded that a thin dielectric film of silicon dioxide ($Si + 2H_2O \rightarrow SiO_2 + 4H^+ + 4e^-$) was present on the surface of the silicide. The film was not reduced with low cathodic polarisations.

The impedance spectra of the $TiSi_2$ electrode at the potentials of the Tafel region were capacitive semicircles with a misplaced centre. The impedance spectra were described by an equivalent electrical circuit, the Faraday impedance of which consisted of a series-connected charge transfer resistance R_1 and a parallel R_2C_2 chain corresponding to the adsorption of atomic hydrogen on the electrode surface. The impedance of the double layer capacitance was modelled using the constant phase element CPE_1. The χ^2 criterion for the circuit was (1.3-3.7)·10^{-4} (when using data modulus weighting), the sum of square deviations was (1.5–4.1)·10^{-2}, and the error in the determination of the values of circuit parameters did not exceed 10 %.

The experimental values of the slopes of lg R_1,E-, lg R_2,E-, and lg C_2,E-dependences were close to the theoretical values of the slopes for the discharge-electrochemical desorption mechanism, in which both stages were irreversible and the transfer coefficients of the stages were not equal, when the Langmuir isotherm for adsorbed atomic hydrogen was fulfilled. The reaction of absorption of hydrogen with the kinetic control proceeded at the same time as the hydrogen evolution reaction.

Keywords: Titanium disilicide $TiSi_2$, Hydrogen evolution reaction, Sulphuric acid solution, Impedance

Acknowledgments: The research was supported by the Perm Research and Education Centre for Rational Use of Subsoil, 2021 and within the state assignment to the ISMAN.

For citation: Tretyakova V. V., Panteleeva V. V., Shein A. B. The kinetics of cathodic hydrogen evolution on titanium disilicide in a sulphuric acid solution. *Kondensirovannye sredy i mezhfaznye granitsy = Condensed Matter and Interphases*. 2022;24(1): 88–94. https://doi.org/10.17308/kcmf.2022.24/9058

Для цитирования: Третьякова В. В., Пантелеева В. В., Шеин А. Б. Кинетика катодного выделения водорода на дисилициде титана в сернокислом электролите. *Конденсированные среды и межфазные границы*. 2022;24(1): 88–94. https://doi.org/10.17308/kcmf.2022.24/9058

✉ Viktoria V. Panteleeva, e-mail: vikpant@mail.ru

1. Introduction

The hydrogen evolution reaction (HER) is an electrocatalytic process whose rate considerably depends on the nature and structure of the electrode material as well as the condition of its surface. Therefore, metals, alloys, intermetallic, and metal-like (carbides, silicides, germanides, nitrides, chalcogenides, and composite materials based on them) compounds were studied as HER catalysts [1–16].

The kinetics of HER on transition metal silicides have not been thoroughly studied. The study of HER on transition metal silicides showed [1–4, 7–9, 10, 13–15] that depending on the nature and concentration of metal and silicon in the compound as well as the pH and composition of the medium, silicides can be characterised by lower or higher hydrogen overpotential as compared to the corresponding pure metals, and it was noted [1, 2, 13] that a thin oxide film of silicon dioxide influences the kinetics of hydrogen evolution on silicides in an acidic media with low cathodic polarisations.

The purpose of this work was to establish the kinetics and mechanism of the hydrogen evolution reaction on titanium disilicide ($TiSi_2$) in sulphuric acid solutions with various concentrations in order to determine the electrochemical activity of $TiSi_2$ in HER.

2. Experimental

The study was conducted using titanium disilicide ($TiSi_2$) obtained by the Bridgman method.

Electrochemical measurements were performed at a temperature of 25°C under natural aeration in unstirred solutions of 0.5 M H_2SO_4; 0.35 M H_2SO_4 + 0.15 M Na_2SO_4; 0.20 M H_2SO_4 + 0.30 M Na_2SO_4; 0.05 M H_2SO_4 + 0.45 M Na_2SO_4. The solutions were prepared using deionised water (with water resistivity of 18.2 MΩ cm and organic carbon content of 4 μg/l) which was obtained using a Milli-Q water purification system by Millipore (France) and chemically pure reagents H_2SO_4 and Na_2SO_4. The measurements were conducted using a potentiostat/galvanostat with a built-in Solartron 1280C frequency analyser by Solartron Analytical (Great Britain) in a YASE-2 electrochemical cell with cathode and anode sections separated by a porous glass diaphragm. A saturated silver chloride electrode was used as the reference electrode and a platinum electrode was used as the auxiliary electrode. The potentials presented in this work are relative to the standard hydrogen electrode.

Before performing the measurements, the working surface of the electrode was polished with abrasive papers with decreasing grain size, degreased with ethyl alcohol, and rinsed with a working solution. Once the electrode was immersed in the solution, it was subjected to cathodic polarisation with a current density of 0.5 mA/cm^2 for 10 minutes, then held with an open circuit potential until a stable potential was established, and then the impedance spectra were recorded. Before the measurement of the impedance spectra, potentiostatic polarisation of the electrode was conducted at each potential until an almost constant current value was established. After that, the impedance was measured at this value of E and lower potentials, and the potential was changed with a fixed step. Cathodic potentiostatic curves were plotted based on the obtained values of i for this value of E. The range of frequencies $f(\omega/2\pi)$ used for impedance measurements was from 20 kHz to 0.02 Hz, while the amplitude of the alternating signal was 5–10 mV.

3. Results and discussion

The cathodic potentiostatic curves of the $TiSi_2$ electrode in sulphuric acid solutions are presented in Fig. 1. There is a linear section with a slope of 0.116-0.120 V on the cathodic silicide curves in the potential region from -0.30 to -0.48 V, and the range of potentials for recording the linear dependence of E on lg$i$ decreases with a decrease in the acidity of the electrolyte (Table 1). The slope increases in the region of $E < -0.48$ V with an increase in cathodic polarisation. The value of hydrogen evolution overpotential at $i = 1$ A/cm^2 for $TiSi_2$ is 0.90–0.96 V, meaning that in the sulphate electrolyte titanium disilicide refers to materials with high hydrogen evolution overpotential and, as a result, it does not have high electrochemical activity in HER.

The kinetic parameters of the hydrogen evolution reaction on the $TiSi_2$ electrode with the potentials of the linear dependence of E on lg i on polarisation curves are close to the theoretical values for the slow stage of charge transfer (Table 1) [17].

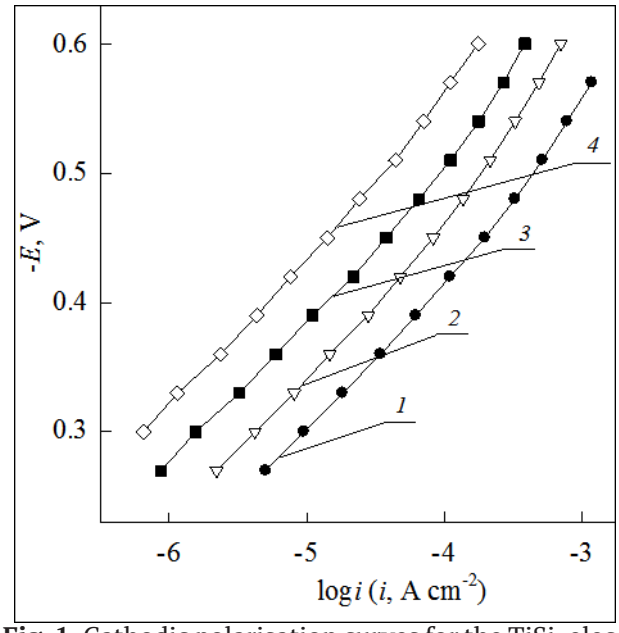

Fig. 1. Cathodic polarisation curves for the $TiSi_2$ electrode in solutions: *1* – 0.5 M H_2SO_4; *2* – 0.35 M H_2SO_4 + 0.15 M Na_2SO_4; *3* – 0.20 M H_2SO_4 + 0.30 M Na_2SO_4; *4* – 0.05 M H_2SO_4 + 0.45 M Na_2SO_4

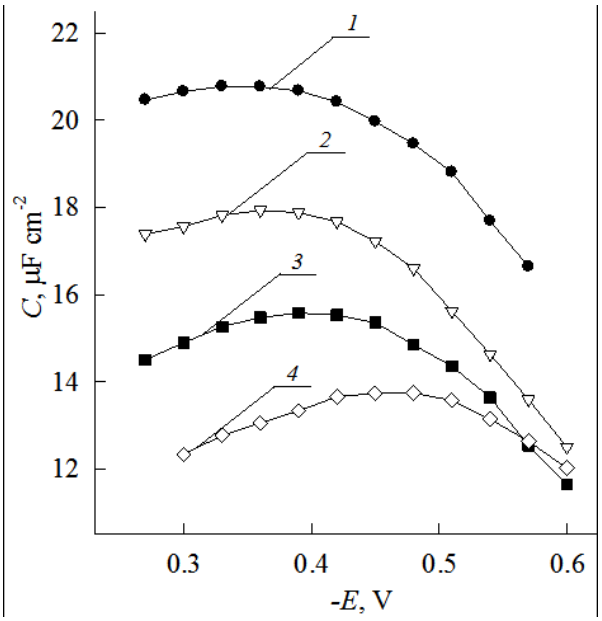

Fig. 2. The dependence of differential capacitance of the $TiSi_2$ electrode on the potential at a frequency of 10 kHz in solutions: *1* – 0.5 M H_2SO_4; *2* – 0.35 M H_2SO_4 + 0.15 M Na_2SO_4; *3* – 0.20 M H_2SO_4 + 0.30 M Na_2SO_4; *4* – 0.05 M H_2SO_4 + 0.45 M Na_2SO_4

The differential capacitance of the $TiSi_2$ electrode at an alternating current frequency of f = 10 kHz in the studied region was ~10–22 μF/cm² and at the potentials of the linear section on the cathodic curves it passed through a mild maximum and decreased with a decrease in the acidity of the medium (Fig. 2). The differential capacitance was determined using the values of the imaginary component of the impedance Z'':

$$C = -\frac{1}{\omega Z''},$$

where ω was the circular frequency of the alternating current ($\omega = 2\pi f$).

In accordance with [18], at room temperature titanium disilicide is a metallic conductor and is characterized by resistivity not exceeding 20 μΩ cm. Therefore, the reduced values of the differential capacitance of the $TiSi_2$ electrode as compared to the capacitance values typical for solid metal electrodes in aqueous electrolyte solutions (~20–40 μF/cm²) cannot be associated with the nature of conductivity and low concentration of charge carriers in the silicide.

The low values of the silicide capacitance were apparently due to the presence of a thin dielectric film of silicon dioxide on its surface ($Si + 2H_2O \rightarrow SiO_2 + 4H^+ + 4e^-$, E^0 = –0.86 V [19]). An oxide film was formed on the silicide at the corrosion potential and was not subject to reduction during cathodic polarisation. The authors [1, 2] also showed that SiO_2 was stable in acidic media with low cathodic polarisations.

Table. 1. Kinetic parameters of hydrogen evolution reaction for the $TiSi_2$ electrode in sulphuric acid solutions

Solution	$-E$, V	$-\left(\frac{\partial E}{\partial \log i}\right)_{c_{H^+}}$, V	$-\eta$, B at i = 1 A/sm^{-2}	$\left(\frac{\partial \log i}{\partial \log c_{H^+}}\right)_E$	$-\left(\frac{\partial E}{\partial \log c_{H^+}}\right)_i$, V
0.5 M H_2SO_4	0.30–0.48	0.120±0.003	0.90±0.02	1.01±0.04	0.123±0.005
0.35 M H_2SO_4 + 0.15 M Na_2SO_4	0.30–0.48	0.119±0.003	0.92±0.02		
0.20 M H_2SO_4 + 0.30 M Na_2SO_4	0.33–0.48	0.116±0.004	0.94±0.04		
0.05 M H_2SO_4 + 0.45 M Na_2SO_4	0.36–0.48	0.117±0.003	0.96±0.03		

The decrease in the differential capacitance due to a decrease in acidity of the electrolyte (Fig. 2) may be associated with the lower rate of chemical dissolution of SiO_2 in solutions with lower acidity. According to [20], the rate of chemical dissolution of various forms of silicon dioxide (quartz or amorphous oxide) was minimal at pH ~(2–3) and increased with deviations from this value in both directions. The pH values of the studied electrolytes were 0.4–1.8 and, therefore, correspond to the descending branch of the curve of the dependence of SiO_2 dissolution rate on the pH of the solution.

The introduction of sodium fluoride (0.005 M) into a solution of 0.5 M H_2SO_4 leading to the dissolution of silicon dioxide [20] resulted in an increase in the differential capacity of the silicide by ~1.3–2.1 times. The higher values of the differential capacitance of silicide in the presence of fluoride confirmed the assumption about the low capacitance of $TiSi_2$ in an acidic fluoride-free solution associated with the presence of a thin oxide film on its surface.

The impedance spectra of the $TiSi_2$ electrodes in the studied solutions were capacitive semicircles with a misplaced centre (Fig. 3) which corresponded to asymmetric maxima in the graph of the dependence of the phase angle φ on the logarithm of the alternating current frequency *f*. The electrode quantity |*Z*| changed in accordance with the shape of the polarisation curves in all solutions (Fig. 1).

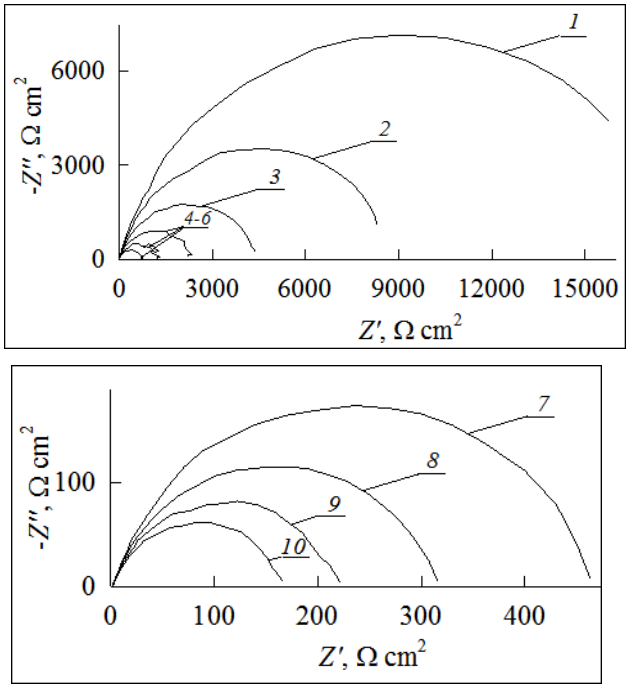

Fig. 3. Impedance spectra of the $TiSi_2$ electrode in 0.20 M H_2SO_4 + 0.30 M Na_2SO_4 at E, V: *1* – –0.33; 2 – –0.36; *3* – –0.39; *4* – –0.42; *5* – –0.45; *6* – –0.48; *7* – –0.51; *8* – –0.54; *9* – –0.57; *10* – –0.60

An equivalent electrical circuit presented in Fig. 4 was used to simulate HER on the $TiSi_2$ electrode at potentials of linear dependence of *E* on lg*i* on cathodic polarisation curves in the studied solutions. The circuit includes the following: R_s is the electrolyte resistance, R_1 is the charge transfer resistance, while resistance R_2 and capacitance C_2 describe the adsorption of atomic hydrogen on the electrode surface and the CPE_1 element simulates double layer capacitance on the inhomogeneous surface of the solid electrode.

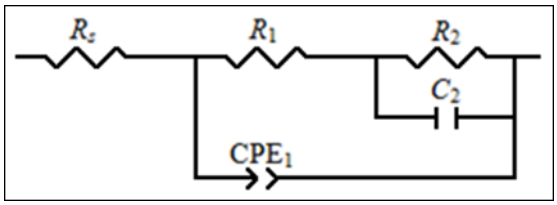

Fig. 4. The equivalent electrical circuit for the $TiSi_2$ electrode in sulphuric acid solutions over the range of hydrogen evolution potentials

The impedance of the constant phase element was:

$$Z_{CPE} = Q^{-1}(j\omega)^{-p}.$$

In this ratio with $p = 1 - \gamma$ the constant phase element is non-ideal capacitance and γ is the value significantly less than 1 (typically $\gamma < 0.2$) [21].

The use of the non-linear least squares method (ZView2 program) showed that the equivalent circuit in Fig. 4 presented a satisfactory description of the experimental impedance spectra of the $TiSi_2$ electrode obtained with *E* ranging from -0.30 to -0.48 V. The χ^2 criterion calculated for this circuit using ZView2 was $(1.3–3.7)\cdot10^{-4}$, the sum of square deviations was $(1.5–4.1)\cdot10^{-2}$, and the error in determining the values of the circuit parameters did not exceed 5% and reached 10% only for the value of R_1. The latter seemed to be associated with the difficulty of the determination of small values of R_1 as compared to the large values of R_2. The values of the equivalent circuit parameters for the 0.20 M

H_2SO_4 + 0.30 M Na_2SO_4 solution are presented in Table 2.

The results of the determination of the numerical values of R_1, R_2, and C_2 parameters of the equivalent circuit in Fig. 4 for the $TiSi_2$ electrode in the studied solutions were analysed depending on the potential in semi-logarithmic coordinates (Fig. 5, Table 3). In the potential region from −0.30 to −0.48 V, the lg X,E dependences, where $X = R_1, R_2, C_2$, were linear, which confirmed that the Langmuir adsorption isotherm for adsorbed atomic hydrogen was fulfilled [22]. The experimental values of the slopes $(\partial \lg X / \partial E)_{c_{H^+}}$ were close to the theoretical values of the slopes for the discharge-electrochemical desorption mechanism, in which both stages were irreversible and the transfer coefficients of te stages were not equal [22].

The reduced values of derivatives $(\partial \lg X / \partial E)_{c_{H^+}}$ according to [23], may be associated with the reaction of absorption of atomic hydrogen by the electrode material proceeding at the same time with the hydrogen evolution reaction. The absence of an additional time constant characterising the hydrogen absorption in the impedance spectra of the $TiSi_2$ electrode (Fig. 3) with the potentials of linear dependence of E on lg$i$ on the polarisation curves indicated that the transition of hydrogen from an adsorbed state to an absorbed state was probably the rate-determining process in the absorption of hydrogen. In this case, the resistance R_2 in the equivalent circuit in Fig. 4 was expressed through the adsorption resistance R_{ads} and the absorption resistance R_{abs}: $R_2 = \frac{R_{ads} R_{abs}}{R_{ads} + R_{abs}}$

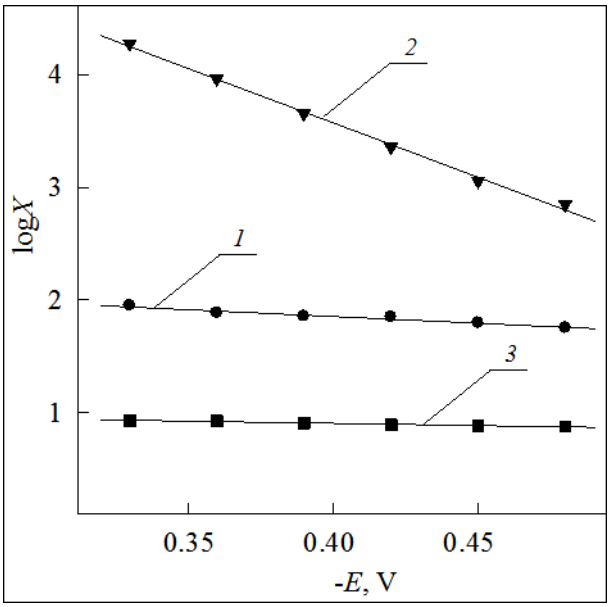

Fig. 5. Dependences of lg$X$ (X: *1* – R_1, *2* – R_2, *3* – C_2) on the potential of the $TiSi_2$ electrode in a solution of 0.20 M H_2SO_4 + 0.30 M Na_2SO_4. Units of measurement: R_1 and R_2 in Ohm×cm², C_2 in μF/cm²

Table 2. The values of the equivalent circuit parameters in Fig. 4 for the $TiSi_2$ electrode in a solution of 0.20 M H_2SO_4 + 0.30 M Na_2SO_4

−E, V	R_1, Ω cm²	R_2, Ω cm²	$C_2 \cdot 10^6$, F·sm^{-2}	$Q_1 \cdot 10^4$, F·sm^{-2}·s$^{(p_1-1)}$	p_1
0.33	89.2	18818	8.51	1.39	0.817
0.36	76.4	9145	8.43	1.50	0.821
0.39	71.7	4507	8.11	1.59	0.803
0.42	70.4	2263	7.83	1.66	0.798
0.45	62.4	1134	7.65	1.65	0.795
0.48	56.5	704.2	7.53	1.66	0.792

Table 3. Slope values $(\partial \lg X / \partial E)_{c_{H^+}}$ (X = R_1, R_2, C_2) for the $TiSi_2$ electrode in sulphuric acid solutions

Solution	−E, V	$\left(\frac{\partial \log R_1}{\partial E}\right)_{c_{H^+}}$, V^{-1}	$\left(\frac{\partial \log R_2}{\partial E}\right)_{c_{H^+}}$, V^{-1}	$\left(\frac{\partial \log C_2}{\partial E}\right)_{c_{H^+}}$, V^{-1}
0.5 M H_2SO_4	0.30-0.48	0.9±0.5	9.1±0.5	0.35±0.03
0.35 M H_2SO_4 + 0.15 M Na_2SO_4	0.33–0.48	1.5±0.2	8.3±0.4	0.23±0.05
0.20 M H_2SO_4 + 0.30 M Na_2SO_4	0.33–0.48	1.2±0.3	9.4±0.6	0.37±0.03
0.05 M H_2SO_4 + 0.45 M Na_2SO_4	0.36–0.48	1.4±0.2	8.8±0.3	0.25±0.04

4. Conclusions

It was established that the hydrogen evolution reaction on titanium disilicide in a sulphuric acid electrolyte proceeded according to the discharge-electrochemical desorption path, both stages were irreversible, and the transfer coefficients of the stages were not equal. The Langmuir isotherm for adsorbed atomic hydrogen was fulfilled. It was suggested that HER was complicated by the hydrogen absorption reaction with the electrode material proceeding with kinetic control (over the whole range of the studied potentials). It was found that titanium disilicide in a sulphuric acid electrolyte is a material with a high hydrogen evolution overpotential and did not have a high electrochemical activity in HER. The presence of a thin oxide film was noted on the electrode surface at low cathodic polarisations.

Author contributions

All authors made an equivalent contribution to the preparation of the publication.

Conflict of interests

The authors declare that they have no known competing financial interests or personal relationships that could have influenced the work reported in this paper.

References

1. Shamsul Huq A. K. M., Rosenberg A. J. J. Electrochemical behavior of nickel compounds: I. The hydrogen evolution reaction on NiSi, NiAs, NiSb, NiS, $NiTe_2$, and their constituent elements. *Journal of The Electrochemical Society.* 1964;111(3): 270–278. https://doi.org/10.1149/1.2426107

2. Vijh A. K., Belanger G., Jacques R. Electrochemical activity of silicides of some transition metals for the hydrogen evolution reaction in acidic solutions. *International Journal of Hydrogen Energy*. 1990;15(11): 789–794. https://doi.org/10.1016/0360-3199(90)90014-P

3. Vijh A. K., Belanger G., Jacques R. Electrolysis of water on silicides of some transition metals in alkaline solutions. *International Journal of Hydrogen Energy*. 1992;15(7): 479–483. https://doi.org/10.1016/0360-3199(92)90146-N

4. Wirth S., Harnisch F., Weinmann M., Schröder U. Comparative study of IVB-VIB transition metal compound electrocatalysts for the hydrogen evolution reaction. *Applied Catalysis B: Environmental*. 2012;126: 225–230. https://doi.org/10.1016/j.apcatb.2012.07.023

5. Shein A. B., Kichigin V. I., Konyk M., Romaka L., Stadnyk Yu. Study of the kinetics and mechanism of the hydrogen evolution reaction on $CeMe_2Ge_2$ electrodes (Me = Fe, Co, Ni). *Chemistry of Metals and Alloys*. 2013;6(3-4): 113–120. https://doi.org/10.30970/cma6.0245

6. Meyer S., Nikiforov A. V., Petrushina I. M., Kohler K., Christensen E., Jensen J. O., Bjerrum N. J. Transition metal carbides (WC, Mo_2C, TaC, NbC) as potential electrocatalysts for the hydrogen evolution reaction (HER) at medium temperatures. *International Journal of Hydrogen Energy*. 2015;40(7): 2905–2911. https://doi.org/10.1016/j.ijhydene.2014.12.076

7. Safizadeh F., Ghali E., Houlachi G. Electrocatalysis developments for hydrogen evolution reaction in alkaline solutions – A Review. *International Journal of Hydrogen Energy*. 2015;40(1);256–274. https://doi.org/10.1016/j.ijhydene.2014.10.109

8. Kichigin V. I., Shein A. B. Kinetics and mechanism of hydrogen evolution reaction on cobalt silicides in alkaline solutions. *Electrochimica Acta*. 2015;164: 260–266. https://doi.org/10.1016/j.electacta.2015.02.198

9. Sapountzi F. M., Gracia J. M., Weststrate C. J., Fredriksson H. O. A., Niemantsverdriet J. W. Electrocatalysts for the generation of hydrogen, oxygen and synthesis gas. *Progress in Energy and Combustion Science*. 2017;58: 1–35. https://doi.org/10.1016/j.pecs.2016.09.001

10. Eftekhari A. Electrocatalysts for hydrogen evolution reaction. *International Journal of Hydrogen Energy*. 2017;42(16): 11053–11077. https://doi.org/10.1016/j.ijhydene.2017.02.125

11. Kichigin V. I., Shein A. B. An electrochemical study of the hydrogen evolution reaction at YNi_2Ge_2 and $LaNi_2Ge_2$ electrodes in alkaline solutions. *Journal of Electroanalytical Chemistry*. 2018;830-831: 72–79. https://doi.org/10.1016/j.jelechem.2018.10.029

12. Karfa P., Majhi K. C., Madhuri R. Group IV transition metal based phospho-chalcogenides@$MoTe_2$ for electrochemical hydrogen evolution reaction over wide range of pH. *International Journal of Hydrogen Energy*. 2019;44(45): 24628–24641. https://doi.org/10.1016/j.ijhydene.2019.07.192

13. Panteleeva V. V., Votinov I. S., Polkovnikov I. S., Shein A. B. Kinetics of cathodic hydrogen evolution manganese monosilicide in sulfuric acid electrolyte. *Kondensirovannye sredy i mezhfaznye granitsy = Condensed Matter and Interphases*. 2019;21(3): 432–440. (In Russ., abstract in Eng.). https://doi.org/10.17308/kcmf.2019.21/1153

14. Kuzminykh M. M., Panteleeva V. V., Shein A. B. Cathodic hydrogen evolution on iron disilicide. I. Alkaline solution. *Izvestiya vuzov. Khimiya i khimicheskaya tekhnologiya = ChemChemTech*. 2019;62(1):38–45. (In Russ., abstract in Eng.). https://doi.org/10.6060/ivkkt.20196201.5745

15. Kuzminykh M. M., Panteleeva V. V., Shein A. B. Cathodic hydrogen evolution on iron disilicide. I. Acidic solution. *Izvestiya vuzov. Khimiya i khimicheskaya tekhnologiya = ChemChemTech*. 2019;62(2): 59–64. (In Russ., abstract in Eng.). https://doi.org/10.6060/ivkkt.20196202.5750

16. Theerthagiri J., Lee S. J., Murthy A. P., Madhavan J., Choi M. Y. Fundamental aspects and recent advances in transition metal nitrides as electrocatalysts for hydrogen evolution reaction: A review. *Current Opinion in Solid State and Materials Science*. 2020;24(1): 100805–100827. https://doi.org/10.1016/j.cossms.2020.100805

17. Rotinyan A. L., Tikhonov K. I., Shoshina I. A. *Theoretical Electrochemistry*. Leningrad: Khimiya Publ.; 1981. 424 p. (In Russ.)

18. Myurarka M. *Silicides for SBIS*. Moscow: Mir Publ.; 1986. 176 p. (In Russ.)

19. Sukhotin A. M. *Handbook of Electrochemistry*. Leningrad: Khimiya Publ.; 1981. 488 p. (In Russ.)

20. Zhang X. G. *Electrochemistry of silicon and its oxide*. Kluwer Academic/Plenum Publishers; 2001. 510 p.

21. Orazem M. E., Tribollet B. *Electrochemical Impedance Spectroscopy*. John Wiley and Sons, Hoboken; 2008. 533 p.

22. Kichigin V. I., Shein A. B. Diagnostic criteria for hydrogen evolution mechanisms in electrochemical impedance spectroscopy. *Electrochimica Acta*. 2014;138: 325–333. https://doi.org/10.1016/j.electacta.2014.06.114

23. Kichigin V. I., Shein A. B. Influence of hydrogen absorption on the potential dependence of the Faradaic impedance parameters of hydrogen evolution reaction. *Electrochimica Acta*. 2016;201: 233–239. https://doi.org/10.1016/j.electacta.2016.03.194

Author information

Valeria V. Tretyakova, Master's degree student, Department of Physical Chemistry, Faculty of Chemistry, Perm State University (Perm, Russian Federation).
https://orcid.org/0000-0002-7629-9307
lera.karaxina@yandex.ru

Viktoria V. Panteleeva, PhD in Chemistry, Associate Professor, Department of Physical Chemistry, Faculty of Chemistry, Perm State University (Perm, Russian Federation).
https://orcid.org/0000-0002-1506-6665
vikpant@mail.ru

Anatoliy B. Shein, DSc in Chemistry, Professor, Head of the Department of Physical Chemistry, Faculty of Chemistry, Perm State University (Perm, Russian Federation).
https://orcid.org/0000-0002-2102-0436
ashein@psu.ru

Received August 18, 2021; approved after reviewing September 10, 2021; accepted February 15, 2022; published online March 25, 2022.

Translated by Marina Strepetova
Edited and proofread by Simon Cox

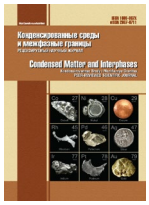

ISSN 1606-867X (Print)
ISSN 2687-0711 (Online)
Condensed Matter and Interphases
Kondensirovannye Sredy i Mezhfaznye Granitsy
https://journals.vsu.ru/kcmf/

Original articles

Research article
https://doi.org/10.17308/kcmf.2022.24/9059

Effect of ethanol vapour sorption on the semiconductor-metal phase transition in powdered vanadium dioxide

E. A. Tutov[1], E. V. Alekseeva[1], A. M. Samoylov[2], O. Ya. Berezina[3]✉, P. P. Boriskov[3]✉

[1]*Voronezh State Technical University,*
84 20-Letiya Oktyabrya ul., Voronezh 394006, Russian Federation

[2]*Voronezh State University,*
1 Universitetskaya pl., Voronezh 394018, Russian Federation

[3]*Petrozavodsk State University,*
33 Lenina pr., Petrozavodsk 185910, Russian Federation

Abstract

We studied the effect of ethanol vapour on the parameters of the semiconductor-metal transition in a polycrystalline vanadium dioxide powder of the stable monoclinic phase α-VO_2. It was synthesised by reducing vanadium pentoxide with oxalic acid while heated in air. The DC electrical resistance of the samples was studied between room temperature and 100 °C in a tubular heater, in a microcompressor-generated air stream with saturated ethyl alcohol vapour. It was found that in the presence of ethanol vapour, the hysteresis loop shifted to higher temperatures by ten degrees and its cooling branch (corresponding to the transition of vanadium dioxide from the metallic phase to the semiconductor phase) became stepped.

Keywords: Vanadium dioxide, Semiconductor - metal phase transition, Ethanol vapour, Sorption

Funding: The study received financing within the framework of state order of the Ministry of Science and Higher Education of the Russian Federation (project No. 0752-2020-0007).

For citation: Tutov E. A., Alekseeva E. V., Samoylov A. M., Berezina O. Ya., Boriskov P. P. Effect of ethanol vapour sorption on the semiconductor-metal phase transition in powdered vanadium dioxide. *Kondensirovannye sredy i mezhfaznye granitsy = Condensed Matter and Interphases.* 2022;24 (1): 95–100. https://doi.org/10.17308/kcmf.2022.24/9059

Для цитирования: Тутов Е. А., Алексеева Е. В., Самойлов А. М., Березина О. Я., Борисков П. П. Влияние сорбции паров этанола на фазовый переход полупроводник –металл в порошковом диоксиде ванадия. *Конденсированные среды и межфазные границы*. 2022;24(1): 95–100. https://doi.org/10.17308/kcmf.2022.24/9059

✉ Petr P. Boriskov, e-mail: boriskov@petrsu.ru; Olga Ya. Berezina, e-mail: berezina@petrsu.ru

1. Introduction

Semiconductor – metal phase transition (SMPT) in vanadium dioxide (VO_2) has been a topical area of research for more than sixty years due to the various practical applications of this effect [1]. Vanadium dioxide as a binary compound with different phase modifications is described in Table 1, their transformation scheme is shown in Figure 1. The structures of vanadium dioxide consist of [VO_6] octahedra. Depending on the synthesis conditions and kinetics, the octahedra can be distorted, connected by edges and vertices in different crystallographic directions, forming two stable modifications (VO_2 (M_1) and VO_2 (R)) and several metastable modifications.

The stable monoclinic M_1 ($P2_1/c$) modification (otherwise called α-VO_2) is built from chains of distorted [VO_6] octahedra, which form a three-dimensional structure with a distance of 0.352 nm between vanadium atoms in adjacent chains and 0.265 nm inside the chain. At temperatures above 68 °C (the SMPT temperature), the distortion of the crystal structure is eliminated, when the localised V-V bonds within the chain are broken and the previously paired electrons are released. As a result, the monoclinic structure transforms

Table 1. Lattice parameters of different vanadium dioxide modifications

VO_2 modifications	Crystal structure (space group)	Lattice parameters			
		a (Å)	*a* (Å)	*a* (Å)	β (°)
VO_2 (M_1)	Monoclinic ($P2_1/c$)	5.7513	4.5259	5.3836	122.618
VO_2 (R)	Tetragonal ($P4_2/mnm$)	4.55	4.55	2.86	-
VO_2 (B)	Monoclinic (C2/m)	12.03	3.69	7.68	106.6
VO_2 (A_L)	Tetragonal (P4/ncc)	8.43	8.43	7.68	-
VO_2 (A_H)	Tetragonal (I4/m)	8.476	8.476	3.824	-
VO_2 (M_2)	Monoclinic (C2/m)	9.07	5.80	4.53	91.9
VO_2 (C)	Monoclinic (I4/mmm)	5.743	4.517	5.375	121.61

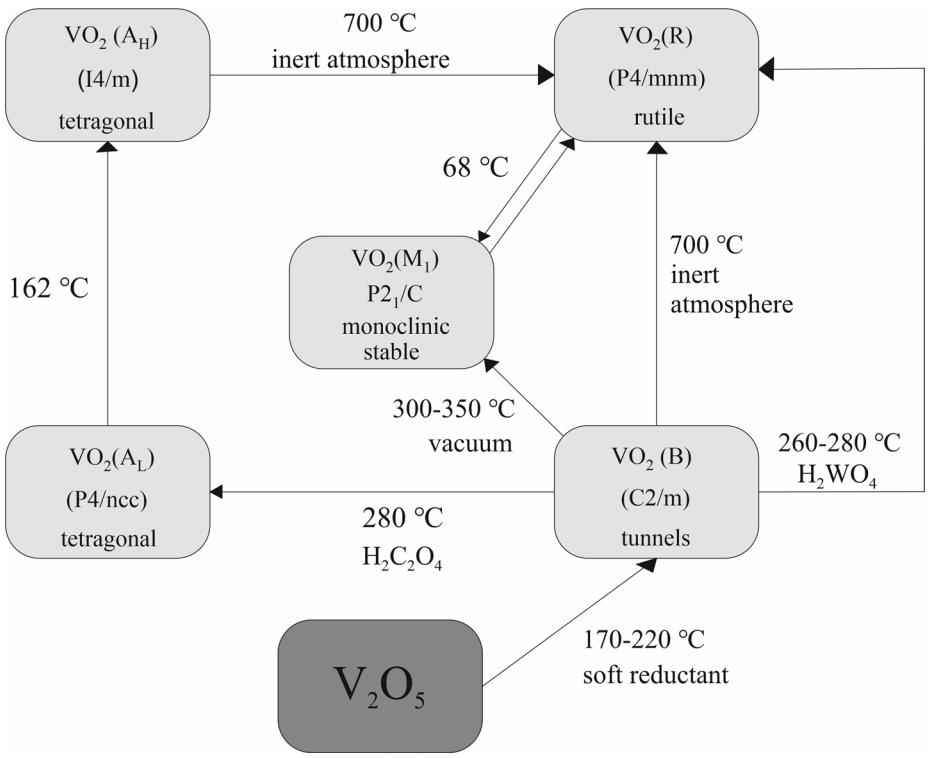

Fig. 1. Technological scheme for the transformations of vanadium dioxide phase modifications (explained in the text)

into a tetragonal (R) ($P4_2/mnm$) rutile structure. In the resulting structure, electrical conductivity, magnetic susceptibility, and light absorption increase dramatically [2]. This allows the M_1 modification to be used as a material for electrical and optical switches, IR-sensitive windows, temperature sensors, and thermochromic indicators.

VO_2 (R) is obtained by heating VO_2 (B) in an inert atmosphere [3]. The rutile (R) modification can also be obtained directly by hydrothermal method. It is similar to the synthesis of VO_2 (B), but it is performed at a higher temperature (260–280 °C) with the addition of tungstic acid (1 %) [4, 5].

Metastable monoclinic modification VO_2 (B) (C2/m) has a characteristic structural feature: channels (tunnels) formed by chains of distorted $[VO_6]$ octahedra. This modification is an important and promising material for lithium-ion battery cathodes because lithium cations can be reversibly introduced into the VO_2 (B) tunnel structure [6]. VO_2 (B) is obtained under hydrothermal conditions at a temperature of about 170–220 °C [4, 7] by treating V_2O_5 with a mild reducing agent. When heated in a vacuum to 300–350 °C, VO_2 (B) turns into VO_2 (M_1). At 700 °C in an inert atmosphere it transforms into the thermochromic modification VO_2 (R) [3].

Metastable VO_2 (A) has two modifications. The low-temperature form (A_L, P4/ncc) changes to the high-temperature (A_H, I4/m) when heated to 162 °C. Both phases have a similar oxygen frame structure in the $[VO_6]$ octahedron, but they have different arrangement of vanadium atoms inside the coordination polyhedron. The abrupt change in the optical properties of VO_2 (A) during the $A_L \leftrightarrow A_H$ phase transition makes it a promising material for optical switches. VO_2 (A_L) can be produced by the reduction of the VO_2 (B) modification with oxalic acid under hydrothermal conditions at 280 °C [5]. The product fraction increases considerably if the starting material is briefly exposed to a pressure of 440 MPa [8]. When VO_2 (A_H) is heated in an inert atmosphere to 700 °C, VO_2 (R) is formed [5].

The monoclinic metastable modification VO_2 (C) (I4/mmm) is close to the monoclinic M1 phase in structure and lattice energy. It has a layered structure and can be used to produce cathodes for lithium-ion batteries. VO_2 (C) is obtained by heating $VO_2 \cdot 0.5H_2O$ semihydrate at 200 °C in a vacuum for 4 days [9].

The semiconductor-metal phase transition changes not only the electrical conductivity of vanadium dioxide, but also its optical characteristics, which is beneficial for the production of thermochromic smart glass. Glazing technologies based on the use of chromogenic materials are called "smart". Chromogenic materials change their optical properties as a result of exposure to electric current, light radiation, changes in temperature, and other factors. Thus, there are electrochromic, photochromic, and thermochromic materials [10]. The heating of vanadium dioxide to 68 °C results in the SMPT, which significantly changes its optical characteristics [11] The transition temperature depends on the vanadium dioxide crystal state, oxygen nonstoichiometry, and doping. The use of composite coatings based on a transparent film matrix filled with thermochromic material makes smart window technology more flexible and affordable [12, 13].

For smart glasses with chromogenic coatings, the ability to reversibly change light transmission parameters is important. When vanadium dioxide is used as a thermochromic filler, the SMPT temperature and the shape of the hysteresis loop can be regulated by surface doping of the oxide under gas adsorption conditions. A chromogenic layer on the inner surface of the glass in a standard window glass unit makes it possible to chemically sensitise the thermochromic material by introducing electron donor gases (e.g., alcohol vapour) into the air between the panes. Some results obtained in this area of research [14] refer mainly to mixed-valence vanadium oxide films.

This paper is devoted to the study of the effect of ethanol vapor on the parameters of the SMPT in single-phase powdered vanadium dioxide.

2. Experimental

Polycrystalline vanadium dioxide powder (*n*-type conductivity as determined by the Seebeck effect) was synthesised by reducing vanadium pentoxide with oxalic acid when heated in air to 600–700 °C according to the reaction:

$$V_2O_5 + H_2C_2O_4 = 2VO_2 + H_2O + 2CO_2.$$

X-ray phase analysis of the powder obtained by the reduction reaction showed the reflexes of vanadium dioxide of the stable α-VO_2 (VO_2 (M_1)) monoclinic phase. At 300 bar, we formed tablets with a diameter of 1 cm and a thickness of 1 mm from the powder. We applied tin foil contacts to the flat surfaces of the tablets. The change of electrical resistance of the samples at direct current was studied in the temperature range from room temperature to 100 °C. The measurements were carried out in a tubular heater in an air stream generated by a microcompressor with saturated ethyl alcohol vapour (about 5% of the volume). The heating and cooling rate was about one degree per minute.

3. Results and discussion

When the samples were heated in air, the sample resistance decreased by two orders of magnitude in the temperature range of 60-80 °C, and the hysteresis loop was slightly asymmetrical (Fig. 2a). In the presence of ethanol vapour, there were significant changes in the parameters of the phase transition. The hysteresis loop shifted to higher temperatures by about ten degrees, and the cooling branch (corresponding to the transition of vanadium dioxide from the metallic phase to the semiconductor phase) became stepped (Fig. 2b).

There is a step on the cooling branch of the hysteresis loop at 80–90 °C (Fig. 2b, branch (2)) under the action of a donor-active gas (ethanol) on the surface of vanadium dioxide. It may result from the asymmetry of the so-called elementary hysteresis loops due to elastic deformation of crystallites during the phase transition [15]. The cooling branch of the thermal hysteresis loop is not multi-step in the absence of donor-active gas on the vanadium dioxide powder surface.

We had previously observed the multi-step shape of both branches of the thermal hysteresis of the semiconductor-metal phase transition in nanocrystalline films of mixed vanadium oxide on silicon in AC conductivity measurements [16]. The steps were formed due to the influence of the size effect on the phase transition in certain groups of crystallites of nearly similar size.

We had also observed "abnormal" electronic semiconductor (VO_2) responses to the chemisorption of electron-donor gas (ethanol) for vanadium dioxide films. Study [17] suggested an energy band model of the structure of vanadium dioxide crystallites that took into account the possible inversion of the conductivity type in the surface layers. An increase up to certain limits (up to inversion) of the electron concentration in the space charge region of the VO_2 surface layer should lead to

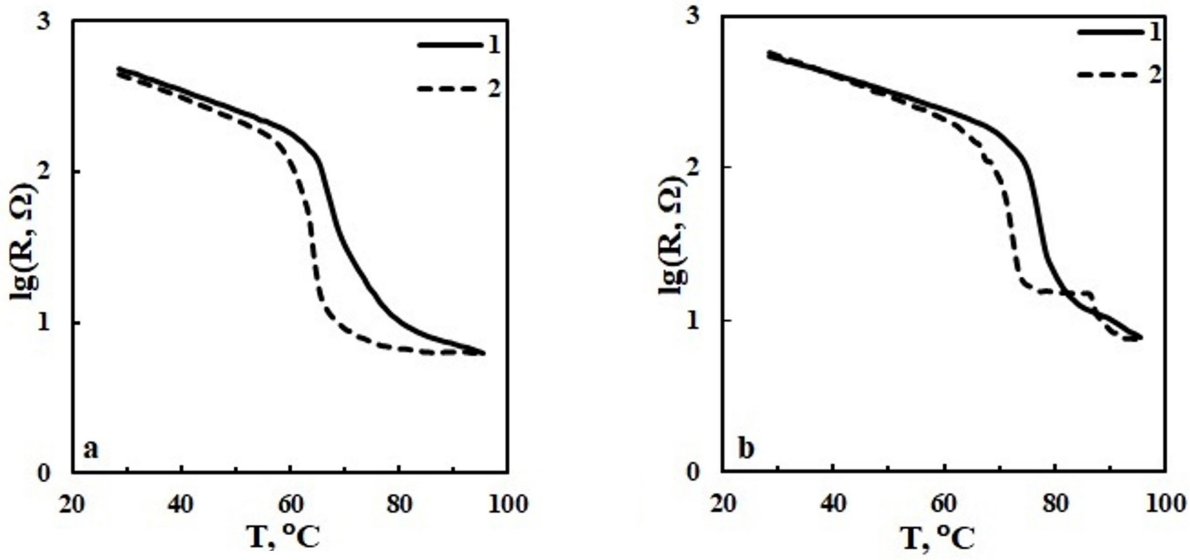

a b

Fig. 2. Dependence of vanadium dioxide resistance on temperature in a clean air stream (a) and in an air stream with saturated ethanol vapour (b): *1* — heating branch, *2* — cooling branch

an increase in the electrical resistance of the material.

4. Conclusions

Thus, using ethanol vapour as an example, this study shows that it is possible to control the semiconductor - metal phase transition parameters in polycrystalline powdered vanadium dioxide by chemisorption of gases.

Authors contributions

All authors made an equivalent contribution to the preparation of the publication.

Conflict of interests

The authors declare that they have no conflict of interest.

References

1. Pergament A. L., Berezina O. Ya., Burdyukh S. V., Zlomanov V. P., Tutov E. A. Vanadium oxide thin films: metal-insulator transition, electrical switching, and modification of the properties by ion implantation. Book chapter in: *Advances in Materials Science Research*, V.41. Maryann C. Wythers (Editor). New York: Nova Science Publishers; 2020. p. 153–182. https://novapublishers.com/shop/advances-in-materials-science-research-volume-41/

2. Chain E. E. Optical properties of vanadium dioxide and vanadium pentoxide thin-films. *Applied Optics*. 1991;30(19): 2782–2787. https://doi.org/10.1364/AO.30.002782

3. Kam K. C., Cheetham A. K. Thermochromic VO_2 nanorods and other vanadium oxides nanostructures. *Materials Research Bulletin*. 2006;41(5): 1015–1021. https://doi.org/10.1016/j.materresbull.2006.03.024

4. Ji S. D., Zhao Y., Zhang F. Jin P. Direct formation of single crystal VO_2 (R) nanorods by one-step hydrothermal treatment. *Journal of Crystal Growth*. 2010;312(2): 282–286. https://doi.org/10.1016/j.jcrysgro.2009.10.026

5. Zhang Y. F., Zhang J. C., Zhang X. Z., Deng Y., Zhong Y. L., Huang C., Liu X., Liu X. H., Mo S. B. Influence of different additives on the synthesis of VO_2 polymorphs. *Ceramics International*. 2013;39(7): 8363–8376. https://doi.org/10.1016/j.ceramint.2013.04.016

6. Ni J. A., Jiang W. T., Yu K., Gao Y. F., Zhu Z. Q. Hydrothermal synthesis of VO_2 (B) nanostructures and application in aqueous Li-ion battery. *Electrochimica Acta*. 2011;56(5): 2122–2126. https://doi.org/10.1016/j.electacta.2010.11.093

7. Zhang Y. F. VO_2 (B) conversion to VO_2 (A) and VO_2 (M) and their oxidation resistance and optical switching properties. *Materials Science-Poland*. 2016;34(1): 169–176. https://doi.org/10.1515/msp-2016-0023

8. Oka Y, Yao T., Yamamoto N. Structural phase-transition of VO_2 (B) to VO_2 (A). *Journal of Materials Chemistry*. 1991;1(5): 815–818. https://doi.org/10.1039/JM9910100815

9. Hagrman D., J. Zubieta C. J., Warren L. M., Meyer M., Treacy M. J. R, Haushalter C. A new polymorph of VO_2 prepared by soft chemical methods. *Journal of Solid State Chemistry*. 1998;138(1): 178–182. https://doi.org/10.1006/jssc.1997.7575

10. Kamalisarvestani M., Saidur R., Mekhilef S., Javadi F. S. Performance, materials and coating technologies of the thermochromic thin films on smart windows. *Renewable and Sustainable Energy Reviews*. 2013;26: 353–364. https://doi.org/10.1016/j.rser.2013.05.038

11. Warwick M., Binions R. Advances in thermochromic vanadium dioxide films. *Journal of Materials Chemistry* A. 2014;2: 3275–3292. https://doi.org/10.1039/C3TA14124A

12. He T., Yao J. Photochromism in composite and hybrid materials based on transition-metal oxides and polyoxometalates. *Progress in Materials Science*. 2006;51: 810–879. https://doi.org/10.1016/j.pmatsci.2005.12.001

13. Gao Y., Luo H., Zhang Z., Kang L., Chen Z., Du J., Kanehira M., Cao C. Nanoceramic VO_2 thermochromic smart glass: A review on progress in solution processing. *Nano Energy*. 2012;1: 221–246. https://doi.org/10.1016/j.nanoen.2011.12.002

14. Tutov E. A., Zlomanov V. P. Effect of chemisorption of donor and acceptor gases on the semiconductor - metal phase transition in vanadium dioxide films. *Physics of the Solid State*. 2013;55: 2351–2354. https://doi.org/10.1134/S1063783413110280

15. Aliev R. A., Klimov V. A. Effect of synthesis conditions on the metal-semiconductor phase transition in vanadium dioxide thin films. *Physics of the Solid State*. 2004;46: 532–536. https://doi.org/10.1134/1.1687874

16. Tutov E. A., Goloshchapov D. L., Zlomanov V. P. Semiconductor - metal phase transition and "tristable" electrical switching in nanocrystalline vanadium oxide films on silicon. *Technical Physics Letters*. 2019;45: 584–587. https://doi.org/10.1134/S1063785019060312

17. Tutov E. A., Manannikov A. V., Al-Khafaji H. I., Zlomanov V. P. Surface and bulk conductivity of vanadium dioxide. *Technical physics*. 2017;62: 390–394. https://doi.org/10.1134/S1063784217030252

Information about the authors

Evgeny A. Tutov, DSc in Chemistry, Associate Professor, Professor at the Department of Physics, Voronezh State Technical University (Voronezh, Russian Federation).
https://orcid.org/0000-0002-5481-8137
tutov_ea@mail.ru

Elena V. Alekseeva, Senior Lecturer at the Department of Physics, Voronezh State Technical University (Voronezh, Russian Federation).
https://orcid.org/0000-0001-6190-6584
alenaalekseewa@mail.ru

Alexander M. Samoylov, DSc in Chemistry, Associate Professor, Professor at the Department of Materials Science and the Industry of Nanosystems, Voronezh State University (Voronezh, Russian Federation).
https://orcid.org/0000-0003-4224-2203
samoylov@chem.vsu.ru

Olga Ya. Berezina, PhD in Physics and Mathematics, Associate Professor at the Department of General Physics, Institute of Physics and Technology, Petrozavodsk State University (Petrozavodsk, Russian Federation).
https://orcid.org/0000-0003-4055-5759
berezina@petrsu.ru

Petr P. Boriskov, PhD in Physics and Mathematics, Leading Engineer, Institute of Physics and Technology, Petrozavodsk State University (Petrozavodsk, Russian Federation).
https://orcid.org/0000-0002-2904-9612
boriskov@petrsu.ru

Received January 24, 2022 approved after reviewing January 31, 2022; accepted February 15, 2022; published online March 25, 2022.

Translated by Anastasiia Ananeva
Edited and proofread by Simon Cox

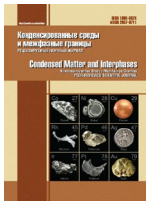

ISSN 1606-867X (Print)
ISSN 2687-0711 (Online)
Condensed Matter and Interphases
Kondensirovannye Sredy i Mezhfaznye Granitsy
https://journals.vsu.ru/kcmf/

Original articles

Research article
https://doi.org/10.17308/kcmf.2022.24/9060

Polycondensation in a spray of aqueous-alcoholic solution of lactic acid

V. B. Fedoseev[1]✉, E. N. Fedoseeva[2]

[1]*G. A. Razuvaev Institute of Organometallic Chemistry, Russian Academy of Sciences, 49 Tropinina str., Nizhny Novgorod 603950, Russian Federation*

[2]*Lobachevsky State University of Nizhny Novgorod, 23 pr. Gagarina, Nizhny Novgorod 603950, Russian Federation*

Abstract

The removal of low molecular weight products of the reaction and heat withdrawal is one of the problems of bulk polycondensation. Polycondensation under spray conditions is an effective way to solve these problems.

Based on the example of the reversible reaction of lactic acid polycondensation, it was shown that size effects can significantly affect the conversion rate, the degree of polymerization, and the rate of processes. Chemical thermodynamics suggests that chemical equilibrium in a spray shifts towards the formation of polylactide. In addition, the recondensation of volatile components (water, lactic acid, solvent) stabilizes the concentration of reagents and the temperature in the spray drops throughout the entire process. Model experiments confirming the obtained regularities are presented. Microscopic observation of sessile drops of aqueous and aqueous-alcoholic lactic acid solutions demonstrated the formation of polylactide under normal conditions (without heating, catalyst, evacuation).

The described regularities are of a thermodynamic nature and are relevant for polymerization and polycondensation processes involving volatile monomers and solvents.

Keywords: Polycondensation, Spray, Polylactide, Microencapsulation, Phase transitions

Funding: The work was carried out in accordance with the state assignment of the G. A. Razuvaev Institute of Organometallic Chemistry, Russian Academy of Sciences.

For citation: Fedoseev V. B., Fedoseeva E. N. Polycondensation in a spray of aqueous-alcoholic solution of lactic acid. *Kondensirovannye sredy i mezhfaznye granitsy = Condensed Matter and Interphases*. 2022;24(1): 101–108. https://doi.org/10.17308/kcmf.2022.24/9060

Для цитирования: Федосеев В. Б., Федосеева Е. Н. Поликонденсация в условиях спрея водно-спиртового раствора молочной кислоты. *Конденсированные среды и межфазные границы*. 2022;24(1): 101–108. https://doi.org/10.17308/kcmf.2022.24/9060

✉ Victor B. Fedoseev, e-mail: vbfedoseev@yandex.ru

1. Introduction

The increased interest in spray technologies is due to the possibility of obtaining products and materials with unique properties. The ease of implementation and the efficiency of spray technologies allow using them in the production of polymeric materials [1, 2], pharmaceutical preparations [3], and in organic synthesis [4]. There are good prospects for spray technologies in which polymerization and other chemical processes occur inside or on the surface of aerosol particles [5]. This allows creating functional materials with a special morphology, for example, inorganic particles coated with a polymer shell [6, 7] or organic particles with an oxide shell [8], hollow spheres [9] and polymer microcapsules filled with components for various purposes [10].

Features and benefits of spray technologies are based on size effects, which contribute to the emergence of conditions and states not typical for macroscopic systems. Size effects are understood as the dependence of the properties and dynamics of processes on the size or volume of the system. In the spray, they become significant for submillimeter drops. In particular, size effects during phase transformations of the liquid–liquid type allow reagents to be involved in the processes for which their interactions with each other is complicated by low mutual solubility [11, 12]. Thermodynamic estimates show that a decrease in volume can lead to the complete mutual solubility of low-soluble components [13,14].

The assessment of the use of the spray technology in organic synthesis was provided in [15], where the synthesis of polylactide (PLA) was one of the examples.

PLA has a wide range of applications as a biocompatible, biodegradable, and thermoplastic polymer. One of the methods for its production is direct synthesis using aqueous organic solutions of lactic acid [16, 17]. The main difficulties of the technology are associated with the removal of a low molecular weight polycondensation product (water), which, like the formation of a high molecular weight product, is accompanied by an increase in viscosity and a slowdown in the heat and mass transfer processes. The consequence is local overheating of the reaction mixture, tarring, and other undesirable chemical transformations.

In the spray, the problems associated with an increase in the viscosity of the reaction mixture are effectively removed due to interfacial heat and mass transfer, and the removal of a low molecular weight product is facilitated by a large specific surface area and surface curvature.

The vapour pressure above the surface of spray drops is higher than in a macrosystem of the same composition, and the concentration of water in the reaction mixture equilibrium with the gaseous medium, decreases with a decrease in the radius of drops (Kelvin equation). This should shift the equilibrium in the polycondensation reaction towards polymer formation.

Size effects at chemical equilibrium can be associated with the difference in the chemical potentials of the components in the bulk and in the near-surface layer. In this case, the effective constant of chemical equilibrium and the rate of processes become a function of the specific surface area, surface activity, and molar volume of the components [15, 18].

In the spray, chemical and phase equilibrium are interconnected through the chemical potentials of the components in different phases. A large specific surface area and small diffusion paths allow to stabilize the temperature and concentrations of reagents due to mass and heat transfer during the recondensation of volatile components between drops [19, 20]. All low molecular weight components of the reaction (water and lactic acid) are present in the gas phase and participate in the recondensation during the polycondensation of lactic acid.

In the formation of insoluble products (polymer) or separation of the solution, size effects change the mutual solubility of the components and lower the upper critical temperature of separation [21, 22]. An increase in the solubility of lactic acid and its oligomers additionally shifts the equilibrium towards polymerization.

The aim of this study was theoretical substantiation of the statement about the advisability of using spray technology as the best alternative to existing methods for the synthesis of PLA. The task of the above model experiments was to experimentally confirm this statement.

2. Results and discussion

2.1. Thermodynamic model of polycondensation under spray conditions

The scheme of equilibrium transformations involving lactic acid, lactide, PLA, and their

thermodynamic properties are given in [23]. The equilibrium constant of the polycondensation reaction K at low degrees of polymerization and low conversion has the form:

$$K = \frac{x_p x_0^{p-1}}{x_1^p} = \frac{x_p}{x_0}\left(\frac{x_0}{x_1}\right)^p, \quad (1)$$

where p is the degree of polymerization, x_0, x_1, x_p are the concentration (mole fraction) of water, monomer, and polymer in the solution, respectively.

At high degrees of polymerization, the polymer passes into the solid phase. If no solid solutions are formed, then $x_p = 1$ and the equilibrium constant takes the form:

$$K_* = \left(\frac{x_0}{x_1}\right)^p x_0^{-1}. \quad (2)$$

The values of K and K_* differ by the correction for the transition energy of the polymer into solution. The reactions of the formation of lactide and PLA from lactic acid are characterized by small positive values of the Gibbs energy [23] and, accordingly, by equilibrium constants close to one.

Phase equilibrium and chemical equilibrium are related through the chemical potentials of the components. This relationship determines the state of drops (radius, composition) and the equilibrium concentrations of components in different phases [19, 20]. For ideal solutions, the condition of equality of chemical potentials in coexisting phases is converted to the equations of Kelvin and Freundlich and Raoult's law. For real solutions, the relationship between the solution concentration x_k, drop radius r, partial pressure in the vicinity of the drop $P_k(r, x_k)$ or external environment $P_{ex,k}$ has a more complex form:

$$P_k(r, x_k) = \gamma_k x_k P_{\infty,k} \exp\left(\frac{2\sigma V_k}{rRT}\right). \quad (3)$$

Here σ is the surface tension, V_k is the molar volume of the component k, R is the universal gas constant, T is temperature, $P_{\infty,k}$ is the vapour pressure above the flat surface of the pure component. Values of γ_k and σ in general depend on the composition of the solution. The equilibrium state of the drop corresponds to the condition $P_k(r, x_k) = P_{ex,k}$, where $P_{ex,k}$ is the partial pressure in the external environment. For low-soluble components, the expression (3) is given in [19,24]. The temperature dependence of the vapour pressure of lactic acid is given in [23]. Its extrapolation to T = 298 K gives $P_{\infty,1}$ ~ 1.5 Pa. Saturated vapour pressure of water at the same temperature $P_{\infty,0}$ = 3.2 kPa.

According to (3) the equilibrium concentration of the volatile component is determined by the droplet radius, vapour pressure, and activity coefficient:

$$x_k = \frac{P_{ex,k}}{\gamma_k P_{\infty,k}} \exp\left(-\frac{2\sigma V_k}{rRT}\right). \quad (4)$$

If all components of the solution are volatile, the following identity is established:

$$\sum x_k = \sum \frac{P_{ex,k}}{\gamma_k P_{\infty,k}} \exp\left(-\frac{2\sigma}{r}\frac{V_k}{RT}\right) = 1. \quad (5)$$

Ratios (3)–(5) determine the equilibrium size and composition of the drops corresponding to the composition of the gaseous medium. For volatile components, this identity limits the conditions for the appearance and existence of a spray by the inequality $\sum P_{ex,k}/P_{\infty,k}\gamma_k > 1$, otherwise the drops evaporate completely. The value $S = \sum P_{ex,k}/P_{\infty,k}$ can be interpreted as the relative supersaturation of vapour.

Identity (5) allows to state that the increase in relative supersaturation S leads to a decrease in the equilibrium drop radius. Positive deviation from the ideal behaviour $\gamma_i > 1$ contributes to an increase in the equilibrium drop radius. Negative deviation from the ideal behaviour $\gamma_i < 1$ lowers the equilibrium drop radius. Drops of solutions with a negative deviation from the ideal behaviour can exist at $S < 1$. These patterns are more complex for solutions containing non-volatile or partially soluble components [19, 20].

Equations (1)–(3) describe the relationship between equilibrium concentrations, degree of polymerization, gas phase composition, and spray drop radius:

$$K = x_p \frac{\gamma_0 P_{\infty,0}}{P_{ex,0}} k^p \exp\left(\frac{2\sigma\left(V_0 + p\left(V_1 - V_0\right)\right)}{rRT}\right), \quad (6)$$

here the multiplier $k = \frac{\gamma_1}{\gamma_0}\frac{P_{ex,0}P_{\infty,1}}{P_{ex,1}P_{\infty,0}}$ depends on the composition of the gas phase and, taking into

account $\gamma_k = \gamma_k(x_i)$, on the concentration of the solution.

The equation (6) describes the main laws of chemical equilibrium in the spray. For example, a decrease in the drop radius (an increase in the exponential) should be compensated by a corresponding decrease in the values of x_p, x_0 or p. The decrease in the value of k (at $r = \text{const}$) is compensated for by the increase in x_p or p shifting the equilibrium towards polycondensation. In other words, the chemical equilibrium in small drops is shifted towards polymer formation, while a decrease in the average radius of spray drops enhances this effect by increasing $P_{ex,1}$ in a spray cloud (3). The transfer of drops in the environment with lower humidity ($P_{ex,0}$) must be accompanied by both a decrease in the radius and an increase in x_p or p.

The decrease in the γ_1/γ_0 ratio leads to a shift of equilibrium towards the formation of a polymer in real solutions. This explains the effectiveness of methods based on the azeotropic distillation of water in the synthesis of PLA [16, 17]. For spray technology, mixtures with $\gamma_0 > 1$, characterized by the lower equilibrium concentration of water in drops are preferable. This further improves the efficiency of the process.

Let us estimate the effect of the solvent composition on the activity coefficients in water–lactic acid–co-solvent mixtures. Let's consider a solution of lactic acid with a concentration of 80 wt. % ($x_0 / x_1 = 1.27$) diluted with two volumes of co-solvent. The values of the activity coefficients of water and monomer are equal in the presence of methyl isobutyl ketone – $\gamma_0 = 0.4$, $\gamma_1 = 1.9$ ($\gamma_1/\gamma_0 = 4.75$), ethanol – $\gamma_0 = 1.1$, $\gamma_1 = 0.8$ ($\gamma_1/\gamma_0 = 0.73$), propanol – $\gamma_0 = 1.2$, $\gamma_1 = 0.8$ ($^3{}_1/^3{}_0 = 0.67$), n-butanol – $\gamma_0 = 1.2$, $\gamma_1 = 1.1$ ($\gamma_1/\gamma_0 = 0.92$), 2-butanol – $\gamma_0 = 1.3$, $\gamma_1 = 1.0$ ($\gamma_1/\gamma_0 = 0.77$). The NRTL parameters for the systems water–lactic acid–methyl isobutyl ketone [25], water–propanol [26], water–ethanol [27], water–butanol-2 [28], water–lactic acid–n-butanol [29] were used in the estimates. The interaction parameters for water–lactic acid provided in the literature for different ternary mixtures can differ significantly [25, 28–30]. Missing parameters of the lactic acid–alcohol interaction were replaced by zeros. In addition to butanol, the authors of [29] describe the use of the NRTL model for aqueous alcoholic solutions of lactic acid with n-pentanol, n-hexanol, and n-heptanol, which form a two-phase system upon such dilution.

From these estimates and equations (3), (4) it follows that in drops of aqueous-alcoholic solutions of lactic acid, the chemical equilibrium will be shifted towards the formation of a polymer. The greatest effect can be expected from solutions containing propanol and 2-butanol.

The use of co-solvents partly solves the problem of viscosity and overheating of the reaction medium [16]. For the azeotropic distillation of water from lactic acid solutions, organic substances of different classes can be used [17].

2.2. Experimental observations of polycondensation in sessile drops

Direct monitoring of the physical and chemical processes occurring in the spray is practically impossible. However, microscopic observations of the behaviour of sessile drops obtained by the deposition of a spray on a solid surface provide some notions. The conducted experiments qualitatively confirmed the possibility of obtaining PLA in a spray and also allowed to reveal some kinetic regularities.

The result of the evolution of drops of lactic acid solutions on a hydrophobized glass slide is shown in Fig. 1. The method described in [15] was used. The drops were in the air gap between the glass slides, which reduced the evaporation rate and eliminated convective currents.

In the general case, after the creation of the spray, rapid evaporation of the droplets occurred, then they were covered with a shell slowing down the evaporation. On the surface of large drops, the appearance, growth and movement of folds was noted. These changes indicated the formation of polymeric capsules in which the processes of polycondensation continued.

The surface shell can be a PLA layer or a saturated solution of oligomers [31].

To test this assumption, a layer of distilled water was applied on a glass slide with capsules formed from an aqueous solution of lactic acid (80 wt%). Drops that fell into the distilled water, without dissolving, were destroyed and detached from the slide, and moved around inside the water layer. The state of the system after water evaporation is shown in Fig. 1a. It shows particles wetted with a

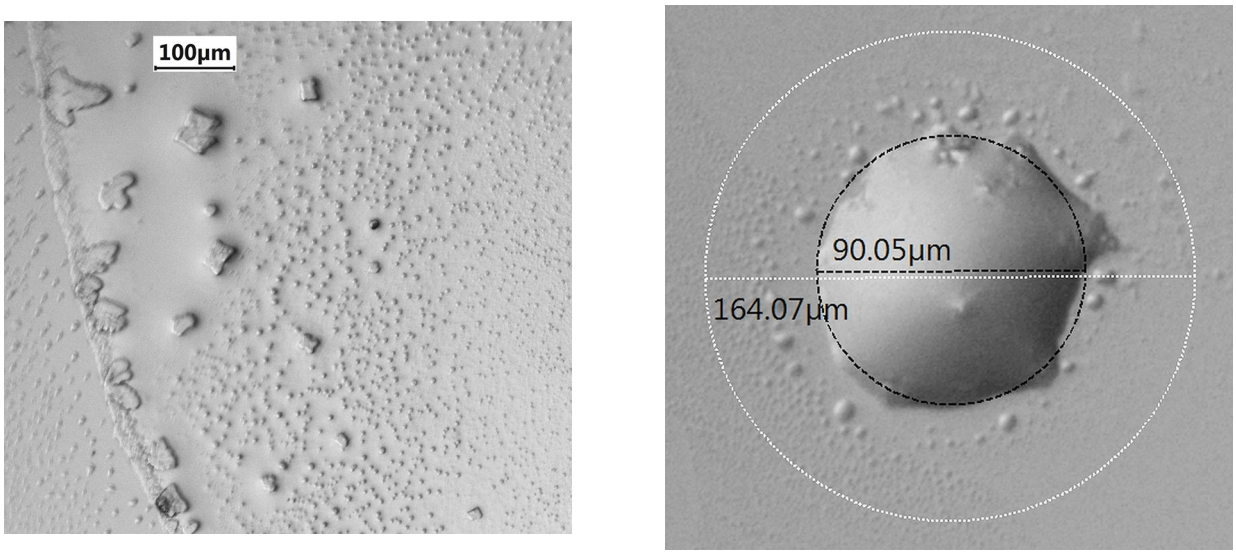

a b

Fig. 1. Structures formed during the destruction of encapsulated drops with distilled water after the evaporation of water (a); the result of the evolution of a large drop of water-alcohol (isopropyl alcohol) lactic acid solution with an indication of the initial and final diameter of the drop (b)

thin layer of non-evaporating solution. The water-insoluble dispersed phase was probably formed by the shells of the destroyed capsules, and the solution surrounding the particles was probably formed by the soluble components (monomer and oligomers) released during the destruction of the capsules. The faceting of individual particles of the dispersed phase (Fig. 1a) shows that the capsule shell was formed either by crystalline PLA or low-soluble oligomers.

The final state of one of the drops of an aqueous-alcoholic solution of lactic acid, prepared by diluting an aqueous solution (80 wt%) with isopropyl alcohol in a ratio of 1 to 2 is shown in Fig. 1b. This state remained unchanged for several days. In the process of evaporation and polycondensation, in the drop appeared inclusions, and many small non-evaporating drops were detected around it. The formation of a fraction of small drops was observed in experiments with both water-alcohol and aqueous solutions of lactic acid. They originate both in the vicinity of large drops and at a considerable distance from them. The causes and examples of the appearance of such satellite drops are described in [20, 32, 33].

The dynamics of the evaporation of drops of a water-alcohol solution of lactic acid at t = 23–25 °C and humidity ~35% is shown in Fig. 2. The radius of drops was determined based on a sequence of micrographs. The shape of the contact spot of most drops initially differed from round and changed during evaporation;

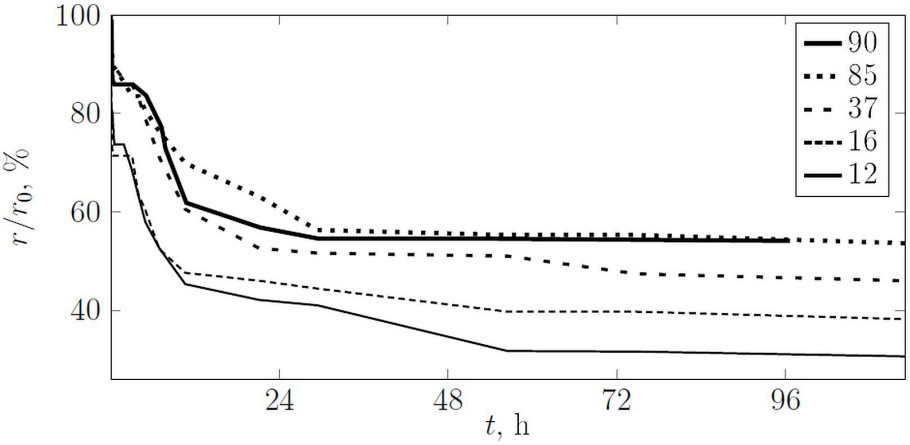

Fig. 2. Dynamics of changes in the relative radius of drops of an aqueous-alcoholic lactic acid solution

therefore, the radius was calculated as half the sum of the maximum and minimum diameters. Normalization of drop sizes by to the initial radius r_0 allows to compare the evaporation rates of drops of different sizes.

The plots shown in Fig. 2 reflect the non-monotonic nature of the process. The evaporation rate was determined based on the change in the drop radius $d(r / r_0) / dt$. The maximal evaporation rate was revealed in the first 5-10 min after the creation of the spray (~ 4%/min). Probably, at this stage, the excess of isopropyl alcohol evaporates, and the solution in drops approaches the azeotrope. After that, the drop sizes stabilized for some time, then decreased again, and the rate increased from zero to ~3%/h. In the last section of the plots, it again asymptotically decreased to 0.

Heterogeneities in the solution, indicating the onset of polycondensation, appeared in large drops 10–15 min after creating the spray. The subsequent decrease in the size of the drops was obviously associated with the processes of polycondensation and azeotropic distillation of the water released in the reaction. The asymptotic slowdown of the processes can be explained by the encapsulation of the drops, which complicated the removal of water, and the increase in conversion.

As can be clearly seen in Fig. 2, the described stages have different durations for large and small drops. In the first minutes, the radius of drops with a radius of 10–20 μm decreased 2 times faster than that of drops with a radius of 40–90 μm. The transition to the asymptotic stage occurred 4–5 h after the creation of the spray for small drops and 5–8 h after the creation of the spray for large drops.

The non-monotonic change of the rate can be explained by the action of at least two reasons:

1. The influence of conversion on the rate of polycondensation. From $x_0 = n_0 / (n_0 + n_{1,\Sigma} - pn_p + n_s)$, where n_0, n_s, and $n_{1,\Sigma}$ are the number of moles of water, alcohol, and the total number of moles of monomer in a drop, we obtain $n_0 \sim (n_{1,\Sigma} - pn_p + n_s)$. Whence it follows that the increase in conversion (pn_p) and removal of the co-solvent (n_s) during azeotropic distillation leads to a decrease in the amount of water in the drop and, accordingly, to a decrease in its radius.

2. The separation of the solution as a result of the formation and increase in the concentration of low-soluble products (oligomers and polymer). The core-shell configuration most often occurs in drops as the result of the separation of the solution. In water-organic mixtures, the shell is usually formed by an organic phase with a lower surface tension. A polymer or a concentrated solution of oligomers encapsulate an aqueous solution of low molecular weight components. Encapsulation occurs in experiments with a spray of both aqueous and water-alcohol solutions. The appearance of a new phase should be accompanied by a change in the chemical equilibrium constants (6) from K till K_*, shifting the equilibrium towards PLA formation.

The dependence of water concentration on radius (4) enhances these effects.

The second aspect is also of separate interest. Polymer capsules have many practical applications [34]. For medical applications, it is important that the PLA-coated capsules formed in the spray do not contain catalysts. Their core may contain concentrated aqueous solutions of pharmaceutical dosage forms and biologically active substances added to the spray solution. At the same time, co-solvents partially miscible with water stimulate the formation of capsules even before the polycondensation stage, which allows to control the properties of the shell, taking into account differences in the equilibrium composition of coexisting phases [35].

3. Conclusions

The above theoretical consideration describes the relationship between the equilibrium composition, the volume of condensed phases, the composition of the gaseous medium, and the drop sizes. The performed estimates allowed stating that during the polycondensation of lactic acid solutions in a spray, the chemical equilibrium shifts towards the formation of a polymer and a significant increase in the conversion and the rate of the process are possible.

Size effects increase the conversion and the rate of polycondensation. In particular, the equilibrium concentration of water in drops is lower than in the macrosystem (4), which leads to a shift in the chemical equilibrium towards polymer formation. The recondensation of solvents and reagents stabilizes the temperature of the droplets and the concentrations of the components in them, contributing to the isothermal course of the reaction without overheating of the reaction medium.

The described patterns are reproduced in model experiments with ensembles of sessile drops of aqueous and aqueous-alcoholic solutions of lactic acid. Experiments demonstrate that the polycondensation in a spray of lactic acid solution proceeds without the use of catalysts, heating, and vacuuming. Under the same conditions, the formation of oligomers and PLA do not occur in the macrosystem.

The results of the theoretical consideration and the experiment allowed stating that the spray technology is the basis for the development of an efficient resource-saving production of PLA, including PLA for medical applications.

These regularities are of a thermodynamic nature and should be exhibited in polycondensation processes involving volatile monomers and solvents. They are relevant in the development of new efficient technologies for the production of polymeric materials.

Author contributions

All authors made an equivalent contribution to the preparation of the publication.

Conflict of interests

The authors declare that they have no known competing financial interests or personal relationships that could have influenced the work reported in this paper.

References

1. Hergeth W., Jaeckle C., Krell M. Industrial process monitoring of polymerization and spray drying processes. *Polymer Reaction Engineering*. 2003;11(4): 663–714. https://doi.org/10.1081/PRE-120026369

2. Sinha-Ray S. Spray in polymer processing. Droplet and spray transport: Paradigms and fpplications. 2018: 31–54. https://doi.org/10.1007/978-981-10-7233-8_3

3. Wanning S., Süverkrüp R., Lamprecht A. Pharmaceutical spray freeze drying. *International Journal of Pharmaceutics*. 2015;488(1–2): 136–153. https://doi.org/10.1016/j.ijpharm.2015.04.053

4. Zhang Y., Suslick K. S. Synthesis of poly(3,4-ethylenedioxythiophene) microspheres by ultrasonic spray polymerization (USPo). *Chemistry of Materials. American Chemical Society* (ACS). 2015;27(22): 7559–7563. https://doi.org/10.1021/acs.chemmater.5b03423

5. Akgün E., Muntean A., Hubbuch J., Wörner M., Sangermano M. Cationic Aerosol photopolymerization. *Macromolecular Materials and Engineearing*. 2015;300(2): 136–139. https://doi.org/10.1002/mame.201400211

6. Poostforooshan J., Rennecke S., Gensch M., Beuermann S., Brunotte G. P., Ziegmann G., Weber A. P. Aerosol process for the *in situ* coating of nanoparticles with a polymer shell. *Aerosol Science and Technology*. 2014;48(10): 1111–1122. https://doi.org/10.1080/02786826.2014.964354

7. Sigmund S., Akgün E., Meyer J., Hubbuch J., Wörner M., Kasper G. Defined polymer shells on nanoparticles via a continuous aerosol-based process. *Journal of Nanoparticle Research*. 2014;16(8): 2533–2536. https://doi.org/10.1007/s11051-014-2533-9

8. Fei B., Lu H., Qi K., Shi H., Liu T., Li X., Xin J. H. Multi-functional microcapsules produced by aerosol reaction. *Journal of Aerosol Science*. 2008;39(12): 1089–1098. https://doi.org/10.1016/j.jaerosci.2008.07.007

9. Berdonosov S. S., Baronov C. B., Kuz'micheva Ju. V., Berdonosova D. G., Melihov I. V. Solid dispersed phases of multilayer and tubular inorganic microparticles. *Rossijskij himicheskij zhurnal*. 2001;45(1): 35–42 (In Russ). Available at: http://www.chem.msu.ru/rus/jvho/2001-1/35.pdf

10. Chicheva P. A., Kurbangaleev V. R., Levchenko K. S., Shmelin P. S., Grebennikov E. P. Preparation of polystyrene microspheres filled with rhodamine G. *Rossijskij himicheskij zhurnal*. 2020;64(4): 46–50 (In Russ., abstract in Eng.). https://doi.org/10.6060/rcj.2020644.5

11. Shishulin A. V., Fedoseev V. B. Thermal stability and phase composition of stratifying polymer solutions in small-volume droplets. *Journal of Engineering Physics and Thermophysics*. 2020;93(4): 802–809. https://doi.org/10.1007/s10891-020-02182-9

12. Fedoseev V. B. The size effect for liquid–liquid phase equilibrium in a ternary system. *Technical Physics Letters*. 2021;47(2): 135–138. https://doi.org/10.1134/S1063785021020036

13. Fedoseev V. B., Fedoseeva E. N. States of a supersaturated solution in limited-size systems. *JETP Letters*. 2013;97(7): 408–412. https://doi.org/10.1134/S0021364013070059

14. Fedoseev V. B., Fedoseeva E. N. Size effects during phase transformations in stratifying systems. *Russian Journal of Physical Chemistry A*. 2014;88(3): 436–441. https://doi.org/10.1134/S0036024414020083

15. Fedoseeva E. N., Fedoseev V. B. Possibilities and peculiarities of spray technologies in organic synthesis. *Kondensirovannye sredy i mezhfaznye granitsy = Condensed Matter and Interphases*. 2020;22(3): 397–405. https://doi.org/10.17308/kcmf.2020.22/3001

16. Poharukova Y. E., Novikov V. T., Glotova V. N. Polycondensation of lactic acid to oligomers in the solution. *Bulletin of the Kuzbass State Technical University*. 2017;(1): 134–139. (In Russ., abstract in Eng.). https://www.elibrary.ru/item.asp?id=28897134

17. Glotova V. N. Improvement of lactide synthesis and purification technology. Cand. tech. sci. diss. Thesis. Tomsk: TPU, 2016. 129 p. (In Russ). Available at: https://elar.urfu.ru/bitstream/10995/40461/1/urfu1572_d.pdf

18. Pavlyukevich N. V., Fisenko S. P., Khodyko Yu. A. Coalescence and diffusion growth of nanoparticles in

closed microvolume of supersaturated solution. *Colloid Journal*. 2010;72(6): 825–829. https://doi.org/10.1134/S1061933X10060141

19. Fedoseev V. B., Fedoseeva E. N. Formation of bi- and polymodal distributions and the non-ostwald behavior of disperse systems. *Journal of Engineering Physics and Thermophysics*. 2019;92(5): 1191–1200. https://doi.org/10.1007/s10891-019-02033-2

20. Fedoseev V. B., Fedoseeva E. N. Formation of monodisperse and narrow disperse ensembles of droplets of aqueous organic solutions in the vapor of volatile components. *Journal of Engineering Physics and Thermophysics*. 2020;93(5): 1116–1122. https://doi.org/10.1007/s10891-020-02212-6

21. Shishulin, A. V., Fedoseev V. B. Features of the influence of the initial composition of organic stratifying mixtures in microsized pores on the mutual solubility of components. *Technical Physics Letters*. 2020;46(9): 938–941. http://dx.doi.org/10.1134/S1063785020090291

22. Shishulin A. V., Fedoseev V. B. On some peculiarities of stratification of liquid solutions within pores of fractal shape. *Journal of Molecular Liquids*. 2019;278: 363–367. https://doi.org/10.1016/j.molliq.2019.01.050.

23. Emel'yanenko V. N., Verevkin S. P., Schick C., Stepurko E. N., Roganov G. N., Georgieva M. K. The thermodynamic properties of s-lactic acid. *Russian Journal of Physical Chemistry A*. 2010;84(9): 1491–1497. https://doi.org/10.1134/S0036024410090074

24. Kuni F. M., Shchekin A. K., Grinin A. P. Theory of heterogeneous nucleation for vapor undergoing a gradual metastable state formation. *Physics-Uspekhi*. 2001;44(4): 331–370. http://dx.doi.org/10.1070/PU2001v044n04ABEH000783

25. Laiadi D., Hasseine A., Merzougui A. Homotopy method to predict liquid-liquid equilibria for ternary mixtures of (water+carboxylic acid+organic solvent). *Fluid Phase Equilibria*. 2012;313(January): 114–120. https://doi.org/10.1016/j.fluid.2011.09.034

26. Toikka M., Samarov A., Toikka A. Solubility, liquid–liquid equilibrium and critical states for the system acetic acid+n-propanol+n-propyl acetate+water at 293.15K and 303.15K. *Fluid Phase Equilibria*. 2014;375: 66–72. https://doi.org/10.1016/j.fluid.2014.04.034

27. Toikka M., Samarov A., Trofimova M., Golikova A., Tsvetov N., Toikka A. Solubility, liquid–liquid equilibrium and critical states for the quaternary system acetic acid–ethanol–ethyl acetate–water at 303.15K and 313.15K. *Fluid Phase Equilibria*. 2014;373: 72–79. https://doi.org/10.1016/j.fluid.2014.04.013

28. Ghanadzadeh Gilani H., Golpour M., Abbasi Souraki B. Ternary equilibrium data of mixtures consisting of 2-butanol, water, and heavy alcohols at T = 298.2 K. *The Journal of Chemical Thermodynamics*. 2012;49: 39–45. https://doi.org/10.1016/j.jct.2012.01.003

29. Domingues L., Cussolin P. A., da Silva J. L., de Oliveira L. H., Aznar M. Liquid-liquid equilibrium data for ternary systems of water+lactic acid+C4-C7 alcohols at 298.2K and atmospheric pressure. *Fluid Phase Equilibria*. 2013;354: 12–18. https://doi.org/10.1016/j.fluid.2013.06.007

30. Faraji S., Mokhtarpour M., Behboudi E., Sadrmousavi A., Shekaari H., Zafarani-Moattar M. T. Vapor-liquid equilibria and computational study for aqueous solutions of novel deep eutectic solvents (amino acid/lactic acid) at 298. *Journal of Chemical and Engineering Data*. 2020;65(7): 3262–3269. https://doi.org/10.1021/acs.jced.9b01169

31. Izhenbina T. N. The solubility of the lactic acid oligomer. *Eurasian Union of Scientists*. 2014;7: 71–72. (In Russ). Availble at: https://www.elibrary.ru/item.asp?id=27642469

32. Littringer E. M., Paus R., Mescher A., Schroettner H., Walzel P., Urbanetz N. A. The morphology of spray dried mannitol particles — The vital importance of droplet size. *Powder Technology*. 2013;239: 162–174. https://doi.org/10.1016/j.powtec.2013.01.065

33. Burlakov V., Goriely A. Thermodynamic limit for particle monodispersity: How narrow can a particle size distribution be? *EPL (Europhysics Letters)*. 2017;119(5): 50001–6. https://doi.org/10.1209/0295-5075/119/50001

34. Wu C., Ying A., Ren S. Fabrication of polymeric micelles with core-shell-corona structure for applications in controlled drug release. *Colloid and Polymer Science*. 2013;291(4): 827–834. DOI: https://doi.org/10.1007/s00396-012-2794-8

35. Toikka A. M., Samarov A. A., Toikka M. A. Phase and chemical equilibria in multicomponent fluid systems with a chemical reaction. *Russian Chemical Reviews*. 2015;84(4): 378–392. http://dx.doi.org/10.1070/RCR4515

Information about the authors

Victor V. Fedoseev, DSc in Chemistry, Leading Researcher, G. A. Razuvaev Institute of Organometallic Chemistry, Russian Academy of Sciences (Nizhny Novgorod, Russian Federation).

https://orcid.org/0000-0001-9281-3137
vbfedoseev@yandex.ru

Elena N. Fedoseeva, PhD in Chemistry, Research Fellow, the Laboratory of Applied Chemistry and Ecology, Lobachevsky State University of Nizhny Novgorod (Nizhny Novgorod, Russian Federation).

https://orcid.org/0000-0002-5066-2331
el.nik.fedoseeva@gmail.com

Received September 11, 20212; approved after reviewing October 20, 2021; accepted February 15, 2022; published online March 25, 2022.

Translated by Valentina Mittova
Edited and proofread by Simon Cox

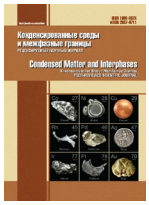

ISSN 1606-867X (Print)
ISSN 2687-0711 (Online)
Condensed Matter and Interphases
Kondensirovannye Sredy i Mezhfaznye Granitsy
https://journals.vsu.ru/kcmf/

Original articles

Research article
https://doi.org/10.17308/kcmf.2022.24/9061

Structural and magnetic properties of Ho-doped $CuFe_2O_4$ nanoparticles prepared by a simple co-precipitation method

Hoang Bao Khanh[1], V. O. Mittova[2], Nguyen Anh Tien[1], Pham Thi Hong Duyen[3]✉

[1]*Ho Chi Minh City University of Education, Ho Chi Minh City 700000, Vietnam*

[2]*Voronezh State Medical University named after N. N. Burdenko, 10 ul. Studencheskaya, Voronezh 394036, Russian Federation*

[3]*Thu Dau Mot University, Binh Duong Province 590000, Vietnam*

Abstract

Nanocrystalline copper (II) ferrite with a spinel structure doped with holmium was synthesized by co-precipitation using an aqueous solution of NaOH as a precipitant and subsequent annealing at 800°C for 60 min. The doping limit was determined by X-ray phase analysis. The similarity of the real and nominal compositions of the doped samples was established by energy-dispersive X-ray spectroscopy using a scanning electron microscope. The obtained particles had an approximately spherical shape, and their size was 40–70 nm (X-ray phase analysis, transmission electron microscopy). The introduction of Ho^{3+} cations to $x = 0.15$ into a $CuFe_2O_4$ spinel lattice led to a decrease in the average size of crystallites, an increase in the coercive force of nanopowders, and a decrease in excess magnetization and saturation magnetization. Synthesized $CuFe_{2-x}Ho_xO_4$ ($x = 0$, 0.1 and 0.15) nanopowders were magnetically hard materials with high coercive force.

Keywords: $CuFe_2O_4$, Ho-doping, Co-precipitation method, Magnetic properties

For citation: Hoang B. K., Mittova V. O., Nguyen A. T., Pham T. H. D. Structural and magnetic properties of Ho-doped $CuFe_2O_4$ nanoparticles prepared by a simple co-precipitation method. *Kondensirovannye sredy i mezhfaznye granitsy = Condensed Matter and Interphases*. 2022;24(1): 109–115. https://doi.org/10.17308/kcmf.2022.24/9061

Для цитирования: Хоанг Б. Х., Миттова В. О., Нгуен А. Т., Фам Т. Х. З. Структура и магнитные свойства нанопорошков $CuFe_{2-x}Ho_xO_4$, синтезированных методом совместного осаждения. *Конденсированные среды и межфазные границы*. 2022;24(1): 109–115. https://doi.org/10.17308/kcmf.2022.24/9061

✉ Pham Thi Hong Duyen, e-mail: duyenpth@tdmu.edu.vn

1. Introduction

The synthesis and study of the characteristics of nanomaterials now attracts a lot of attention, since nanoparticles possess a set of properties different from those of macrosized analogues [1–5]. Among the magnetic materials, nanocrystalline ferrites with an MFe_2O_4 type spinel structure (M = Co, Ni, Zn, Cu) are distinguished by high values of magnetic permeability, saturation magnetization, and are used to create new multifunctional materials, such as high-frequency devices, due to a decrease in the energy of Foucault's currents and, accordingly, an increase in the duration of their operation [4, 6–9]. In addition, ferrites with a spinel structure are cheaper and more stable (in time and temperature) compared to metals and alloys.

Ferrites with an MFe_2O_4 spinel structure doped with various metal cations are usually synthesized by methods such as sol–gel technology [6–9], hydrothermal synthesis [10], solid phase reaction [11], or coprecipitation with the addition of organic compounds [12]. The studies [4, 13] describe the features of the formation of nanopowders of ferrites – spinels MFe_2O_4 (M = Zn, Co, Ni) by a simple co-precipitation method via the hydrolysis of cations in boiling water followed by the addition of appropriate precipitants in the absence of surface active substances (SAS). According to literature, $CuFe_2O_4$ in the form of nanocrystals doped with holmium ($CuFe_{2-x}Ho_xO_4$), were not synthesized in a similar way.

Thus, the purpose of this study was the synthesis and investigation of the magnetic properties of nanocrystalline ferrite – copper (II) spinel, doped with holmium, formed by a simple chemical coprecipitation method.

2. Experimental

The starting materials were aqueous solutions of copper (II), iron (III), and holmium (III) nitrates (analytical grade reagents) with molar ratio $Cu^{2+} : Fe^{3+} : Ho^{3+} = 1 : (2-x) : x$ (x = 0, 0.1, 0.15, and 0.2). An aqueous solution of NaOH was used as a precipitant. An aqueous solution of a mixture of $Cu(NO_3)_2 \cdot 3H_2O$, $Fe(NO_3)_3 \cdot 9H_2O$, and $Ho(NO_3)_3 \cdot 5H_2O$ (50 mL) was added dropwise to 450 mL of boiling water with stirring using a magnetic stirrer. After the introduction of salts, boiling was continued for another 10 min, while the solution acquired a brown-red colour, then the system was cooled to room temperature, and the 5% NaOH solution was added dropwise until the complete precipitation of Cu^{2+}, Fe^{3+} and Ho^{3+} cations similarly to [13–14]. The resulting precipitate was stirred for 60 min and then precipitated within 15 min. After separation on a vacuum filter, the precipitate was washed with distilled water until pH ~ 7.0 was reached and dried at room temperature. Annealing was carried out in a muffle furnace at 800°C for 60 min. Such an annealing regime was chosen based on the results of [13, 15].

The phase compositions of the samples were determined using X-ray phase analysis (XRD, D8-ADVANCE diffractometer, CuK_α-radiation, λ = 1.5406 Å, 2θ = 10–80°). The average crystal size (D_{av}, nm) of $CuFe_{2-x}Ho_xO_4$ samples was calculated using the Scherrer formula.

The shape and size of the particles were determined using transmission electron microscopy (TEM, electron microscope JEM-1400).

The actual qualitative and quantitative elemental composition of the samples was studied by energy dispersive X-ray spectroscopy (EDX) using an FE-SEM S-4800 scanning electron microscope. The quantitative elemental composition was determined as the average of the values obtained at five different points of each sample.

The hysteresis loop and magnetic characteristics of $CuFe_{2-x}Ho_xO_4$ (x = x = 0, 0.1, 0.15 and 0.2) nanopowders at room temperature, including saturation magnetization (M_s,), coercive force (H_c, Oe) and residual magnetization (M_r) were recorded using a Microsene EV11 magnetometer with a vibrating sample under the action of a magnetic field in the range from –16,000 to +16,000 Oe.

3. Results and discussion

X-ray diffraction patterns of powders of a nominal composition of $CuFe_{2-x}Ho_xO_4$ (x = 0, 0.1, 0.15, and 0.2), obtained by co-deposition after annealing at 800°C for 60 min are shown in Fig. 1. For samples with values x = 0, 0.1 and 0.15, peaks corresponding to the standard peaks of $CuFe_2O_4$ spinel phase (JCPDS: 04-001-9258; Copper Iron Oxide) were obtained. On the diffraction pattern of a sample with a nominal degree of doping

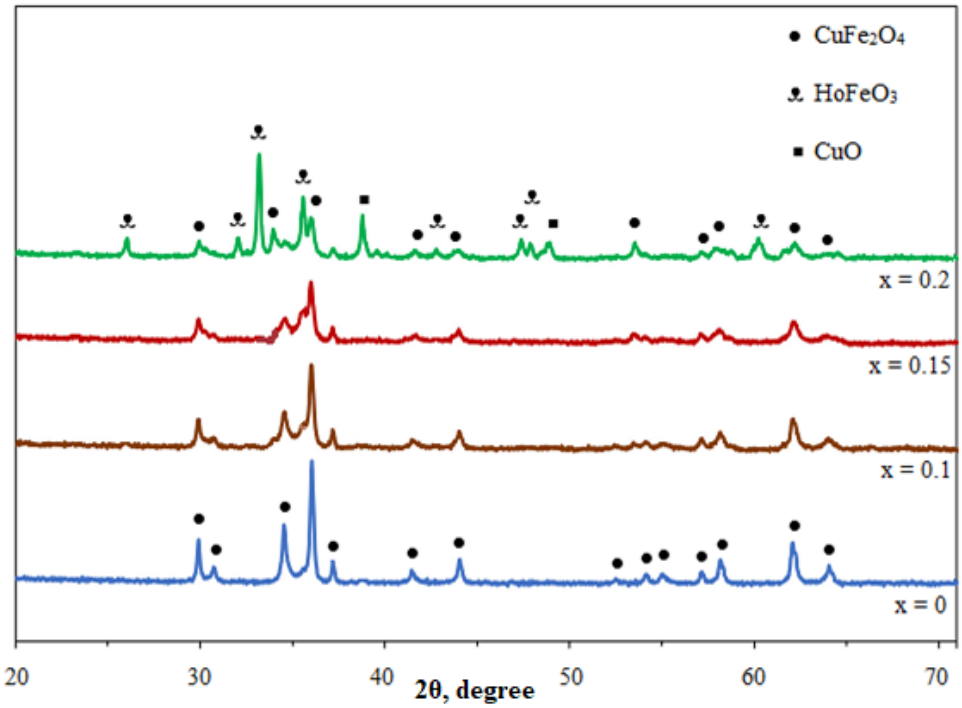

Fig. 1. X-ray diffraction patterns of samples of nominal composition $CuFe_{2-x}Ho_xO_4$ synthesized by co-precipitation after annealing at 800°C for 60 min

$x = 0.2$ in addition to the peaks of the phase with the copper(II) spinel structure $CuFe_2O_4$, peaks corresponding to the following phases: CuO (JCPDS: 04-004-5685; Copper Oxide) and $HoFeO_3$ (JCPDS: 01-084-8725; Holmium Iron Oxide) were revealed.

Thus, according to XRD data, the limit for the doping of ferrite – copper spinel with holmium from $x = 0.15$ to $x = 0.2$ after annealing at 800 °C for 60 min was established. The limiting level of doping was due to the difference in the ionic radii of the substituted element and the dopant, the ionic radius Ho^{3+} ($r = 1.04$ Å) was much larger than the ionic radius of Fe^{3+} ($r = 0.65$ Å) [16–17]. An increase in the degree of doping in the $CuFe_2O_4$ lattice led to a decrease in the value of the angle 2θ for the peak with the highest intensity (Table 1). This once again indicates the successful doping of copper spinel ferrite with holmium and incorporation of the latter into the $CuFe_2O_4$ lattice. The analysis of the crystal sizes determined using the Scherrer formula [18] based on X-ray diffractometry data showed a decrease in D_{av} with an increase in the degree of doping of copper ferrite with Ho^{3+} ions from $x = 0$ to $x = 0.15$, followed by an increase at $x = 0.2$ (Table 1). Such an anomaly at $x = 0.2$ could be related to the phase inhomogeneity of the samples when two impurity phases appear (CuO and $HoFeO_3$) (Fig. 1), which causes an error in the calculation using the Scherrer formula. The reduction of the average crystal size of $CuFe_{2-x}Ho_xO_4$ (D_{av}) with an increase in the content of Ho^{3+} cations from $x = 0.0$ to $x = 0.15$ is explained by the fact that the substitution of Fe^{3+} cations ($r = 0.65$ Å) by Ho^{3+} cations with a large ionic radius ($r = 1.04$ Å) causes

Table 1. Characteristics of $CuFe_{2-x}Ho_xFeO_4$ samples synthesized by co-precipitation after annealing at 800 °C for 60 min

Samples, nominal composition	2θ, °	D_{av}, nm	H_c, Oe	M_r, emu/g	M_s, emu/g
$CuFe_2O_4$	36.0510	54.6	940.72	13.03	23.64
$CuFe_{1.9}Ho_{0.1}O_4$	36.0301	46.2	1320.11	10.81	21.32
$CuFe_{1.85}Ho_{0.15}O_4$	36.0119	37.8	1501.12	9.15	18.29
$CuFe_{1.8}Ho_{0.2}O_4$	35.5868	42.9	1317.82	6.40	13.14

an increase in the defectiveness of the lattice and, accordingly, increased internal stresses, as a result of which the growth of crystals is inhibited. Similar results were observed in the study [19], in which the substitution of Fe^{3+} in the $CuFe_2O_4$ lattice by doping with Ce^{3+} cations (r = 1.14 Å) led to a decrease in the average crystal size from 25.36 to 18.53 nm with a change in x from 0.0 to 0.5.

Determination of the real elemental composition of $CuFe_2O_4$ and $CuFe_{1.85}Ho_{0.15}FeO_3$ samples showed that peaks were observed only for the elements Cu, Fe, O, and Ho, and their content was very close to the nominal composition. Impurities of other elements were not revealed (Fig. 2).

TEM images of $CuFe_2O_4$ (A) and $CuFe_{1.85}Ho_{0.15}O_4$ (B), nanopowders annealed at 800°C for 60 min are

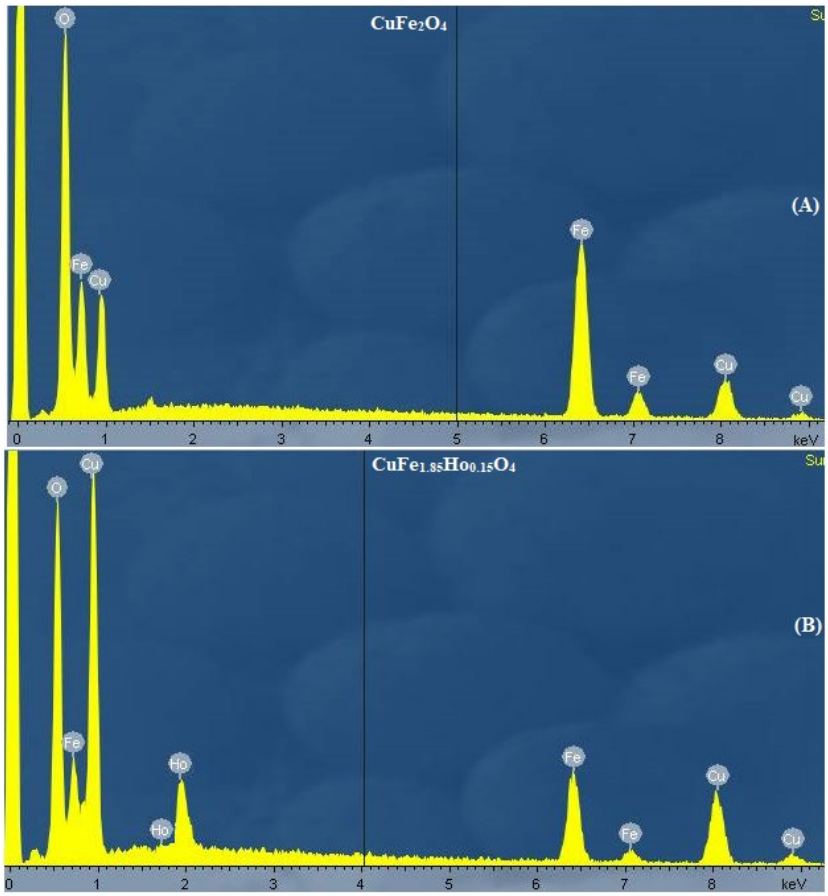

Fig. 2. EDX - X-ray diffraction patterns of $CuFe_2O_4$ (A) and $CuFe_{1.85}Ho_{0.15}O_4$ (B), samples synthesized by co-precipitation after annealing at 800 °C for 60 min

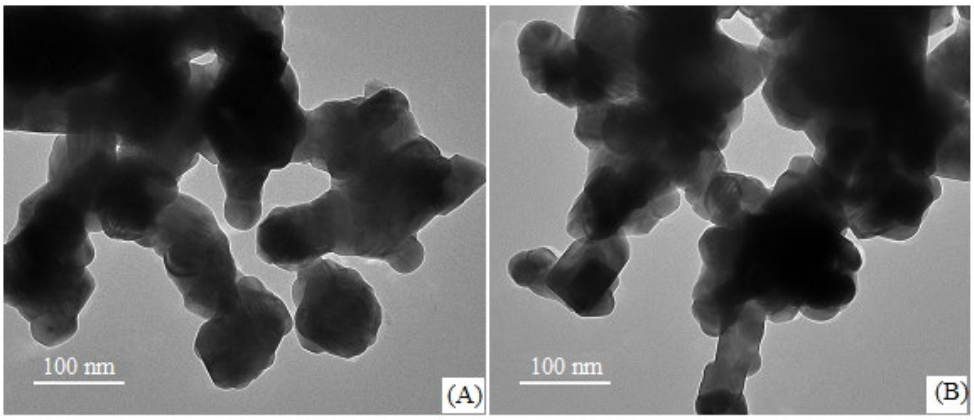

Fig. 3. TEM images of $CuFe_2O_4$ (A) and $CuFe_{1.85}Ho_{0.15}O_4$ (B), nanoparticles synthesized by co-precipitation after annealing at 800 °C for 60 min

shown in Fig. 3. It can be seen that the obtained particles have an approximately spherical shape, and their size was 40–70 nm. The particles were mainly aggregated.

A study of the magnetic characteristics at room temperature showed that the doping of crystal lattice of spinel $CuFe_2O_4$ with Ho^{3+} affected not only the structural characteristics of crystals, but also the magnetic properties of $CuFe_{2-x}Ho_xO_4$ nanopowders (Fig. 4 and Table 1).

Magnetic parameters such as excess magnetization (M_r, emu/g) and saturation magnetization (M_s, emu/g) of $CuFe_{2-x}Ho_xO_4$ samples (nominal composition x = 0, 0.1, 0.15, and 0.2) after annealing at 800 °C for 60 min decreased with increase in Ho^{3+} content, but the coercive force (H_c, Oe) increased with increase in dopant content. An increase in the coercive force is explained by the fact that an increase in the dopant content in $CuFe_2O_4$ crystals led to an increase in their magnetic anisotropy [20–21]. Regardless of the dopant content, the synthesized $CuFe_{2-x}Ho_xO_4$ nanopowders had high values of magnetic characteristics: H_c = 940.72÷1501.12 Oe, M_r = 13.03÷6.40 emu/g, M_s = 23.64÷13.14 emu/g, which opens up prospects for their application as magnetically hard materials for the manufacture of permanent magnets or magnetic recording on hard disks and tapes [20].

4. Conclusions

Ferrite nanopowders $CuFe_{2-x}Ho_xO_4$ (x = 0, 0.1 and 0.15) were synthesized by a simple co-precipitation method, using a 5% NaOH aqueous solution as the precipitant. The obtained $CuFe_{2-x}Ho_xO_4$ samples after annealing of the precipitates at 800°C for 60 min had an average particle size of 40–70 nm. Doping limit of spinel ferrite $CuFe_2O_4$ with Ho^{3+} was detected at a nominal value of x = 0.15. The reduction of the average size (D_{av}) of $CuFe_{2-x}Ho_xO_4$ crystals with an increase in the content of Ho^{3+} cations from x = 0.0 to x = 0.15 is explained by the fact that the substitution of Fe^{3+} cations (r = 0.65 Å) by Ho^{3+} cations with a large ionic radius (r = 1.04 Å) causes an increase in the defectiveness of the lattice and, accordingly, increased internal stresses, as a result of which the growth of crystals is inhibited. Synthesized $CuFe_{2-x}Ho_xO_4$ nanoparticles are characterized by higher values of the coercive force and excess magnetization and, accordingly, are magnetically hard materials.

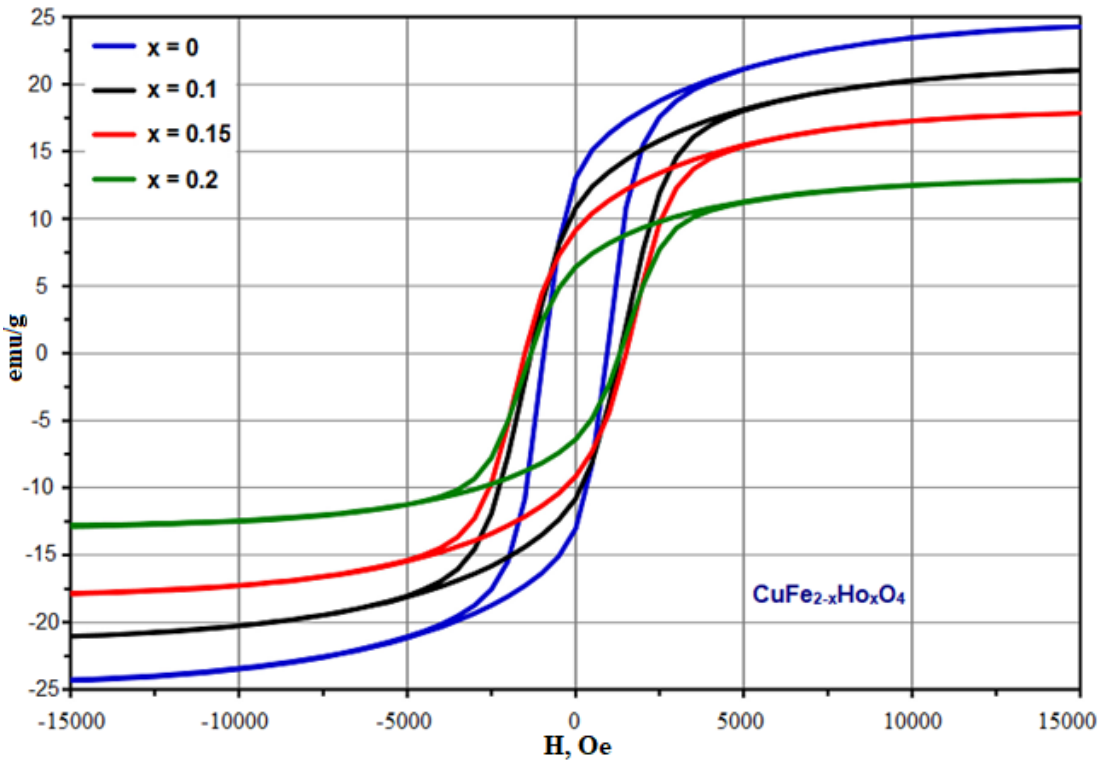

Fig. 4. Field dependences of the magnetization of $CuFe_{2-x}Ho_xO_4$ nanopowders synthesized by co-precipitation after annealing at 800 °C for 60 min

Author contributions

The authors contributed equally to this article.

Conflict of interests

The authors declare that they have no known competing financial interests or personal relationships that could have influenced the work reported in this paper.

References

1. Knurova M. V., Mittova I. Ya., Perov N. S., Al'myasheva O. V., Nguyen A. T., Mittova V. O., Bessalova V. V., Viryutina E. L. Effect of the degree of doping on the size and magnetic properties of nanocrystals $La_{1-x}Zn_xFeO_3$ synthesized by the sol – gel method. *Russian Journal of Inorganic Chemistry*. 2017;62: 281–287. https://doi.org/10.1134/S0036023617030081

2. Bahadur A., Hussain W., Iqbal S., Ullah F., Shoaib M., Liu G., Feng K. A morphology controlled surface sulfurized $CoMn_2O_4$ microspike electroncatalyst for water splitting with excellent OER rate for binder-free electrocatalytic oxygen evolution. *Journal of Materials Chemistry A*. 2021;20(9): 12255–12264. https://doi.org/10.1039/D0TA09430G

3. Berezhnaya M. V., Mittova I. Ya., Perov N. S., Al'myasheva O. V., Nguyen A. T., Mittova V. O., Bessalova V. V., Viryutina E. L. Production of zinc-doped yttrium ferrite nanopowders by the sol-gel method. *Russian Journal of Inorganic Chemistry*. 2018;63(6): 742–746. https://doi.org/10.1134/S0036023618060049

4. Nguyen A. T., Phan P. H. N., Mittova I. Ya., Knurova M. V., Mittova V. O. The characterization of nanosized $ZnFe_2O_4$ material prepared by co-precipitation. *Nanosystems: Physics, Chemistry, Mathematics*. 2016;7(3): 459–463. https://doi.org/10.17586/2220-8054-2016-7-3-459-463

5. Bui X. V., Nguyen A. T. Sol-gel synthesis, crystal structure and magnetic properties of nanocrystalline praseodymium orthoferrite. *Kondensirovannye sredy i mezhfaznye granitsy = Condensed Matter and Interphases*. 2021;23(2): 196–203. https://doi.org/10.17308/kcmf.2021.23/3429

6. Ngo T. P. H., Le T. K. Polyethylene glycol-assisted sol-gel synthesis of magnetic $CoFe_2O_4$ powders as photo-fenton catalysts in the presence of oxalic acid. *Journal of Sol-Gel Science and Technology*. 2018;88: 211–219. https://doi.org/10.1007/s10971-018-4783-y

7. Huynh M. M., Do D. P., Tran T. N., Nguyen H. K. H., Tran Q. H., Luu T. X. T., Le T. K. Synthesis of magnetic $Mn_2O_3/CuFe_2O_4$ catalysts for the aerobic oxidation synthesis of p-hydroxybenzaldehyde. *Catalysis Letters*. 2018;148: 924–932. https://doi.org/10.1007/s10562-017-2293-0

8. Sivakumar P., Ramesh R., Ramanand A., Ponnusamy S., Muthamizhchelvan C. Synthesis and characterization of $NiFe_2O_4$ nanoparticles and nanorods. *Journal of Alloys and Compounds*. 2013;563: 6–11. https://doi.org/10.1016/j.jallcom.2013.02.077

9. Hamid A., Niloofar S., Samane A., Samira G., Mohammad M. G., Ayat M., Nasibeh T. Nanocrystalline $CuFe_{2-x}Sm_xO_4$: synthesis, characterization and its photocatalytic degradation of methyl orange. *Journal of Materials Science: Materials in Electronic*. 2016;27: 4689–493. https://doi.org/10.1007/s10854-016-4347-2

10. Kesavan G., Nataraj. N., Chen S. M., Lin L. H. Hydrothermal synthesis of $NiFe_2O_4$ nanoparticles as an efficient electrocatalyst for the electrochemical detection of bisphenol A. *New Journal of Chemistry*. 2020;44: 7698–7707. https://doi.org/10.1039/D0NJ00608D

11. Douaa B., Muthafar F. A. H., Farah T. M. N. Structural and electrical properties of $CuLa_yFe_{2-y}O_4$ ferrites. *Iraqi Journal of Physics*. 2013;11(21): 102–109. Available at: https://www.iasj.net/iasj/article/88008

12. Hosseini S. A. Morphologies and magnetic properties of dysprosium doped copper ferrite by changing the types of chelating agent. *Journal of Materials Science: Materials in Electronic*. 2017;28: 1086–1091. https://doi.org/10.1007/s10854-016-5632-9

13. Nguyen A. T., Nguyen T. D., Mittova V. O., Berezhnaya M. V., Mittova I. Ya. Phase composition and magnetic properties of $Ni_{1-x}Co_xFe_2O_4$ nanocrystals with spinel structure, synthesized by Co-precipitation. *Nanosystems: Physics, Chemistry, Mathematics*. 2017;8(3): 371–377. https://doi.org/10.17586/2220-8054-2017-8-3-371-377

14. Pham T. H. D., Nguyen A. T. Optical and magnetic properties of orthoferrite $NdFeO_3$ nanomaterials synthesized by simple co-precipitation method. *Kondensirovannye sredy i mezhfaznye granitsy = Condensed Matter and Interphases*. 2021;23(4): 600–606. https://doi.org/10.17308/kcmf.2021.23/3680

15. Nguyen A. T., Nguyen T. T. L., Bui X. V., Nguyen T. H. D., Lieu D. H., Le T. M. L., Pham V. Optical and magnetic properties of $HoFeO_3$ nanocrystals prepared by a simple co-precipitation method using ethanol. *Journal of Alloys and Compounds*. 2020;834: 155098. https://doi.org/10.1016/j.jallcom.2020.155098

16. Housecroft C. E., Sharpe A. G. *Inorganic Chemistry, 2nd edition*. Pearson: Prentice Hall; 2005. 987 p.

17. Vo Q. M., Mittova V. O., Nguyen V. H., Mittova I. Ya., Nguyen A. T. Strontium doping as a means of influencing the characteristics of neodymium orthoferrite nanocrystals synthesized by co-precipitation method. *Journal of Materials Science: Materials in Electronics*. 2021;32: 26944–26954. https://doi.org/10.1007/s10854-021-07068-x

18. Mehdi R. N., Mohsen B., Ali S. N., Mansoureh R. J. Nanocrystalline Ce-doped copper ferrite: synthesis,

characterization, and its photocatalyst application. *Journal of Materials Science: Materials in Electronics*. 2016;26: 11691–11697. https://doi.org/10.1007/s10854-016-5305-8

19. Elayakumar K., Manikandan A., Dinesh A., Thanrasu K., Kanmani K. R., Thilak R. K., Slimani Y., Jaganathan S. K., Baykal A. Enhanced magnetic property and antibacterial biomedical activity of Ce^{3+} doped $CuFe_2O_4$ spinel nanoparticles synthesized by sol-gel method. *Journal of Magnetism and Magnetic Materials*. 2019;478: 140–147. https://doi.org/10.1016/j.jmmm.2019.01.108

20. Cullity B. D., Graham C. D. *Introduction to Magnetic Materials*, *2nd ed.* Canada: John Wiley & Sons, Inc., Publication; 2009. 568 p.

21. Nguyen A. T., Pham L. T., Mittova I. Ya., Mittova V. O., Nguyen T. T. L., Nguyen V. H., Bui X. V. Co-doped $NdFeO_3$ nanoparticles: synthesis, optical and magnetic properties study. *Nanomaterials*. 2021;11: 937. https://doi.org/10.3390/nano11040937

Information about the authors

Hoang Bao Khanh, 3rd year student, Faculty of Chemistry, Ho Chi Minh City University of Education (Ho Chi Minh City, Vietnam).
https://orcid.org/0000-0001-9029-1443
hoangbaokhanhhcmue@gmail.com

Valentina O. Mittova, PhD in Biology, Assistant Professor of Clinical Laboratory Diagnostics Department, Voronezh State Medical University named after N. N. Burdenko, Ministry of Health of the Russian Federation (*Voronezh,* Russian Federation).
https://orcid.org/0000-0002-9844-8684
vmittova@mail.ru

Anh Tien Nguyen, PhD in Chemistry, Chief of Inorganic Chemistry Department, Ho Chi Minh City University of Education (Ho Chi Minh City, Vietnam).
https://orcid.org/0000-0002-4396-0349
tienna@hcmue.edu.vn

Pham Thi Hong Duyen, Master in Chemistry, Lecturer of Institute of Applied Technology, Thu Dau Mot University (Binh Duong Province, Vietnam)/
https://orcid.org/0000-0002-7350-0634
duyenpth@tdmu.edu.vn

Received January 10, 2022; approved after reviewing January 28, 2022; accepted for publication February 15.02.2022; published online March 25, 2022.

Translated by Valentina Mittova
Edited and proofread by Simon Cox

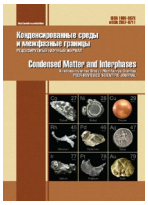

ISSN 1606-867X (Print)
ISSN 2687-0711 (Online)
Condensed Matter and Interphases
Kondensirovannye Sredy i Mezhfaznye Granitsy
https://journals.vsu.ru/kcmf/

Original articles

Research article
https://doi.org/10.17308/kcmf.2022.24/9062

Investigation of the effect of a multicomponent additive on the structure formation and hardening of cement composites

M. A. Shvedova✉, O. V. Artamonova, G. S. Slavcheva

Voronezh State Technical University,
84 ul. 20-Letiya Oktyabrya, Voronezh 394006, Russian Federation

Abstract

The development and application of multicomponent multifunctional additives for cement composites is an important research area since the use of such additives allows controlling both the rheological properties of the freshly prepared mixture and the physical and mechanical characteristics of the finished composite.

This work proposes to use a multicomponent multifunctional additive with the composition of "SiO_2 nanoparticle - superplasticiser - polypropylene fibre" for the modification of cement composite materials based on sand and chalky flour. We studied the peculiarities of the influence of this additive on the technological characteristics of mixtures (plasticity and form stability) and the processes of setting-up, hydration, structure formation, and strength gain of the composite materials.

It was shown that the introduction of this additive allows increasing the plasticity limit and structural strength and reducing relative plastic deformations of the cement mixture at the manufacturing stage. At the same time, this additive accelerates the processes of setting-up, hydration, and strength gain of cement composites. It was proved that the increase in strength is due to the formation of a dense structure of hydrated new growths of the cement substance formed by phases of low and highly basic calcium silicate hydrates of various compositions and morphologies, as well as the absence of a portlandite phase.

The optimal ratio of indicators of plasticity and form stability of cement mixtures and the strength of composites based on them obtained by using the studied additive allows us to recommend to use this additive in the innovative construction 3D printing technology.

Keywords: Cement hardening systems, Modification, Structure formation, Multifunctional additives, Rheological characteristics, Compressive strength

Acknowledgements: The experimental studies were carried out using the facilities of the Professor Borisov Centre for Collective Use, Voronezh State Technical University which is partly supported by the Ministry of Science and Education of the Russian Federation, Project No. 075 – 15 – 2021 – 662.

For citation: M. A. Shvedova, O. V. Artamonova, G. S. Slavcheva Investigation of the effect of a multicomponent additive on the structure formation and hardening of cement composites. *Kondensirovannye sredy i mezhfaznye granitsy = Condensed Matter and Interphases*. 2022;24(1): 116–128. https://doi.org/10.17308/kcmf.2022.24/9062

Для цитирования: Шведова М. А., Артамонова О. В., Славчева Г. С. Многокомпонентные добавки для модифицирования цементных композитов. *Конденсированные среды и межфазные границы*. 2022;24(1): 116–128. https://doi.org/10.17308/kcmf.2022.24/9062

✉ Maria A. Shvedova, e-mail: marishwedowa@mail.ru

1. Introduction

The emergence and development of new construction technologies, such as the construction of unique high-rise buildings and structures and construction 3D printing, requires improving existing and creating new cement-based composite materials with a set of specific properties. Therefore, during the initial stage, the freshly prepared mixture should have specified fabricability indicators. In particular, for the innovative 3D printing process, of fundamental importance are such fabricability indicators as plasticity, form stability, and accelerated setting-up times which are required to create a structure using off-form additive manufacturing. What is more, resulting composite material must have high physical and mechanical properties (density, compressive strength, bending strength, frost resistance, etc.) to ensure the standard service life of the constructed building or structure.

To create such composite materials, it is necessary to control the formation of their structure in a targeted manner at each scale (micro, ultramicro, and nano) [1], and, accordingly, at each stage of the evolutionary route of the solid phase formation in the cement hardening system: phase nucleation, growth of particles, their agglomeration and spontaneous structure formation [2]. A variety of existing formulation and technological factors (chemical and mineralogical composition of the initial components, the ratio of the mass of water to the mass of cement, mechanical and chemical activation of the binder, mixing conditions and modes, and the use of chemical additives, in particular, nanoadditives) allows controlling the formation of the structure of the cement hardening system at different scales (from nano to micro) [3].

The simplest and most accessible factor for controlling the structure of a cement composite is the use of chemical additives of various nature (inorganic and organic), morphology, and dispersion. Most often, active mineral additives are used as inorganic additives, for example, microsilica, microalumina, and metakaolin [4], as well as chemically synthesised products, for example, calcium nitrate, nitrite, and chloride, sodium silicate, ammonium chloride [5], etc. Various surface-active substances, in particular super- and hyperplasticisers, are typical representatives of organic additives [5, 6]. In addition, to improve the physical and mechanical properties of cement composites, disperse reinforcing components such as polypropylene, glass, basalt, or steel fibres are being used more often [7–9].

The above mentioned individual additives are involved in the structural formation of cement hardening systems at various scales and therefore have a selective effect on the properties of the cement composite. In this regard, it is relevant to study the use of multicomponent multifunctional additives which include inorganic, organic, and micro-reinforcing components in their composition, which will determine the multifunctionality and additivity of their action when obtaining the resulting composite.

To ensure the maximum efficiency of a multicomponent additive, it is necessary to select an inorganic component in accordance with the conditions of molecular, morphological, and topological selection [10]. This means that the crystal-chemical structure of the component particles should be close to those of the cement clinker minerals, which will allow them to form the optimal crystal structure of the material (denser, with fewer pores and voids). For cement hardening systems, amorphous silicon dioxide-based additives will meet these conditions. This is confirmed both by the literature data [11–15] and the results of our own studies [16, 17]. At the same time, the dispersion of SiO_2 particles, which are a part of multicomponent additives, can be different (micro-, ultra-, and nano-). It should be noted that nanosized SiO_2 particles influence the formation of the structure of cement hardening systems during the nucleation stage of the solid phase particles (nanoscale). It is advisable to use a superplasticiser as an organic component of the additive, which will prevent the growth and agglomeration of SiO_2 particles and will solve the complex technological problem of their uniform distribution in the volume of the cement system [16]. Thus, the action of the superplasticiser will manifest itself at the ultrascale level of the formation of the composite structure. Various types of fibres can be used as a micro-reinforcing component, which will contribute to the additional strengthening of the cement composite at the microscale level by preventing

the propagation of cracks formed in the process of the spontaneous structure formation.

In this paper, we propose to use a multi-component multifunctional additive of the following composition: "nanosized SiO_2 particles – superplasticiser – polypropylene fibre" for the modification of cement composites. Previously, in our own studies [16], we found that the addition of the composition "nanosized SiO_2 particles – superplasticiser" has a positive effect on the processes of hydration, structure formation, and strength gain of cement systems without fillers and aggregates.

Thus, the purpose of this work was to study the effect of a multicomponent multifunctional additive of the composition "nanosized SiO_2 particles – superplasticiser – polypropylene fibre" on the rheological characteristics and the processes of setting-up, hydration, structure formation, and strength gain of cement composite materials based on quartz sand and chalky flour.

2. Experimental

For experimental studies, modified cement systems were obtained. Their initial components were Portland cement (C), grade CEM I 42.5 (GOST 31108-2016), process water (W) (GOST 23732-2011), superplasticiser (SP) based on polycarboxylate esters, grade Sika® ViscoCreat® T100. Chalky flour (CF) containing at least 95% of $CaCO_3$ (GOST 32761-2014) was used as a filler. The particle size of chalky flour was between 2 and 55 μm. Quartz sand (S) with a fineness modulus $M_f \leqslant 1.25$ (GOST 8736-2014) was used as an aggregate.

As a modifier, we used a complex nano-sized additive (CNA) with the composition of SiO_2 particle – SP, Sika® ViscoCreat® T100 ($\omega(SiO_2)$ = 0.01%, ω(SP) = 0.2% of the mass of cement) with an average particle size of SiO_2 between 5 and 10 nm obtained by sol-gel synthesis using the procedure described in detail in [10]. It should be noted that this modifier was a mixing liquid. A 12 mm long polypropylene fibre (PF), brand SikaFiber® PPM-12 (ISO 9001:2008, EN 14889-2:2008), was used as a reinforcing component. Its content was 0.5% of the mass of cement. To obtain a multicomponent multifunctional additive, the required amount of superplasticiser was added to the mixing liquid and thoroughly mixed. Next, a polypropylene fibre was added to the resulting solution and mixed again.

Cement systems with the composition C–W–SP–CNA–S, C–W–SP–CNA–S–PF, C–W–SP–CNA–CF, and C–W–SP–CNA–CF–PF were obtained by mixing dry components (cement, sand or cement and chalky flour) and the resulting multi-component multifunctional additive in a mixer for 3 minutes. When obtaining viscoplastic mixtures, the mass ratios of C:CF and C:S were 1:1 and 1:1.25, respectively. The water-cement ratio (the ratio of the mass of water to the mass of cement – formulation and technological parameter, W/C) in systems with sand was 0.26, and in systems with chalky flour was 0.37. These ratios are optimal and were determined experimentally from preliminary studies. The C–W–SP–CNA system (W/C = 0.24) was recognised as a reference system.

The rheological behaviour of the obtained viscoplastic mixtures was evaluated by the methods of compressive rheometry [18–20]. To conduct compression tests, we used cement-water paste to make cylinder samples with the radius R equal to their height h_0 = 25 mm. The tests were carried out using the INSTRON 5982 universal floor hydraulic testing system.

To assess the plasticity of mixtures, the compression test was performed at a constant strain rate of 5 mm/s [18]. The curves "load N – displacement Δ" obtained as a result of testing were interpreted as dependencies of the reduced load F^* on the relative change in sample height h_i/R:

$$F_i^* = \frac{Ph_i}{\pi R^2},$$

where $h_i = (h_0 - \Delta)$, h_0 is the initial height of the sample, Δ is the displacement at the i-th moment of time, the value R was taken as a constant equal to the sample radius at the beginning of the test.

At the first points of inflexion of the obtained experimental curves, the estimate of the plastic yield value K_i(I) was calculated:

$$K_i(\frac{h}{R}) = \frac{\sqrt{3}}{2} F^*.$$

To assess the form stability, a compression test was performed at a constant load rate of

ν = 0.5 N/s [19, 20]. As a result of experimental studies, we obtained the following curves "relative displacement Δ – time *t*", "load *N* – relative displacement Δ", which were used to calculate the values of the structural strength of cement systems at the moments corresponding to the beginning of deformation and the beginning of cracking of the samples according to the formula:

$$\sigma = \frac{P}{\pi R^2}.$$

As a result, the plasticity and form stability of mixtures under conditions simulating the action of compressive stresses during extrusion and layering were evaluated by the following criteria:

– Estimation of plastic yield value K_i (I).

– Structural strength σ_0 at the beginning of deformation, which is responsible for the ability of the system to resist deformation under load.

– Plastic strength σ_{pl} and the value of relative plastic deformations Δ_{pl} at the beginning of cracking. They characterise the ability of the system to deform without destruction.

It should be noted that the optimal values of the plasticity and form stability criteria for viscoplastic cement mixtures were determined in [20] and were: K_i(I) = 1.0–2.5 kPa, σ_0 = 3–5 kPa, σ_{pl} = 30–40 kPa, Δ ⩽ 0.05 mm/mm.

The kinetics of setting-up of the resulting viscoplastic systems was studied by the penetrometer method [21]. Value P_{pl} was calculated as the reduced value of penetration resistance:

$$P_{pl} = \frac{4N}{\pi d^2},$$

where *N* is penetration resistance of the mixture when a plunger with a standard diameter is immersed to a depth of 5 mm, kN; *d* is the plunger diameter, m^2. The method error was 10%.

The phase composition of the cement brick was determined by powder diffraction (ARL X'TRA diffractometer, CuK_α is radiation, λ = 1.541788 Å). The obtained data were processed using the PDWin 4.0 software package [22]. The value of the degree of hydration of the modified cement hardening systems was calculated by the content of the alite phase 3CaO SiO_2 (C_3S) by comparing their XRD patterns with the XRD pattern of the original cement clinker [23]:

$$D_h(C_3S) = (1 - \frac{I_{mod}}{I_0}) \times 100\%.$$

where I_{mod} is the intensity of the diffraction maximum at *d* = 2.75 Å of the C_3S phase of the samples of different compositions by types of additives and the timing of cement hydration; I_0 is the intensity of the diffraction maximum at *d* = 2.75 Å of the C_3S phase of the original cement.

The microstructure of the cement brick was assessed using scanning electron microscopy (SEM) (JEOL JSM-7001F scanning electron microscope).

The kinetics of the strength gain of the studied cement hardening systems was determined by the destruction of sample cubes with the size of 5×5×5 cm using an INSTRON Sates 1500HDS testing machine. To ensure the statistically reliable results of physical and mechanical tests, the number of samples in the series was 6. The measurement uncertainty was 0.5%.

3. Results and Discussion

3.1. Plasticity and form stability of modified systems

Figure 1 shows the curves of the dependence of the reduced load F^* on the relative change in sample height h_i/R.

The studied cement systems were characterised by two types of curves. The C–W–SP–CNA–P, C–W–SP–CNA–S–PF, and C–W–SP–CNA–CF systems had a horizontal section between two points of inflexion, which is characteristic of viscoplastic fluid before the destruction of the structure. The curves of the C–W–SP–CNA–P and C–W–SP–CNA–CF–PF systems were almost horizontal and did not have a pronounced plasticity region. In this case, the value of the plastic yield value $K_i(I)$ (Table 1) for the system with quartz sand, compared to the reference system, increased by 2.3 times, while in the system with carbonate flour it decreased by 1.6 times. In microreinforced cement systems, the plasticity limit values increased by 2.6 times in the C–W–SP–CNA–S–PF system, and by 1.1 times in the C–W–SP–CNA–CF–PF system.

As a result of the experimental investigation of form stability of the studied systems two types of curves were obtained: "relative displacement Δ – time *t*" (Fig. 2a) and "relative displacement –

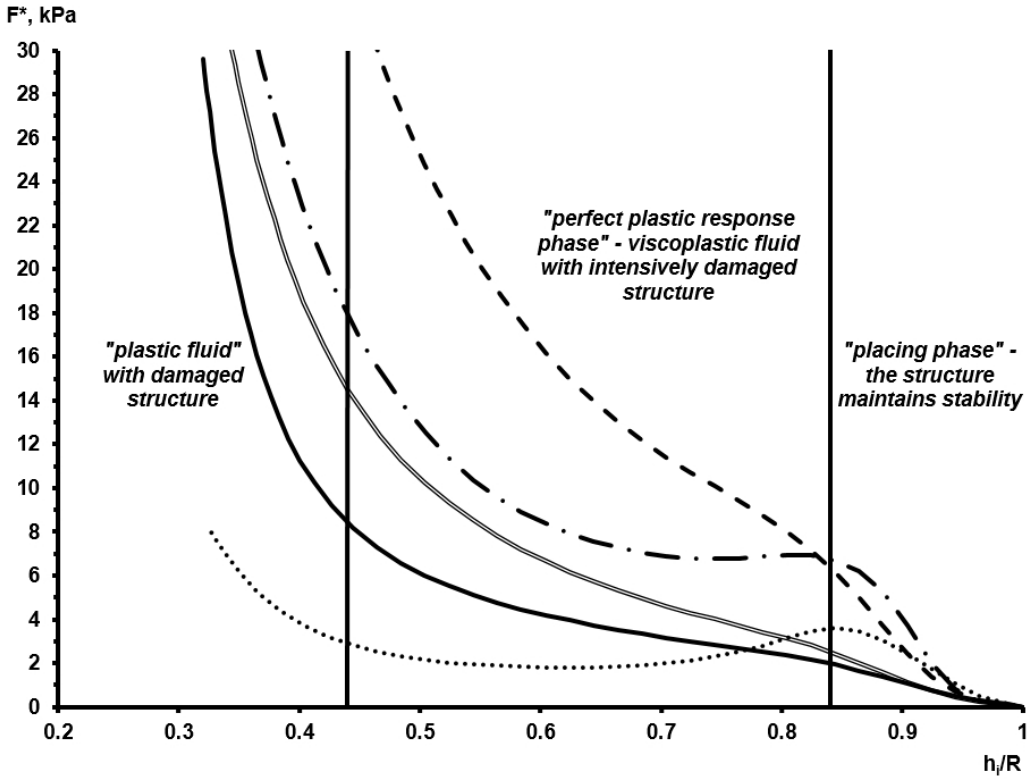

Fig. 1. Curves of the dependence of the reduced load F^* on the relative change in sample height h_i/R. Designated: ━ – C–W–SP–CNA; •••• - C–W–SP–CNA–S; – – – – C–W–SP–CNA–S–PF; –•–•– – C–W–SP–CNA–CF; ═ – C–W–SP–CNA–CF–PF

Table 1. Rheological characteristics of modified cement systems

System	Plastic yield value $K_i(I)$, kPa	Structural strength σ_0, kPa	Plastic strength σ_{pl}, kPa	Relative plastic deformation Δ_{pl}, mm/mm
C–W–SP–CNA	1.42	1.64	41.20	0.13
C–W–SP–CNA–S	3.28	1.17	57.80	0.07
C–W–SP–CNA–S–PF	3.66	5.44	26.75	0.03
C–W–SP–CNA–CF	0.90	1.43	42.48	0.14
C–W–SP–CNA–CF–PF	1.54	3.04	40.75	0.07

load σ" (Fig. 2b). The first type of curves was characterised by three sections: the "phase stability", which characterised the absence of deformations under loads; "plastic phase", which characterised the ability of the system to deform without destruction, and "cracking phase", in which cracking occurred before the complete destruction of the structure. On the "relative displacement – load σ" curves, the moment when microcracks appeared in the systems corresponded to a sharp drop in the load.

The analysis of the obtained results allowed establishing that the studied systems had form stability indicators (σ_0, σ_{pl}, Δ_{pl} Table 1) close to optimal [20].

At the same time, the C–W–SP–CNA–CF–PF and C–W–SP–CNA–S–PF systems had the highest structural strength. In these systems, the values of σ_0 increased by 2.1 and 4.6 times, respectively, compared to the same systems without fibre. It should be noted that the values of maximum structural strength and minimum plastic deformations were achieved in the C–W–SP–CNA–S–PF system and were 5.44 kPa and 0.03 mm/mm, respectively.

The effect of CNA on the rheological behaviour of the studied systems was that nanosized SiO_2

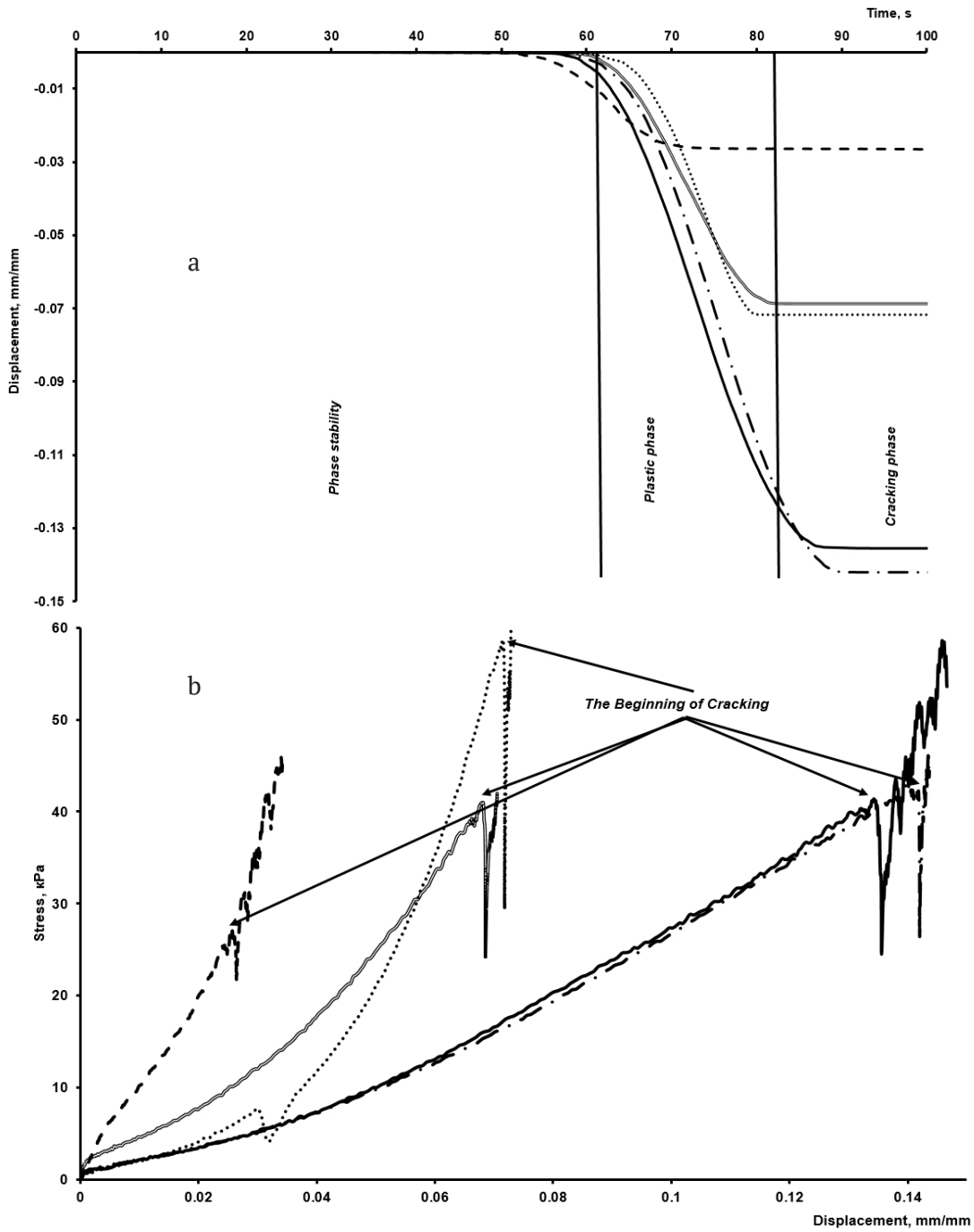

Fig. 2. Dependence curves a) "relative displacement Δ – time *t*"; b) "load σ – relative displacement Δ". Designated: ▬ – C–W–SP–CNA; •••• – C–W–SP–CNA–S; – – – – C–W–SP–CNA–S–PF; –•–•– – C–W–SP–CNA–CF; ═ – C–W–SP–CNA–CF–PF

particles contributed to the intensification of the processes of dissolution and hydration of clinker minerals, which could result in the increase of the ionic strength of the disperse medium, which would lead to its destruction and a partial decrease in the structural strength of the cement system. At the same time, the superplasticiser which was part of the CNA, due to mono- and polymolecular adsorption on the surface of cement clinker particles reduced their interfacial energy, which resulted in their dispersion. In this case, part of the immobilised water was released, which provided for an increase in the plasticity of the mixture and, accordingly, a slight decrease in

structural strength. Obviously, the polypropylene fibre provided cement systems with additional rigidity, which led to a decrease in their plasticity, an increase in structural strength, and a decrease in relative plastic deformations.

It should be noted that the rheological characteristics of the studied cement systems were affected not only by the used CNA but also by the type and dispersion of the components used as aggregates and fillers. Quartz sand and chalky flour used in the work are substances of a polyfraction composition which differ in their crystal-chemical nature and dispersion. Due to the relatively large size of its particles, quartz sand located between the grains of cement clinker created a denser spatial packing of solid phase particles, which led to an increase in the rigidity of the cement system. Chalky flour helped to reduce the plastic yield value and, accordingly, the aggregative stability of cement systems. This was due to the fact that, firstly, its particles have a smaller size compared to sand. Secondly, these particles have a sufficiently active surface and are capable of forming polymolecular layers of adsorbed water, which leads to an increase in the plasticity of the cement system.

Thus, in terms of plasticity and form stability, the nanomodified cement system with chalky flour was quite plastic and prone to flow, whereas the nanomodified cement system with quartz sand was more rigid. It should be noted that the introduction of a polypropylene fibre allowed increasing the plastic yield value ($K_i(I)$) by 1.1 and 2.6 times and structural strength (σ_0) by 2.1 and 4.6 times and reducing relative plastic deformations (Δ_{pl}) by 2 and 2.3 times in the systems with quartz sand and chalky flour, respectively. The acceptable values of the plasticity and form stability criteria (K_i(I) = 1.54 kPa, σ_0 = 3.04 kPa, and Δ_{pl} = 0.07 mm/mm) were achieved in the C–W–SP–CNA–CF–PF system.

3.2. Kinetics of early structure formation of modified cement hardening systems

According to the obtained results (Fig. 3), the beginning of the setting-up process of the studied cement hardening systems varied between 105 and 210 minutes.

The process of setting-up proceeded most rapidly in the C–W–SP–CNA–CF–PF and C–W–SP–CNA–S–PF systems. Values of plastic strength of 582–585 kPa corresponding to the beginning of setting-up were achieved in these systems

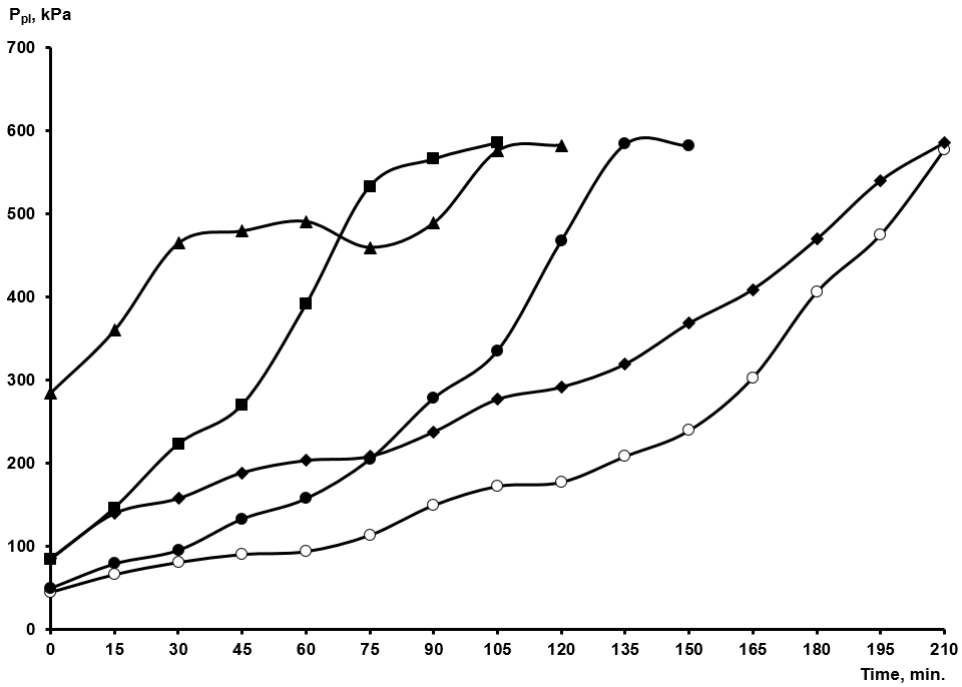

Fig. 3. Curves of the dependence of plastic strength of the studied cement hardening systems on time. Designated: ○ – C–W–SP–CNA; ♦ – C–W–SP–CNA–S; ▲ – C–W–SP–CNA–S–PF; ● – C–W–SP–CNA–CF; ■ – C–W–SP–CNA–CF–PF

within 105 and 120 minutes, respectively. In the C–W–SP–CNA–CF system, similar values of P_{pl} were achieved after 150 minutes, and in the C-W-SP-CNA and C-W-SP-CNA-S systems, they were reached after 210 minutes.

The influence of CNA on the setting-up processes of cement systems was determined by the combined action of its constituent components. For example, the superplasticiser helped to increase the plasticity of cement systems. The mechanism of action was discussed above. At the same time, nanosized SiO_2 particles, due to their high values of surface energy, also acted as ready-made crystallisation centres and chemically could be directly involved in heterogeneous processes of phase formation of hydrated compounds. At the same time, in combination with the effect of the polypropylene fibre, this led to an increase in the values of plastic strength and acceleration of setting-up processes.

It should be noted that the setting-up processes proceeded most rapidly in the nanomodified system with chalky flour, whereas the system based on quartz sand had lower values of plastic strength regardless of the presence of the polypropylene fibre in the system. This was probably due to the fact that the finer grain size of chalky flour allowed obtaining the maximum possible packing density of the particles of the dispersed phase under the given conditions, which, in combination with the CNA effect, contributed to the acceleration of the setting-up process of the cement hardening system.

3.3. Phase composition and microstructure of the studied systems

According to X-ray diffraction analysis (Table 2), after 28 days of hardening, the studied systems were characterised by rather high values of hydration degrees *(D_h),* from 88 to 93%. The highest value of D_h (93%) was achieved in the C-W-SP-CNA reference system.

In cement systems with quartz sand, the dominant phase was quartz (SiO_2), and in systems with chalky flour, it was calcium carbonate ($CaCO_3$) (Fig. 4, Table 2). The main hydrate phases in the reference and quartz sand systems were low and highly basic calcium silicate hydrates

Table 2. Phase composition and degree of hydration of the studied cement systems (duration of hardening 28 days)

System	D_h, %	Phase composition
C–W–SP–CNA	93	$(CaO)_x \cdot SiO_2 \cdot zH_2O$ $xCaO \cdot SiO_2 \cdot zH_2O$ $CaO \cdot SiO_2 \cdot H_2O$ $2CaO \cdot SiO_2 \cdot H_2O$
C–W–SP–CNA–S	89	SiO_2 $CaO \cdot SiO_2 \cdot H_2O$ $2CaO \cdot SiO_2 \cdot H_2O$ $(CaO)_x \cdot SiO_2 \cdot zH_2O$ $xCaO \cdot SiO_2 \cdot zH_2O$
C–W–SP–CNA–S–PF	90	SiO_2 $CaO \cdot SiO_2 \cdot H_2O$ $2CaO \cdot SiO_2 \cdot H_2O$ $(CaO)_x \cdot SiO_2 \cdot zH_2O$ $xCaO \cdot SiO_2 \cdot zH_2O$
C–W–SP–CNA–CF	88	$CaCO_3$ $3CaO \cdot SiO_2 \cdot H_2O$ $3CaO \cdot Al_2O_3 \cdot CaCO_3 \cdot 11H_2O$ $CaO \cdot SiO_2 \cdot H_2O$
C–W–SP–CNA–CF–PF	88	$CaCO_3$ $3CaO \cdot SiO_2 \cdot H_2O$ $3CaO \cdot Al_2O_3 \cdot CaCO_3 \cdot 11H_2O$ $CaO \cdot SiO_2 \cdot H_2O$

$(CaO)_x \cdot SiO_2 \cdot zH_2O$, $xCaO \cdot SiO_2 \cdot zH_2O$, $CaO \cdot SiO_2 \cdot H_2O$, and $2CaO \cdot SiO_2 \cdot H_2O$.

The phase composition of cement systems with chalky flour was represented by low and highly basic calcium silicate hydroxides ($3CaO \cdot SiO_2 \cdot H_2O$ and $CaO \cdot SiO_2 \cdot H_2O$, respectively), as well as a small amount of the calcium hydrocarboaluminate phase $3CaO \cdot Al_2O_3 \cdot CaCO_3 \cdot 11H_2O$.

Therefore, the type of aggregate and filler did not affect the degree of hydration of the studied systems, however, they had a significant effect on the phase composition of hydration products. Due to its inertness, quartz sand did not take part in the reactions of hydration and the formation of new growths of the cement brick, whereas chalky flour, due to the relatively active surface of its particles, was able to partially participate in heterogeneous processes of phase formation resulting in the formation of the $3CaO \cdot Al_2O_3 \cdot CaCO_3 \cdot 11H_2O$ compound. It should be noted that calcium carbonate is able to interact with the aluminate component of Portland cement clinker provided that there is an excess of calcium ions.

It should be noted that the portlandite phase ($Ca(OH)_2$) was absent in all of the studied systems. This was probably due to the fact that nanosized SiO_2 particles are capable of exhibiting a pozzolanic effect: due to their size and high surface energy, they are able to bind free calcium hydroxide into low and highly basic calcium silicate hydrates. In this case, free $Ca(OH)_2$ can be formed in the studied systems in two cases: as a result of the alite hydration reaction (both in systems with quartz sand and in systems with chalky flour) and as a result of the formation of calcium hydrocarboaluminate (in systems with chalky flour). Then, the following chemical transformations take place:

1) dissolution and hydration of alite and tricalcium aluminate:

$$Ca_3SiO_5 + 3H_2O \rightarrow 3Ca^{2+} + 4OH^- + H_2SiO_4^{2-}$$

$$Ca_3Al_2O_6 + 6H_2O \rightarrow 3Ca^{2+} + 2Al^{3+} + 12OH^-$$

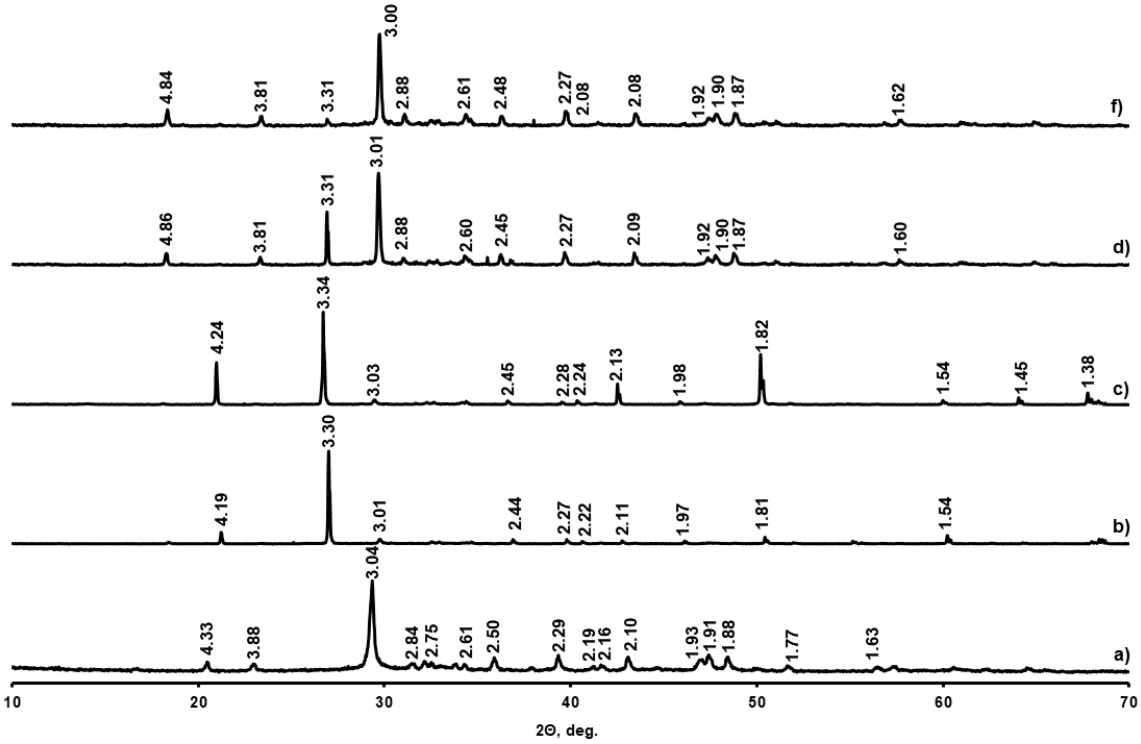

Fig. 4. X-Ray diffraction patterns of the studied cement hardening systems. Designated: a) C–W–SP–CNA; b) C–W–SP–CNA–S; c) C–W–SP–CNA–S–PF; d) C–W–SP–CNA–CF; e) C–W–SP–CNA–CF–PF SiO_2 (d = 4.25, 3.35, 2.45, 1.82, 1.38 Å); $CaCO_3$ (d = 3.34, 3.03, 2.28, 2.07, 1.59 Å); $(CaO)_x \cdot SiO_2 \cdot zH_2O$ (d = 3.05, 2.93, 2.31, 1.67, 1.62 Å); $xCaO \cdot SiO_2 \cdot zH_2O$ (d = 3.06, 2.80, 2.65, 2.14, 2.06 Å); $CaO \cdot SiO_2 \cdot H_2O$ (d = 4.24, 3.01, 2.78, 2.50, 1.89 Å); $2CaO \cdot SiO_2 \cdot H_2O$ (d = 2.92, 2.75, 1.93, 1.86, 1.75 Å); $3CaO \cdot SiO_2 \cdot H_2O$ (d =3.26, 3.01, 2.88, 2.47, 2.08 Å); $3CaO \cdot Al_2O_3 \cdot CaCO_3 \cdot 11H_2O$ (d =3.78, 2.85, 2.52, 2.34, 2.09 Å)

2) formation of calcium hydrocarboaluminate and low and highly basic calcium silicate hydrates:

$$9Ca^{2+} + 2Al^{3+} + 12OH^{-} + CaCO_3 + 11H_2O \rightarrow$$
$$\rightarrow 3CaO{\cdot}Al_2O_3{\cdot}CaCO_3{\cdot}11H_2O + 6Ca(OH)_2$$

$$xCa^{2+} + 2(x-1)OH^{-} + H_2SiO_4^{2-} \rightarrow$$
$$\rightarrow (CaO)_x - (SiO_2) - (H_2O)_y$$

The X-ray diffraction data correlated with the SEM data (Fig. 5).

In all studied systems, a sufficiently dense structure was formed with a large number of coalescence and intergrowth contacts between crystallites. What is more, the reference system C–W–SP–NA was characterised by the formation of a predominantly amorphous-crystalline structure from a loose tobermorite-like gel (Fig. 5a). The microstructure of cement systems with sand and chalky flour (Fig. 5b, c) was more crystallised and was represented by crystallites of acicular and fibrous morphology, which probably belonged to low and highly basic calcium silicate hydroxides. In addition, lamellar crystallites adjoining each other were present in the C–W–SP–CNA–CF system (Fig. 5c). Most likely, they were formed by calcium hydrocarboaluminate.

3.4. Kinetics of the strength gain of the studied systems

Physical and mechanical testing of compressive strength showed that after 28 days of hardening, all systems had sufficiently high strength characteristics (Table 3, Fig. 6): R_{com} = 82–93 MPa. What is more, the C–W–SP–CNA reference system had the highest indicator of compressive strength both on the 1st and 28th day of hardening.

With the introduction of an aggregate (quartz sand) and a filler (carbonate flour) into the cement hardening system, its strength, as was to be expected, decreased slightly. The polypropylene fibre, which is part of a multicomponent multifunctional additive, as was to be expectedly, increased their strength. Additionally, at the early stages of hardening (days 1 and 3), regardless of the presence of a polypropylene fibre in the cement system, the system with chalky flour had the lowest values for compressive strength. On day 7 and during the remaining hardening time, regardless of the type of filler, the systems were characterized by close values of R_{com}.

It should be noted that for some systems a drop in strength was observed on the kinetic curves of strength gain (Fig. 6). In the C–W–SP–CNA reference system, it occurred on the 7th day of hardening, and in the C–W–SP–CNA–S and C–W–SP–CNA–CF systems it was observed on the 14th day of hardening. This behaviour of the systems was probably associated with the recrystallisation of primary hydrate formations. However, there was no drop in strength in the C–W–SP–CNA–S–PF and C–W–SP–CNA–CF–PF systems, which was probably due to the presence of the polypropylene fibre in their composition, which contributed to additional strengthening of the systems and compensated the decline in strength that occurred on the 14th day of hardening.

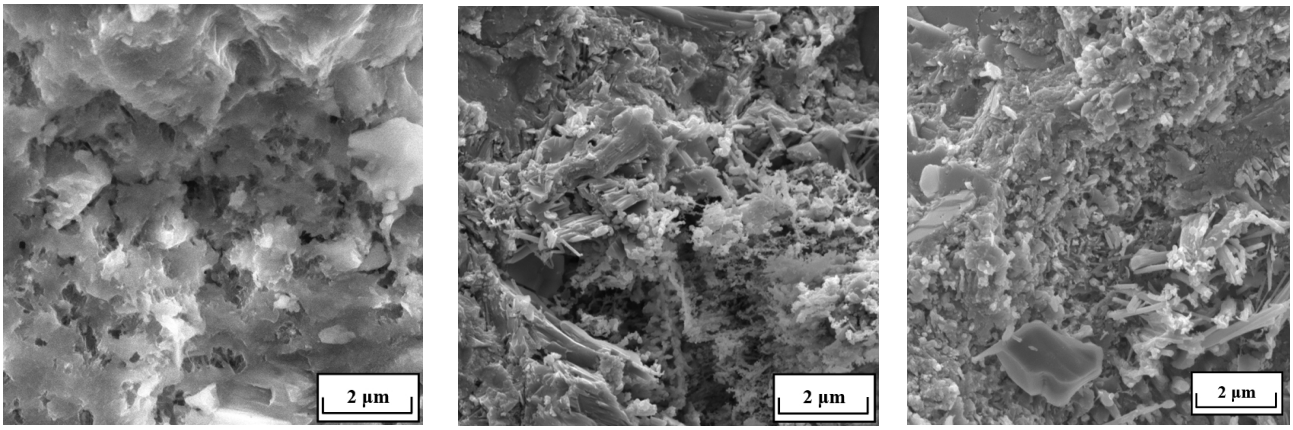

a b c

Fig. 5. Micrographs of the studied cement hardening systems (SEM data). Designated: a) C–W–SP–CNA; b) C–W–SP–CNA–S; c) C-W–SP–CNA–CF

Table 3. Results of physical and mechanical tests of cement hardening systems for compressive strength

No	System	Time, days				
		1	3	7	14	28
		Compressive strength, MPa				
1	C–W–SP–CNA	65	75	70	84	93
2	C–W–SP–CNA–S	53	60	73	67	82
3	C–W–SP–CNA–S–PF	44	62	67	73	85
4	C–W–SP–CNA–CF	38	43	67	59	82
5	C–W–SP–CNA–CF–PF	35	60	69	73	82

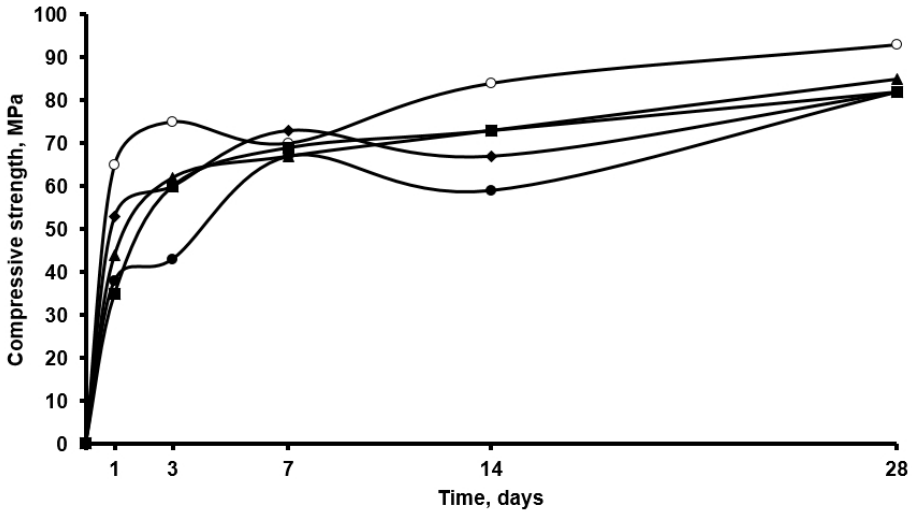

Fig. 6. Kinetic curves of strength gain of the studied cement hardening systems. Designated: ○ – C–W–SP–CNA; ♦ – C–W–SP–CNA–S; ▲ – C–W–SP–CNA–S–PF; ● – C–W–SP–CNA–CF; ■ – C–W–SP–CNA–CF–PF

Therefore, a multicomponent multifunctional additive contributed to the intensification of the process of strength gain in composites based on quartz sand and chalky flour. This effect was probably due to the synergistic effect of all components of the additive but mainly due to nanosized SiO_2 particles which, firstly, performed a catalytic role and acted as ready-made crystallisation centres, they were also directly involved in the formation of hydrated phases of the cement brick. Secondly, they increased the packing density of the system of dispersed particles and changed the porosity structure of the cement composite. This led to a change in the evolutionary route of the structure formation of the cement hardening system at the nanoscale level. What is more, the superplasticiser was able to influence the structure formation of the cement hardening system at the ultramicroscale level, whereas the polypropylene fibre influenced the structure formation at the microscale level due to micro-reinforcement and additional zoning of the composite structure. As a result, the studied cement composites achieved sufficiently high strength characteristics at the early stages of their hardening.

4. Conclusion

We studied the multicomponent multifunctional additive with the composition "nanosized SiO_2 particles – superplasticiser - polypropylene fibre" for the rheological properties of cement composites with quartz sand and chalky flour, as well as the processes of their setting-up, hydration, structure formation, and strength gain. It was established that when this additive is used in cement composites, acceptable values of fabricability indicators (plasticity and form stability) are achieved and the setting-up processes are accelerated. It was shown that a dense structure is formed in modified cement composites mainly from low and highly basic calcium silicate hydrates of various compositions, which provides them with sufficiently high

strength properties throughout the entire hardening time. The obtained results determine the effectiveness of the used additive for modern cement composites and are of high practical importance: high plasticity and form stability of mixtures obtained by using the multifunctional additive determines the possibility of using them in the innovative technology of off-form additive manufacturing. The developed compositions of mixtures have been submitted for patenting and can be offered for commercial sale.

Author contributions

M. A. Shvedova: text writing and editing, conducting experimental studies, systematisation and description of the results. O. V. Artamonova, G. S. Slavcheva: scientific leadership, research concept, methodology development, text writing and editing, final conclusions.

Conflict of interests

The authors declare that they have no known competing financial interests or personal relationships that could have influenced the work reported in this paper.

References

1. Artamonova O. V., Chernyshov E .M. Concepts and foundations of nanomodification technologies for structures of building composites. Part 1. General problems of fundamentality, the main directions of research and development. *Stroitel'nye materialy = Building Materials*. 2013;9: 82–90. (In Russ.). Available at: https://elibrary.ru/item.asp?id=20278771

2. Artamonova O. V., Chernyshov E. M. To the problem of conceptual models of management of the evolutionary route of formation of nanomadified solid systems in tht structure of construction composites. *Izvestiya vysshih uchebnyh zavedenij. Stroitel'stvo = News of Higher Educational Institutions. Construction*. 2018;5(713): 44–57. (In Russ., abstract in Eng.). Available at: https://elibrary.ru/item.asp?id=35618470

3. Nizina T. A., Selyaev V. P., Balykov A. S., Volodin V. V., Korovkin D. I. Optimization of compositions of multicomponent fine-grained fiber-reinforced concrete modified at various scale levels. *Nanotekhnologii v stroitel'stve: nauchnyj internet-zhurnal = Nanotechnologies in construction: an online scientific journal*. 2017;9(2): 43–65. (In Russ.). https://doi.org/10.15828/2075-8545-2017-9-2-43-65

4. Kalpana M., Vaidevi C., Vijayan D. S., Benin S. R. Benefits of metakaolin over microsilica in developing high performance concrete. *Materials Today: Proceedings*. 2020;33(1): 977–983. https://doi.org/10.1016/j.matpr.2020.06.566

5. Ratinov V. B., Rozenberg T. I. *Additives in concrete*. Moscow: Stroyizdat Publ.; 1989. 188 p. (In Russ.)

6. Izotov V. S., Sokolova Yu. A. *Chemical additives for concrete modification*. Moscow: Paleotip Publ.; 2006. 244 p. (In Russ.)

7. Kakooei S., Akil H. M., Jamshidi M., Rouhi J. The effects of polypropylene fibers on the properties of reinforced concrete structures. *Construction and Building Materials*. 2012;27(1): 73–77. https://doi.org/10.1016/j.conbuildmat.2011.08.015

8. Shaikh F. U. A., Luhar S., Arel H. S., Luhar I. Performance evaluation of Ultrahigh performance fibre reinforced concrete – A review. *Construction and Building Materials*. 2020;232: 117152. https://doi.org/10.1016/j.conbuildmat.2019.117152

9. Zeyad A. M. Effect of fibers types on fresh properties and flexural toughness of self-compacting concrete. *Journal of Materials Research and Technology*. 2020;9(3): 4147–4158. https://doi.org/10.1016/j.jmrt.2020.02.042

10. Artamonova O. V. *Synthesis of nanomodifying additives for the technology of building composites*. Voronezh: Voronezhskij GASU Publ.; 2016. 100 p. (In Russ.)

11. Plank J., Sakai E., Miao C. W., Yu C., Hong J. X. Chemical admixtures – chemistry, applications and their impact on concrete microstructure and durability. *Cement and Concrete Research*. 2015;78: 81–99. https://doi.org/10.1016/j.cemconres.2015.05.016

12. Kalashnikov V. I., Tarakanov O. V. About the use of complex additives in new generation concrete. *Stroitel'nye materialy = Building materials*. 2017;1-2: 62–67. (In Russ., abstract in Eng). Available at: https://elibrary.ru/item.asp?id=28392793

13. Kaprielov S. S., Shejnfel'd A. V., Dondukov V. G. Cements and additives for the production of high-strength concrete. *Stroitel'nye materialy = Building materials*. 2017;11: 4–10. . (In Russ., abstract in Eng). Available at: https://elibrary.ru/item.asp?id=30744332

14. Tao Y., Rahul A. V., Lesage K., Yuan Y., K. V. Tittelboom, De Schutter G. Effects of colloidal nanosilica/polycarboxylate ether superplasticizer nanocomposite and graphene oxide on properties of fly ash blended cement. *Construction and Building Materials*. 2020;262: 120767. https://doi.org/10.1016/j.conbuildmat.2020.120767

15. Liu J., Yu C., Shu X., Ran Q., Yang Y. Recent advance of chemical admixtures in concrete. *Cement and Concrete Research*. 2019;124: 105834. https://doi.org/10.1016/j.cemconres.2019.105834

16. Artamonova O. V., Slavcheva G. S., Chernyshov E. M. Effectiveness of combined nanoadditives for cement systems. *Inorganic Materials*. 2017:53(10):

1080–1085. https://doi.org/10.1134/S0020168517100028

17. Slavcheva G. S., Artamonova O. V., Shvedova M. A., Britvina E. A. Effect of viscosity modifiers on structure formation in cement systems for construction 3D printing. *Inorganic Materials*. 2021;57: 94–100. https://doi.org/10.1134/S0020168521010143

18. Russel N., Lanos C. Plastic fluid flow parameters identification using a simple squeezing test. *Applied Rheology*. 2003;13(3): 3–5. https://doi.org/10.1515/arh-2003-0009

19. Perrot A., Rangeard D., Pierre A. Structural built-up of cement-based materials used for 3D-printing extrusion techniques. *Materials and Structures*. 2016;49: 1213–1220. https://doi.org/10.1617/s11527-015-0571-0

20. Slavcheva G. S., Babenko D S., Shvedova M. A. Analysis and criteria evaluation of rheological behavior of mixtures for 3D construction printing. *Stroitel'nye materialy = Building materials*. 2018;12: 34–40. (In Russ.). https://doi.org/10.31659/0585-430X-2018-766-12-34-40

21. Lootens D., Joussett O., Matinie L., Roussel N., Flatt R. J. Yield stress during setting of cement pastes from penetration test. *Cement and Concrete Research*. 2009;39: 401–408. https://doi.org/10.1016/j.cemconres.2009.01.012

22. *JCPDS – International Centre for Diffraction Data*. © 1987 – 1995. JCPDS – ICDD. Newtown Square, PA. 19073. USA. Available at: https://www.icdd.com/

23. Bullard J. W., Jennings H. M., Livingston R. A. Mechanisms of cement hydration. *Cement and Concrete Research*. 2011;41: 1208–1223. https://doi.org/10.1016/j.cemconres.2010.09.011

Information about authors

Maria A. Shvedova, PhD applicant, engineer at the Department of Chemistry and Chemical Technology of Materials, Voronezh State Technical University (Voronezh, Russian Federation).

https://orcid.org/0000-0002-6484-8719
marishwedowa@mail.ru

Olga V. Artamonova, PhD in Technical Sciences, Associate Professor, Professor at the Department of Chemistry and Chemical Technology of Materials, Voronezh State Technical University (Voronezh, Russian Federation).

https://orcid.org/0000-0001-9157-527X
ol_artam@rambler.ru

Galina S. Slavcheva, PhD in Technical Sciences, Associate Professor, Professor at the Department of Technology of Building Materials, Products, and Structures, Voronezh State Technical University (Voronezh, Russian Federation).

https://orcid.org/0000-0001-8800-2657
gslavcheva@yandex.ru

Received October 18, 2021; approved after reviewing October 27, 2021;accepted for publication February 15, 2022; published online March 25, 2022.

Translated by Irina Charychanskaya
Edited and proofread by Simon Cox

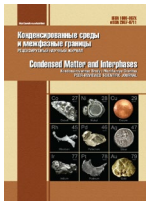

ISSN 1606-867X (Print)
ISSN 2687-0711 (Online)
Condensed Matter and Interphases
Kondensirovannye Sredy i Mezhfaznye Granitsy
https://journals.vsu.ru/kcmf/

Original articles

Research article
https://doi.org/10.17308/kcmf.2022.24/9063

A model of interdiffusion occurring during the formation of thin metal films on single-crystal silicon under conditions of limited solubility of the components

N. N. Afonin[1]✉, V. A. Logachova[2]

[1]*Voronezh State Pedagogical University,*
86 ul. Lenina, Voronezh, 394043, Russian Federation

[2]*Voronezh State University,*
1 Universitetskaya pl., Voronezh, 394018, Russian Federation

Abstract

Thin metal films are used in semiconductor and microelectronic devices to form ohmic and non-ohmic contacts to single-crystal silicon. A common feature of the used Me–Si systems is the low mutual solubility of elements and the polycrystalline nature of metal films. Solid-phase interactions during the deposition of metals on single-crystal silicon and the subsequent vacuum annealing results in the redistribution of the elements near the Me/Si interface. An important task facing the material science of solid-state electronics is to develop a mechanism of solid-phase interaction of metal thin films and single-crystal silicon. The aim of our study – was to develop a quantitative model of interdiffusion in the Me–Si system under conditions of limited solubility of the components.

The article suggests a mechanism of formation of Me–Si systems based on the diffusion and segregation of silicon near the intergrain boundaries of the metal and the limited formation of complexes during the diffusion-induced penetration of metal into silicon. The article suggests a model of reactive interdiffusion in thin metal film – single-crystal silicon systems under conditions of limited solubility of the components. Mathematical modelling was used to study the interaction of magnetron-sputtered metals Ti, W, and Nb with single-crystal silicon during isothermal vacuum annealing. The numerical analysis of experimental distributions of concentrations of Me and Si obtained by Rutherford backscattering spectroscopy allowed us to determine their individual diffusion coefficients in Me-Si systems.

The model can be used for empirical studies of the redistribution of the elements of two-layer systems with limited solubility, as well as to forecast the technological conditions for the production of electronic devices.

Keywords: Modelling, Reactive interdiffusion, Limited solubility, Metal thin films, Single-crystal silicon.

For citation: Afonin N. N., Logachova V. A. A model of interdiffusion occurring during the formation of thin metal films on single-crystal silicon under conditions of limited solubility of the components. *Kondensirovannye sredy i mezhfaznye granitsy = Condensed Matter and Interphases*. 2022;24(1): 129–135. https://doi.org/10.17308/kcmf.2022.24/9063

Для цитирования: Афонин Н. Н., Логачева В. А. Модель взаимодиффузии при формировании тонких плёнок металлов на монокристаллическом кремнии в условиях ограниченной растворимости компонентов. *Конденсированные среды и межфазные границы*. 2022;24(1): 129–135. https://doi.org/10.17308/kcmf.2022.24/9063

✉ Nikolay N. Afonin, e-mail: nafonin@vspu.ac.ru

1. Introduction

Thin films of metals such as Al, Pt, Nb, Au, Ag, Co, Pd, Ni, Ti, and W [1] are used in semiconductor and microelectronic devices to obtain ohmic and non-ohmic contacts to silicon. The contacts are typically constructed by depositing a metal on silicon followed by annealing in an inert medium. The interaction between the metal and the semiconductor is considered to have the following effect: the presence of the metal in the crystal lattice of silicon results in the weakening and breaking of covalent Si-Si bonds and the formation of mobile silicon atoms [2]. The flow of silicon atoms is directed towards the metal-silicon interface, while the metal atoms flow in the opposite direction. This results in the interdiffusion and redistribution of both metal in silicon and silicon in the metal film. The difference in the diffusion coefficients of the atoms moving towards each other results in the Kirkendall effect [3], which comes in the form of the motion of the interface in the diffusion couple.

Physicochemical interaction between metals and silicon results in the formation of eutectic systems. When the electronegativity of the diffusing metal atoms is significantly different from that of Si, a solid-phase reaction of the formation of silicide can take place [1, 4]. It is assumed that silicide phases with various concentrations of silicon and metal are formed layer-by-layer on the Me/Si interface [5].

A common feature of the used Me-Si systems is that after its deposition on silicon and during the following annealing in an inert medium, the metal remains in a polycrystalline state. The heat treatment facilitates the faster movement of grain boundaries in the metal and faster diffusion of Si in the metal film. However, the existing understanding of the interdiffusion in the Me-Si system does not take into account the role of grain boundaries in the process of diffusion-controlled growth of silicide phases and the formation of solid solutions over a wide range of temperatures.

Another feature of the used Me-Si systems is the limited solubility of silicon in the crystallites of metal and limited solubility of metal in single-crystal silicon. The existing literature does not provide enough details regarding the diffusion mechanism of the used metals in silicon and diffusion of silicon in metal.

To control the redistribution of the components near the metal-silicon interface and obtain the electrical and technological parameters of the formed structures required for the semiconductor and microelectronic devices, it is necessary to develop a mechanism for the solid-phase interaction of thin metal films and single-crystal silicon. Therefore, an important task facing the material science of solid-state electronics is to simulate the processes of interdiffusion, segregation, and solid-phase chemical reactions in the Me-Si system.

The purpose of our study was to develop a model of interdiffusion occurring during the formation of the thin metal film – a single-crystal silicon system under conditions of limited solubility of the components.

2. Description of the model

Let's assume that when a metal interacts with single-crystal silicon, its crystal lattice partially disintegrates. Some of the silicon atoms from the crystal lattice become free and transfer to a free mobile state. In the single-crystal Si, they move as self-interstitial atoms, while in the metal film they move – in the intergrain space.

Silicon has low solubility in metal crystallites. Therefore, regarding the dissolution of silicon in the metal film, we shall assume that silicon does not diffuse and dissolve in the crystallites of metal. However, under conditions of low solubility in crystallites, deep diffusion of silicon may occur along the grain boundaries together with the solubility in the intergrain space containing a large concentration of defects. As a result, the solubility limit of silicon in the intergrain space may be significantly higher than that in the crystallite volume.

Grain boundaries contain unsaturated coordinate bonds appearing on the surface of the metal grains and serve as trap centres for silicon, characterising the presence of vacant positions for silicon trapping. We assume that the mechanism of silicon trapping by metal is accompanied by a release of free metal (silicon replaces metal in the traps). Then, the formation of a solid solution of silicon in metal can be described as a diffusion penetration of mobile silicon from the single-crystal phase to the intergrain space of the metal film followed by a partial segregation trapping by

vacant trap centres. As a result, Me and Si atoms moving in the film become immobilised on the Me grain boundaries, losing their mobility.

This stage of the process is carried out by the mechanism of physical adsorption without chemical interactions resulting in the formation of compounds (silicides). The stage is topochemical and takes place in the Me film volume as a result of diffusion penetration of silicon. It is localised on the grain boundaries where the energy loss induced by bond deformation is minimal and there is some free volume facilitating the reorientation of the reacting particles. The trapping of silicon proceeds until there are no vacant traps. Along with the process of silicon trapping, the solution becomes saturated with dissolved silicon. In terms of numerical value, the concentration of traps corresponds to the solubility limit of silicon in the intergrain space of a polycrystalline metal and constitutes fraction *r* of the total concentration of the metal.

Regarding the process of dissolution of metal in the single-crystal silicon phase, let's assume that along with the diffusion penetration of metal into silicon, the decomposition of the solid solution of metal in silicon takes place resulting in the formation of stationary multiparticle complexes containing intrinsic point defects in silicon and metal atoms. This process limits the solubility of metal in single-crystal silicon.

A large number of metals can produce silicides with various concentrations of components, when interacting with silicon. With regard to the suggested mechanism, this ability can be interpreted as follows. The intergrain space of the metal film has an increased concentration of defects and therefore enough free volume for the potential formation of silicides whose molar volumes are different from that of the metal. During the later stages of the process and with an increased annealing temperature, a chemical absorption stage with the formation of metal enriched silicides can occur near the Me/Si interface, on the side of the metal film and in its depth. On the silicon side of the Me/Si interface, silicon enriched silicides can be formed based on the obtained complexes. The required free volume will be provided for by the intrinsic point defects in silicon. In this case, silicides do not grow layer-by-layer on the Me/Si interface. Rather, they are formed inside an extended reaction zone next to it compatible with the initial Me film. The large extent of this zone indicates a relatively slow solid-phase reaction as compared to the rate of diffusion of mobile Si and metal atoms.

[6] suggested a convenient (from the point of view of numerical analysis) mathematical description of the interdiffusion process for a binary system with unlimited solubility. It does not take into account the chemical transformations that may occur during the interdiffusion and is based on the assumption that the molar volume of the system is invariable, regardless of the changes in its composition. In [6], the process is described by means of a boundary value problem for two diffusion equations which contain an effective interdiffusion coefficient which is a linear combination of individual diffusion coefficients of all the components.

The theory suggested in [6] is applied to the formation and growth of interface phases in the diffusion zone [7-10].

[11] for the first time developed the theory suggested in [6] as applied to bulk reactions of the formation of metal silicides during the interaction between the film of the silicide-forming Ni and SiC. However, the model suggested in [11] cannot be used to describe the redistribution of the components inside an extended reaction zone. We believe that this can be down to the fact that the model does not account for the changes in the molar volume of the system during the solid-phase reaction of the formation of silicides.

[12–14] used the mathematical description from [6] in a quantitative model which developed the theory suggested in [6] as applied to the reactive interdiffusion in two-layer metal-metal oxide systems with limited solubility of the components. This model can be used to describe the formation of complex polycrystalline Co–TiO_2 and Fe–TiO_2 thin-film systems which form not by layer-by-layer growth at the metal-oxide interface, but throughout the film thickness of TiO_2.

[15] developed the theory suggested in [6] and introduced a model of reactive interdiffusion in nonstoichiometric polycrystalline oxide film systems with limited solubility under vacuum annealing conditions. The model was used to describe the formation of the phases of complex

oxides distributed along the depth of the system of two nonstoichiometric polycrystalline oxides of titanium and cobalt [16].

The application of the model suggested in [6] to the metal film - single-crystal silicon system with limited solubility of the components has not been studied yet.

In our study, we considered the following components of the system.

– Stationary silicon atoms A which constitute the lattice of single-crystal silicon.

– Mobile silicon atoms B formed as a result of interaction between the metal and silicon.

– Vacant trap centres Ct for mobile silicon in the intergrain space of the metal.

– Silicon atoms Bt trapped in the intergrain space of the metal.

– Mobile (free) metal atoms C.

– Stationary complexes C_p in silicon containing metal and silicon atoms.

The total concentration of silicon was comprised of the following elements:

– concentration of silicon C_A at the points of the silicon crystal lattice A;

– concentration C_B of mobile silicon B;

– concentration C_{Bt} of silicon trapped by Bt traps in the intergrain space of the metal; and

– silicon concentration C_{Cp} in metal-silicon complexes C_p:

$C_A + C_B + C_{Bt} + C_{Cp}$.

The total concentration of metal was comprised of the following elements:

– concentration of mobile (free) metal C;

– metal concentration in the vacant trap centres for mobile silicon in the intergrain space of the metal C_{Bt};

– metal concentration C_{Cp} in metal-silicon complexes C_p:

$C_C + C_{Bt} + C_{Cp}$.

The elements of the system capable of diffusion-induced migration are mobile metal atoms C and mobile silicon atoms B released in the presence of the metal from the crystal lattice of silicon. If the beginning of the reference system is the outer border of the Me film, then, with the ratio of individual diffusion coefficients being ($D_C >> D_B$), the Me-Si grain boundary will move towards the surface of the film system as a result of the Kirkendall effect [3]. The elements not capable of diffusion-induced migration will serve as inert markers in the Smigelskas and Kirkendall experiment [3].

In our study, the qualitative nature of the process determines that the molar volume of the system is invariable. Therefore, we assume that the diffusion of Me and Si in the Me-Si system can also be described by means of the mathematical formalism suggested in [6]. Let's determine the effective interdiffusion coefficient for the simulated system as

$$D^* = \frac{D_B \cdot C_C + D_C \cdot C_B}{C_{tot}}, \quad (1)$$

where D_B and D_C – are individual diffusion coefficients of the mobile components - of free silicon and metal respectively, $C_{tot} = C_A + C_B + C_C + C_{Cp} + C_{Bt} + C_{Ct}$ – is the total concentration of all the components of the system.

Let us assume that the rate of destruction of silicon A at the points of the crystal lattice and the rate of generation of mobile silicon B are directly proportional to the concentration of silicon C_A at the points of its crystal lattice A and the concentration of metal C_C in silicon C. The equation describing the concentration of silicon C_A at the points of the crystal lattice A is presented as follows:

$$\frac{\partial C_A}{\partial t} = \frac{\partial}{\partial x}\left(D^* \frac{\partial C_A}{\partial x}\right) - k_1 \cdot C_C \cdot C_A. \quad (2)$$

Let's assume that mobile silicon B participates in three processes:

– formation of silicon as a result of the destruction of the crystal lattice at a rate that is directly proportional to the concentration of atoms at the points of the silicon crystal lattice A and the concentration of atoms of the mobile metal C;

– diffusion of the metal film in silicon and the intergrain space by means of segregation trapping at a rate directly proportional to the concentration C_{Ct} of vacant traps Ct of the metal and the concentration C_B of mobile silicon B;

– trapping of the stationary complexes C_p in silicon at a rate directly proportional to the concentration of atoms of the mobile metal C.

Then, the equation for the concentration C_B of mobile silicon B can be presented as follows:

$$\frac{\partial C_B}{\partial t} = \frac{\partial}{\partial x}\left(D^* \frac{\partial C_B}{\partial x}\right) + \\ + k_1 \cdot C_A \cdot C_C - k_2 \cdot C_{Ct} \cdot C_B - k_3 \cdot C_B \cdot C_C. \quad (3)$$

Silicon is trapped in the intergrain space of the metal at a rate directly proportional to the concentration C_B of mobile silicon B and the concentration C_{Ct} of vacant traps C_t. The equation for the concentration C_{Bt} of silicon Bt trapped in the intergrain space of the metal is

$$\frac{\partial C_{Bt}}{\partial t} = \frac{\partial}{\partial x}\left(D^* \frac{\partial C_{Bt}}{\partial x}\right) + k_2 \cdot C_{Ct} \cdot C_B \ . \quad (4)$$

The rate of trapping Ct in the intergrain space of the metal is directly proportional to the concentration of traps C_{Ct} and the concentration C_B of mobile silicon B. The equation for the concentration C_{Ct} of vacant trap centres C_t is

$$\frac{\partial C_{Ct}}{\partial t} = \frac{\partial}{\partial x}\left(D^* \frac{\partial C_{Ct}}{\partial x}\right) - k_2 \cdot C_B \cdot C_{Ct}. \quad (5)$$

The diffusion equation for the concentration C_C of the mobile metal C takes into account the fact that the metal is released from the traps in the intergrain space of the metal according to the exchange mechanism. It also takes into account the trapping of stationary complexes in silicon at a rate directly proportional to the concentration C_B of mobile silicon B:

$$\frac{\partial C_C}{\partial t} = \frac{\partial}{\partial x}\left(D^* \frac{\partial C_C}{\partial x}\right) + k_2 \cdot C_{Ct} \cdot C_B - k_3 \cdot C_B \cdot C_C. \quad (6)$$

The equation for the concentration C_{Cp} of metal atoms immobilised in C_p complexes takes into account the fact that the rate of bonding of mobile Me to the metal-silicon complexes is directly proportional to the concentration C_B of mobile silicon B and the concentration C_C of metal C in silicon:

$$\frac{\partial C_{Cp}}{\partial t} = \frac{\partial}{\partial x}\left(D^* \frac{\partial C_{Cp}}{\partial x}\right) + k_3 \cdot C_B \cdot C_C. \quad (7)$$

For equations (2)-(7), t – is the time, x – is the depth from the outer surface of the metal film, and k_1, k_2, and k_3 – are rate constants of the formation of mobile silicon, its trapping in the metal film, and formation of metal-silicon complexes respectively.

At the Me-Si interface, the condition for the reflection for all the components of the system is

$$\frac{\partial C_A}{\partial x} = \frac{\partial C_B}{\partial x} = \frac{\partial C_C}{\partial x} = \frac{\partial C_{Cp}}{\partial x} = \frac{\partial C_{Bt}}{\partial x} = \frac{\partial C_{Ct}}{\partial x} = 0$$

when $x = 0$ and $x = L$, (8)

where L is the thickness of the solution region in silicon.

The initial conditions for equations (2)–(7) when simulating the redistribution are the following:

$C_A(x, 0) = 0$, $C_{Ct}(x,0) = r \times N_{SC}$,
$C_C(x,0) = (1 - r) \times N_{SC}$, when $0 \le x \le h$, (9)

$C_A(x, 0) = N_{SA}$, $C_{Ct}(x,0) = 0$, $C_C(x,0) = 0$,
when $h < x \le L$, (10)

$C_B(x, 0) = 0$, $C_{Bt}(x, 0) = 0$, $C_{Cp}(x, 0) = 0$
when all $0 \le x \le L$, (11)

where h is the thickness of the metal film, N_{SA} is the intrinsic concentration of Si atoms ($N_{SA} = 4.98 \cdot 10^{22}$ cm^{-3}), N_{SC} is the intrinsic concentration of metal atoms ($N_{SC} = 5.68 \cdot 10^{22}$ cm^{-3} for Ti, $6.34 \cdot 10^{22}$ cm^{-3} for W, and $5.55 \cdot 10^{22}$ cm^{-3} for Nb), and r is the number of traps for Si atoms in the intergrain space of Me.

The set of equations (2)–(7) with the concentration dependant interdiffusion coefficient (1) was solved numerically by means of the factorization method using implicit conservative difference schemes [17].

The model had the following parameters: individual diffusion coefficients of Me and Si, rate constants k_1, k_2, and k_3, and r.

Fig. 1 *a-c* shows experimental (points *1, 2*) and calculated (curves *1′, 2′*) concentrations of distributions of Me and Si along the depth of the Me-Si film system obtained by means of Rutherford backscattering spectroscopy (RBS) after magnetron deposition of Me (Ti, W, Nb) on single-crystal silicon and vacuum annealing at $T = 673$ K, $t = 30$ min. The experimental and calculated distributions were in good agreement when $k_1 = 1. \cdot 10^{-26}$ cm^3/c, $k_2 = 1. \cdot 10^{-18}$ cm^3/c, and $k_3 = 1. \cdot 10^{-19}$ cm^3/c were identical for all the metals used, and the model parameters were the ones given in Table 1. The obtained curves demonstrate that the dominating diffusant for all the studied systems is mobile silicon (curves *3′* in

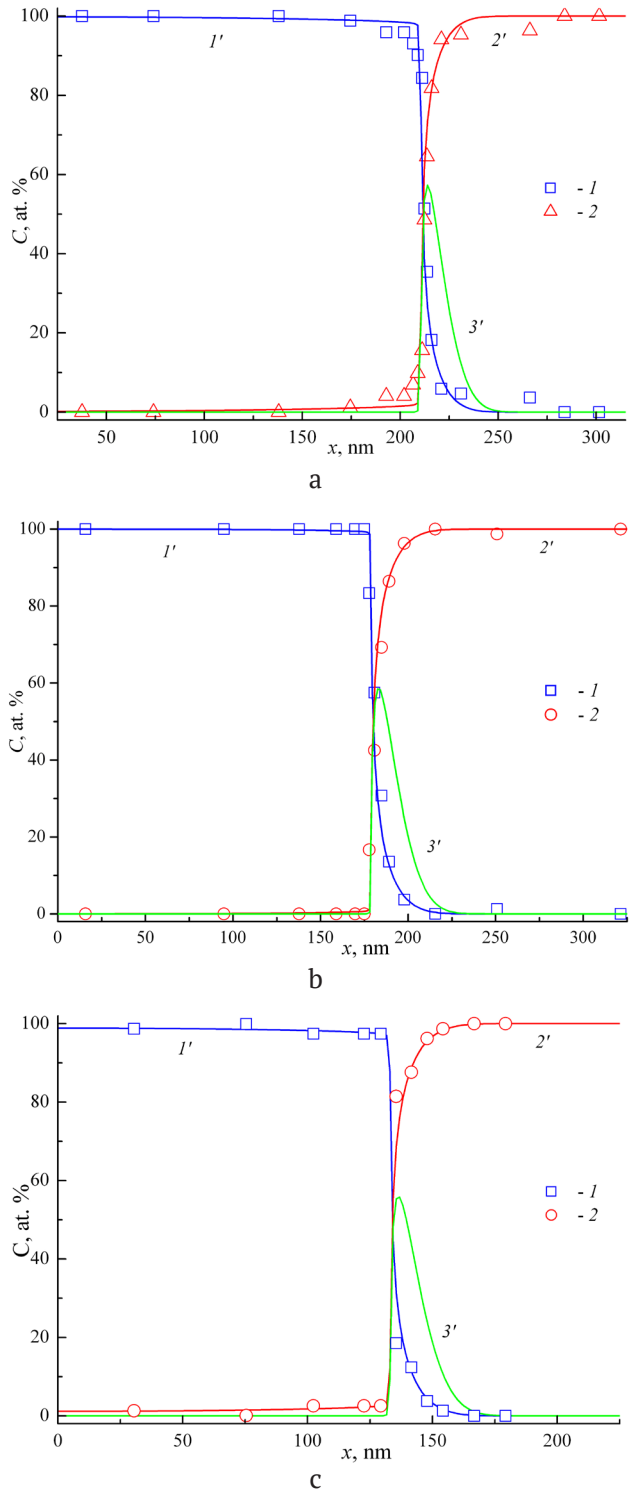

Fig. 1. Experimental (RBS) (points (symbols) *1, 2*) and calculated (curves *1′, 2′, 3′*) distributions along the depth of the Me–Si system of the total concentration *C* of metal (*1′*), silicon (*2′*), and its mobile atoms (*3′*). *1* – Me, *2* – Si; curves: *1′* – Me, *2′* – Si after magnetron sputtering and vacuum annealing at T = 673 K, t = 30 min. (*a*) – Ti, (*b*) – W, (*c*) – Nb.

Table 1. Parameters of the model for Ti, W, and Nb in the Me-Si system

Metal	$D_B \times 10^{14}$ cm²/s	$D_C \times 10^{16}$ cm²/s	r
Ti	4.0	4.0	0.02
W	1.0	6.0×	0.008
Nb	6.0	4.0	0.028

Fig. 1 *a-c*). Its distribution maximum is located at the Me/Si interface.

3. Conclusions

In our study, we developed a model of interdiffusion occurring during the formation of the polycrystalline metal film – single-crystal silicon system with limited solubility of the components. The model is based on the knowledge of solubility of silicon in the intergrain space of the metal, its segregation on the intergrain traps, and the solubility of metal in silicon limited by the complex formation process. Using the numerical analysis of the experimental distribution of concentrations of the elements of Me(Ti, W, Nb)–Si systems within the model, we determined the individual diffusion coefficients for metal and silicon, as well as the number of traps for Si atoms in the intergrain space of Me.

The model can be used to describe the redistribution of the elements of the Me-Si systems for the synthesis conditions ensuring the chemical interaction between metal and silicon and the formation of silicides. It also describes the mechanism of the possible formation of silicide phases near the Me/Si interface as the deep interdiffusion of the elements rather than layer-by-layer growth on the Me/Si interface.

The article also demonstrated that mathematical formalism suggested in [6] for the description of the interdiffusion in binary systems with unlimited solubility, can be used to describe the redistribution of the elements of Me-Si systems with limited solubility of the components.

The model can be used for empirical studies of the interdiffusion processes in Me-Si systems with limited solubility as well as to forecast the technological conditions for obtaining ohmic and non-ohmic Me-Si contacts in micro- and nanoelectronic devices.

Author contributions

Afonin N. N. – scientific leadership, research concept, simulation, text writing, final conclusions. Logachova V. A. – conducting research, review and text writing, editing the text.

Conflict of interests

The authors declare that they have no known competing financial interests or personal relationships that could have influenced the work reported in this paper.

References

1. Murarka S. P. *Silicides for VLSI applications*. Elsevier Science; 1983. 200 p.

2. Thin Films: Interdiffusion and Reactions (Eds: J. M. Poate, K. N. Tu and J. W. Mayer). New York: Wiley; 1978. 578 p.

3. Smigelskas A. D., Kirkendall E. O. Zinc diffusion in alpha-brass. *Transactions of the American Institute of Mining and Metallurgical Engineers*. 1947;171: 130–142.

4. Adamchuk V. K., Lyubinetsky I. V., Shikin A. M. Peculiarities of silicon interaction with noble- metals. *Soviet Technical Physics Letters* 1986;12(17): 1056–1060. Available at: https://www.elibrary.ru/item.asp?id=42823964

5. Prasad S., Paul A. Growth mechanism of phases by interdiffusion and diffusion of species in the niobium–silicon system. *Acta Materialia*. 2011;59: 1577–1585. https://doi.org/10.1016/j.actamat.2010.11.022

6. Darken L. S., Diffusion, mobility and their interrelation through free energy in binary metallic systems. *Transactions of the American Institute of Mining and Metallurgical Engineers.* 1948;175: 184–201. 10.1007/ s11661- 010- 0177- 7 .

7. Gurov K. P., Kartashkin B. A., Ugaste Yu. E. *Mutual diffusion in multiphase metallic systems*. (Ed. K. P. Gurov. Moscow: Nauka Publ.; 1981. 352 p. (In Russ.)

8. Barge T., Gas P. d'Heurle F.M. Analysis of the diffusion controlled growth of cobalt silicides in bulk and thin film couples. *Journal of Materials Research.* 1995;10: 1134–1145. https://doi.org/10.1557/JMR.1995.1134

9. Milanesea C., Buscagliab V., Magliaa F., Anselmi-Tamburinia U. Reactive growth of niobium silicides in bulk diffusion couples. *Acta Materialia*. 2003;51(16): 4837–4846 https://doi.org/10.1016/S1359-6454(03)00323-9

10. Gas P., D'Heurle F. Diffusion processes in silicides: A comparison between bulk and thin film phase formation. *MRS Online Proceedings Library.* 1995;402: 39–50. https://doi.org/10.1557/PROC-402-39

11. Aleksandrov O. V., Kozlovski V. V. Simulation of interaction between nickel and silicon carbide during the formation of ohmic contacts. *Semiconductors.* 2009;43: 885–891 (). https://doi.org/10.1134/S1063782609070100

12. Afonin N. N., Logacheva V. A. Modeling of the reaction interdiffusion in the polycrystalline systems with limited component solubility. *Industrial laboratory. Diagnostics of materials*. 2019;85(9):35-41. (In Russ.) https://doi.org/10.26896/1028-6861-2019-85-9-35-41

13. Afonin N. N., Logacheva V. A. Interdiffusion and phase formation in the Fe–TiO_2 thin-film system. *Semiconductors*. 2017;51: 1300–1305. https://doi.org/10.1134/S1063782617100025

14. Afonin N. N., Logacheva V. A. Cobalt modification of thin rutile films magnetron-sputtered in vacuum. *Technical Physics*. 2018;63: 605–611). https://doi.org/10.1134/S1063784218040023

15. Afonin N. N., Logachova V. A. Modeling of interdiffusion and phase formation in the thin-films two-layer system of polycrystalline oxides titanium and cobalt. *Kondensirovannye Sredy i Mezhfaznye Granitsy = Condensed Matter and Interphases*. 2019;21(3): 358–365. https://doi.org/10.17308/kcmf.2019.21/1157

16. Afonin N. N., Logachova V. A. Reactive interdiffusion of components in a non-stoichiometric two-layer system of polycrystalline titanium and cobalt oxides. *Kondensirovannye Sredy i Mezhfaznye Granitsy = Condensed Matter and Interphases*. 2020;22(4): 430–437. https://doi.org/10.17308/kcmf.2020.22/3058

17. Samarskii A. A., Theory of difference schemes. Moscow: Nauka Publ.; 1977. 656 p. (In Russ.)

Information about the authors

Nikolay N. Afonin, DSc in Chemistry, senior research fellow, professor at the Department of Science and Technology Studies, Voronezh State Pedagogical University, Voronezh Russian Federation.

https://orcid.org/0000-0002-9163-744X
nafonin@vspu.ac.ru

Vera A. Logachova, PhD in Chemistry, senior research fellow at the Department of General and Inorganic Chemistry, Voronezh State University, Voronezh, Russian Federation.

https://orcid.org/0000-0002-2296-8069
kcmf@main.vsu.ru

Received January 1, 2022; approved after reviewing February 15, 2022; accepted for publication March 15, 2022; published online March 25, 2022.

Translated by Yulia Dymant
Edited and proofread by Simon Cox

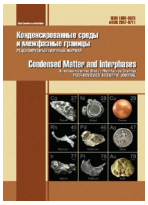

ISSN 1606-867X (Print)
ISSN 2687-0711 (Online)
Condensed Matter and Interphases
Kondensirovannye Sredy i Mezhfaznye Granitsy
https://journals.vsu.ru/kcmf/

Professor Mahammad B. Babanly's anniversary

In January, Mahammad B. Babanly, an outstanding scientist and our good friend, celebrated his 70th birthday.

Babanly was born in 1952. In 1968–1973 he studied at the Faculty of Chemistry of Baku State University, graduated with honours, and enrolled on a PhD programme. In 1977 he defended his PhD thesis at Belarusian State University, and in 1988 he defended his doctoral thesis in the field of "inorganic chemistry" at Moscow State University. In 1990 Babanly gained the title of full professor.

At Baku State University he has worked as a junior researcher (1977–1979), senior researcher (1979–1983), lecturer (1983–1986), associate professor (1986-1989), and professor (1989–1994). From 1992 to 1994 he was vice-rector at Baku State University. In 1994–2005 he was head of the Department of General and Inorganic Chemistry at Baku State University, and from 2006 to the end of March of 2014 he was a professor at this department and scientific supervisor of the "Inorganic material science" research laboratory. At the Institute of Catalysis and Inorganic Chemistry, Azerbaijan National Academy of Sciences, he was deputy director for research from 2014 and became executive director in 2021.

Professor Babanly is a renowned scientist who has created a new scientific field and a scientific school in the field of chemistry, thermodynamics, and material science of complex inorganic semiconductors. In the late 1970s, he was the first to introduce the EMF method into the traditional set of methods for the study of phase equilibria (PE) of three-component semiconductor systems and started a new comprehensive approach to the study of their PE and thermodynamic properties (TP). As part of this approach, he developed a thermodynamically strict method for the calculation of integral thermodynamic functions of ternary and more complex condensed phases based on the partial molar quantities of one of the components and the phase diagram of the corresponding system. Continuing to develop this field of study, he was the first to use solid electrolytes with cationic conductivity for the physicochemical study of complex semiconductor chalcogenides in the late 1980s. Thus he significantly expanded the possibilities of the EMF method so it could be applied to many systems that could not be studied using the traditional version of this method. He also found a new type of potential formation reactions in complex concentration cells and developed a technique for their practical application in thermodynamic studies.

Regular comprehensive studies of the PE and TP of complex semiconductor systems have been conducted under the supervision of Mahammad B. Babanly for over 30 years. For the first time, a set of consistent data on PE and TP was obtained for over 100 three-component chalcogen-containing systems based on thallium, copper, and silver, while dozens of quaternary and quinary systems were studied along stable planes (quasi-ternary and mutual systems). Multiple new compounds and phases of variable compositions

were discovered, and the researchers established the nature of their formation, homogeneity regions, types and parameters of the crystal lattice, standard thermodynamic functions of formation, thermodynamic functions of melting and polymorphic transformations, as well as other properties.

Over the last 10 years, Professor Babanly and his colleagues have also been developing physicochemical bases for obtaining ternary and more complex chalcogenide phases that are topological insulators. Comprehensive studies of single crystals of a series of such phases that were grown by them together with their colleagues from EU countries and Japan showed that it is a promising solution for the new generation quantum computers and spintronics.

The issues raised in the works of Professor Babanly are highly important for the development of fundamental inorganic chemistry and, in particular, physicochemical analysis, chemical thermodynamics, and material science of complex inorganic systems.

Babanly has published more than 1,000 research papers, including 4 monographs, over 550 articles, and 5 patents. Over 200 articles have been published in the international journals included in Science Citation Index (Nature Communications, Journal of Alloys and Compounds, Physical Review Letters, Physical Review B, Mettalkunde, International Journal of Materials Research, and journals of the Russian Academy of Sciences, such as Russian Journal of Inorganic Chemistry, Inorganic materials, Physical Chemistry Journal, Electrochemistry, and others). He has also repeatedly presented his reports at numerous international and regional scientific conferences.

Most scientific results obtained by Professor Babanly and his colleagues have been included into such fundamental reference works as "Phase equilibria diagrams", "Ternary alloys", "State diagrams of metal systems", etc., as well as into the databases of the information agencies Springer, Elsevier, Tomson Reuters, and others.

M. Babanly continues to form and develop his own scientific school. He has supervised 2 doctoral dissertations and 35 PhD theses. Among the scientists with a PhD degree supervised by him are researchers from Syria, Afghanistan, Vietnam, and Korea.

M. Babanly maintains close academic connections with many research organisations of the European Union, Japan, Russian Federation, and Ukraine resulting in numerous joint publications.

Professor Babanly actively participates in the scientific and social life of the Republic of Azerbaijan. In previous years he was a member, the chair, and deputy chair of the Expert Board on Chemistry of the State Commission for Academic Degrees under the President of the Republic of Azerbaijan, a member of the Academic Council of Baku State University as well as several dissertation boards. At present, he is the member of the dissertation board at the Institute of Catalysis and Inorganic Chemistry and the editorial boards of the Turkish Journal of Chemistry, Russian Journal of Inorganic Chemistry, Condensed Matter and Interphases, Physics and Chemistry of Solid State, New Materials, Compounds and Applications and Chemical Problems, and Azerbaijan Chemistry Journal.

In 2000, he was awarded with a Taraggi Medal by the Decree of the President of the Republic of Azerbaijan. In 2011 he received a prize and a diploma of the Praesidium of the Russian

Academy of Sciences for a series of research articles published in the journals of the Russian Academy of Sciences.

In 2016, he was awarded with the Thomson Reuters Special Prize for the most cited "Outstanding Scientific Article".

In 2016, he won the "Scientist of the Year" competition held by the Science Development Fund under the President of the Republic of Azerbaijan.

He also received diplomas from the Russian Journal of Inorganic Chemistry as the author of the most cited articles in 2019 and 2020.

For his scientific achievements he was repeatedly awarded with honorary certificates by the Ministry of Education of the Republic of Azerbaijan, the Department of Chemistry of Azerbaijan National Academy of Sciences, and the rector of Baku State University.

Mahammad B. Babanly is a long-time friend of the Faculty of Chemistry who has come to Voronezh many times and acted as the chair of the Physicochemical Analysis section of the All-Russian Conference with International Participation "PHYSICAL AND CHEMICAL PROCESSES IN CONDENSED MATTER AND INTERPHASE BOUNDARIES". He has repeatedly presented plenary reports that were memorable, attracted great interest, and were discussed by scientists from various cities of Russia for a long time. We are grateful to M. B. Babanly for his active work on the editorial board of the journal "Condensed Matter and Interphases" as an editor, reviewer, and author. Thanks to him, the editorial portfolio includes articles by his colleagues from Azerbaijan that are cited in international scientific databases. We hope that no outside challenges will interfere with our cooperation and future meetings.

We would like to congratulate Professor Mahammad B. Babanly on his 70th birthday and wish him good health, success, and new achievements in his further endeavours!

The team of the Faculty of Chemistry of Voronezh State University,

The Editorial Board of the journal Condensed Matter and Interphases

Translated by Marina Strepetova

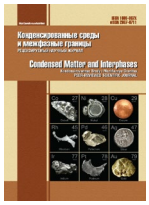

ISSN 1606-867X (Print)
ISSN 2687-0711 (Onine)
Condensed Matter and Interphases
Kondensirovannye Sredy i Mezhfaznye Granitsy
https://journals.vsu.ru/kcmf/

Guide for Authors – 2022

Manuscripts should be submitted as single **Microsoft Word 2003** files.
Preferred font 12 pt Times New Roman (please, do not use any other fonts, except for Symbol), 1.5 spaced lines, 1.25 cm first-line indent. Decimal values (e.g. 0.1; 0.9; 2.3) should be written using a decimal point.

Review/Original article/Short communication
https://doi.org/10.17308/kcmf.2022.24/0000

Modelling of interdiffusion and phase formation in thin-film two-layer systems of polycrystalline oxides of titanium and cobalt

(All proper nouns should be capitalized; titles and subtitles should be left-aligned)

N. N. Afonin*[1], V.A. Logacheva[2]
[1]*Voronezh State Pedagogical University,*
86 ul. Lenina, Voronezh 394043, Russian Federation
(Official name and address of the organisation)
[2]*Voronezh State University,*
1 Universitetskaya pl., Voronezh 394018, Russian Federation

Abstract

The abstract should be 200–250 words and include the following sections.

Purpose: States the problem considered in the article, its importance, and the purpose of the research.

Experimental: Provides information about the objects being studied and the methods used.

Conclusions: Provides a brief description of the principal results, major conclusions, and their scientific and practical relevance.

Keywords: Please, provide 5–10 keywords for the principal concepts, results, and terms used in the article.

Funding: This work was funded by RFBR according to the research project No. 18–29–24128.

Acknowledgments: The DTATGA, XRD and SEM studies were performed on the equipment of the Engineering Center of Saint Petersburg State Institute of Technology.

For citation: Afonin N. N., Logacheva V. A. Modelling of interdiffusion and phase formation in the thin-film two-layer system of polycrystalline oxides of titanium and cobalt. *Kondensirovannye sredy i mezhfaznye granitsy = Condensed Matter and Interphases.* 2022;24(1): 000–000. https://doi.org/10.17308/kcmf.2022.24/0000

*Nikolay N. Afonin, nafonin@vspu.ac

Article structure

The main text of the manuscript should have the following structure.

1. Introduction

The introduction (1–2 pages) states the problem under consideration, its relevance, and the most important tasks that need to be resolved. Describe the scientific problems which have not yet been solved and which you sought to solve in your research. The introduction should contain a short critical review of previously published works in this field and their comparative analysis. It is recommended that the analysis is based on 20–30 studies (at least 15 references to scientific papers, no more than 20% of references to the author's own works, at least 30% of references should be to original articles by international authors, at least 50% of the references should be to articles published within the previous 5 years). **The purpose** of the article is indicated by the problem statement.

The Vancouver reference style is used in the journal: bibliographic references in the text of the article are indicated by numbers in square brackets; in the references section, the references are numbered in the order they are mentioned in the text.

Example of references in-text citations:

Single crystals of difluorides of alkaline earth elements are widely used as photonics materials [1–3] as well as matrices for doping with rare-earth ions [4, 10].

References should primarily be made to original articles published in scientific journals indexed by global citation databases. References should indicate the names of all authors, the title of the article, the name of the journal, year of publication, volume (issue), number, pages, and DOI (Digital Object Identifier https://search.crossref.org/). If a DOI is lacking, a link to the online source of the article must be indicated. References to dissertation abstracts are acceptable if the texts are available online. It is vital that our readers can find any of the articles or other sources listed in the reference section as fast as possible. Links to unpublished literature sources or sources not available online are unacceptable.

2. Experimental

The experimental section (2–3 pages) provides the details of the experiment, the methods, and the equipment used. The object of the study and the stages of the experiment are described in detail and the choice of research methods is explained.

3. Results and discussion

Results and discussion (6–8 pages) should be brief, but detailed enough for the readers to assess the conclusions made. It should also explain the choice of the data being analysed. Measurement units on graphs and diagrams should be separated with a coma. **Formulae should be typed using Microsoft Office Equation 3 or Math Type** and aligned on the left side. Latin letters should be in italics. Do not use italics for Greek letters, numbers, chemical symbols, and similarity criteria.

All subheadings should be in italics.

Example:

1.1. X-ray diffraction analysis

Example of figure captions in the text of the article: Fig. 1, curve *1*, Fig. 2b.

A complete list of figures should be provided at the end of the paper after the information about the authors.

Figures and tables should not be included in the text of the article. They should be placed on a separate page. Figures should also be **submitted as separate** *.tif, *.jpg, *.cdr, or *.ai. files. **All**

figures should have a minimum resolution of 300 dpi. Name each figure file with the name of the first author and the number of the figure.

4. Conclusions

Conclusions (1 paragraph) should briefly state the main conclusions of the research. Do not repeat the text of the article. The obtained results are to be considered with respect to the purpose of the research. This section includes the conclusions, a summary of the results, and recommendations. It states the practical value of the research and outlines further research problems in the corresponding field.

Contribution of the authors

At the end of the Conclusions the authors should include notes that explain the actual contribution of each co-author to the work.

Example 1:

Nikolay N. Afonin – Scientific management, Research concept, Methodology development, Writing – original draft, Final conclusions.

Vera A. Logachova – Investigation, Writing – review & editing.

Example 2:

The authors contributed equally to this article.

Conflict of interests

The authors declare that they have no known competing financial interests or personal relationships that could have influenced the work reported in this paper.

References

(The references are to be formatted according to the Vancouver Style. The reference list should only include articles published in peer-reviewed journals)

***Examples*:**

Articles in scientific journals

1. Luo Y., Zhao J. Plasmon-exciton interaction in colloidally fabricated metal nanoparticle-quantum emitter nanostructures. *Nano Research*. 2019;12(9): 2164–2171. https://doi.org/10.1007/s12274-019-2390-z

2. Alexandrov A. A., Mayakova M. N., Voronov V. V., Pominova D. V., Kuznetsov S. V., Baranchikov A. E., Ivanov V. K., Fedorov P. P. Synthesis upconversion luminophores based on calcium fluoride. *Kondensirovannye sredy i mezhfaznye granitsy = Condensed Matter and Interphases*. 2020;22(1): 3–10. https://doi.org/10.17308/kcmf.2020.22/2524

3. Ryabtsev S. V., Shaposhnik A. V., Samoylov A. M., Sinelnikov A. A., Soldatenko S. A., Kushchev S. B., Ievlev V. M. Thin films of palladium oxide for gas sensors. *Doklady Physical Chemistry*. 2016;470(2): 158–161. https://doi.org/10.1134/s0012501616100055

Books: print

4. Kofstad P. *Nonstoichiometry, diffusion, and electrical conductivity in binary metal oxides*. Wiley-Interscience; 1972. 382 p.

5. Fedorov P. P., Osiko V. V. Crystal growth of fluorides. In: *Bulk Crystal Growth of Electronic. Optical and Optoelectronic Materials*. P. Capper (ed.). Wiley Series in Materials for Electronic and Optoelectronic Applications. John Wiley & Son. Ltd.; 2005. pp. 339-356. https://doi.org/10.1002/9780470012086.ch11

References to online sources

6. NIST Standard Reference Database 71. *NIST Electron Inelastic-Mean-Free-Path Database: Version 1.2*. Available at: www.nist.gov/srd/nist-standard-reference-database-71

Conference proceedings: individual papers

7. Afonin N. N., Logacheva V. A., Khoviv A. M. Synthesis and properties of functional nanocrystalline thin-film systems based on complex iron and titanium oxides. In: *Amorphous and microcrystalline*

semiconductors: Proc. 9th Int. Conf., 7–10 July 2014. St. Petersburg: Polytechnic University Publ.; 2014. p. 356–357. (In Russ.)

Information about the authors

This section should include the full last and first name(s) of the author(s), their academic degree, academic title, affiliation, position, city, country, e-mail, and ORCID (register for an ORCID here https://orcid.org/register).

Example:

Nikolay N. Afonin, DSc in Chemistry, Research Fellow, Professor at the Department of Science and Technology Studies, Voronezh State Pedagogical University (Voronezh, Russian Federation).
https://orcid.org/0000-0002-9163-744X mailto:nafonin@vspu.ac.ru
nafonin@vspu.ac.ru

Vera A. Logachova, PhD in Chemistry, Research Fellow at the Department of General and Inorganic Chemistry, Voronezh State University (Voronezh, Russian Federation).
https://orcid.org/0000-0002-2296-8069 kcmf@main.vsu.ru" kcmf@main.vsu.ru

Valery V. Voronov, PhD in Physics and Mathematics, Head of the Laboratory, Prokhorov General Physics Institute of the Russian Academy of Science (Moscow, Russian Federation).
https://orcid.org/0000-0001-5029-8560 voronov@lst.gpi.ru

Received 30 January 2021; Approved after reviewing 15 February 2021; Accepted 15 March 2021; Published online 25 March 2021.

A complete list of figures should be provided at the end of the paper after the information about the authors.

Example:

Fig. 1. Dependences of the parameters *a* and *c* of the tetragonal lattice of nanocrystalline PdO films on the oxidation temperature T_{ox}: *1* – single-phase PdO films, *2* – heterophase PdO + Pd films; *3* – data of the ASTM standard [22, 23]

Table 1. The values of relative electronegativity (ENE) of some chemical elements [30] and the proportion of the ionic component of the chemical bond in binary compounds of the AB composition formed by these elements

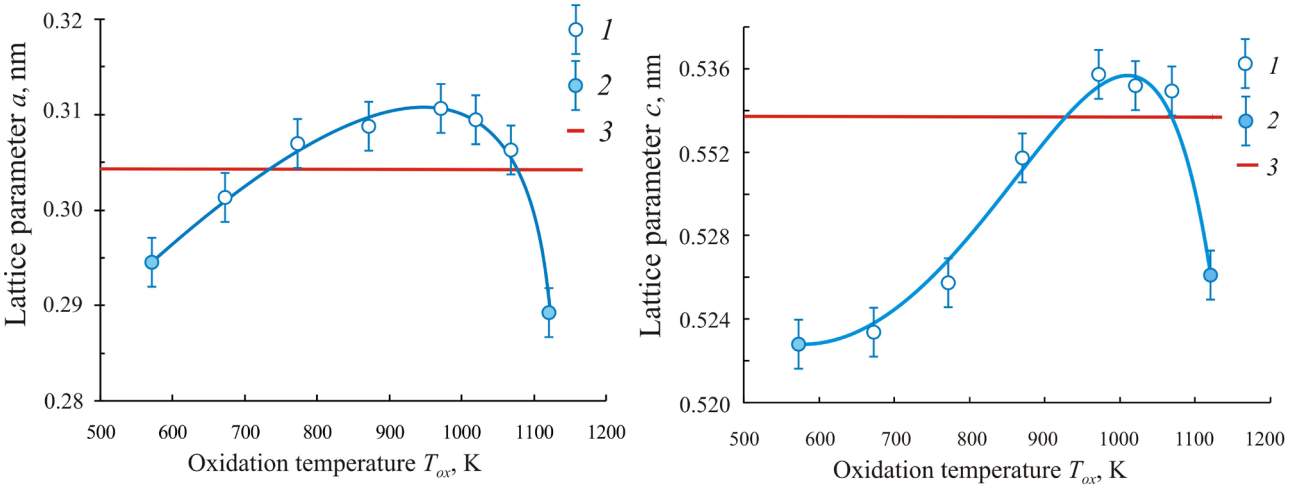

a *b*

Fig. 1. Dependences of the parameters *a* and *c* of the tetragonal lattice of nanocrystalline PdO films on the oxidation temperature T_{ox}: *1* – single-phase PdO films; *2* – heterophase PdO + Pd films; *3* – data of the ASTM standard [22, 23]

Table 1. Values of the ionic radii of palladium Pd^{2+} and oxygen O^{2-} [30–32]

Ion	Coordination number CN	Coordination polyhedron	Values of ionic radii R_{ion}, nm
Pd^{2+}	4	Square (rectangular)	0.078 [30]; 0.086 [31]; 0.078 [32]
O^{2-}	4	Tetragonal tetrahedron	0.132 [30]; 0.140 [31]; 0.124* [31]; 0.132 [32]

*The values of ionic radius were obtained on the basis of quantum mechanical calculations.

ACCOMPANYING DOCUMENTS

(The following documents should be submitted as PDF files)

1. Covering letter (with authorisation for open access publication)
2. License agreement (signed by all authors) https://journals.vsu.ru/kcmf/Licensingcontract

EDITING AND PROOFREADING

When the layout is ready it is sent back to the authors for proofreading. The article should be sent back to the publisher within a maximum of three days. The authors may only correct printing mistakes and introduce minor changes to the text or tables.